Overcoming the efficiency bottleneck of metal sulfide solar cells

Wallace, Suzanne

Award date:
2019

Awarding institution:
University of Bath

Overcoming the efficiency bottleneck of metal sulfide solar cells

submitted by

Suzanne K. Wallace

for the degree of Doctor of Philosophy

of the

University of Bath

Department of Chemistry

April 2019

Acknowledgments

No man is an island[1], and this was certainly the case for me during my 'PhD journey'. Consequently, I have many people to thank for their time, patience, insights and inspiration.

I would like to thank the Centre for Doctoral Training in Sustainable Chemical Technologies at the University of Bath for the support, opportunities and diverse training the centre has provided me with. I would like to thank all members of the Walsh group for their support and knowledge during my PhD, but I would particularly like to thank: Dr. Jarvist Frost, Dr. Katrine Svane, Dr. Keith Butler, Dr. Jonathan Skelton and my primary supervisor Prof. Aron Walsh. I would like to thank my supervisor for his ceaseless enthusiasm, trust and insights, but also for the example he set to me during my PhD: to work hard, but also to enjoy your work.

I would like to thank many researchers for sharing their knowledge with me during collaborative projects or placements. Firstly, developers of the FHI-aims electronic structure software package at Duke University for taking the time to (hopefully!) make me a more informed user: Prof. Volker Blum, Dr. William Huhn, Tong Zhu and Victor Yu. I would also like to thank Dr. Alin Marin Elena from the EnergyMaterials:ComputationalSolutions project for computational support. I would like to thank the many experimental scientists who have taken the time to fill in the many gaps in my knowledge and (hopefully!) make me a more realistic theorist: Prof. David Mitzi at Duke University and researchers in the PVTEAM project: Prof. David Fermin, Dr. Devendra Tiwari, Prof. Laurie Peter, Prof. Mark Weller and Dr. Jake Bowers. I would also like to thank Oliver Weber, Mako Ng, Prof. Chris Bowen and Dr. Vaia Adamaki for their patience in the lab during my masters research project. I would like to thank many researchers from my placement at the National Renewable Energy Lab, again, for taking the time to share their knowledge with me, in particular: Dr. Stephan Lany, Dr. Elisabetta Arca, Dr. Anuj Goyal and Dr. Prashun Gorai.

Finally, I would like to thank my 'London family' for making a big city feel like home. I would also like to thank my biological family. I would first like to thank my Mum and sister for the support they have always given to me, but also for letting me off for all of the times that I have been glued to my laptop whilst in their company. I would also like to thank my partner, Ben, whose boundless curiosity always reminded me of why I love what I do, even at the more frustrating moments of research.

[1] from 'Devotions upon Emergent Occasions' by John Donne

Summary

The rapid increase in computational processing power and advancement of materials simulation techniques has enabled materials simulations to contribute towards the discovery and optimisation of materials for various applications. The application forming the motivation for this study is thin-film solar cells. There are two main contributions that simulations could make towards the advancement of such technologies. Firstly, to improve fundamental knowledge and understanding of materials to aid in the identification of factors limiting device performance. Such knowledge can be used to assist in the development of optimised synthesis procedures for the materials and devices. Secondly, simulations can allow for the discovery of new materials altogether that are not currently utilised for a given application, but may have relevant properties that are superior to the materials used in existing technologies.

The first results chapter in this work focuses on investigating a possible origin of the underperformance of solar cells based on the earth-abundant and non-toxic candidate solar absorber material kesterite-structured Cu_2ZnSnS_4 (CZTS). Specifically, this chapter focuses on the possible role of Cu/ Zn disorder in limiting the performance of CZTS solar cells. The second results chapter identifies candidate photoactive ferroelectric ('photoferroic') solar absorbers, motivated by the possibility of enhanced photovoltaic performance from photovoltaic phenomena observed in ferroelectric materials. The final chapter seeks to provide insights for the optimisation of new solar cell technologies based on the absorber materials identified in the previous chapter and to further assess their likely performance in a solar cell. This chapter draws on insights gained from previous studies on more mature solar cell technologies. A major theme throughout this work is the role that the defect physics of the absorber material has on determining the performance of a solar cell composed of that material.

Publications during the course of the PhD

7. Finding a junction partner for candidate solar cell absorbers enargite and bournonite from electronic band and lattice matching
   SK Wallace, KT Butler, Y Hinuma, A Walsh
   Journal of Applied Physics. 125, 055703 (2019)

6. Perspective: Dielectric and Ferroic Properties of Metal Halide Perovskites
   JN Wilson, JM Frost, SK Wallace, A Walsh
   APL Materials 7 (1), 010901 (2019)

5. Atomistic insights into the order-disorder transition in Cu_2ZnSnS_4 solar cells from Monte Carlo simulations
   SK Wallace, JM Frost, A Walsh
   Journal of Materials Chemistry A 7 (1), 312-321 (2019)

4. Candidate photoferroic absorber materials for thin-film solar cells from naturally occurring minerals: enargite, stephanite, and bournonite
   SK Wallace, KL Svane, WP Huhn, T Zhu, DB Mitzi, V Blum, A Walsh
   Sustainable Energy & Fuels (6), 1339-1350 (2017)

3. The steady rise of Kesterite solar cells
   SK Wallace, DB Mitzi, A Walsh
   ACS Energy Letters 2 (4), 776-779 (2017)

2. Vibrational spectra and lattice thermal conductivity of kesterite-structured Cu_2ZnSnS_4 and $Cu_2ZnSnSe_4$
   JM Skelton, AJ Jackson, M Dimitrievska, SK Wallace, A Walsh
   APL Materials 3 (4), 041102 (2015)

1. Facet-dependent electron trapping in TiO_2 nanocrystals
   SK Wallace, KP Mckenna
   The Journal of Physical Chemistry C 119 (4), 1913-1920 (2015)

Contents

Page

List of Figures **xii**

List of Tables **xiii**

1 Introduction **1**
1.1 The case for new absorber materials for solar cells 1
1.1.1 Terawatt-scale power production from renewable resources 1
1.1.2 Current commercial solar cell technologies and limitations 2
1.1.3 Examples of emerging metal sulfide solar absorbers 6
1.2 The role of computational modelling in material design and optimisation 7
1.3 Format of thesis 9

2 Theoretical background **10**
2.1 Models of perfect, periodic solids 10
2.1.1 Electrons in periodic solids 10
2.1.2 Reciprocal space and the reciprocal lattice 11
2.1.3 Bloch's theorem 12
2.1.4 Electronic band structure 13
2.2 Solar cell devices 17
2.2.1 The photovoltaic effect 17
2.2.2 Solar cell junctions 18
2.3 Absorber material properties for efficient solar cells 23
2.3.1 Electronic band gap and optical absorption 23
2.3.2 Charge-carrier effective mass 26
2.4 Impact of absorber layer defects on solar cell performance 27
2.4.1 Types of crystal defect 28
2.4.2 Optical properties of defective solids 29

3 Methodology **32**
3.1 Electronic structure calculations 32
3.1.1 Quantum theory of materials 32
3.1.2 Treatments of electron-electron interactions 34
3.1.3 Implementation for periodic solids 44
3.2 First principles prediction of electronic band offsets 54
3.3 Modelling imperfect solids: Point defects in the dilute limit 58
3.3.1 The problem of periodicity 59
3.3.2 Finite-size corrections to defect supercells 62
3.4 Modelling imperfect solids: Extended antisite defects 67
3.4.1 The Monte Carlo method for thermodynamic disorder 68

4 Performance bottlenecks of Cu_2ZnSnS_4 solar cells **71**
4.1 Motivations and challenges for Cu_2ZnSnS_4 solar cells 71
4.1.1 Publication: The steady rise of kesterite solar cells 71
4.2 Impact of defects on Cu_2ZnSnS_4 solar cells 77
4.3 Defects beyond the dilute limit in Cu_2ZnSnS_4 80
4.3.1 Monte Carlo model for Cu/Zn disorder in Cu_2ZnSnS_4 82
4.3.2 Publication: Atomistic insights into the order-disorder transition in Cu_2ZnSnS_4 from Monte Carlo simulations 85
4.4 Electronic band tailing in Cu_2ZnSnS_4 98
4.4.1 Fluctuations in electrostatic potential from Monte Carlo simulations of Cu/Zn disorder 99

5 Screening for candidate photoferroic solar absorbers **103**
5.1 Observed phenomena in photoactive ferroelectric materials 103
5.2 Publication: Candidate photoferroic absorber materials for thin-film solar cells from naturally occurring minerals: enargite, stephanite, and bournonite 105
5.3 Outlook: High-throughput screening for candidate photoferroics 119

6 Theoretical insights for new solar absorbers **121**
6.1 Development of new solar cell device architectures 121
6.1.1 Publication: Finding a junction partner for candidate solar cell absorbers enargite and bournonite from electronic band and lattice matching 122
6.2 Predicting and tuning the impact of absorber layer defects 132
6.2.1 Tunability of equilibrium defect concentrations 132

6.2.2 Predicting the impact of point defects 133
6.2.3 Defect physics of enargite, Cu_3AsS_4 136

7 Closing remarks **145**
7.1 Cu/ Zn disorder in Cu_2ZnSnS_4 solar cells 145
7.2 Candidate photoferroic absorbers in solar cells 146
7.3 Future of theory and simulation for photovoltaic materials 147

Bibliography **148**

A Appendix **172**
A.1 Supplemental material for: 'Atomistic insights into the order-disorder transition in Cu_2ZnSnS_4 solar cells from Monte Carlo simulations' . . . 172
A.2 Supplemental material for: 'Candidate photoferroic absorber materials for thin-film solar cells from naturally occurring minerals: enargite, stephanite and bournonite' 180
A.3 Supplemental material for: 'Finding a junction partner for candidate solar cell absorbers enargite and bournonite from electronic band and lattice matching' 196

List of Figures

1-1 Theoretical Shockley-Queisser detailed-balance efficiency limit as a function of optical band gap (highest black line) for AM1.5 solar spectrum. The record efficiencies for different materials are plotted for the corresponding band gaps, where materials below the lower two grey lines are achieving conversion efficiencies less than 75% and 50% of their theoretical efficiency limit respectively. 4

2-1 Electron energy levels of a single atom (left) and the formation of a quasi-continuous band of allowed energies in a solid crystal when many atoms are brought close together (right). 11

2-2 Energy-wave vector diagrams: (a) the free electron parabola, (b) modification due to a periodic crystal lattice, (c) along crystallographic directions. 13

2-3 a) Atomic orbital bases, χ, at each n lattice sites with lattice spacing a. b) 1D chains of s-orbitals for states $k = 0$ and $k = \frac{\pi}{a}$ where opposite parity of the orbitals is indicated by the shaded or unshaded regions. c) An s electronic band. d) 1D chains of p-orbitals for states $k = 0$ and $k = \frac{\pi}{a}$ where opposite parity of the orbitals is indicated by the shaded or unshaded regions. e) a p electronic band. 15

2-4 Schematic of the photovoltaic effect: a semiconductor under illumination with some built-in electrical asymmetry to drive the separation of charge carriers to be fed into an external circuit and an external load to do electrical work. Optical excitation of an electron-hole pair in absorber layer is indicated in the green box. Layers for the PV cell are purposely not labelled (except for the absorber layer) because the specific architecture of the devices varies for different PV technologies. 17

2-5 The formation of a Schottky barrier junction between an n-type semiconductor and a metal and the splitting of the electron Fermi level ($E_{F,n}$) under illumination 20

2-6 (a) p-n junction formed between a p-type and n-type semiconductor, in the dark and in thermal equilibrium indicating the difference in work functions (Φ_W) and built-in bias (V_{bi}). b) p-n junction under illumination indicating the direction of flow of minority carriers in the case of a p-type (orange) and n-type (blue) absorber layer. 22

2-7 The electronic band structure of a) silicon and b) GaAs. Schematic representation of the absorption process in an indirect and direct band gap material (c and d respectively). 24

2-8 a) A comparison of the absorption coefficients of the indirect band gap semiconductor Si and the direct band gap semiconductors GaAs and $CH_3NH_3PbI_3$ across a range of incident photon energies. b) Schematic of a the band structure of a photoexcited semiconductor with electrons near the bottom of the conduction band, holes near the top of the valence band, where the particular material has both heavy- and light-hole bands (labelled HH and LH in the figure respectively). 26

2-9 Examples of intrinsic point defects (a) and (b) and an extrinsic point defect (c). 28

2-10 Ionisation levels of intrinsic point defects in the band gaps of Cu_2ZnSnS_4 30

2-11 The influence of increased donor impurity density on the conduction band profile showing low (a), medium (b) and high (c) densities of impurities. (d) Optical absorption spectrum of a typical direct band gap semiconductor with the absorption coefficient, α_0, proportional to the extended density of states in the Urbach tail. 31

3-1 a) Calculated radial wavefunction, $r\psi(r)$, for the 1s and 2s orbitals of a lithium atom. b) Schematic representation of a numeric atom-centred orbital (NAO) basis function as used in the FHI-aims software package. c) Schematic representation of a pseudopotential and pseudo-wavefunction (both shown by blue solid lines) and corresponding original Coulomb potential and wavefunction (both shown by dashed red lines), where both red and blue lines converge at distances beyond the core region. 46

3-2 Schematic representation of iterative local geometry optimisation procedure with nested self-consistent solution of the Kohn-Sham equations to determine the ground state electron density for each ionic configuration. Darker blue represent iterative steps for geometry optimisation, lighter blue represent SCF electronic convergence. 50

3-3 Visualisation of minima in the potential energy landscape of a molecular system. 51

3-4 Ni radial functions to construct basis sets with increasingly tight convergence criteria as implemented in the software package FHI-aims. . . . 52

3-5 a) The energy dispersion relation for electrons moving in a crystal, illustrating how the function can be approximately represented by a finite number of k-points, forming an equally-spaced mesh. b) convergence of total energy and c) optical dielectric function for the same material. . . 53

3-6 a) Energy diagram of a semiconductor with flat bands to the surface. Indicating the band edges (CBM/LUMO and VBM/HOMO), vacuum level (E_{VAC}), work function (WF), band gap E_{g}, ionisation potential (IP) and electron affinity (EA). b) Schematic representation of the implementation of 3D periodic boundary conditions for a 2D surface slab model (finite direction indicated by the orange arrow). 55

3-7 Planar average (blue line) and macroscopic average (orange line) of the potential across the finite direction of a slab model indicating the slab region, vacuum gap and surface dipole energy, D_{s}. 56

3-8 A charge-neutral defect interacting with periodic images of itself across periodic boundary conditions in 2D (a) and the longer-ranged Coulombic interactions of charged defect with a charge q (b). 59

3-9 Visual descriptions of terms in the equation for the formation energy of charged defects. 61

3-10 The difference in the atom-site potentials V_{Ga} and V_{As} between a supercell containing a vacancy V_{As}^{3+} and the defect-free host. 62

3-11 a) Schematic of first-order Markov-Payne (MP) correction of electrostatic interactions in a periodic DFT calculation of a charged defect where the defect is modelled as a point charge. b) Multipole expansion of a charge density, from the lowest order for $m, l = 0$. 64

4-1 V_{OC} versus band gap of high performance CZTSSe devices (>9% efficiency) indicated by circles with best devices based on other photovoltaic materials shown for comparison by diamond symbols: Methylammonium lead iodide (MAPI), amorphous silicon (a-Si), organic photovoltaic films (OPV), crystalline silicon (c-Si) and polycrystalline silicon (pc-Si). The oblique lines give a constant V_{OC} deficit from 0.8 V to 0 V. The green points correspond to CZTSSe films that are partially ordered (PO) or partially disordered (PD) due to disorder amongst Cu and Zn. . 78

4-2 The internal quantum efficiency (IQE), band gap as determined from the IQE inflection point and the photoluminescence spectra of high performance devices with thin-film absorber layers of (a) CIGSSe (E_g = 1.19 eV) and (b) CZTSSe (E_g = 1.13 eV). 79

4-3 Probability of nearest neighbour $[Cu_{Zn}^{-} + Zn_{Cu}^{+}]$ defect formation as a function of temperature based on the equilibrium defect concentration from classical thermodynamics. 81

4-4 Typical periodic boundary conditions for the two-dimensional Ising model. 82

4-5 Example outputs of 2D slices of cation sub-lattice of Cu_2ZnSnS_4 from Eris Monte Carlo simulations of Cu-Zn disorder from an initially ordered lattice showing the top two layers of the lattice when simulations are performed at temperatures $T = 0$ K (a) and at sufficiently high temperatures for Cu-Zn substitutions (b). 84

4-6 Schematic of band gap fluctuations (a) and electrostatic potential fluctuations (b) where the band gap is only maintained in the case of (b). . 98

4-7 Electronic band structure of Cu_2ZnSnS_4 calculated with the HSE06 hybrid-DFT functional, total and partial density of states, and schematic plot of the band components. 99

4-8 Distributions of on-site electrostatic potentials of Sn (top panels) and Cu (bottom panels) with increasing simulation temperature (left to right). The distribution broadens from one delta function for Sn ions at $T = 0$ K (corresponding to one crystallographically distinct Sn site) and broadens from two delta functions for Cu at $T = 0$ K corresponding to the Cu $2a$ and $2c$ sites in Cu_2ZnSnS_4. 100

4-9 2D histograms showing on-site electrostatic potentials in units of V for Cu (a) and Sn (b) in a (001) Cu-Sn plane minus the average on-site potential for each species within the same plane in our Cu_2ZnSnS_4 lattice model for complete ($S = 0$) equilibrium thermodynamic Cu/ Zn disorder at 950 K. Any deviation from 0 potential demonstrates the spatial fluctuation in electrostatic potential across the plane and empty sites in (a) show where Zn ions have substituted onto Cu $2a$ sites. 102

6-1 The change of the defect formation energy, $\Delta H_{D,q}$, in Cu_2ZnSnS_4 as a function of the Fermi energy at one point in the chemical potential space for phase-stable Cu_2ZnSnS_4. The most stable charge state is plotted for a given Fermi energy. 134

6-2 a) The real component of the electron wavefunction of the highest occupied state in Cu_3AsS_4. b) Partial electronic density of states (pDOS) of Cu_3AsS_4, where the top of the valence band has been set to 0 eV. 136

6-3 a) Unit cell of enargite (Cu_3AsS_4) and b) $2 \times 2 \times 2$ supercell containing 128 atoms with dimensions $14.86 \times 12.91 \times 12.33 Å^3$. 137

6-4 Phase diagram for enargite (Cu_3AsS_4) calculated with the HSE06 functional and including spin-orbit coupling. 141

6-5 Ionic dielectric constant of enargite (Cu_3AsS_4) calculated from density functional perturbation theory with the PBEsol functional with increasing k-grid density. 142

List of Tables

6.1 Elemental energies of components in enargite (Cu_3AsS_4) in their standard states calculated with the HSE06 functional and including SOC. . 139
6.2 Formation energies of stable secondary phases for the phase diagram of Cu_3AsS_4 calculated with the HSE06 functional and including SOC. . . . 139
6.3 Formation energies of unstable secondary phases with formation energy as listed on the Materials Project database of up to 0.1 eV per atom above the convex hull for the phase diagram of Cu_3AsS_4 calculated with the HSE06 functional and including SOC. 140
6.4 Intersection points in chemical potential space from the phase diagram for enargite (Cu_3AsS_4) shown in Fig. 6-4, where μ_i is referenced to the total energy of the element phase in its standard state. 140
6.5 Formation energies, $\Delta H_{D,q=0}$ of charge neutral vacancies in enargite (Cu_3AsS_4) at all 10 intersection points in the chemical potential space for enargite from Table 6.4. E_{tot} are total energies of the defective supercells and defects are labelled according to their spacegroup (sg) and unique structure (s) as identified by crystal symmetry using Transformer libraries. 144

Chapter 1

Introduction

1.1 The case for new absorber materials for solar cells

1.1.1 Terawatt-scale power production from renewable resources

It is now widely accepted that the world is heading towards a major energy crisis with the current major sources of energy, namely fossil fuels, eventually being unable to meet increasing global demand for energy. Furthermore, there is the ever present worry of climate change linked to increased carbon dioxide emissions from the burning of fossil fuels. Renewable, low-carbon alternatives, such as solar power, are therefore clearly desirable [1]. Recent years have seen a rapid increase in solar power generation installations, with the global grid-connected photovoltaic (PV) capacity growing from 1.3 GW in 2000 to 139 GW in 2014 [2], with approximately a doubling in the cumulative installed capacity every two years [3]. Creative business models have spurred investment in residential solar systems [4] and great improvements in technology, price and performance have helped to facilitate this growth. However, solar energy still only provides a minor fraction of the world's energy with an overall share of global power generation of less than 2% reported in 2017 [5].

Solar power is by far the largest source of energy available to us and it is also the most widely geographically distributed [6]. The Sun supplies of energy to the Earth each year, which is around 10^4 times more than mankind's current annual energy consumption. Assuming a fairly modest module efficiency of 20% and 50% losses related to storage and secondary conversion, 1.6% of the Earths land area would be required for solar-generated power to meet current world energy needs [7]. Although

this would be a fairly large area, it would not be completely unrealistic. For instance, this area would be less than 5% of the area used for agriculture worldwide [7]. The area required could also be reduced through improvements in the efficiency of PV modules and be more easily met by making use of building-integrated PV (BIPV) innovations, largely made possible by newer, flexible, thin-film PV technologies which are discussed further in section 1.1.2. Additionally, BIPV allows for more subtle or aesthetically-pleasing means of solar energy generation. This may seem like a minor consideration when using terms such as 'energy crisis' and 'global warming', however, in certain residential or touristic areas (even without constraints related to historical preservation) solar panels are not permitted due to their detrimental visual impact[1].

We must also consider the economic feasibility of current solar cell technologies for large-scale projects. Many countries have made considerable efforts to increase the percentage of their energy supplied from renewable resources. Germany, for example, introduced feed-in tariffs (FiTs) to encourage investment in solar power. FiTs set the rate a utility company had to pay for renewable generated energy and guarantee the provider of renewable energy a specific rate for a long period of time, typically fifteen to twenty years. As this cost was higher than fossil-fuel-based electricity, the higher price was then passed on to all customers of the utility company to spread out the cost. This resulted in an increase of 6% on the average electricity bill [8]. With the prevalence of fuel poverty, the social implications of such a cost increase must also be considered in assessing the viability and sustainability of a particular power source. Ultimately, solar power-generation technologies must at least become cost-competitive with conventional fossil-fuel based power sources. In the next section, both commercial solar cell technologies that are currently available and emerging technologies are discussed to understand why solar power is currently not cost competitive, and how emerging technologies may be able to improve the status quo for global solar power generation.

1.1.2 Current commercial solar cell technologies and limitations

It was first observed in 1839 by Edmond Becquerel that sunlight could be used to generate electricity. Becquerel discovered that if silver chloride was placed in an acidic solution, connected to platinum electrodes and exposed to sunlight, an electric current flowed. However, the effect was small and poorly understood before Albert Einstein's discovery of the photoelectric effect and explanation of the phenomena by the quantum nature of light in 1904 [9]. Even then, it was not until the development of semicon-

[1]Conwy Marina Village Management Co. Ltd., personal communication, April 17, 2018

ductor technology during the silicon revolution of the 1950's that solar cells capable of generating significant amounts of electricity were fabricated.

The first silicon solar cell was created in 1954 in the Bell Laboratories with cells achieving efficiencies of 6%. Originally solar cells were developed for extraterrestrial energy generation, such as the 108 solar cells used to supply energy to the Vanguard satellite in 1958 [9]. The first oil crisis in 1973, however, highlighted the dependency of many economies on fossil fuels and the need to address the security of energy supply. As a consequence, solar cell research was no longer limited to only high-cost crystalline devices for extraterrestrial applications, but also into creating cheaper, commercial, thin-film solar cell technologies using absorber materials such as amorphous silicon, cadmium telluride (CdTe) and copper indium gallium diselenide (CIGS) [10].

Crystalline silicon is still the dominant solar cell technology with silicon-wafer based PV technology accounting for approximately 95% of the total production in the global PV market in 2017 [11]. Silicon is the second most abundant element in the Earth's crust [12]. When considering this aspect alone, it seems to be a plausible material to use in large-scale solar power generation. Over 60 years of development have seen device efficiencies increase up to 26.7% for the current record device [13] and 15-18% for the more common industrial cells [14]. As can be seen from Fig. 1-1, the best performing silicon devices are now very close to achieving conversion efficiencies close to their theoretical limit, as predicted by the Shockley-Quiesser limit [15] for the optical band gap of the absorber. The fall in manufacturing costs is even more dramatic, more than halving between 2008 and 2013 and being a hundred times lower than they were in 1977. This development was largely aided by progress in semiconductor technology driven by the silicon chip industry, with the solar industry benefiting from advances in silicon manufacturing processes and even making use of waste silicon produced that was not of a high enough grade for silicon chips [9]. Although the development of silicon-based technologies has clearly revolutionised the modern computer, the optical properties of silicon do not make it ideal for use as a solar absorber material in a photovoltaic device and despite the dramatic reduction in manufacturing costs, the technology is still not able to be cost-competitive with fossil-fuel power generation.

The primary issue with silicon is that its optical band gap of 1.1 eV is indirect. The importance of the electronic band gap in relation to PV performance will be discussed further in section 2.3. For now, it is just noted that the key consequence of the indirect nature of the band gap of silicon is that it is not a very strong absorber of sunlight (compared to for instance newer, thin-film technologies which are discussed next), resulting in a low optical absorption coefficient compared to these newer tech-

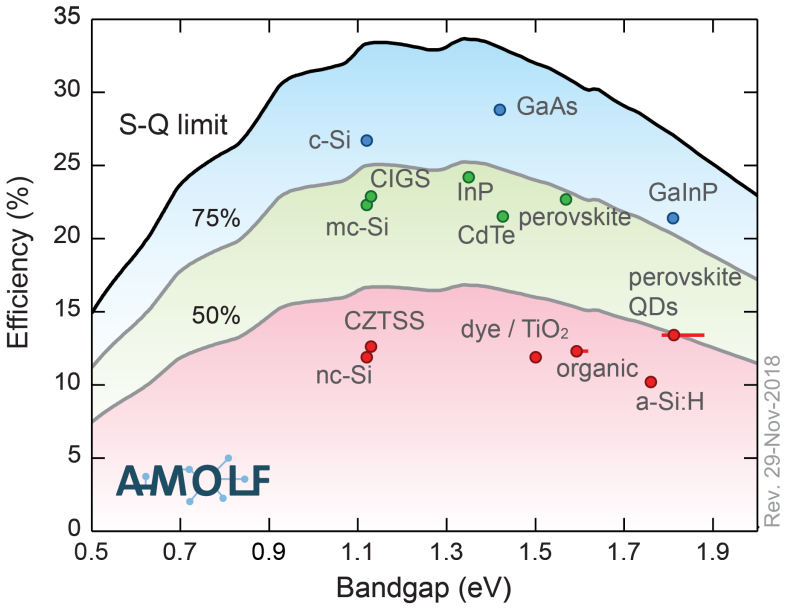

Figure 1-1: Theoretical Shockley-Queisser detailed-balance efficiency limit [15] as a function of band gap (highest black line) for AM1.5 solar spectrum. The record efficiencies for different materials are plotted for the corresponding band gaps, where materials below the lower two grey lines are achieving conversion efficiencies less than 75% and 50% of their theoretical efficiency limit respectively. Figure reproduced with permission from Ref. 7 and Ref. 16.

nologies. To absorb the same amount of sunlight with a silicon solar cell requires a thicker layer of the material than in thin-film technologies. PV devices are very sensitive to defects and impurities. This point is discussed further in section 2.4, but the consequence for a thick layer of silicon is that very high quality, non-defective material is necessary to enable charge carrier collection before electron-hole recombination occurs, which results in high manufacturing costs. The devices are made from flat sheets of crystalline or multi-crystalline silicon called wafers that consist of very high quality silicon (99.999999% pure) [17]. The production processes of silicon wafers have been thoroughly optimised, but are still very energy-intensive, time-consuming and complex [18].

Beyond silicon

The 'holy grail' of research into new materials for PV devices would be to find materials that are strong absorbers of sunlight, could be produced cost-effectively and

composed of materials that are abundant enough for large-scale fabrication of the devices. Thin-film solar cell devices make use of materials that are much more optically thick than silicon (i.e. stronger absorbers of sunlight with direct optical band gaps and higher optical absorption coefficients), which require less material to absorb the same amount of sunlight. The consequence of the reduction in the thickness of the absorber layer is that it is then less important for the material to be of as high-quality as in crystalline silicon devices, which enables the use of low-cost and low-energy fabrication methods [18]. Many thin-film technologies are also light-weight and flexible, allowing for more options for innovative deployment of the modules, such as building integrated photovoltaics (BIPV) and portable devices.

Examples of commercial thin-film technologies include CIGS ($Cu(In,Ga)(S,Se)_2$) and CdTe. In the case of thin-film $CuInSe_2$ devices, it has even been found that the 'lower quality' poly-crystalline material has a higher performance than its single crystal counterpart [19, 20]. Theoretical studies of the electronic properties of the grain boundaries in $CuInSe_2$ have provided an explanation for this unusual observation based on beneficial band offsets at the grain boundaries [21, 22]. This effect is a special case for this material, but it embodies the general ideology of thin-film technology well - namely to produce materials able to convert sunlight into electricity as efficiently as possible, with the simplest synthesis techniques possible. Other innovations in PV technology include the use of multiple energy threshold devices to overcome the Shockley-Quiesser limit [15] for a single band gap solar cell, such as in tandem solar cells where semiconductor p-n junctions of increasing band gap are placed on top of each other in order to capture more of the solar spectrum. Typically these more complicated device architectures result in higher fabrication costs. Research efforts are therefore largely focused on reducing the fabrication cost of multi-junction devices [23].

Current mainstream solar cell technologies, such as Si wafers and thin-film CdTe and CIGS solar cells, are unlikely to be able to provide solar electricity at the terawatt scale due to the scarcity of Te and In and the relatively long energy payback time for crystalline Si due to the cost and energy intensive fabrication of Si wafers [24]. Models have quantified such statements with a predicted In-constrained growth potential of power generation from CIGS PV technology of 20 GW per year in 2020 due to competing applications of In, such as in liquid crystal displays [25]. To significantly increase the contribution of solar power to the global power supply, it is therefore necessary to develop more economically viable earth-abundant materials for sustainable PV electricity generation. Furthermore, there must be considerable technological breakthroughs that would enable low-cost manufacturing of high-efficiency devices with enough of a cost

benefit to outweigh the initial cost outlay in optimising the manufacturing process of the whole device as has been done for silicon over the past 60 years. For this purpose, there is a drive for solar absorber materials with more optimal properties, such as a direct and sunlight matched band gap (as in thin-film technologies such as CdTe and CIGS), but also for materials that are composed of only earth-abundant components.

1.1.3 Examples of emerging metal sulfide solar absorbers

The magnitude of the optical band gap is the most fundamental, necessary property of a semiconductor in order to have the potential to produce a high-efficiency solar cell device. Other important material properties for the absorber material in a PV device are discussed in section 2.3, but for now it is just noted that to maximise the energy harvesting potential of the PV device, a band gap for the absorber that is direct in nature and closely matched to the major component of the solar spectrum is desirable, this corresponds to a range of approximately 1.0 eV to 1.7 eV [26]. The optical band gap is the most fundamental and obvious screening criteria to use when selecting new candidate absorber materials for photovoltaic devices. The band structure of semiconductors will be discussed further in section 2.1.1, but for now it will just be noted that metal tellurides, selenides and sulfides typically have band gaps closer to the optimal energy range for PV applications than corresponding oxides. This is due to the chalcogen p-orbital (which is usually the dominant component of the valence band maximum) being higher in energy than the oxygen p-orbitals in corresponding metal oxides, which typically have band gaps that are too wide for PV applications. Of metal tellurides, selenides and sulfides, sulfur stands out in the interests of abundance and minimising toxicity.

SnS is an example of a non-toxic and earth-abundant metal sulfide that has received research interest for solar cell applications. SnS has a direct band gap within the optimal range for sunlight absorption of between 1.30 eV [27] and 1.43 eV [28]. However, record power conversion efficiencies (PCE) of PV devices are at around just 4% [29]. The low-performance of SnS devices has been attributed to several factors including the defect physics [30], non-optimal band alignment in devices [31] and phase impurity [32] of the material.

Kesterite-structured Cu_2ZnSnS_4 (CZTS) has also received a large amount of research interest for PV applications, also due to the highly desirable earth-abundance and non-toxicity of its constituent elements, along with promising optical properties. The band

gap of CZTS has been predicted [33] and measured [34] to be direct with a magnitude of 1.5 eV. The record device efficiencies are more than double that of SnS-based solar cells. However, CZTS solar cells still fall far short of their theoretical maximum PCE of 28% predicted from the Shockley-Quiesser limit based on the optical band gap and have considerably lower performance than CdTe and CIGS solar cells as shown in Fig. 1-1. The current confirmed record device efficiency of a sulfide-selenide alloy is 12.6% [35], while that of the pure sulfide material lags even further behind at behind at 9.1% [36]. A large component of this work seeks to investigate possible origins of the performance deficit of CZTS solar cells. The other major component of this work looks to identify photoactive ferroelectric (or 'photoferroic') materials so that alternative routes to high-efficiency solar cells may be explored by exploiting novel PV phenomena observed in ferroelectric materials. This is discussed in more detail in section 5.1.

1.2 The role of computational modelling in material design and optimisation

The discovery of new functional materials by experimental methods is largely hindered by high costs and the time-consuming optimisation of synthesis procedures [37]. However, with the rapid increase in computational processing power and the availability of large-scale supercomputers, we are entering a very exciting era in computational materials design [38]. Furthermore, electronic structure theory has advanced to a level where it is possible to obtain good quantitative agreement with experiment without using adjustable parameters fit to experiment, i.e. from first principles. The only inputs into these calculations are electronic mass, electronic charge, atomic numbers and masses of the constituent atoms in the material. From this, it is possible to obtain to fairly high accuracy the structure, lattice constants, charge densities and various electronic, magnetic, optical and transport properties [39]. Therefore theory and simulation of materials has reached a point of possessing predictive power for material properties relevant for various applications, completely independent of experimental measurement.

There are two main contributions that computational simulations could make towards the technological breakthroughs needed for economically-viable, large-scale solar energy generation. Firstly, by predicting relevant properties of materials that are not currently utilised in solar cells and screening for certain desirable properties, material simulations are able to aid in the discovery of new materials that may be capable of out-performing

current solar cell technologies. Such an approach allows for a less time-consuming screening of potential new materials for a given application before attempting to prepare just the most promising candidates in the laboratory. Experimental validation of predicted properties, however, is always an important follow up to account for additional features of the physical system not initially accounted for in the model. In the case of candidate solar absorbers, for example, the optical properties are often initially predicted for the perfect bulk crystal. In reality materials contain various types of defects. Methods exist to model different forms of defects in a crystalline system, some of which are discussed later in this work. However, this typically quite complex and idiosyncratic feature of the system is often not considered initially, largely due to the vast range of possible defect features in a material. The defect physics of a material is a prime example of an area in which knowledge and understanding is developed symbiotically between works from experiment and theory. Secondly, material simulations are able to provide valuable, atomistic insight on scales that cannot be probed experimentally to improve fundamental understanding of known photovoltaic materials, which may enable improvements in existing solar cell technologies. Defect physics is again a prime example of this. Theory can probe on the atomic scale to aid in the interpretation of experimental data obtained from a variety of different measurements.

In this work, materials modelling techniques are developed and applied to make both types of contribution to the field. A model is developed to improve current atomic-scale understanding of the candidate earth-abundant, non-toxic solar absorber material Cu_2ZnSnS_4 (CZTS) and to provide a tool for assessing possible origins of the underperformance of this particular solar cell technology. This is the subject of chapter 4. Materials modelling is also used to predict the relevant properties of candidate photoferroic absorbers that are not currently utilised in solar cell technologies to identify those that are most likely to be worthy of further study. In chapter 5, the screening criteria and methodologies used in this study for identifying candidate photoferroic absorbers are discussed and some relevant calculated material properties for the candidates are presented. In chapter 6, the use of material simulations and theoretical insights to assess the likely performance of a material in a solar cell device is discussed further. In particular, knowledge gained from previous studies on more mature PV technologies is drawn upon when examining the potential of the candidate photoferroic materials for solar cell applications.

1.3 Format of thesis

The following thesis is in the 'alternative format' which is a thesis incorporating academic papers that are published, accepted, submitted, or written as if for publication. All papers included in the thesis are labelled as publications and begin with a statement of authorship. Supplemental material for each paper are included as appendices. All papers included in this thesis are first-author works, but contributions to the works from co-authors are indicated in the statement of authorship.

Chapter 2

Theoretical background

2.1 Models of perfect, periodic solids

To relate the properties observed for a material to its underlying atomic and electronic structure, and also to predict properties that have not yet been measured, it is necessary to have a suitable model for the material. Theoretical models of crystalline solids are based around the existence of translational symmetry in a crystal lattice such that the lattice can be constructed by periodically repeating a small unit cell of atoms. The Bravais lattice specifies the periodic array in which the repeated units of the crystal are arranged. A crystal lattice can therefore be described by its underlying Bravais lattice and the arrangement of atoms, ions or molecules within a particular unit cell, i.e. the basis [40]. The smallest possible unit cell that can be periodically repeated to represent the bulk, periodic crystal is called the primitive unit cell.

2.1.1 Electrons in periodic solids

Electrons bound to an atom in atomic orbitals have a number of possible discrete energy levels. When a pair of atoms are brought together to form a molecule, the atomic orbitals combine to form pairs of molecular orbitals arranged with energy levels slightly higher and slightly lower in energy than the original energy levels, referred to as antibonding and bonding orbitals respectively. When a large number of atoms are brought together to form a solid the original discrete energy levels are broadened into new energy levels that are so closely spaced that they are considered to be a quasi-continuous band of allowed energies. This is illustrated in Fig. 2-1.

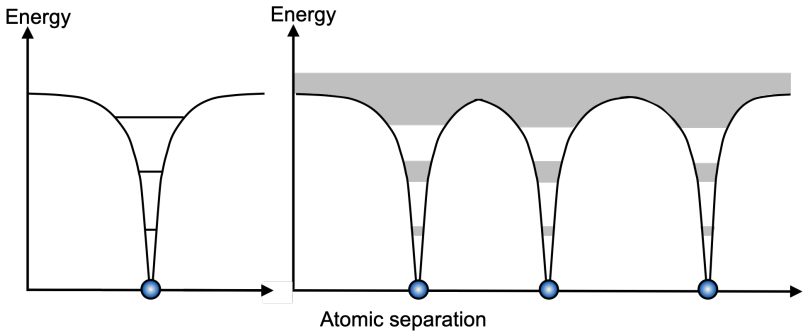

Figure 2-1: Electron energy levels of a single atom (left) and the formation of a quasi-continuous band of allowed energies in a solid crystal when many atoms are brought close together (right). Figure adapted from Ref. 41.

The energy distribution of the bands depends upon the electronic properties of the constituent atoms of the crystal and the strength of the bonds between them. The highest-energy band (containing the valence electrons) is the valence band (VB). The lowest unoccupied band is the conduction band (CB). If the VB is only partially filled or if it overlaps in energy with the CB, then the solid is a metal. The availability of empty states at energies close to that of the occupied states facilitates easy scattering of valence electrons into neighbouring states, thereby allowing for the transport of heat and charge. Hence metals conduct both heat and electric current. In a semiconductor or insulator, the VB is completely full and separated from the next unoccupied CB by an energy gap called the band gap, E_{g} [42]. In the simplest model, the CB is separated from the VB by a constant $\mathrm{E_g}$. This is called the flat band model and is often shown in schematics of junctions for PV device architectures, which will be discussed in section 2.2.2. In real structures, the band architecture is more complicated than this simple model, like the band structures shown later in section 2.3 [43].

2.1.2 Reciprocal space and the reciprocal lattice

Another important concept in the theoretical modelling of periodic structures is reciprocal space and the reciprocal lattice. The spatial properties of a crystal can be described as a sum of components in Fourier space, otherwise known as reciprocal space or k-space. As a simple example, the reciprocal lattice of a perfect single crystal is an infinite periodic 3D array of points with spacings that are inversely proportional to the distances between the planes in the lattice in real space. Vectors in real space have dimensions of length, whereas vectors in reciprocal space have dimensions of inverse

length. This can be compared directly to the wavevector $\left(k = \frac{2\pi}{\lambda}\right)$ of an excitation such as a phonon or a moving electron. The Wigner-Seitz primitive cell is the most common choice of primitive cell with the full symmetry of the Bravais lattice. It represents the region of space around the real space lattice point that is closer to that point than to any other lattice point. The Wigner-Seitz primitive cell of the reciprocal lattice is called the first Brillouin zone of the real space lattice. For example, the reciprocal of the bcc lattice is face-centred cubic (fcc), therefore the first Brillouin zone of the bcc lattice is the fcc Wigner-Seitz primitive cell. As the full symmetry of the reciprocal lattice is contained within the first Brillouin zone, it is only necessary to sample k-points within this single unit cell of the reciprocal lattice when calculating the electronic ground state of a periodic structure.

2.1.3 Bloch's theorem

To understand the behaviour of electrons in solids, Bloch's theorem is invoked to describe the wave function of a particle in a periodic potential. The electron is considered as a wave propagating in a periodic structure, i.e. the periodic crystal lattice [44]. The Schrödinger equation (SE) must be solved to determine the energy of electrons in a solid. The energy of a single, independent electron in a perfect crystal is described by the one-electron SE

$$\left[\left(-\frac{\hbar^2}{2m}\right)\nabla^2 + V(\boldsymbol{r})\right]\psi = \epsilon\psi, \tag{2.1}$$

where the first term is the kinetic energy of the electron, $V(\boldsymbol{r})$ is the effective periodic potential energy experienced by the electron in the crystal, ψ is the electron wavefunction and ϵ is the eigenenergy of the electron. For a solid, the infinite array of atomic potentials making up the crystal must be accounted for, as opposed to just the few associated with a molecule. For this purpose the periodicity of crystalline solids is exploited to determine the probability distribution of electrons in an infinite solid [42].

The spatial dependence of the potential experienced by an outer electron in a crystal for multi-electron systems was considered by Felix Bloch. Bloch determined that the total potential is the sum of two parts. Firstly, the electrostatic potential due to the array of atomic cores. For a perfect lattice this should have the translational periodicity of the lattice. Secondly, the potential due to all other electrons. Bloch assumed that the charge density would have the same long-term average value in every unit cell of the crystal and therefore would be periodic [45]. The periodicity of the crystal lattice means that the probability distribution of the electrons must also be periodic, with no preference for an electron to occupy a particular site within one unit cell than the

equivalent site in any other unit cell. Furthermore, as the lattice is infinite, electrons in a periodic solid should form delocalised states which extend throughout the crystal in a similar manner to an electron in free space.

Bloch's theorem states that the wavefunction which satisfies Eq. 2.1, subject to a periodic potential, should be of the form

$$\phi_k(\boldsymbol{r}) = U(\boldsymbol{r})\mathrm{e}^{i\boldsymbol{k}\cdot\boldsymbol{r}}. \tag{2.2}$$

The Bloch function shown in Eq. 2.2 is a product of a function $U(\boldsymbol{r})$, which possesses the periodicity of the lattice, and a plane wave part, $\mathrm{e}^{i\boldsymbol{k}\cdot\boldsymbol{r}}$, where $\boldsymbol{k}$ is the wavevector of an electron in the crystal [42].

2.1.4 Electronic band structure

The one-electron wavefunctions from Eq. 2.1 can be solved for each electronic band and wavevector, $\boldsymbol{k}$ [42], to give the energy dispersion relation or electronic band structure of the crystal, $E(\boldsymbol{k})$ versus $\boldsymbol{k}$ [45]. The impact of a medium with a discrete structure, such as a crystal lattice, on the energy dispersion relation of a free electron can be seen by comparing Fig. 2-2a to Fig. 2-2b. $E(\boldsymbol{k})$ of a material is usually plotted against $\boldsymbol{k}$ just for the most important directions in the crystal, such as that shown in Fig. 2-2c. A periodic medium does not suppress the propagation of waves, as would be expected in disordered or amorphous structures, but introduces limiting frequencies and wavelengths for the propagation.

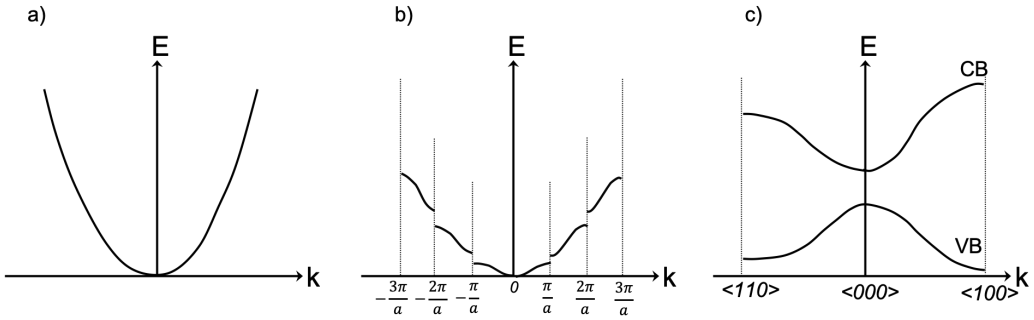

Figure 2-2: Energy-wave vector diagrams: (a) the free electron parabola, (b) modification due to a periodic crystal lattice, (c) along crystallographic directions. Figure a and b adapted from Ref. 44, figure c adapted from Ref. 42.

The parabola for the free electron (shown in Fig. 2-2a) is modified in a periodic crystal by the introduction of discontinuities at values of $|\boldsymbol{k}|$ corresponding to multiples of $\frac{\pi}{a}$, as

shown by Fig. 2-2b [46], where a is the spacing of the planes of atoms in the direction $E(\boldsymbol{k})$ has been plotted. The point $|\boldsymbol{k}| = \frac{\pi}{a}$ is the Brillouin zone boundary. At these points the electron wavefunction is a standing wave and the gradient of $E(\boldsymbol{k})$ disappears [42]. The lower limit of the wavelength is set by the lattice spacing, a, giving an upper limit of the wave vector, $|\boldsymbol{k}|$, of $\frac{\pi}{a}$. The appearance of such energy gaps implies that electrons in a periodic crystal may only have kinetic energies corresponding to certain bands, whilst being free to propagate in the lattice [46]. Due to the periodicity of the crystal lattice, $|\boldsymbol{k}|$ that differ by multiples of $\frac{2\pi}{a}$ cannot be distinguished and $E(\boldsymbol{k})$ repeats for $|\boldsymbol{k}| > \frac{\pi}{a}$. Therefore, all information for the energy dispersion relation, E($\mathbf{k}$) vs. $|\boldsymbol{k}|$, of the material is contained in the range $0 < |\boldsymbol{k}| < \frac{\pi}{a}$ and so only this region needs to be plotted, as in Fig. 2-2c [42].

To relate plots such as Fig. 2-2c to the formation of bands of allowed energies when atoms are brought close together to form a solid (as discussed earlier in this section and shown in Fig. 2-1), it is conceptually useful to first consider an infinite 1D chain of atoms, before extending the concepts to 3D. A wealth of information on this subject can be found in Ref. 47, but here the concepts are just outlined briefly. Again for conceptual simplicity, this outline will focus on 1D chains of s and p atomic orbitals but a much more thorough description including higher dimensions and other atomic orbitals can be found in Ref. 47. Following the nomenclature used in Ref. 47, if we consider a 1D chain with lattice points $\mathrm{n} = 1, 2, 3, \ldots, \infty$, lattice spacing a and an atomic orbital basis at each lattice site denoted by $\chi_1, \chi_2, \chi_3, \ldots, \chi_\infty$ (shown in Fig. 2-3a), we can write Bloch functions (such as that shown earlier in Eq. 2.2) for all possible states as

$$\phi_k = \sum_n \chi_n \mathrm{e}^{ikna}. \tag{2.3}$$

The wave vector, k, is used as an index for the irreducible representation of different states.

As outlined above, all unique information for the band structure is contained in the range $0 < k < \frac{\pi}{a}$. Substituting these limits of k into Eq. 2.3, for $k = 0$ gives

$$\phi_0 = \sum_n \chi_n \mathrm{e}^0 = \sum_n \chi_n, \tag{2.4}$$

and for $k = \frac{\pi}{a}$ gives

$$\phi_{\frac{\pi}{a}} = \sum_n \chi_n \mathrm{e}^{i\pi n} = \sum_n \chi_n (-1)^n. \tag{2.5}$$

1D chains of s- and p-orbitals for these limiting values of k are shown in Fig. 2-3b and d

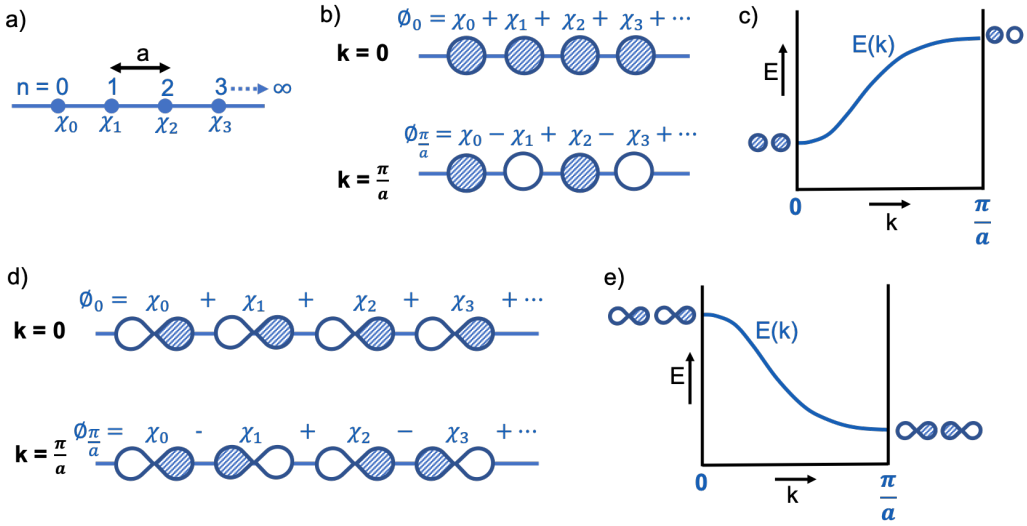

Figure 2-3: a) Atomic orbital bases, χ, at each n lattice sites with lattice spacing a. b) 1D chains of s-orbitals for states $k = 0$ and $k = \frac{\pi}{a}$ where opposite parity of the orbitals is indicated by the shaded or unshaded regions. c) An s electronic band. d) 1D chains of p-orbitals for states $k = 0$ and $k = \frac{\pi}{a}$ where opposite parity of the orbitals is indicated by the shaded or unshaded regions. e) a p electronic band. Figure adapted from Ref. 47.

respectively. In the case of the s-orbital chain, for the $k = 0$ state, all adjacent orbitals are of the same parity (indicated by the shading in the figure), therefore this is the arrangement of the atomic orbitals that maximises bonding, making this is the lowest energy state. The $k = \frac{\pi}{a}$ state, however, results in every other s-orbital being out-of-phase and therefore this is the most antibonding state and is the highest energy state. Consequently, when plotting E(k) against k for a 1D chain of s-orbitals from $k = 0$ to $k = \frac{\pi}{a}$, the plot curves upwards from the lowest to highest energy arrangements, as shown in Fig. 2-3c. The opposite is the case for a 1D chain of p-orbitals (as shown in Fig. 2-3e) due to the topology of the p-orbital. In this case, bonding is maximised and hence the energy is at a minimum for the $k = \frac{\pi}{a}$ arrangement.

Effective mass approximation

A useful concept used to simplify the dynamics of an electron in a crystal lattice in the band theory of solids is that of the effective mass approximation. The effective mass is a convenient parameter determined from the curvature of the maxima and minima of the VB and CB respectively along particular paths in momentum space to account for the influence of a periodic lattice on a free carrier. This approximation enables an

electron in a periodic crystal to be treated as though it were a free particle but with a different mass in calculations of charge transport [46]. The influence of the effective mass of charge carriers in a solar absorber material on the efficiency of a PV device composed of that material will be discussed in section 2.3.

Electrical conductivity of semiconductors

The band theory of a semiconductor can also be used to understand the electrical conductivity of the material. At 0 K electrons are classically considered to have no kinetic energy and therefore occupy the lowest energy states available. Quantum mechanically, electrons are considered to possess only a 'zero point' energy at 0 K from fluctuations in their lowest energy state due to the Heisenberg uncertainty principle. The energy of the highest energy state filled is called the Fermi energy, E_{F}. However, at temperatures above 0 K, electrons may have sufficient kinetic energy to access higher energy states above E_{F}, leaving behind some empty states below E_{F}. The distribution for electrons in thermal equilibrium at finite-temperatures is described by Fermi-Dirac statistics, where Eq. 2.6 gives the probability that an electronic state of energy E will be occupied at some temperature T, where k_{B} is the Boltzmann constant [42]

$$f(E) = \frac{1}{\mathrm{e}^{(E-E_F)/k_{\mathrm{B}}T} + 1}. \tag{2.6}$$

In a semiconductor at 0 K, the VB is fully occupied by electrons and the CB is completely unoccupied and so electrical conduction is not possible. However as temperature is increased it may become possible for electrons to access unoccupied states in the CB if they have sufficient energy to overcome the band gap, allowing for some electrical conduction. Typically, the band gap of an electrical insulator is too large for this to occur. It is also possible for the energy gap to be decreased by defects and doping [42], which will be mentioned in regards to the impact on PV performance in section 2.4. The band gap of a semiconductor, and in particular the magnitude of the band gap, is also an important property for the photovoltaic effect where electrons are optically excited across this energy gap by incident photons, which will be outlined in the next section.

2.2 Solar cell devices

2.2.1 The photovoltaic effect

A solar cell device converts incident solar energy directly into electrical energy. Solar energy can be described as either a spectrum of electromagnetic radiation, in the classical-wave theory of light, or as a flux of packets of energy (photons), in the quantum theory of light. Electrical energy is a flow of charge carriers able to do work in an external circuit [48]. Voltage is generated in a solar cell device by the photovoltaic effect (PVE). The terms 'solar cell' and 'photovoltaic (PV) cell' are therefore often used interchangeably. The explanation for the PVE uses ideas from the quantum theory of light [49].

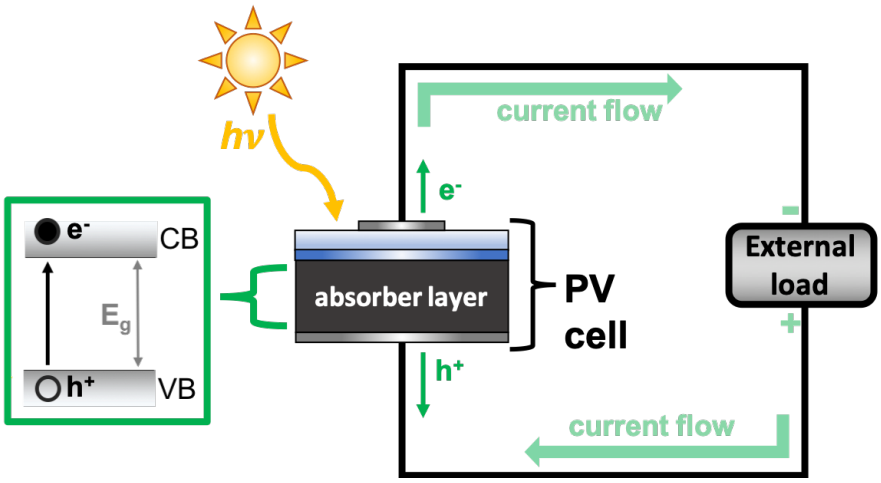

Figure 2-4: Schematic of the photovoltaic effect: a semiconductor under illumination with some built-in electrical asymmetry to drive the separation of charge carriers to be fed into an external circuit and an external load to do electrical work. Optical excitation of an electron-hole pair in absorber layer is indicated in the green box. Layers for the PV cell are purposely not labelled (except for the absorber layer) because the specific architecture of the devices varies for different PV technologies.

Semiconducting materials can be used as the absorber layer in a PV device, the presence of an optical band gap, E_g, in the electronic structure of the material is vital for the PVE. In the case of a perfectly pure semiconductor, only photons with energies higher than the intrinsic E_g can be absorbed to excite an electron from the VB into the CB to produce an electron-hole pair, as shown in the green box in Fig. 2-4. In order for this process to be induced by sunlight, the magnitude of E_g must be within the range of the photon energies that make up the solar spectrum. E_g of a semiconductor is also

necessary for the electrons that have been optically excited to gain extra electrochemical potential energy, which provides the potential difference, or electromotive force, that will later drive electrons through a load in an external circuit to do electrical work. If electrons are instead promoted through a continuum of energy levels, as in a metal, excited electrons would quickly decay back to the ground state via intermediate energy levels, thus dissipating the potential energy gained. In the conventional PV effect, E_g of the material sets the upper limit for the voltage that can be generated. The voltage at open circuit (when current is zero), V_{OC}, is the maximum possible potential difference across the terminals of the solar cell. However, in order for the cell to do any electrical work, both voltage and current (and hence power) must be non-zero when a load is connected in the external circuit [42].

In the absence of a driving force to separate the photoexcited electron and hole, the pair would quickly recombine and relax back to the ground state of the material with the emission of a photon of an energy equal to the energy of the electronic transition that has just occurred. In a PV device there is a 'built-in' electrical asymmetry that provides an electric field to pull electrons away before they can relax and drive them towards electrical contacts to be fed into an external circuit. An electric field is effective for charge separation because it drives positively and negatively charged carriers in opposite directions [50]. There are various ways to provide the electrical asymmetry, such as: through connecting a metal and a semiconductor to form a Schottky barrier junction and connecting a p-type semiconductor to an n-type semiconductor to form a p-n junction. These types of device architectures are outlined in the next section. In section 5.1, novel PV phenomena in bulk materials with internal electric fields, but without the need for such junctions, will be outlined and a search for candidate 'photoferroic' materials is presented in chapter 5. The motivation of this investigation was to find materials where it may be possible to exploit the internal electric fields of polar crystals for enhanced local charge carrier separation.

2.2.2 Solar cell junctions

As discussed in the previous section, an electrical asymmetry is vital for the PVE. A light absorber material must be connected to an external circuit by paths of different resistance for positive and negative charge carriers, i.e. for holes and electrons. This can be provided by spatial variation in the electronic environment, such as the junction between two electronically distinct materials. An electrostatic field can be established by creating a junction with a gradient in the work function (Φ_W), electron affinity (EA)

or band gap (E_{g}), which are all labelled in Fig. 2-5 for both a semiconductor and a metal. The fields established by gradients in EA or E_{g} are usually small, whereas more substantial electric fields can be achieved by a gradient in Φ_{W} [50]. Φ_{W} is the energy required to remove the least tightly bound electron from a material and is given by

$$\Phi_W = E_{\mathrm{vac}} - E_{\mathrm{F}}, \tag{2.7}$$

where E_{vac} and E_{F} are both labelled in Fig. 2-5. E_{vac} is the energy of the vacuum level (where an electron is considered to be completely separated from the material). It is worth noting that the concept of the 'vacuum level' here is different to that used in theoretical materials modelling (discussed later in section 3.2) where the 'vacuum level' is considered to be the energy of an electron *infinitely* separated from the material. E_{F} is the Fermi level. At temperatures above 0 K, E_{F} is considered the energy at which there is a 50% chance of the state being occupied. For a metal, Φ_{W} is defined by EA (indicated in Fig. 2-5). For a semiconductor, Φ_{W} can be controlled by doping of the material since E_{F} is dependant upon the doping. Doping can introduce additional possible energy states into the band gap of material, therefore doping can influence the energy of the state that has a 50% chance of the state being occupied. For instance, a semiconductor doped n-type will have E_{F} closer to the CB and has a smaller Φ_{W} than if it was doped p-type.

When creating a junction between materials with different Φ_{W}, the potential difference to drive photoexcited charge carriers across the junction is created by the difference in Φ_{W} of the two materials [50]. In early PV devices, the asymmetric junction was a Schottky barrier contact between a metal and a semiconductor but now more effective p-n junctions are used in solar cells, which are formed by joining together p-type and n-type semiconductors [49]. In both types of junction, the junction will develop a photovoltage provided that it presents a barrier to majority carrier currents [50]. In the next sections the formation of an electrical asymmetry at a metal-semiconductor is outlined, the limitations of this type of junction in a solar cell is explained and then the formation of an electrical asymmetry at a semiconductor-semiconductor junction is outlined.

Metal-semiconductor junctions

When two materials are isolated, their E_{F} are independent. When they are brought into electrical contact and allowed to reach thermal equilibrium there is no net current flow. Therefore, by definition, E_{F} must be constant across the junction [51]. The Fermi

levels must line up across the junction as shown on the right hand side of Fig. 2-5. If the two materials have different Φ_W, E_{vac} must then change between the two materials by an amount equal to the difference in Φ_W between the two materials. The electrostatic field created by a gradient in the vacuum level energy is $\frac{1}{q}\nabla E_{vac}$. To achieve this gradient, free carriers at the junction redistribute themselves.

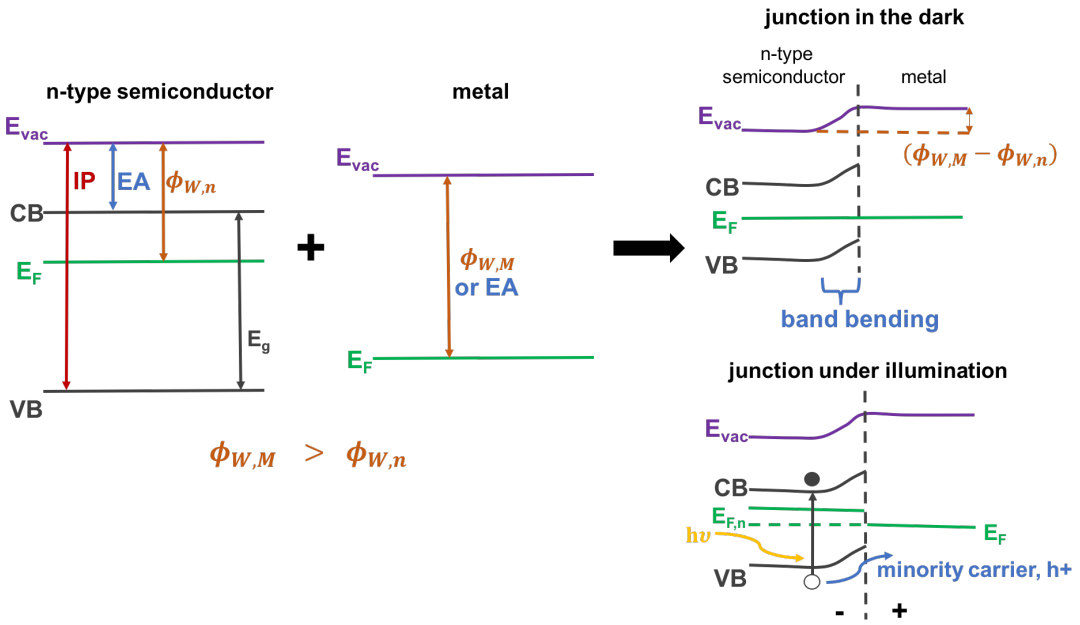

Figure 2-5: The formation of a Schottky barrier junction between an n-type semiconductor and a metal and the splitting of the electron Fermi level ($E_{F,n}$) under illumination. Adapted from Ref. 50 and 52.

In the case of a junction between a metal and an n-type semiconductor, if the metal has a larger Φ_W than the n-type semiconductor, electrons flow from the semiconductor to the metal. A layer of fixed positive charge in the semiconductor and a negative charge on the metal are left behind until a charge gradient builds up that is large enough to prevent any further transport of charge carriers. An electric field that still exists in a material in equilibrium is called a 'built-in' electric field [50]. In this case, the field would drive any excess electrons towards the positively charged side of the junction (the n-type semiconductor) and holes towards the metal side, i.e. it will provide a barrier to the flow of majority n-type carriers from the semiconductor to the metal.

As can be seen in Fig. 2-5, once the semiconductor-metal junction has formed, the CB of the bulk semiconductor is lower than that at the interface, resulting in a spatial variation in electrostatic potential towards the semiconductor-metal interface. This is

the region where E_{vac} is changing, the materials possess a net charge and it is called the space-charge or depletion region as it is devoid of any charge carriers [51]. The potential is distributed across the two materials at the interface but drops off further from the interface and the electric field falls to zero. As metals do not store charge as in a semiconductor, this distance is vanishingly small on the metal side of the junction, but on the semiconductor side this region is typically around 1 micron. The E_{g} and EA of the semiconductor do not vary, therefore the VB and CB levels change in parallel with E_{vac} at the interface, this effect is called 'band bending' and the amount the bands bend is called the 'built-in bias', V_{bi}. In the case of a junction between a p-type semiconductor and a metal, if the metal has a smaller Φ_{W} than the semiconductor, the semiconductor band instead bends downwards at the interface and presents a barrier to the flow of holes from the semiconductor into the metal, which are now the majority carriers. If instead Φ_{W} of the metal is larger than that of a p-type semiconductor or smaller than that of an n-type semiconductor, the bands will instead bend in such a way as to encourage majority carrier transport across the junction. Majority carriers therefore do not accumulate at the interface to develop the potential difference at the interface necessary for the PVE. This is an Ohmic contact, as opposed to a barrier and is not the type of 'solar cell junction' that provides a means for electron-hole separation.

If incident photons have an energy greater than the E_{g} of the semiconductor in a Schottky barrier junction, then an electron-hole pair can be photoexcited (as depicted in Fig. 2-4). The system is now no longer in equilibrium as the density of electrons and holes has increased and is no longer described by the Fermi-Dirac equilibrium distribution function given in Eq. 2.6. The space charge region of the junction will cause the photoexcited electron-hole pair to be separated. In the case of a junction between an n-type semiconductor and a metal, electrons will accumulate in the semiconductor and holes in the metal. The semiconductor will become negatively charged and the potential difference across the junction will be reduced. E_{F} in the semiconductor will now be different for electrons and holes, it has been split into a 'quasi-Fermi level' for electrons. Far from the junction the electron quasi E_{F} will now be larger than in the metal and larger than it was in the semiconductor before illumination, as shown in Fig. 2-5. There are now different distribution functions for electrons in the CB and holes in the VB. It is assumed that the system reaches a new state of quasi-thermal equilibrium because relaxation of photoexcited electrons within the CB and holes in the VB is on a much faster timescale compared to relaxation between the bands. In each case, the charge carriers are able to establish a new quasi-thermal equilibrium within the bands, with associated quasi-Fermi levels for electrons in the CB and holes in the VB, $E_{\mathrm{F,n}}$ and $E_{\mathrm{F,p}}$ respectively [42]. The illumination has generated a photovoltage

equal to the difference in the Fermi level in the metal and the semiconductor [50]. The quasi-Fermi level gradient can be considered as a driving force for conduction [42].

A Schottky barrier junction can therefore facilitate photovoltaic energy conversion, but it suffers from certain limitations which impact the maximum achievable photovoltages. For example, a barrier height greater than approximately half of the band gap of the semiconductor will cause minority carriers to outnumber majority carriers close to the interface region, causing an inversion layer. The junction then becomes carrier rich and cannot sustain a photovoltage. Also if the barrier region at the junction is small and the semiconductor layer is highly doped, tunneling of majority carriers across the junction may occur, reducing the effectiveness of the barrier. Many of these problems can be overcome by using a semiconductor-semiconductor p-n junction [50], outlined next.

Semiconductor p-n junctions

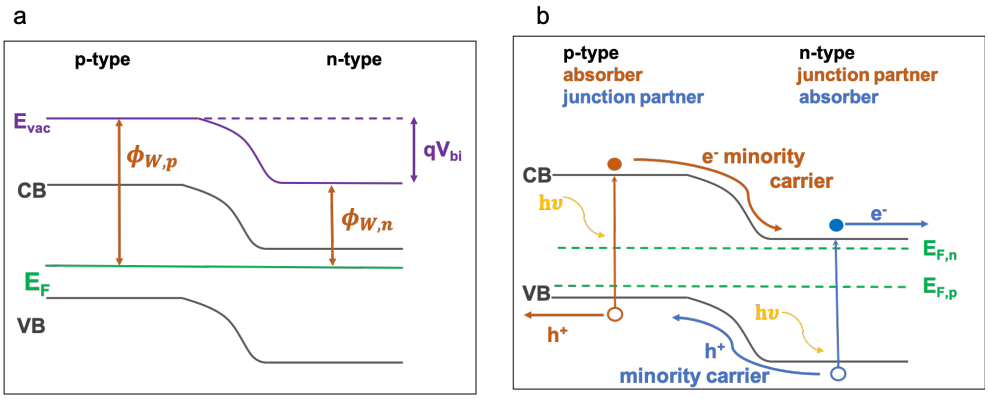

Figure 2-6: a) p-n junction formed between a p-type and n-type semiconductor, in the dark and in thermal equilibrium indicating the difference in work functions (Φ_W) and built-in bias (V_{bi}). Adapted from Ref. 50. b) p-n junction under illumination indicating the direction of flow of minority carriers in the case of a p-type (orange) and n-type (blue) absorber layer. Adapted from Ref. 53.

For certain semiconductors, such as Si, it is possible for the material to be doped both n- and p-type depending on the valence of the dopant species relative to the host lattice, i.e. it is ambipolar. In this case, it is possible to form a junction between electrically distinct p-type and n-type semiconductors by doping different regions of the same material differently to form a 'homojunction'. Since Φ_W of the p-type is larger than that of the n-type region, an electric field is established at the junction due

to the difference in electrostatic potential, as shown in Fig. 2-6a. Under illumination this will drive photoexcited electrons towards the n-type layer and holes towards the p-type layer, as shown in Fig. 2-6b. The junction region is depleted of both electrons and holes [50].

For many of the materials being studied for use as absorber layers in thin-film solar cells, such as chalcogenide-based materials, it is not possible, or is very difficult, to achieve ambipolar doping [54, 55]. Therefore to achieve a p-n junction for many thin-film PV devices it is necessary to form an interface between two different materials with different energy gaps, lattice constants and even slightly different crystal structures. Due to such mismatches, defects are expected to be more prevalent at heterojunction interfaces than at homojunction interfaces. In section 6.1.1 band alignments that have been proposed for reducing the impact of defects at p-n heterojunctions will be discussed and suggestions for heterojunction partners for the candidate photoferroic solar absorber materials are presented.

2.3 Absorber material properties for efficient solar cells

The most fundamental, necessary requirement for a solar absorber material in a PV device is that it possesses a band gap (E_g) across which an electron can be excited. As discussed in the previous section, the magnitude of this E_g must also be somewhere within the energy range of the solar spectrum so that sunlight can induce this excitation. The next most fundamental requirement of a solar absorber material is that it must allow for the transport of charge carriers out of the absorber material layer, into a collection electrode and on to an external circuit in order to do electrical work. Provided these necessary conditions are met and some sort of spatial asymmetry (outlined above) is present to drive electrons away from their point of promotion, the material should exhibit the PVE [56]. However, how well it will actually peform in a solar cell is determined by more stringent criteria and other material properties.

2.3.1 Electronic band gap and optical absorption

Firstly, the actual value of the E_g within the range of the solar spectrum is of importance. It is ideal for the value to be as close as possible to the region of photon energies that make up the majority of the solar spectrum. The optimal range for E_g under typical radiation conditions is approximately 1.0 eV to 1.7 eV [26]. The upper

limit of the power conversion efficiency (PCE) of incident photon energy into electrical energy by a device made from a particular absorber material based on its E_g was first calculated by Shockley and Quiesser in 1961 [15]. A plot of theoretical efficiency limit as a function of E_g was shown in Fig. 1-1, as well as the record efficiencies of various PV technologies.

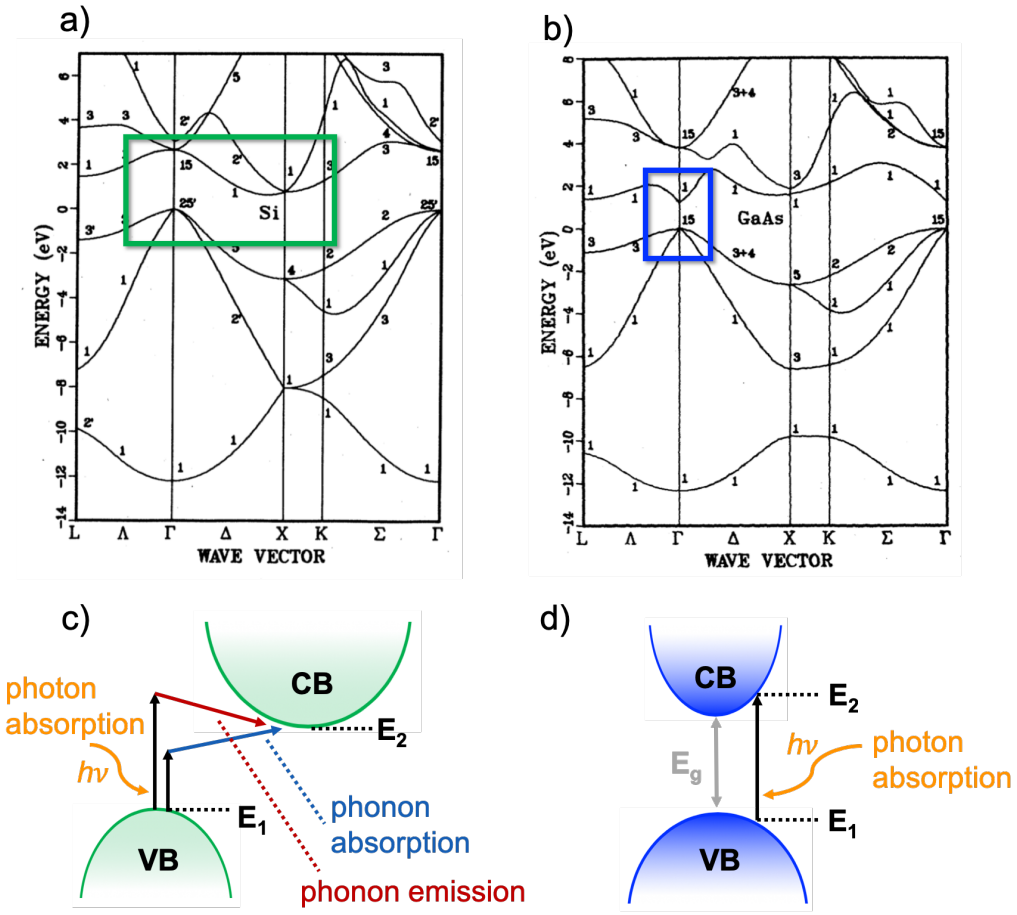

Figure 2-7: The electronic band structure of a) silicon and b) GaAs, reproduced with permission from Ref. 57. Schematic representation of the absorption process in an indirect and direct band gap material (c and d respectively), adapted from Ref. 58.

It is not only the value of E_g that is of importance. More intricate details of the band structure of the material can also impact on the performance of a solar cell device made from the material. Whether the band structure shows a band gap that is direct or indirect can have an impact on the performance of a solar cell made from the material. Fig. 2-7 shows the band structures of Si and GaAs, where Si possesses an indirect band gap and GaAs possesses a direct band gap, i.e. the extrema of the VB and CB occur

at the same value of **k** for the latter but not for the former. The excitation of an electron from the valence band maximum to the conduction band minimum is called fundamental absorption, as there are several other optical absorption transitions that can occur in a semiconducting material, especially in a defective material, and this point will be discussed more in section 2.4. Both the total energy and momentum of all particles involved in the absorption process must be conserved. Photons do possess momentum ($\frac{h}{\lambda}$), however, this is very small compared to the range of crystal momenta and so the electron momentum is effectively conserved during photon absorption. For a direct transition, the absorption coefficient of a material for a given photon energy, hν, is proportional to the probability, p_{12}, of the transition of an electron from the initial state E_1 to the final state E_2, the density of electrons in the initial state, $g_{\mathrm{v}}(E_1)$, and the density of available final states, $g_{\mathrm{c}}(E_2)$. This is then summed over all possible transitions between states where $E_2 - E_1 = \mathrm{h}\nu$. Since the electron momentum is conserved during a direct transition, the crystal momentum in the valence band is approximately the same as that of the final state in the conduction band at energy E_2 [51].

For an indirect band gap semiconductor, such as silicon shown at the top of Fig. 2-7, the valence band maximum occurs at a different crystal momentum to that of the conduction band minimum. As discussed earlier, the momentum of a photon is far less than that of crystal momenta. In order to conserve the momentum of an electron during an optical transition across an indirect band gap, momentum must be either provided by the lattice or released to the lattice usually in the form of the particle representation of a lattice vibration, known as a phonon, as indicated in the top right schematic of Fig. 2-7. Since both a phonon and an electron are needed to make an indirect transition possible, the optical absorption coefficient, α, depends not only on the density of states of the electrons, as for a direct transition, but also on the availability of emitted or absorbed phonons with the required momentum. Therefore, α for an indirect transition compared to a direct transition is typically relatively small and more heavily dependent on temperature [42].

The α of a material determines the penetration depth, $\frac{1}{\alpha}$, of light incident on the material [61]. Fig. 2-8a shows the absorption coefficients of GaAs and Si across a range of wavelengths. The figure shows a less steep onset of absorption for Si compared to GaAs As discussed earlier, Si possesses an indirect band gap, while GaAs possesses a direct band gap. The implication of the differing α and therefore different optical penetration depths of absorber layers is that materials which are stronger absorbers require less material to absorb the light. This forms the basis of thin-film solar cell

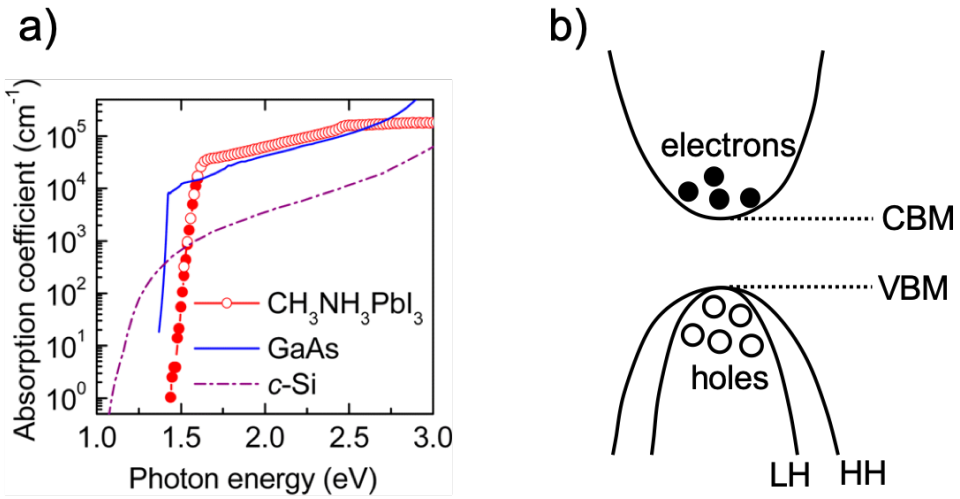

Figure 2-8: a) A comparison of the absorption coefficients of the indirect band gap semiconductor Si and the direct band gap semiconductors GaAs and $CH_3NH_3PbI_3$ across a range of incident photon energies. Figure reproduced with permission from Ref. 59. b) Schematic of a the band structure of a photoexcited semiconductor with electrons near the bottom of the conduction band, holes near the top of the valence band, where the particular material has both heavy- and light-hole bands (labelled HH and LH in the figure respectively). Figure adapted from Ref. 60.

technologies. On the other hand, materials with a weaker onset of absorption, as is often the case for materials with an indirect band gap such as Si, a thicker layer of absorber material is required to absorb the same amount of light [51]. This is undesirable if the particular material contains rare or expensive components and also results in higher demands on material quality as charge carriers must be transported through the absorber material in order to be collected. Thin-film PV technologies typically require a less high-quality and defect-free absorber layer as charge carriers do not have to travel through as much of the material in order to reach a collection electrode. However, defects in the absorber layer do still play a decisive role in determining the device performance of thin-film film PV technology, and this point is discussed much more in section 2.4.

2.3.2 Charge-carrier effective mass

As mentioned in section 2.1.1, another property of importance that can be derived from the electronic band structure of a material, i.e. the plot of $E(\boldsymbol{k})$ vs. k, is the effective mass, m^*. m^* is related to the curvature of the band at the top of the VB (for

holes) or at the bottom of the CB (for electrons). m^* can be calculated by a quadratic least-squares fit to the band extrema when using the parabolic approximation. The curvature of the plot can then be used to obtain m^* with

$$m^* = \left(\frac{1}{\hbar^2} \frac{\partial^2 E}{\partial k^2} \right)^{-1}. \tag{2.8}$$

Just from a quick inspection of the band structure of a material, a more steeply curved shape to the band extrema indicates a lower effective mass and therefore satisfies a necessary condition for higher carrier mobility. Fig. 2-8b shows a schematic of the band structure of a direct band gap semiconductor that has both heavy- and light-hole bands at the valence band maximum, where the flatter band corresponds to the heavy-hole band. The m^* of electrons or holes are the masses they seem to carry for transport properties [62]. For example, in $ZnSnO_3$ the hole m^* has been calculated to be large, indicating that hole mobility will be poor in this material. Poor mobility will make carrier extraction difficult, which has been linked to the low photocurrents observed in this material [63]. However, small m^* should just be considered as a necessary but not a sufficient condition for good carrier mobility as the effect of the effective mass on the transport properties could be overshadowed by other factors, such as the scattering of charge carriers by defects in a real, non-ideal material.

2.4 Impact of absorber layer defects on solar cell performance

Although the main framework for modelling solid-state systems (as outlined at the start of this chapter) is built around perfect, periodic systems; in reality absolutely perfect systems do not exist. Deviations from the perfect crystal lattice structure (i.e. defects) can strongly influence the performance of electronic devices. There is an energy cost associated with the creation of a defect, but in many cases the free energy of a system can be lowered by the incorporation of a certain concentration of defects due to an increase in the configurational entropy of the system [64]. Methods for modelling defects in solids are discussed in section 3.3, but here the impact of defects in the absorber layer on the performance of a solar cell is discussed.

2.4.1 Types of crystal defect

There are many different possible types of crystal defect. If a defect does not involve any atoms that are foreign to the host crystal, then the defect is called an intrinsic or native defect. Defects involving foreign atoms (impurities) are referred to as extrinsic defects. Fig. 2-9b and 2-9c show some examples of extrinsic and intrinsic defects. This work is primarily interested in the fundamental material properties of candidate solar absorber materials, so only intrinsic defects are considered. In real systems, however, impurities are sometimes unintentionally present in the growth or processing environment, or may be introduced intentionally to tune the optoelectronic properties of the material. Defects are usually classified as point or extended defects. Point defects usually involve isolated atoms in localised regions of a host crystal, such as those shown in Fig. 2-9. There are a number of different possible point defects, such as: vacancies, interstitials and antisites, which correspond to the removal, insertion or substitution of species from the perfect host lattice respectively. Extended defects may involve rows of atoms, such as a dislocation defect. Another possible type of defect is a defect complex, which is composed of a small number of point defects.

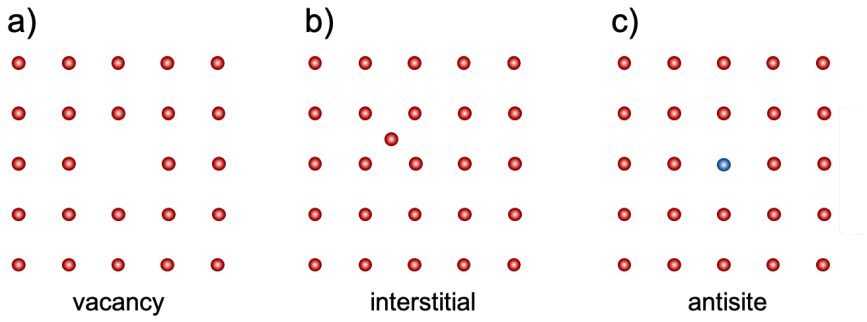

Figure 2-9: Examples of intrinsic point defects (a) and (b) and an extrinsic point defect (c).

The electrical properties of semiconductors can be modified significantly by the incorporation of very small amounts of impurities or defects. It is often the case that less than one defect per million of host atoms is sufficient to alter the properties of a semiconductor [45]. This sensitivity to defects is one of the reasons why semiconductors find many uses in device applications. For example, luminescence centres in wide-band-gap materials can be used to emit light at specific wavelengths or single-spin centres provided by defects can act as artificial atoms and serve as a qubit in a quantum computer [65]. In order to control the electrical properties of a material by introducing defects, typically processes must first be developed to produce a fairly defect-free material, be-

fore intentionally introducing particular defects [45]. In the case of solar cell devices, however, the presence of defects can be detrimental depending on the nature of the defect [66], which will be discussed next.

2.4.2 Optical properties of defective solids

Low defect concentrations

When defects are present at sufficiently low concentrations such that defect-defect interactions are neglible, the defects are considered isolated point defects in the 'dilute limit'. Certain point defects result in additional energy levels in between the valance-band maximum (VBM) and conduction-band minimum (CBM), i.e. within the band gap of the material. An example for intrinsic point defects in the absorber material Cu_2ZnSnS_4 is shown in Fig. 2-10. Electrically active defects have at least one charge state for the defect that produces a defect level in the band gap. This level then has an associated defect wavefunction, a state to which the electron is added to or removed when the charge state of the defect changes. If the defect level is positioned close enough to the band edges such that the defect is likely to be thermally ionised at room temperature, then the defect is conventionally referred to as 'shallow'. If the defect produces a level in the band gap and far from the band-edge, it is a referred to as 'deep'. Another way of defining a defect as 'shallow' or 'deep' is based on the degree of localisation of the wavefunction. If a defect wavefunction is delocalised (on the order of many lattice constants) then the defect has the characteristics of a shallow defect. If the wavefunction is instead localised on the length scale of an atomic bond then this indicates a deep level defect [65].

There are different 'flavours' of defects [66]. Shallow defects can be beneficial to improve electrical conductivity for carrier extraction from an absorber materials. Typically deep levels are thought to be the most detrimental to solar cell device performance [68]. Defects that produce mid-gap states act as Shockley-Read-Hall recombination sites [69], which is regarded as the most important recombination process in real, non-perfect semiconductors. It is a form of non-radiative recombination where a charge carrier is trapped in the defect state before recombining with a charge carrier of opposite polarity. This type of recombination is known to be detrimental to device performance as it results in energy input from sunlight not being converted into electricity [70].

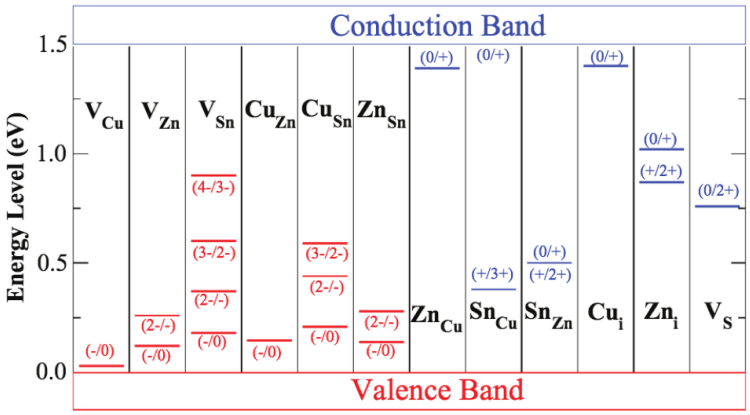

Figure 2-10: Ionisation levels of intrinsic point defects in the band gaps of Cu_2ZnSnS_4. Figure reproduced with permission from Ref. 67.

High defect concentrations

The energy band model described in section 2.1.1 has been successful in explaining many aspects of the behaviour of solids and a large amount of experimental data has supported the theoretical predictions made using this model. Its main drawback is that it assumes a perfect, or nearly perfect, crystal lattice. It applies well to single crystals and polycrystalline substances, but omits important physical characteristics when used to study materials that are amorphous or heavily disordered such that the structure deviates significantly from the periodicity of the crystal [44]. Low concentrations of impurities and defects can be modeled by considering the introduction of distinct additional donor and acceptor energy levels within the band gap of a material (as discussed above) and the scattering of electrons and holes in the solid.

At higher defect concentrations, it is possible to observe a phenomena called 'band tailing'. At sufficiently high concentrations, defect levels interact to form a band. For example, for high n-type doping the impurity band merges with the conduction band, causing a rigid shift of the conduction band towards the valence band [72]. The band profile can be modified with increasing donor density as shown in Fig. 2-11a-c.

Such a tail of band states into the band gap is often referred to as a Lifshitz tail [73], it can be observed experimentally and is most noticeable in heavily doped and amorphous semiconductors [71]. Electronic band tailing can result in the absorption coefficient, α_0, (which was discussed as a key property for PV materials in section 2.3) showing an exponential decline. This effect, illustrated in Fig. 2-11d, is referred to as the Urbach tail [74] and is widely observed in disordered semiconductors [71]. Such tailing can

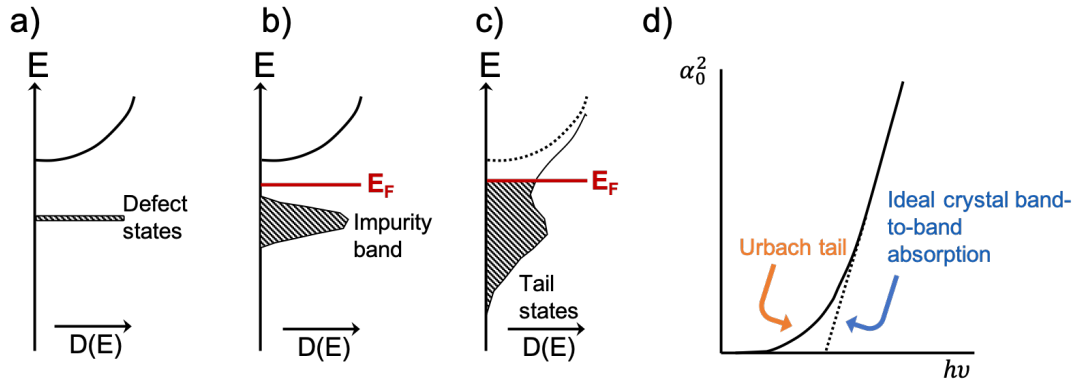

Figure 2-11: The influence of increased donor impurity density on the conduction band profile showing low (a), medium (b) and high (c) densities of impurities. Figure reproduced with permission from Ref. 46. (d) Optical absorption spectrum of a typical direct band gap semiconductor with the absorption coefficient, α_0, proportional to the extended density of states in the Urbach tail. Figure adapted from Ref. 71.

be quantified by the Urbach energy and it has recently been proposed that there is a direct link between the Urbach energy and open circuit voltage deficit in standard PV materials [75, 76].

Chapter 3

Methodology

3.1 Electronic structure calculations

3.1.1 Quantum theory of materials

The properties of materials are determined by their constituent electrons and nuclei and how they interact with each other. Nuclei are massive (compared to electrons) and can usually be described using classical mechanics with interactions via Coulomb's law. However, as hypothesised by de Broglie in his PhD thesis in 1924 [77, 78] and demonstrated experimentally by Davisson and Germer in 1928 [79] with electron diffraction, electrons exhibit wave-like behavior in addition to particle-like behavior and do not obey classical mechanics [80]. The behaviour of the electrons largely determines the physical and chemical properties of a material [81], such as the bonding that holds the material together and many of the observed macroscopic properties such as the optical, electrical and magnetic properties [39]. To describe the behaviour of electrons, it is necessary to use quantum mechanics.

Quantum mechanical systems can be described by the Schrödinger equation (SE), which can describe the energy of the electrons and nuclei within a material where electrons interact with the positively charged atomic nuclei through an electrostatic potential [82]. The time-dependent SE for a one-electron system is given by

$$\left(-\frac{\hbar^2}{2m}\nabla^2 + \hat{V}\right)\psi(r,t) = i\,\hbar\frac{\partial\psi(r,t)}{\partial t}, \tag{3.1}$$

where the first term on the left hand side of the equation is related to the electron's

kinetic energy, the second term to the electron's potential energy ($\hat{V}$) and ψ is used to denote the one-electron wavefunction.

For systems containing more than one electron we must consider the many-body SE and this soon becomes a very complex problem. This is due to the many electrons in the system interacting with each other as well as with the nuclei. The SE for a system containing M nuclei and N electrons is given by

$$\left\{-\frac{\hbar^2}{2m}\left(\frac{\nabla_{n_1}^2}{m_1}+...+\frac{\nabla_{n_M}^2}{m_M},\frac{\nabla_{e_1}^2}{m_e}+...+\frac{\nabla_{e_N}^2}{m_e}\right)+V\left(\boldsymbol{R_1},...,\boldsymbol{R_M},\boldsymbol{r_1},...,\boldsymbol{r_N}\right)\right\}$$
$$\Psi(\boldsymbol{R_1},...,\boldsymbol{R_M},\boldsymbol{r_1},...,\boldsymbol{r_N},t)=i\hbar\frac{\partial\Psi(\boldsymbol{R_1},...,\boldsymbol{R_M},\boldsymbol{r_1},...,\boldsymbol{r_N},t)}{\partial t}, \quad (3.2)$$

where uppercase $\boldsymbol{R}$ denotes nuclear coordinates and lowercase $\boldsymbol{r}$ denotes electron coordinates [82]. This is a very complex mathematical problem for most systems. For example, the many-body wavefunction, Ψ, in Eq. 3.2 for $1\,\mathrm{cm}^3$ of a typical metal would be a function of approximately 10^{23} variables.

When dealing with such systems, the Born-Oppenheimer approximation is almost universally used. As electrons are fast moving relative to the nuclei, they are considered to be moving in the classical field generated by static nuclei. This approximation decouples the nuclear and electronic degrees of freedom, allowing us to separate the ionic and electronic wavefunctions. When using the Born-Oppenheimer approximation it is also assumed that nuclear motion cannot cause electronic transitions, therefore the electrons will remain in their ground state. There is now no explicit time dependence for the electron density as electrons are assumed to always be in their ground state for the instantaneous ionic configuration and that they transition adiabatically to their ground state for each ionic configuration. This approximation is generally more suitable for semiconductors than for metals as phonon energies are usually less than the energy of the electronic band gap in a semiconductor and hence ionic motion cannot excite electrons to higher energy states [81]. Ψ for electrons in the system is now no longer a function of t and so it is the solution of the time-independent SE for the system of ions and electrons that is of interest and the ionic system can be considered separately from the electronic system which is subjected to the classical electric field of a stationary ionic system.

The general form of a time-independent SE for the electronic system is given by

$$\hat{H}\Psi(\mathbf{r_1},...,\mathbf{r_N},\sigma_1,...,\sigma_N)=E\Psi(\mathbf{r_1},...,\mathbf{r_N},\sigma_1,...,\sigma_N), \quad (3.3)$$

where $\hat{H}$ is the Hamiltonian operator used to determine the total energy of a system with the wavefunction Ψ. Lowercase $\boldsymbol{r}$ are the electronic coordinates and σ is used to denote the spin of electrons, which was omitted in earlier equations for simplicity. The Born-Oppenheimer Hamiltonian for the electrons is given by

$$\hat{H} = -\sum_i \frac{\hbar^2}{2m}\nabla_i^2 - \frac{1}{4\pi\epsilon_0}\sum_i\sum_l \frac{Ze^2}{|\mathbf{r_i} - \mathbf{R_l}|} + \frac{1}{8\pi\epsilon_0}\sum_{ij,i\neq j}\frac{e^2}{|\mathbf{r_i} - \mathbf{r_j}|}, \tag{3.4}$$

where l are the ionic sites, Z is the nuclear charge, m is the electron mass, i is the index of the electron and j are the indices of all other electrons in the system. The first term is the kinetic energy of the electrons, the next terms are related to the potential energy of the electrons. The second term is the Coulomb attraction between electrons and static nuclei and the third term is the Coulomb repulsion between different electrons [81].

Although we can write out the electron Hamiltonian as shown above, we do not know the exact form of the many-body wavefunction in Eq. 3.3. The third term in the expression for the Hamiltonian, the summation of electron-electron interactions in the system, is the cause of a dramatic rise in computational expense as the system size (and hence number of interacting electrons) increases. In the next section some of the various approaches that have been developed to treat electron-electron interactions are outlined and those utilised in this work are highlighted.

3.1.2 Treatments of electron-electron interactions

Approximations of the many-body wavefunction

As we do not know the exact form of the many-body wavefunction, Ψ, the simplest way to avoid the dramatic rise in complexity in the many-body SE from electron-electron interactions with increased system size is to approximate the form of Ψ in a manner that allows us to decouple electron-electron interactions. In the 'independent particle approximation', as used in the Hartree method, electrons are treated as independent and are included in an average electron-electron interaction scheme. The method involves assuming approximate forms of both the Hamiltonian and the many-body wavefunction. The electron-electron interaction term in the Hamiltonian in Eq. 3.4 is replaced by one that accounts for only the repulsion between an electron and the average position of all other electrons, the electrons therefore interact with an average effective potential instead of many, many interactions between all pairs of electrons in

the system. This is an example of a mean field approximation. As electrons are considered to be independent, the many-body wavefunction can be written as the product of single-electron wavefunctions (or orbitals) as

$$\Psi_H = \psi_1(\boldsymbol{r_1}, \sigma_1)\psi_2(\boldsymbol{r_2}, \sigma_2)...\psi_N(\boldsymbol{r_N}, \sigma_N), \tag{3.5}$$

where $\psi_i(\boldsymbol{r_i}, \sigma_i)$ is the wavefunction of a single electron i at position r_i with spin σ_i [81]. To solve the many-body SE, the Hartree method pioneered the self-consistent field method [39]. Firstly, the variational principle is invoked to set up an inequality for the groundstate energy, E_0, of the system (i.e. the minimum total energy) to find an approximate value of E_0 and the corresponding set of ψ_i

$$E = \langle\Psi|\hat{H}|\Psi\rangle \geq E_0, \tag{3.6}$$

where the middle term is the expectation value of a state of the system described by the many-body wavefunction Ψ. Many properties of interest can be determined from E_0 of the system and from changes in the energy of the system in response to particular perturbations. E_0 can be used to determine various structural properties such as equilibrium bond lengths, surface configurations and the most likely defect structures in a material.

The Hartree equation is given by

$$\left[-\frac{\hbar^2}{2m_e}\nabla^2 + V_I(\boldsymbol{r}) + V_H(\boldsymbol{r})\right]\psi_i(\boldsymbol{r}) = \epsilon_i\psi_i(\boldsymbol{r}), \tag{3.7}$$

where

$$V_H(\boldsymbol{r_i}) = \frac{1}{4\pi\epsilon_0}\sum_{j\neq i}\int\frac{e^2|\psi_j|^2}{|\boldsymbol{r_i} - \boldsymbol{r_j}|}\mathrm{d}^3r_j, \tag{3.8}$$

and

$$V_I(\boldsymbol{r_i}) = -\frac{1}{4\pi\epsilon_0}\sum_l\frac{Ze^2}{|\boldsymbol{r_i} - \boldsymbol{R_l}|}. \tag{3.9}$$

The solution of the Hartree equation depends on the Hartree potential ($V_H(\boldsymbol{r_i})$), shown in Eq. 3.8. However, $V_H(\boldsymbol{r_i})$ depends on the solution of the Hartree equation itself to obtain ψ_i. The solution of the Hartree equation therefore involves a self-consistent procedure. A guess is made for $V_H(\boldsymbol{r_i})$ and then Eq. 3.7 is solved. Then the solution is used to calculate $V_H(\boldsymbol{r_i})$ with Eq. 3.8 and the Hartree equation is solved again with this new value for $V_H(\boldsymbol{r_i})$. The procedure is repeated until input and output potentials are the same, within a specified tolerance [81].

There are a number of large drawbacks of the Hartree method. The mean-field approach to obtaining the Hartree potential is flawed due to spurious self-interactions. As every electron is included in the average electron density, when calculating the electron-electron interaction term each electron will also be interacting with itself. The next large omission of the Hartree method is electron correlation. The probability of finding an electron at $\boldsymbol{r_1}$ is uncorrelated to finding one at $\boldsymbol{r_2}$ because it can be written as a product of two one-electron probabilities. Paraphrasing John Perdew from his talk at the 2015 'Hands-on workshop density-functional theory and beyond: First-principles simulations of molecules and materials' helps to explain why this is neglecting some behaviour of the electron density: electron correlation can be likened to shoppers at a busy shopping mall where many people are moving around but in such a way that they try to avoid bumping into each other. Neglecting this effect can lead to results as unphysical as the dissociation of the H_2 molecule [81].

Lastly, the basic Hartree method described above does not account for electron exchange. Although the spin of the electron is included in Eq. 3.5, it actually plays no role in the Hartree method. The many-body wavefunction needs to be antisymmetric under particle exchange as required by the Pauli Exclusion Principle for fermions. This requirement can be expressed as

$$\Psi(\boldsymbol{r_1}\sigma_1, ..., \boldsymbol{r_i}\sigma_i, ..., \mathbf{r_j}\sigma_j, ...) = -\Psi(\boldsymbol{r_1}\sigma_1, ..., \boldsymbol{r_j}\sigma_j, ..., \boldsymbol{r_i}\sigma_i, ...). \tag{3.10}$$

According to the Pauli Exclusion Principle, no two fermions can occupy the same quantum state. The spin quantum number therefore should be taken into account. The Hartree-Fock (H-F) extension to this method is able to account for this latter flaw [81].

The requirement shown in Eq. 3.10 can be satisfied by using the Slater determinant as the trial wavefunction, as given by

$$\Psi(\boldsymbol{r_1}\sigma_1, ..., \boldsymbol{r_N}\sigma_N) = \frac{1}{\sqrt{N!}} \begin{bmatrix} \psi_1(\boldsymbol{r_1}\sigma_1) & \psi_1(\boldsymbol{r_2}\sigma_2) & \dots & \psi_1(\boldsymbol{r_N}\sigma_N) \\ \psi_2(\boldsymbol{r_1}\sigma_1) & \psi_2(\boldsymbol{r_2}\sigma_2) & \dots & \psi_2(\boldsymbol{r_N}\sigma_N) \\ \vdots & \vdots & \vdots & \vdots \\ \psi_N(\boldsymbol{r_1}\sigma_1) & \psi_N(\boldsymbol{r_2}\sigma_2) & \dots & \psi_N(\boldsymbol{r_N}\sigma_N) \end{bmatrix}, \tag{3.11}$$

where N is the number of electrons.

When using the Slater determinant as the trial wavefunction, each electron is now surrounded by an 'exchange hole' in which the probability of finding another electron

is very small. The exchange term in the H-F method also cancels the self-interaction in the Hartree potential as a result of the antisymmetry. However, the H-F method still neglects Coulomb repulsion correlation effects that arise due to electrons moving in such a way to avoid each other. It includes some correlation effects between parallel spin electrons from the explicit treatment of exchange interactions, but neglects correlations between opposite spin electrons. The exchange term tends to lower the total energy of the system due to the tendency to keep two electrons with the same spin apart, however, the Coulomb correlations reduce the exchange interaction between electrons with parallel spins, so the H-F method overestimates the strength of the exchange interaction. The H-F method is better suited to compact systems such as atoms or molecules but describes conduction electrons in solids poorly [81] and, despite the approximations used, is still very computationally demanding [83].

Coulomb correlations can be introduced by using the Configuration Interaction method which involves writing the many-body wavefunction as a weighted sum of H-F wavefunctions for different electronic configurations. This method has been successful for atoms and molecules, but is very difficult to apply for large molecules or solids [81] and is therefore not used at all in this work where calculations have only been performed for solid-state systems. For solids, density functional theory (DFT) is usually the methodology of choice, which is outlined in the next section.

Electron density methods

The essence of density functional theory (DFT) is to write the total energy as a functional of a simpler quantity to provide a more feasible approach to solving the many-body Schrödinger equation. The methods described above solve the many-body Schrödinger equation by approximating the many-body wavefunction, Ψ, which involves the coordinates of all electrons in the system and therefore is a function of 3N variables, where N is the number of electrons in the system which is typically large for most systems of interest. If the system is instead described by the electron density, $n(\boldsymbol{r})$, instead of Ψ the key quantity in the equation would instead be a function of 3 variables [84].

The earliest electron density method was the Thomas-Fermi theory proposed in 1927 [85, 86]. In the original method, the kinetic energy of the system is approximated as an explicit functional of the electron density, simplified to a non-interacting homogeneous electron gas with density equal to the local density at any given point. However, approximations used in this method are too crude to account for many essential physical

and chemical aspects of matter, such as the electronic shell structures of atoms and the binding of molecules [87].

In 1964 Hohenberg and Kohn provided two theorems (and corresponding proofs) which formulated DFT as an exact theory of many-body systems [88]. The ansatz provided by Kohn and Sham a year later [89] then allowed for the construction of useful, approximate ground state functionals for real systems of many electrons. The two Hohenberg-Kohn theorems are as follows:

1. The external potential, $V_{\text{ext}}(\mathbf{r})$, for a system of interacting electrons is a unique functional of the ground state electron density, $n(\mathbf{r})$. The total ground state energy, E, of a many-electron system therefore is also a unique functional of $n(\mathbf{r})$, $E[n(\mathbf{r})]$.

2. The total energy functional, $E[n(\mathbf{r})]$, for the total energy has a minimum equal to the ground state energy at the ground state electron density.

Combining both Hohenberg-Kohn theorems says that the ground state energy of a system can be determined from the unique ground state electron density by minimising the energy functional, $E[n(\mathbf{r})]$, with respect to the electron density, $n(\mathbf{r})$. However, this does not yet tell us anything about the form of $E[n(\mathbf{r})]$.

The approach proposed by Kohn and Sham in 1965 involves replacing the original interacting many-body problem by an auxiliary system that can be solved more easily. This auxiliary system involves independent electrons, but an interacting density. The assumption made here is that the ground state density of the original interacting system is the same as that of some auxiliary non-interacting system, where all complex many-body interaction are incorporated into an exchange-correlation functional of the electron density, $E_{\text{xc}}[n(\mathbf{r})]$. When the Kohn-Sham equations are solved, the ground state electron density of the original system is then determined, with accuracy limited only by the approximate form of $E_{\text{xc}}[n(\mathbf{r})]$ [90].

Using the Born-Oppenheimer approximation, E[n($\mathbf{r}$)] can be expressed as

$$E[n(\mathbf{r})] = \langle\Psi|V_{\text{ext}}|\Psi\rangle + \langle\Psi|T + V_{\text{EE}}|\Psi\rangle = \langle\Psi|V_{\text{ext}}|\Psi\rangle + F[n(\mathbf{r})], \tag{3.12}$$

where the first term is the external potential from the interaction between electrons and nuclei and the second term is usually denoted as $F[n(\boldsymbol{r})]$. This term is a functional of the electrons only where T is the functional for the electron kinetic energy and V_{EE} is for electron-electron interactions.

$F[n(\boldsymbol{r})]$ can be split into three parts as

$$F[n(\boldsymbol{r})] = T[n(\boldsymbol{r})] + \frac{e^2}{2}\int\int \frac{1}{4\pi\epsilon_0}\frac{n(\boldsymbol{r})n(\boldsymbol{r'})}{|\boldsymbol{r}-\boldsymbol{r'}|}\mathrm{d}^3r\mathrm{d}^3r' + E_{\mathrm{xc}}[n(\boldsymbol{r})], \tag{3.13}$$

where $T[n(\boldsymbol{r})]$ is the kinetic energy of a non-interacting electron gas of density $n(\boldsymbol{r})$ in its ground state, the second term is the classical Coulomb repulsion energy between the electrons and the last term then contains all of the many-body effects of the electronic system, including: exchange, correlation and part of the total kinetic energy [84].

Substituting Eq. 3.13 into Eq. 3.12, Eq. 3.12 can be re-written as

$$E[n(\boldsymbol{r})] = \int V_{\mathrm{ext}}(\boldsymbol{r})n(\boldsymbol{r})\mathrm{d}^3r + T[n(\boldsymbol{r})] + \frac{e^2}{2}\int\int \frac{1}{4\pi\epsilon_0}\frac{n(\boldsymbol{r})n(\boldsymbol{r'})}{|\boldsymbol{r}-\boldsymbol{r'}|}\mathrm{d}^3r\mathrm{d}^3r' + E_{\mathrm{xc}}[n(\boldsymbol{r})]. \tag{3.14}$$

If Eq. 3.14 is minimised subject to the constraint that the integral of the electron density over the whole system volume is equal to the number of electrons in the system

$$\int n(\boldsymbol{r})\mathrm{d}^3r = N, \tag{3.15}$$

this gives

$$\frac{\partial T[n(\boldsymbol{r})]}{\partial n(\boldsymbol{r})} + V_{\mathrm{ext}}(\boldsymbol{r}) + \int \frac{e^2}{4\pi\epsilon_0}\frac{n(\boldsymbol{r'})}{|(\boldsymbol{r})-(\boldsymbol{r'})|}\mathrm{d}^3\boldsymbol{r'} + \frac{\partial E_{\mathrm{xc}}[n(\boldsymbol{r})]}{\partial n(\boldsymbol{r})} - \mu = 0, \tag{3.16}$$

where the third term is the Hartree potential (V_{H}), the fourth term is the exchange-correlation potential (V_{xc}) and the fifth term is the Lagrange multiplier.

Kohn and Sham noted that, apart from the inclusion of $E_{\mathrm{xc}}[n(\boldsymbol{r})]$, Eq. 3.12 is identical to Hartree's expression for energy. Without the corresponding term in Eq. 3.16, $V_{\mathrm{xc}}[n(\boldsymbol{r})]$, this could be solved in a similar manner to the Hartree method by using the substitution

$$n(\boldsymbol{r}) = \sum_{i=1}^{N}|\psi_i(\boldsymbol{r})|^2, \tag{3.17}$$

and solving

$$\left(-\frac{\hbar^2}{2m_e}\nabla^2 + V_{\mathrm{ext}}(\boldsymbol{r}) + V_{\mathrm{H}}(\boldsymbol{r})\right)\Psi_i(\boldsymbol{r}) = \epsilon_i\Psi_i(\boldsymbol{r}). \tag{3.18}$$

If $n(\boldsymbol{r})$ can be defined in terms of one-electron orbitals, as in Eq. 3.17, but by also including $V_{\mathrm{xc}}(\boldsymbol{r})$ through an effective potential, $V_{\mathrm{eff}}(\boldsymbol{r})$, as shown in

$$V_{\mathrm{eff}}(\mathbf{r}) = V_{\mathrm{ext}}(\mathbf{r}) + V_{\mathrm{H}}(\mathbf{r}) + V_{\mathrm{xc}}(\mathbf{r}), \tag{3.19}$$

then the Kohn-Sham (KS) equations

$$\left(-\frac{\hbar^2}{2m_e}\nabla^2 + V_{\text{eff}}(\mathbf{r})\right)\Psi_i(\mathbf{r}) = \epsilon_i\Psi_i(\mathbf{r}), \tag{3.20}$$

can be solved self-consistently, analogously to solving Eq. 3.18 in the Hartree method.

The set of fictitious, non-interacting one-electron wavefunctions in Eq. 3.17 are called the KS orbitals. However, these do not correspond to the physical atomic orbitals of the system. The KS orbitals are used to reproduce the correct ground state electron density when mapping the interacting electron system onto an auxiliary system of independent particles, which move in the KS potential from Eq. 3.19. Although solving Eq. 3.20 is very similar to the Hartree method and reduces the many-electron problem to a set of one-electron problems, unlike the Hartree or H-F methods, DFT includes the effects of electron correlations as well as exchange because of the $V_{xc}(\boldsymbol{r})$ term. While the H-F method treats exchange exactly, it neglects correlations completely. The form of $V_{xc}(\boldsymbol{r})$ is not known therefore some approximation has to be made for this function. Exchange and correlation are both included in DFT, but only approximately. However, reasonable accuracy has been achieved with these approximate forms [84]. In the next section common approximations used in DFT will be outlined and those utilised in this work will be highlighted.

Exchange-correlation functionals, $E_{\text{xc}}[n(\boldsymbol{r})]$

In 1965 Kohn and Sham also developed the first approximate form for the exchange-correlation functional, the local density approximation (LDA). Due to the explicit separation of the independent particle kinetic energy and long-ranged Hartree terms in Eq. 3.14, the remaining exchange-correlation energy contributions can be approximated by a local or nearly-local functional of the electron density [90]. In this approximation, it is assumed that the electron density, $n(\boldsymbol{r})$, varies very slowly in space such that the electron gas in a small volume could be considered as approximately uniform locally, close to the limit of the homogeneous electron gas (HEG) [91]. This approximation would then allow for the use of the exchange-correlation energy of the HEG to evaluate the form of the exchange-correlation functional, as given by

$$E_{\text{xc}}[n(\boldsymbol{r})] = \int \epsilon_{\text{xc}}(n(\boldsymbol{r}))n(\boldsymbol{r})\mathrm{d}^3r, \tag{3.21}$$

where $\epsilon_{\mathrm{xc}}(n(\boldsymbol{r}))$ is the exchange-correlation energy per particle of a uniform gas of density $n(\boldsymbol{r})$ [84]. A simple analytic form is known for the exchange energy of the HEG and the correlation energy of the HEG has been calculated using Monte Carlo methods in Ref. 92 [91].

This approach can also be extended to spin-polarised systems with the localised spin density approximation (LSDA) where there is an unequal number of spin-up and spin-down electrons. In this case, $E_{\mathrm{xc}}[n(\boldsymbol{r})]$ is split into separate parts for the spin-up and spin-down electron densities [84].

Although the LDA has given remarkably good results for some systems, such as simple metals where the electron density more closely resembles the HEG, performance is poorer for more inhomogeneous systems, like atoms where the density must continuously approach zero outside of the atom [91]. The accuracy of the LDA is not sufficient for purposes such as predicting binding energies for chemical reactions, subsequent works therefore have sought to construct improved functionals. The gradient expansion approximation (GEA) was suggested by Kohn and Sham [89] where $E_{\mathrm{xc}}[n(\boldsymbol{r})]$ is expanded in terms of gradients of the electron density in Taylor series and truncated at some order [84]. The exact exchange-correlation energy is related to the concept of an 'exchange-correlation hole' in which all other electrons are excluded. The integration over this hole in the electron density is equal to one electron, hence the combination of the electron and the exchange-correlation hole gives a net neutral unit. The LDA approximates the exchange-correlation hole to be a sphere, while the inclusion of gradients in the electron density allows for more elaborate shapes for the exchange-correlation hole [90].

The GEA was not found to give systematic improvements over the LDA and important conditions such as the sum rules for the exchange-correlation holes were violated. The large density gradients in real materials cause the low-order gradient expansions to break down. Generalised-gradient expansions (GGAs) have been proposed instead. Here functionals are constructed that are functions of both electron density, $n(\boldsymbol{r})$, and gradients in the density, $\nabla n(\boldsymbol{r})$, which do satisfy sum rules. The general, spin-polarised form of a GGA is

$$E_{\mathrm{xc}}^{\mathrm{GGA}}[n_{\uparrow}(\mathbf{r}), n_{\downarrow}(\mathbf{r})] = \int \mathrm{d}^3 r f[n_{\uparrow}(\mathbf{r}), n_{\downarrow}(\mathbf{r}), \nabla n_{\uparrow}(\mathbf{r}), \nabla n_{\downarrow}(\mathbf{r})], \tag{3.22}$$

where various functions are used for f in the equation and $n_{\uparrow}(\boldsymbol{r})$ and $n_{\downarrow}(\boldsymbol{r})$ correspond to the density of spin up and spin down electrons respectively. Various GGAs have been developed to improve the predictive power of DFT and have demonstrated sufficient

accuracy to now be utilised by the chemistry community. The rapidly varying electron density in atoms leads to a greater lowering of exchange energy in atoms and molecules than in solids, this results in a reduction in the binding energy which is not accounted for by the LDA. The use of density gradients in the GGA is able to correct for some of the overbinding from the LDA [91].

Some GGA functionals are semi-empirical due to their use of fits to experimental data. An example of one of the less empirical functionals is the PBE functional [93], where the main parameterisation is in the LDA component and otherwise fundamental physical constants are favoured over empirical fits. Semi-empirical GGAs can accurately represent small molecules, but usually fail for delocalised electrons in the uniform gas or for simple metals. First-principles numerical GGAs can be constructed from electron density-gradient expansions for the exchange-correlation hole surrounding the electron in a system of slowly varying density with spurious long-range terms cut off to satisfy sum rules on the exact hole [93]. However, accurate atomic exchange energies require violating the gradient expansion for slowly varying densities, which are more appropriate when modelling solids. A gradient expansion that works well for an atomic system is likely to perform poorly for a solid. For this reason, an alternative PBE functional has been developed for solids, the PBEsol functional [94]. In this work, the PBEsol functional is often used for obtaining geometries. However, there are still some shortcomings in the simulation of semiconductors for PV applications with semilocal functionals such as PBEsol. A notable issue is the band gap error where the electronic band gap of semiconductors and insulators is often substantially underestimated compared to experimental measurements [95]. Significant improvements in the computational prediction of this important material property have been achieved with some 'beyond-DFT' methods. One method for this, which is utilised in this work, is hybrid density functionals which are introduced in the next section.

Hybrid-DFT

Various hybrid density functionals have been developed to improve upon standard DFT. One such approach is to incorporate some exact, non-local H-F exchange into a pure GGA functional. The exchange component, x, of this hybrid exchange-correlation functional, $E_{\mathrm{xc}}^{\mathrm{hybrid}}[n(\boldsymbol{r})]$, is expressed as a linear combination of the exchange components of the DFT functional, $E_{\mathrm{xc}}^{\mathrm{DFT}}[n(\boldsymbol{r})]$, and the H-F functional, $E_{\mathrm{xc}}^{\mathrm{HF}}[n(\boldsymbol{r})]$, with

some mixing parameter a as

$$E_{\mathrm{xc}}^{\mathrm{hybrid}}[n(\mathbf{r})] = E_{\mathrm{xc}}^{\mathrm{DFT}}[n(\mathbf{r})] + a(E_{\mathrm{x}}^{\mathrm{HF}}[n(\mathbf{r})] - E_{\mathrm{x}}^{\mathrm{DFT}}[n(\mathbf{r})]). \tag{3.23}$$

The H-F method tends to underbind atoms in molecules [96]. Although electron exchange is treated exactly, the method completely neglects electron correlation and therefore the modelled system entirely lacks a mechanism by which the electron arrangement could act to lower the total energy of the system. Hence the total energy of the system may be overestimated. DFT however, in particular the LDA, overbinds atoms in molecules and overly favours the formation of bonds [96]. The approximation of a more uniform electron density than what may exist in the system in reality when constructing such electron density functionals may result in the assumption of a stronger, more uniform bonding arrangement, artificially lowering the total energy of the system. Some types of hybrid density functionals have been constructed to improve upon both methods by combining them, but the ways in which the functionals are combined differs for different hybrid functionals.

In this work, the HSE06 hybrid functional [97] is frequently used for calculations of electronic properties. This functional has been demonstrated to produce accurate electronic properties with predicted electronic band gaps for semiconductors much closer to experimental values than those produced using semilocal functionals such as PBE and PBEsol [98]. The HSE06 functional involves two adjustable parameters. Firstly, the mixing parameter a, as in Eq. 3.23, but also a parameter ω which determines the screening of the exact exchange in the construction of this functional. The HSE06 functional uses PBE as the GGA functional, incorporates 25% H-F exchange (with $a{=}\frac{1}{4}$) and uses $\omega = 0.11\,\mathrm{bohr}^{-1}$ for the screening parameter [97].

The exact H-F exchange is very computationally expensive to calculate for large molecules and solids. Kohn has shown that the range of the exchange interaction in insulators decays exponentially as a function of the band gap [99]. Therefore, convergence with distance is very slow for small gap or metallic systems [100]. Screened hybrid functionals, such as the HSE06 functional, have been introduced to reduce the computational expense of the inclusion of exact H-F exchange. In the case of the HSE06 functional, a screened Coulomb potential is applied to the exchange interaction only to screen the long-range component of the H-F exchange [97]. This restricts the Fock exchange calculations to small electron-electron separations [101]. The Coulomb operator is split into short-range (SR) and long-range (LR) components as shown in the first and second

terms, respectively, on the right-hand side of

$$\frac{1}{r} = \frac{\mathrm{erfc}(\omega r)}{r} + \frac{\mathrm{erf}(\omega r)}{r}, \tag{3.24}$$

and ω defines the separation range. All of the terms for the hybrid exchange energy are split into their short- and long-ranged components in

$$E_{\mathrm{x}}^{\mathrm{hybrid}} = aE_{\mathrm{x}}^{\mathrm{HF,SR}}(\omega) + aE_{\mathrm{x}}^{\mathrm{HF,LR}}(\omega) + (1-a)E_{\mathrm{x}}^{\mathrm{PBE,SR}}(\omega) + E_{\mathrm{x}}^{\mathrm{PBE,LR}}(\omega) - aE_{\mathrm{x}}^{\mathrm{PBE,LR}}(\omega). \tag{3.25}$$

Numerical tests indicated that the LR H-F and PBE exchange contributions to this functional are small and tend to cancel each other [100], therefore these terms are neglected in the expression for the exchange-correlation energy in

$$E_{\mathrm{xc}}^{\mathrm{HSE06}} = aE_{\mathrm{x}}^{\mathrm{HF,SR}}(\omega) + (1-a)E_{\mathrm{x}}^{\mathrm{PBE,SR}}(\omega) + E_{\mathrm{x}}^{\mathrm{PBE,LR}}(\omega) + E_{\mathrm{c}}^{\mathrm{PBE}}. \tag{3.26}$$

When the adjustable parameter $\omega = 0$, the LR term becomes zero and the SR term is the full Coulomb operator, equivalent to an unscreened hybrid functional. When $\omega \to \infty$, the HSE functional becomes identical with the semilocal PBE functional. The values chosen for a and ω in the HSE06 functional have been found to be close to the optimum in terms of accuracy and computational efficiency in a systematic study varying these parameters in hybrid functionals [101]. However, the study also identifies alternative values for the two parameters for improved accuracy over the HSE06 functional and also parameters which were found to match the accuracy of the HSE06 functional but with reduced screening length and hence reduced computational expense. Improvement in the accuracy and transferability of density functionals to various systems is an on going area of research.

3.1.3 Implementation for periodic solids

Concepts for the theoretical modelling of periodic solids were outlined at the start of section 2.1. These principles are also used in electronic calculations of solid state systems through the implementation of periodic boundary conditions (PBCs) to simulate an infinite, bulk system using only a unit cell of the crystal. The only deviations from the basic implementation of PBCs are in section 6.1.1. This work involved calculating surface properties of candidate solar absorber materials to investigate possible candidate solar cell heterojunction partners. Methodology for this study will be outlined in section 3.2. The other deviation from simple PBCs for electronic structure calculations in this work is the simulation of point defects in the dilute limit using the supercell

method [102]. This method will be discussed further in section 3.3.

In the rest of this section, approaches used in this work for electronic structure calculations of periodic solid-state systems will be outlined with comments on their relative merits for chemical accuracy and computational efficiency. Representations of the wavefunction in different electronic structure software packages that are used in this work will first be described. Then the general workflow for geometric and electronic optimisation will be outlined. The section concludes with a discussion of determining the most appropriate setup for electronic structure calculations in terms of an optimal compromise between chemical accuracy and computational efficiency.

Representations of wavefunctions for electronic structure calculations

The exact, analytical solution of the Schrödinger equation for H gives us wavefunctions corresponding to the familiar 1s, 2s, 2p, etc. atomic orbitals. In the non-relativistic case (where there is no spin-orbit coupling), the wavefunction can be decoupled as a product of space and spin. Since the nuclear potential acting on the electron is spherically symmetric, the spatial part of the orbital can be described by angular momentum quantum numbers, $\mathrm{L} = \{\mathrm{l}, \mathrm{m_l}\}$ [103]. This is shown for the hydrogenic one-electron atom in

$$\psi_{nlm}(r, \theta, \phi) = R_n(r) Y_{lm}(\theta, \phi), \tag{3.27}$$

where the full wavefunction is described by the product of the radial and angular distribution functions and expressed in spherical coordinates. The radial component is related to the probability of finding an electron at a particular distance from the nucleus and the angular component is necessary to account for electronic orbitals that are not spherical in shape.

In a solid, the wavefunctions tend to be atom-like close to each atom. Atomic wavefunctions are closely related to the radial atomic-like functions used in electronic structure codes to represent wavefunctions for solid-state systems [103]. Fig. 3-1a shows calculated 1s and 2s orbitals for the Li atom, while fig. 3-1b and c show representations of wavefunctions used in different electronic structure software packages for solids, which will be discussed below. Accurate description of the electronic structure of atoms is a vital starting point for computing the properties of valence electrons in molecules or solids, which predominantly determine the bonding in the material [104]. This knowledge is the basis for constructing numeric atom centred orbitals (NAOs) and ab initio pseudopotentials (PPs) as used in the Fritz Haber Institute ab initio molecular simula-

tions (FHI-aims) [105] software package and the Vienna Ab-initio Simulation Package (VASP) [106] to predict the electronic structure of molecules and solid state systems.

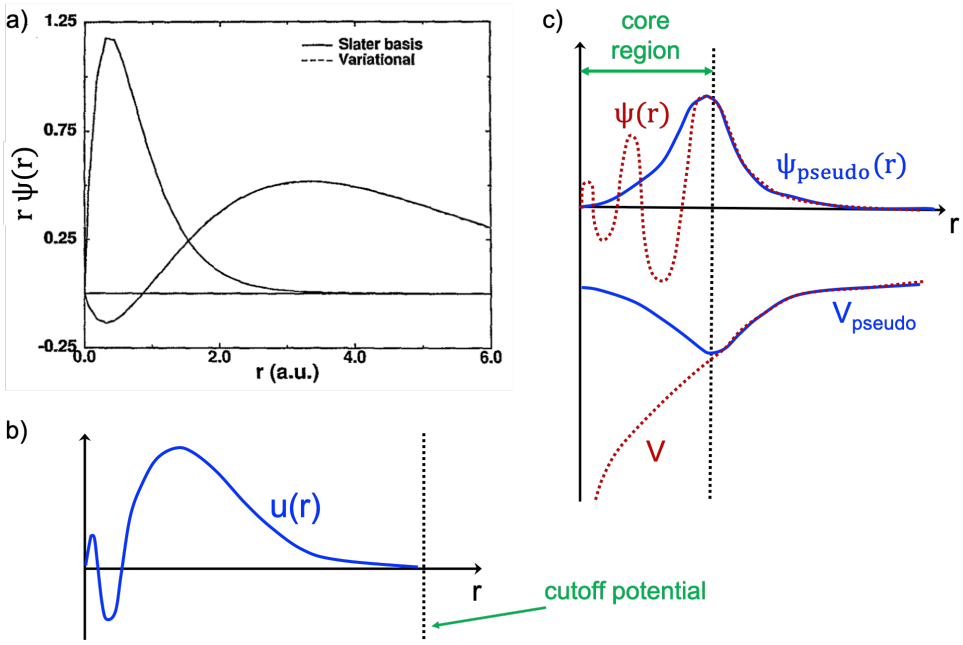

Figure 3-1: a) Calculated radial wavefunction, $r\psi(r)$, for the 1s and 2s orbitals of a lithium atom. Figure reproduced with permission from Ref. 107. b) Schematic representation of a numeric atom-centred orbital (NAO) basis function as used in the FHI-aims software package. Figure adapted from Ref. 108. c) Schematic representation of a pseudopotential and pseudo-wavefunction (both shown by blue solid lines) and corresponding original Coulomb potential and wavefunction (both shown by dashed red lines), where both red and blue lines converge at distances beyond the core region. Figure adapted from Ref. 109.

Eq. 3.28 shows the expansion of the KS orbitals in terms of a set of known functions, called a basis set

$$\psi(\boldsymbol{r}) = \sum_j c_j \phi_j(\boldsymbol{r}). \tag{3.28}$$

Constructing a basis set of linearly independent functions allows the use of linear matrix methods and efficient computational tools to solve the KS eigenvalue problem. There are different options for how to mathematically represent the wavefunction. In this work, two different software packages are used for electronic structure calculations, which make use of different functions for their basis sets.

In the FHI-aims software package, numeric atom-centred orbital (NAO) basis functions

$$\phi_{\mathrm{NAO}}(\boldsymbol{r}) = \frac{u_i(\boldsymbol{r})}{r} Y_{lm}(\Omega), \tag{3.29}$$

are the basis set used. This basis set for each atomic species has been established from iterative automated construction based on dimers [108]. The radial shape, $u_i(\boldsymbol{r})$, is numerically tabulated and so fully flexible, enabling the creation of optimised element-dependent basis sets that are as compact as possible to minimise computational expense. A schematic represenatation of a NAO is shown in Fig. 3-1b. The NAO basis set used in FHI-aims is localised and highly scalable for use on modern high-performance computing (HPC) systems with multiple processors. The localised nature of the basis set has the benefit of no additional computational cost for vacuum gaps in the simulation unit cell. This implementation of electronic structure calculations is an example of an 'all-electron' approach, which has benefitted greatly from advances in HPC technology.

In the VASP software package [106] plane waves (PW)

$$\phi_{\mathrm{PW}}(\boldsymbol{r}) = c\mathrm{e}^{i(\boldsymbol{k}+\boldsymbol{G}).\boldsymbol{r}}, \tag{3.30}$$

are used as the basis set. Plane waves are a natural choice for describing the smoothly varying region of the wavefunction far from the atom cores, i.e. in the interstitial regions. Even a small number of plane waves can accurately represent such a function. However, as can be seen from Fig. 3-1a and 3-1c, the wavefunction oscillates much more rapidly closer to the atom core. This results in much poorer convergence of a plane-wave expansion of the functional. This would require a much larger basis set to accurately describe the system, hence increasing the computational expense [110]. To improve computational efficiency, without sacrificing chemical accuracy, one technique implemented in the VASP electronic structure code is a formalism of the projector-augmented wave (PAW) method [111] that makes use of the pseudopotential and frozen-core approximations [112], outlined next.

A key concept is to distinguish between 'core' and 'valence' electrons. Core electrons are tightly bound to the nuclei and their wavefunctions are well localised at lattice sites [110]. Core electrons usually do not take part in bonding between atoms, therefore it is the valence electrons far from the atom centres that are the most important for determining the bonding in solids. This is the justification for the frozen-core approximation, where core electron states are pre-calculated in an atomic environment and kept unchanged during the course of subsequent calculations for the solid-state system [113]. The strong Coulomb potential of the nucleus and effects of tightly bound

core electrons are replaced by an effective ionic potential acting on valence electrons [104]. The rapid oscillations of the frozen states, however, are used in the orthogonalized plane wave (OPW) method to accelerate the convergence of the expansion used to represent the valence electrons. All solutions of the KS equation corresponding to different energies should be orthogonal to all of the core functions [110].

Furthermore, to accurately describe bonding in solids, it is not necessary to accurately describe the wavefunction at all distances from the nucleus. For a given material there will be some critical radius from the ion cores where physically relevant processes begin to take place, such as inter-atomic wavefunction overlap for bond formation. This is where the pseudopotential approximation is invoked. The true ionic potential is replaced by a much smoother pseudopotential within some critical radius. The aim is that the corresponding pseudo-wavefunction will be smooth and therefore can be represented by fewer plane waves, whilst still reproducing the original wavefunction in the physically relevant regions of space. Fig. 3-1c is a schematic representation of the Coulomb potential, the pseudopotential that is smoothed close to the core region and the corresponding original wavefunction and the pseudo-wavefunction. High-quality pseudopotentials are vital for accurate electronic structure calculations with this method.

The PAW method combines ideas of the linear augmented-plane-wave (LAPW) method [114] with ultrasoft pseudopotential methods [115, 116, 117]. Ultrasoft PPs reduce the number of plane waves needed by relaxing the norm-conservation requirement for the charge density for the PP. As the norm of the pseudo-wavefunction is not conserved, there is a charge deficit which is compensated by augmentation charges introduced into the core regions [110]. To combine this with ideas from the LAPW method, the all-electron valence wavefunction, ψ_{AE}, is separated into smooth pseudo-wavefunctions, ψ_{PP}, and rapidly varying contributions localised within the core region, projectors and auxiliary localised functions respectively. In the PAW approach, integrals are evaluated as a combination of integrals of smooth functions extending throughout space and localised contributions from radial integration over 'muffin-tin' spheres [104]. The ψ_{AE} is related to the ψ_{PP} by a linear transformation. The KS equations are solved to obtain ψ_{PP}, which are then transformed back to true wavefunctions (which also incorporate the localised core-region functions) before calculating the charge density and total energy [110]. Although the two electronic structure codes described here represent the wavefunction differently when performing electronic structure calculations, a benchmark study comparing results from 15 different solid-state DFT codes to compute the equation of states for 71 elemental crystals showed that all codes converged towards the

same result, within error margins comparable to those of experimental measurements [118].

Iterative electronic and geometric optimisation

In this section, the process of optimising the geometry (ionic structure) and electronic structure of a given solid towards the minimum energy configuration (i.e. the ground state) using the self-consistent field (SCF) method for a given electron density functional will be outlined. The SCF method was introduced when discussing the Hartree method for determining V_{H} and ψ_i that give the minimum total energy for the system within a set tolerance, but it also utilised in the KS formalism of DFT. It is common to use experimental X-ray diffraction data for the atomic arrangement in a solid as a starting point for electronic structure calculations. However, the exact minimum energy arrangement of ions and electrons modelled with a specific exchange-correlation functional will differ slightly. Therefore, an important step in calculating the electronic structure of a material is first to find the minimum energy arrangement of the ions and, in the case of solid-state systems, the lattice parameters for the unit cell that results in the lowest total energy for the given exchange-correlation functional.

The general procedure for local structure optimisation involves displacing ions in the system (either just ionic coordinates within the unit cell or also including the unit cell dimensions), calculating the electronic structure self-consistently for this static ionic arrangement using the SCF method as indicated in Fig. 3-2, repeatedly until the forces on the ions are below a given threshold and hence are close enough to their equilibrium, minimum energy positions. The process of geometry optimisation can also be described as searching the potential energy landscape of the system to find the minima, as illustrated in Fig. 3-3. Most electronic structure software packages provide options for different optimisation algorithms to converge the system towards a minimum in the potential energy surface. A common approach is to use gradients in the total energy of the system to compute forces on the ions. These methods include the conjugate gradient method and Quasi-Newton appproaches [121].

The chemical accuracy and computational efficiency compromise

Earlier in this section the different mathematical representations of the KS orbitals (i.e. the basis sets) in the electronic structure software packages FHI-aims and VASP were discussed. However, all types of representation are an approximation. It may

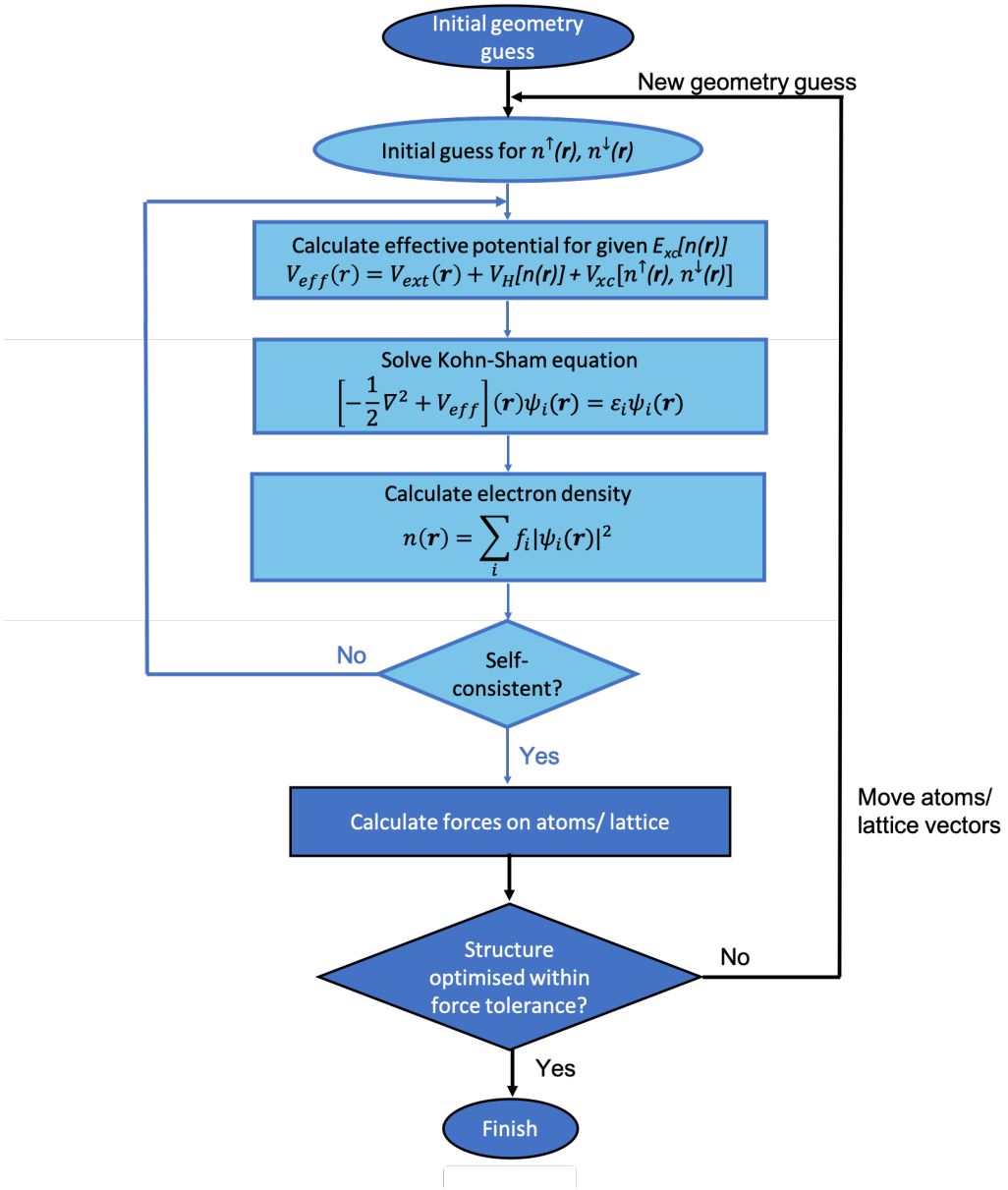

Figure 3-2: Schematic representation of iterative local geometry optimisation procedure with nested self-consistent solution of the Kohn-Sham equations to determine the ground state electron density for each ionic configuration. Darker blue represent iterative steps for geometry optimisation, lighter blue represent SCF electronic convergence. Fig. adapted from Ref. 119.

be necessary to use an infinite set of basis functions to completely represent the KS orbitals. In practice, the basis set must be truncated at some point and then we must check for convergence in the properties of interest with respect to this basis set

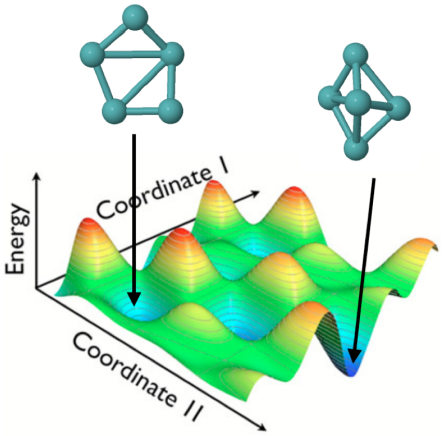

Figure 3-3: Visualisation of minima in the potential energy landscape of a molecular system. Figure reproduced with permission from Ref. 120.

truncation [122].

When using FHI-aims, a user can select from a hierarchy of basis (sub)sets that have been organised into 'tiers' and tabulated for expected levels of accuracy for each chemical species. The inclusion of additional radial functions (and their angular momenta) for each species are grouped into these tiers, which start from the minimal basis of free-atom like radial functions but users are always recommended to add at least one set of further radial functions that have been optimised to describe a chemical bond with that species. When using pre-defined calculation settings ('species_defaults'), additional radial functions are included in the basis set for each species until the required accuracy is reached for settings referred to as 'light', 'intermediate', 'tight' and 'really_tight'. These species_default settings also define other parameters used in the calculation to achieve the desired level of accuracy, such as the highest order used in the multipole decomposition of the electron density for the calculation of the Hartree potential and the integration grid when the Hamiltonian matrix elements are numerically integrated. The default tight settings are intended to provide meV-level converged energy differences [123]. However, users are still encouraged to test the convergence for particular systems. Higher tiers may be required for problematic systems, but it may also be the case that less are required to achieve the desired level of accuracy and hence the computational expense of the calculation could be reduced. Fig. 3-4 shows the radial wavefunctions necessary to achieve the 'tight' level of convergence for Ni, where 'H' in the figure refers to hydrogen-like orbitals.

The equivalent to the process described above for FHI-aims for electronic structure

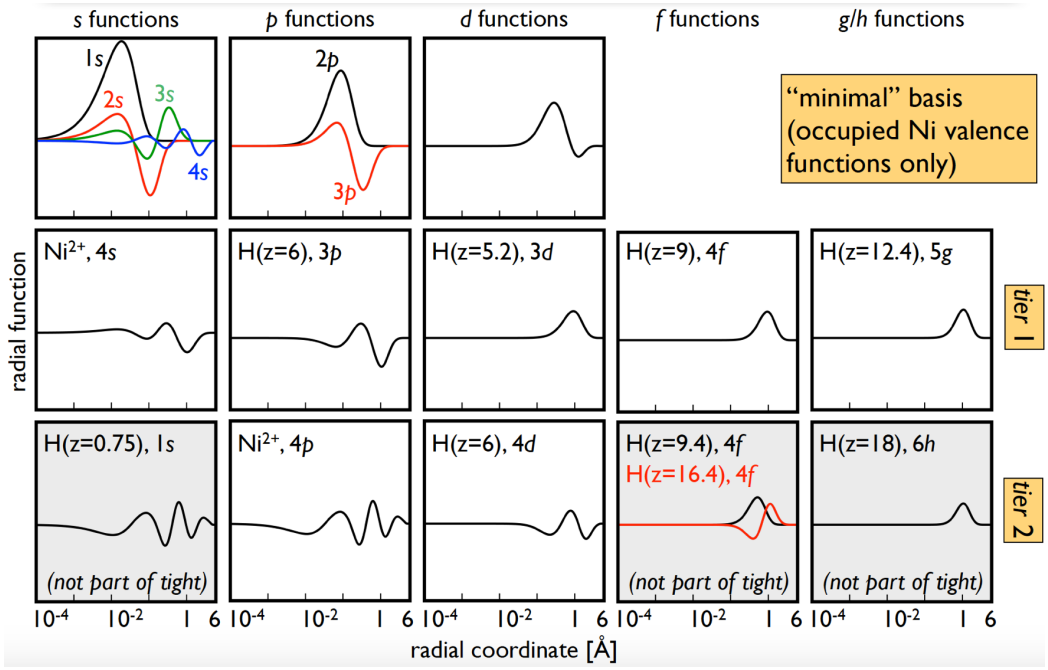

Figure 3-4: Ni radial functions to construct basis sets with increasingly tight convergence criteria as implemented in the software package FHI-aims [105]. Figure reproduced with permission from Ref. 108.

calculations with VASP is to converge the cutoff energy of the plane wave basis set to achieve the level of convergence desired for the property of interest. In principle, an infinite number of plane waves of increasing frequency (and hence energy) may be necessary in the plane wave expansion. However, in practise this set must be truncated at some point. Similar to the process described above for FHI-aims, the size of the plane wave basis set (determined by the cutoff energy) must be tested to ensure the desired property, often the total energy of the material, is converged to within an acceptable range. Smoother and weaker pseudopotentials require lower cutoff energies [122].

For both software packages, the inclusion of a larger basis set increases the computational expense of the calculation, but takes the approximate representations of the KS orbitals closer to the true form and hence improves the accuracy of the calculated material properties for the given electron density functional. Determining the optimal compromise between computational expense and chemical accuracy for the material property of interest is an important process in electronic structure calculations. The other calculation setting that must be considered in such a way is the density of the k-grid when sampling the Brillouin zone.

As discussed in section 2.1, only the first Brillouin zone of the crystal is needed to

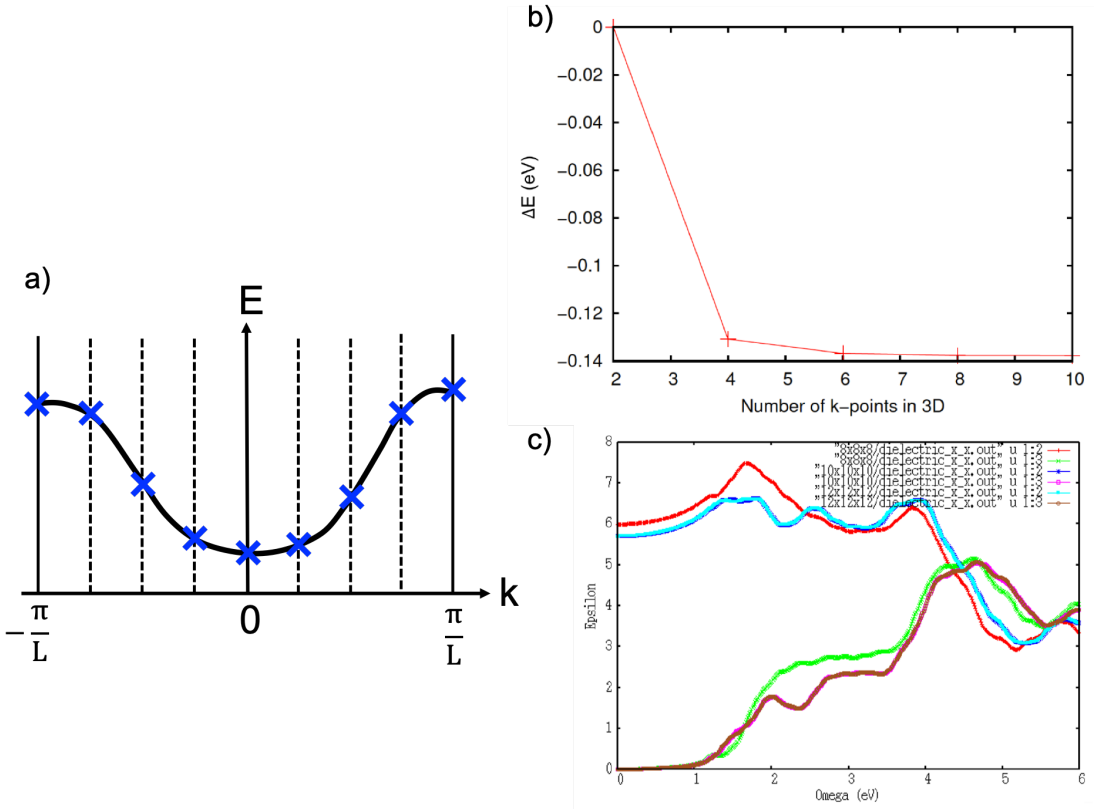

Figure 3-5: a) The energy dispersion relation for electrons moving in a crystal, illustrating how the function can be approximately represented by a finite number of k-points, forming an equally-spaced mesh. Figure adapted from Ref. 124. Convergence of b) total energy and c) optical dielectric function for the same material.

fully describe the influence of the periodic lattice on electrons in the solid. Each electron occupies a state of definite $\boldsymbol{k}$. In an infinite, periodic crystal structure an infinite number of electrons would result in an infinite number of k-points. For many properties of interest, it is necessary to integrate over the Brillouin zone, such as

$$\frac{1}{\Omega_{\mathrm{BZ}}} \int_{\mathrm{BZ}} F(E)\delta(E_{n\boldsymbol{k}} - E)\mathrm{d}\boldsymbol{k}, \tag{3.31}$$

which is used to obtain the density of electronic states [124].

Electron wavefunctions will be almost identical for values of $\boldsymbol{k}$ that are sufficiently close, so the wavefunctions over a region of reciprocal space can be represented by considering the wavefunction at a single k-point. Therefore, in practise the integral in Eq. 3.31 is instead evaluated numerically as a weighted sum over special k-points, forming a k-point mesh or grid [124]. A common choice for the k-point grid is an equally spaced

grid in the Brillouin zone called the Monkhorst-Pack grid [125] This approximation is illustrated in Fig. 3-5a. The choice here when setting up an electronic structure calculation is a balance between more k-points for a more accurate representation of the Brillouin zone and fewer k-points to reduce the computational expense of the calculation. Similar to the process described above for the basis set size, the calculated value of a property of interest should be converged with respect to the k-grid density. Certain properties require a denser k-grid than others. This is demonstrated in the examples in Fig. 3-5b and c where the total energy in Fig. 3-5b required a $6 \times 6 \times 6$ k-grid to achieve convergence, whereas the optical dielectric function (ϵ) in Fig. 3-5c of the same material required a $10 \times 10 \times 10$ k-grid.

3.2 First principles prediction of electronic band offsets

The methodology outlined here is used in the study presented in section 6.1.1 to screen for candidate junction partners that are predicted to have optimal electronic band offsets for forming a solar cell heterojunction with the absorber layers of interest in the study. The vital function of a solar cell heterojunction (as discussed in section 2.2.2) is the separation of photoexcited minority charge-carriers. When selecting a junction partner, therefore, want to know if electrons will easily flow between the conduction bands or holes between the valence bands of the two materials forming the junction. The important material properties to determine this are the electron affinities (EAs) and ionisation potentials (IPs) of the two materials. These are shown schematically in Fig. 3-6a. The EA and IP are referenced to the energy of the vacuum level (E_{vac}). The concept of the 'vacuum level' used here for theoretical modelling of surfaces differs from that discussed in section 2.2.2. Here, E_{vac} is the energy of an electron infinitely separated from the material. The EA corresponds to the energy involved in adding an electron to the CB of a material while the IP corresponds the the energy involved in removing an electron from the VB of the material. These quantities are influenced by the bulk binding energy of the material, but as electrons are added to or removed from the surface of a material, are also influenced by the dipole that arises from the redistribution of charges at a surface. It is therefore necessary to also simulate the surface of the material to compute these quantities.

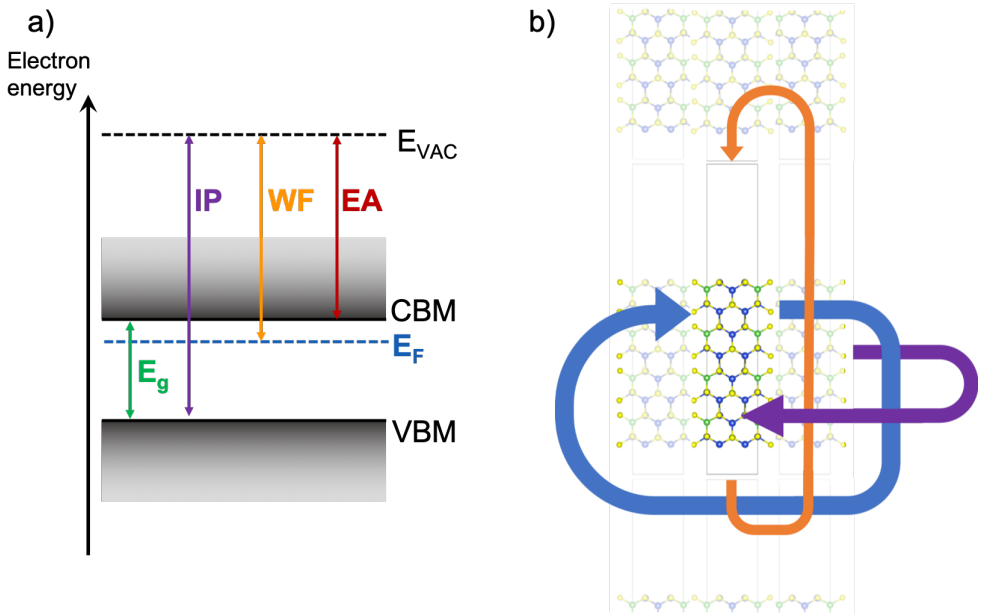

Figure 3-6: a) Energy diagram of a semiconductor with flat bands to the surface. Indicating the band edges (CBM/LUMO and VBM/HOMO), vacuum level (E_{VAC}), work function (WF), band gap E_{g}, ionisation potential (IP) and electron affinity (EA). Figure adapted from Ref. 126. b) Schematic representation of the implementation of 3D periodic boundary conditions for a 2D surface slab model (finite direction indicated by the orange arrow).

Surface models

It is common to simulate a 2D surface with 3D periodic boundary conditions, where only two directions are intended to be bulk-like. Atoms interact with neighbours across a boundary in 3D, therefore a sufficiently large vacuum gap is required in the 'finite direction' to ensure that the surfaces from either end of the slab do not interact with each other [122]. This is shown schematically in Fig. 3-6b where the orange arrow indicates interactions in the finite direction with atoms separated by a large vacuum gap.

For a given crystal structure, there are a large number of possible surface terminations when creating the slab model. Where experimental data is available, often this can provide guidance for which terminations are likely to be the most energetically likely to form or to be of the greatest technological interest and therefore inform the design of the slab models. In cases where there is no such experimental data, surface terminations with no net dipole perpendicular to the surface are expected to have the lower surface energies and therefore be more likely to form [127]. The latter informed the choice of

surface terminations for the slab models used in section 6.1.1.

Calculation of ionisation potentials

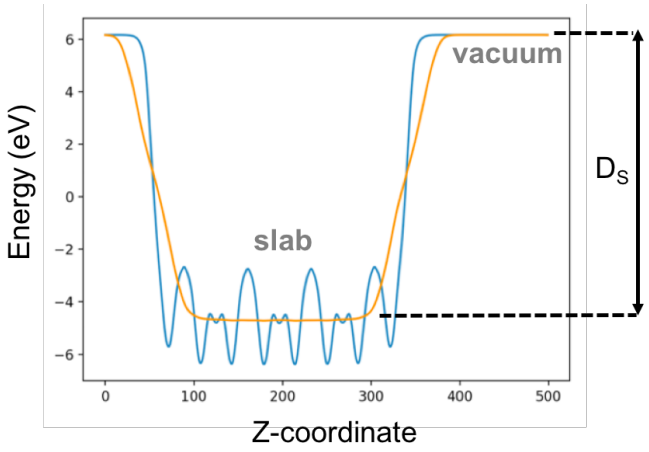

Figure 3-7: Planar average (blue line) and macroscopic average (orange line) of the potential across the finite direction of a slab model indicating the slab region, vacuum gap and surface dipole energy, D_s. Plot generated using the MacroDensity python library [128].

The position of the valence band energy with respect to the vacuum level, i.e. the IP, is a physically well-defined quantity and can be measured using techniques such as photoelectron spectroscopy or Kelvin probe microscopy. The IP can also be quantified using first-principles calculations. In section 6.1.1, the macroscopic average technique is used to decompose contributions from the bulk and the surface of the material when calculating the IP [129]. Firstly, in the slab models discussed above, if we define the z-axis as the finite direction (i.e. normal to the surface), then the geometry of the slab models is periodic in the (x, y) planes. This allows for the simplification of the charge density to a function of the z-coordinate only by taking planar averages [130], as shown in

$$\bar{f}(z) = \frac{1}{S}\int_S f(x, y, z)\mathrm{d}x\mathrm{d}y, \tag{3.32}$$

where S is the surface area of planar slices. The macroscopic average is then obtained from

$$\bar{\bar{f}}(z) = \frac{1}{a}\int_{z-\frac{a}{2}}^{z+\frac{a}{2}} \bar{f}(z)\mathrm{d}z, \tag{3.33}$$

where a is the unit cell length in the finite direction.

Fig. 3-7 shows the rapid oscillations in the planar average of the potential for each layer in the slab, the plateau far from the slab into the vacuum gap (blue line) and also the smoother macroscopic average of the planar potential (orange line). The difference between the macroscopic average of the vacuum potential and the bulk-like region of the surface slab is then used to obtain the surface dipole energy, D_{s}, as shown in Fig. 3-7. The eigenvalue of the valence band maximum (VBM) of the bulk, ϵ_{VBM} and D_{s} are then used to obtain IP as

$$IP = D_{\mathrm{s}} - \epsilon_{\mathrm{VBM}}. \tag{3.34}$$

The other important quantity for determining band offsets at semiconductor-semiconductor junctions is the EA. As shown in Fig. 3-6a, this is defined as the conduction band energy with respect to the vacuum level and can be obtained by subtracting the value of the electronic band gap from the IP of the material.

Electron affinity rule

Once the IPs and EAs of the two materials forming the heterojunction have been determined, the electron affinity (or Anderson's) rule can be used to calculate offsets between the conduction bands and valence bands of two semiconductors brought into contact [131, 132]. To obtain the band offsets from the electron affinity rule, the vacuum level of the two materials either side of the heterojunction are aligned to the same energy, the difference between the distance between the CBM and the vacuum (EA) of each material is used to predict the conduction band offset (E_{c}), as

$$\Delta E_{\mathrm{c}} = EA_{\mathrm{abs}} - EA_{\mathrm{jp}}, \tag{3.35}$$

where EA_{abs} denotes the electron affinity of the absorber layer and EA_{jp} is that of the wider-gap heterojunction partner. If E_{g} of each material is also taken into account then the same model can be used to predict the valence band offset (E_{v}) through the difference in the ionisation potentials ($IP = EA + E_{\mathrm{g}}$) as

$$\begin{aligned} \Delta E_v &= E_{\mathrm{g,abs}} - E_{\mathrm{g,jp}} - \Delta E_{\mathrm{c}} \\ &= (EA_{\mathrm{jp}} + E_{\mathrm{g,jp}}) - (EA_{\mathrm{abs}} + E_{\mathrm{g,abs}}) \\ &= IP_{\mathrm{jp}} - IP_{\mathrm{abs}}. \end{aligned} \tag{3.36}$$

It is worth noting that this method is an idealised model. The band energies for each junction partner are calculated in the limit of a large vacuum, while the vacuum separation between the two materials is taken to zero when forming the electrical

contact. It does not account for possible interface effects, such as intermixing of species at a heterojunction, or consider the effects of finite temperature on band offsets [133]. However, this method is used in the study in section 6.1.1 to provide the initial screening process to limit the search space for device optimisation of the absorber layers in that study.

3.3 Modelling imperfect solids: Point defects in the dilute limit

When a solid forms a regular crystal the energies of the bands, i.e. the band structure, can be predicted exactly, as discussed in section 2.1.1, from electronic structure calculations [42]. The electronic band structure of a semiconductor provides a rich source of information for how the material may perform as a solar cell absorber layer. However, in reality, absolutely perfect systems do not exist. The energy cost associated with the creation of a defect can often be countered by the increase in the configurational entropy of the system from the addition of the defect [64]. There are several types of possible defects in solids, some of which were described in section 2.4.

Defects are usually present in materials in very small concentrations, such that the concentrations are quantified in units of parts per million of host atoms. For this reason, models of defects often aim to simulate the 'dilute limit' where defect-defect interactions are negligible. This section outlines approaches developed in the literature for periodic electronic structure calculations of the formation energy of isolated point defects in the dilute limit. These methods are applied in section 6.2 to provide the first insights into the defect physics (and likely associated impact on PV performance) of some of the candidate photoferroic absorbers identified in chapter 5. Defect formation energies under specific synthesis conditions can be used to infer the likely concentrations of particular defects, which may have different impacts on PV performance [66]. However, in cases where defect concentrations exceed that which would be considered the dilute limit, alternative modelling approaches are necessary [134, 135]. In section 3.4, a method is outlined which is used in chapter 4 to simulate extended antisite defects in a material with large extents of substitutional disorder, beyond what would be considered as the dilute limit. In this case, the methodology is used to investigate high concentrations of Cu/ Zn disorder in Cu_2ZnSnS_4.

3.3.1 The problem of periodicity

As discussed in section 2.1, models of crystalline solids are built around the translational symmetry of periodic crystal lattices. This property is exploited in electronic structure calculations where, typically, the smallest possible unit cell is used to represent the crystal structure and periodic boundary conditions (PBCs) are used to simulate an infinite, bulk crystal. It is then possible to predict the bulk properties of the material by solving quantum mechanical equations for the electronic structure of just this small unit cell. However, the introduction of a point defect into this simulated system produces a situation such as that shown in 2D for a slice of the system in Fig. 3-8a. With the implementation of 3-dimensional PBCs for a 3D system, this would correspond to an infinite 3D array of highly concentrated point defects. Defect wavefunctions in adjacent unit cells may overlap. However, in real, crystalline systems defects are typically present in parts per million. To correctly represent isolated point defects, interactions between defect periodic images must be negligible [136].

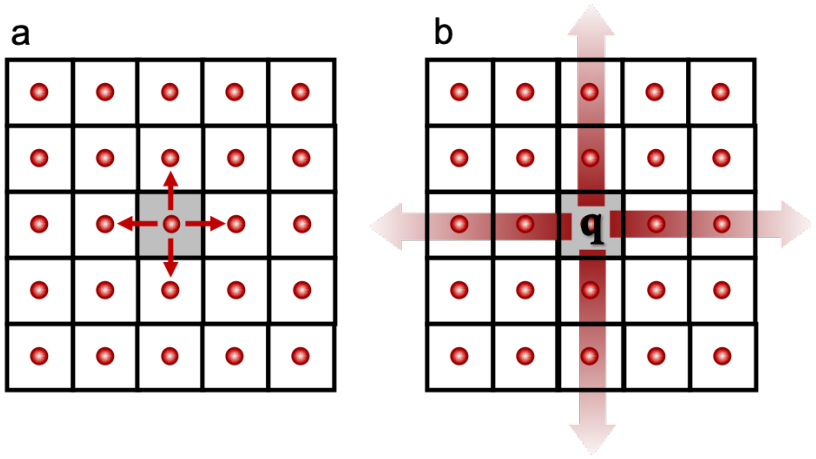

Figure 3-8: A charge-neutral defect interacting with periodic images of itself across periodic boundary conditions in 2D (a) and the longer-ranged Coulombic interactions of charged defect with a charge q (b).

The supercell method is a common approach to simulate defects in the dilute limit and is the method that is utilised in section 6.2. This approach involves repeating the primitive unit cell a finite number of times in 3D and then embedding the defect within this larger unit cell so that the defect will be separated from its periodic image by a greater distance. If this distance is sufficiently large, the properties of an isolated defect can be represented by this model [136].

Charge neutral point defects

The formation energy, $\Delta H_{D,q=0}$, of charge neutral point defects in a supercell can be obtained by comparing the total energy calculated for the defective supercell to that of an equivalent perfect supercell of the host crystal and then considering the species added to or removed from the perfect supercell when the particular defect is formed, as given by

$$\Delta H_{D,q=0} = E_{D,q=0} - E_{\text{host}} + \sum_i n_i(E_i + \mu_i), \tag{3.37}$$

where $E_{D,q=0}$ is the total energy of the defective supercell, E_{host} is the total energy of an equivalent supercell of the perfect, bulk host crystal, n_i is the number of atoms of species i added to ($n_i > 0$) or removed from ($n_i < 0$) the chemical reservoir when the defect is formed. μ_i is the chemical potential of species i [137], referenced to the total energy of the pure element in its standard state, E_i. The chemical potential of a species i is the change in energy when one particle of type i is added to the system [138]. In Eq. 3.37, μ_i allows us to describe the formation energy for defects in various growth conditions, such as rich or poor in particular species. If $\mu_i = 0$ then the element is so rich that the pure element phase can form [139].

Charged point defects

Additional complexities arise when attempting to obtain the formation energy of a charged isolated point defect. Firstly, there is a strong and long-ranged Coulomb interaction between charged supercells in PBCs (indicated in Fig. 3-8b) and this converges slowly with increased supercell size. Secondly, the charge of the defect system does not match that of the perfect bulk reference system. It is therefore necessary to introduce an electron chemical potential to account for the change in energy when electrons are added to or removed from the system when creating a defect in a given charge state. Thirdly, electronic structure calculations with PBCs for a charged unit cell (effectively) include a neutralising homogeneous background charge to avoid infinite charge, which is not present in the calculation for the perfect equivalent supercell [136]. Consequently, the expression for the defect formation energy given in Eq. 3.37 for a charge neutral defect must be modified to

$$\Delta H_{D,q} = E_{D,q} - E_{\text{host}} + \sum_i n_i(E_i + \mu_i) + q[\epsilon_{\text{F}} + \epsilon_\nu + \Delta\nu_{0/b}] + E^q_{\text{corr}}. \tag{3.38}$$

Additional terms in Eq. 3.38 compared to Eq. 3.37 are: q (the charge state of the defect), ϵ_{F} (position of the Fermi level in the band gap), $q\epsilon_{\nu}$ (energy of bulk VBM) and $\Delta\nu_{0/b}$ (term used to align the electrostatic potential of the VBM for the bulk and defect supercells) and E^{q}_{corr} (usually represents multiple post-DFT calculation corrections, one such correction is that for interactions between a charged defect and its periodic images, the 'image-charge' correction but another is the 'band filling' correction, both of which are outlined later). The terms in Eq. 3.38 are explained pictorially in Fig. 3-9.

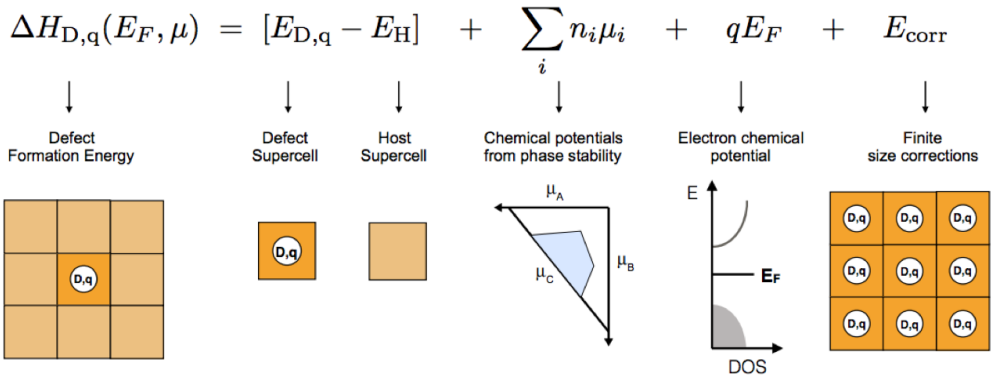

Figure 3-9: Visual descriptions of terms in the equation for the formation energy of charged defects. Figure reproduced with permission from Ref. 140.

In theory, it is possible to continually increase the supercell dimensions to allow estimations of the magnitude and decay behavior of the different effects to be obtained and, from this, extrapolate to the formation energy of a defect in the limit of an infinitely large supercell. A scaling rule for the correction to the defect formation energy for a supercell with a cubic shape was identified by Castleton et al [141] and is of the form

$$\Delta H_{D,q}(L) = \Delta H_{D,q}(L \to \infty) + \frac{a_1}{L} + \frac{a_3}{L^3}, \tag{3.39}$$

where L is the length of the side of the cubic supercell.

Due to computational limitations, it is usually not feasible to perform calculations with sufficiently large supercells to remove all spurious defect-defect interactions, especially for the long-ranged Coulombic interaction of charged defects, as depicted in Fig. 3-8b. Furthermore, the band gap error in standard-DFT can cause large errors in the calculated properties of defects [142, 143]. For this reason, methods beyond standard-DFT such as hybrid-DFT (outlined in section 3.1) may be used to more accurately predict the electronic structure. However, the computational expense for such methods is increased further, hence performing calculations for larger supercells becomes a

less feasible endeavor. Methods such as the supercell approach are used to minimise the impact of defect-defect interactions on calculated properties and various finite-size correction schemes have been developed to correct a posteriori for any remaining effects whenever possible [136]. These correction schemes have been compared to the extrapolation scheme described above to compare their relative effectiveness for various types of defects [144], although uncertainties in the extrapolation method could be comparable to the errors between different correction schemes [145]. Some of the existing finite-size correction schemes are outlined in the next section.

3.3.2 Finite-size corrections to defect supercells

Potential alignment

The formation energy of a charged defect depends on the Fermi level, as shown in Eq. 3.38 and this is referenced to the VBM of the host as the defect formation energy is related to the energy required to add or remove electrons to or from the VBM of the host from or to a Fermi reservoir [146]. However, there are a number of differences between the perfect, bulk system and the charged defect supercell which will cause the average of the potential (even at distances far from the defect) to differ between the perfect and defect supercell, as shown in Fig. 3-10.

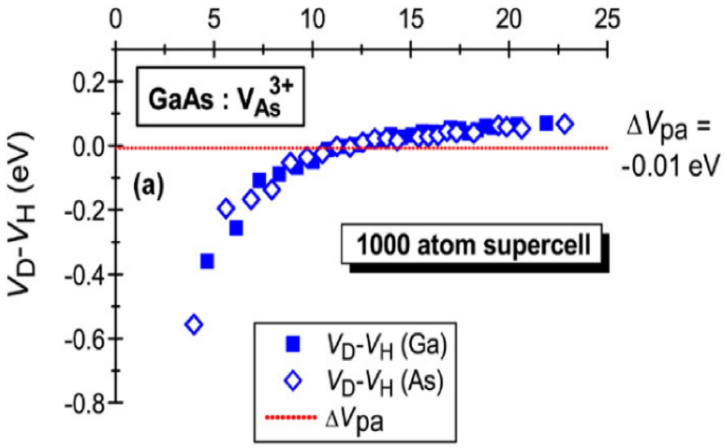

Figure 3-10: The difference in the atom-site potentials V_{Ga} and V_{As} between a supercell containing a vacancy V_{As}^{3+} and the defect-free host. Figure reproduced with permission from Ref. 142.

Firstly, as the formation of a defect involves addition or removal of ions, this will cause a

change in the potential of the system when forming a defect. Secondly, ionic relaxations during defect formation will also perturb the electrostatic potential in the system. Lastly, as already mentioned, when a charged defect is embedded in a supercell in a periodic electronic structure calculation, there will also be a compensating background charge. Otherwise, the Ewald summation performed in the electronic structure code to calculate the electrostatic energy of the system diverges, i.e. the system has an infinite charge. The effect of including a compensating homogeneous background charge is equivalent to setting the average electrostatic potential to zero [136]. In practise this corresponds to removing a constant in the Fourier transform of the electrostatic potential and the consequence of this treatment is that the eigenvalues are defined only up to an undetermined constant [147, 148].

This correction step of course will only be applied to the charged defect supercell in the electronic structure calculations, and not to the perfect host. To make matters worse, spurious defect-image charge (which will be discussed in the next section) may also interact with this 'homogeneous background charge'. It is therefore necessary to align the average electrostatic potential in the perfect host supercell to that of the charged defect supercell before computing the defect formation energy through comparisons of the two systems with Eq. 3.38.

Different approaches for potential alignment have been proposed in the literature, including using averages over the electrostatic potential in a small sphere around an atom, as in the Lany-Zunger (LZ) scheme [142], and through the average over transversal planes in the 'alignment-like' term in the Freysoldt, Neugebauer, Van de Walle (FNV) scheme [149, 147]. In both cases, the treatment involves comparing the averaged potential in the bulk-like region of the defect supercell (i.e far from the defect site) to that of a perfect bulk system. Although the electronic structure far from the defect may be similar in the defect supercell and the perfect reference, the average electrostatic potential in equivalent regions of each system could differ by a constant, due to the treatment described above [144]. However, there is some debate in the literature as to whether this potential alignment step is required as a separate correction step, or, if it is in fact accounted for in the image-charge correction (ICC) [147], which is discussed next for various correction schemes.

Image-charge correction

Image-charge corrections (ICCs) are applied a posteriori to calculated total energies of charged defect supercells to account for the spurious interactions of defects with

their periodic images, which were depicted in Fig. 3-8, and also with the neutralising 'homogeneous background charge'. Most ICC methods involve creating a separate, classical model for these unwanted electrostatic interactions and then subtracting the energy of this interaction from the DFT calculation.

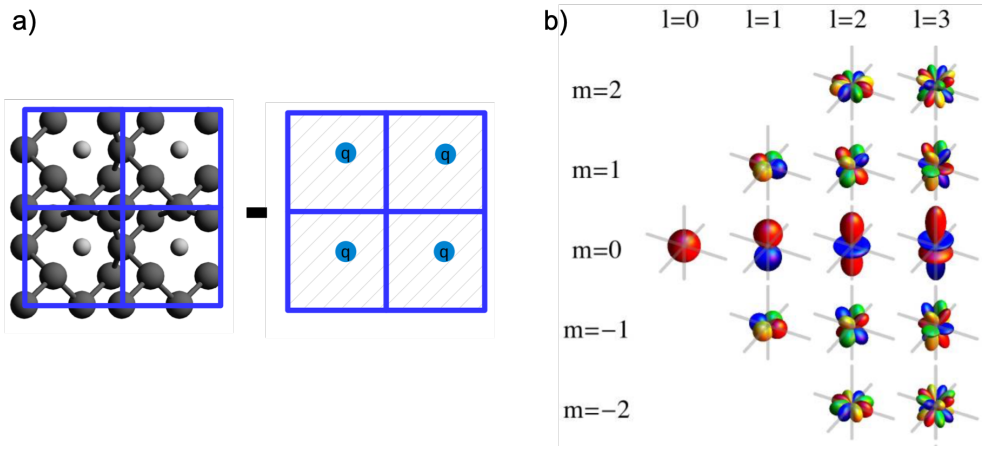

Figure 3-11: a) Schematic of first-order Markov-Payne (MP) correction of electrostatic interactions in a periodic DFT calculation of a charged defect where the defect is modelled as a point charge. Reproduced with permission from Ref. 145. b) Multipole expansion of a charge density, from the lowest order for m,l = 0. Figure reproduced with permission from Ref. 150

The simplest electrostatic model that can be used to quantify the spurious electrostatic interactions in a periodic calculation of a charged defect in a supercell involves approximating the defect as a point charge. The point charge and its periodic images are then considered to interact with each other through a classical dielectric background that represents the host crystal. This is shown schematically in Fig. 3-11a where the left figure is the DFT calculation of the defect and the right figure is the model system used to determine the spurious interaction energy to substract from the DFT calculation.

The magnitude of interactions between the charged defect with its periodic images can be estimated from the screened Madelung-like energy of an array of point charges. This approach was first used by Leslie and Gillan (LG) [151]. The Markov-Payne (MP) correction improves upon this picture with a less approximate form for the defect-induced charge density that is still localised, but allowed to be more extended than a point charge [152]. For cubic supercells, the MP correction is written as

$$E_{\text{corr}}^{\text{MP}} = E_{\text{MP1}} + E_{\text{MP2}} + ... = \frac{q^2\alpha}{2\epsilon_s L} - \frac{2\pi qQ}{3\epsilon_s L^3} + O(L^{-5}), \tag{3.40}$$

where the E_{MP1} term (or the 'first-order MP correction') is equivalent to the corrections applied by LG where ϵ is the static (low frequency) dielectric constant of the host crystal and α is the Madelung constant which is only dependant upon the shape of the host supercell. Later terms in Eq. 3.40 are due to a multipole expansion of the charge density for higher-order terms. An example of a multipole expansion of a charge density is shown in Fig. 3-11b, with the $m, l = 0$ charge density corresponding to the lowest order term in the expansion. Eq. 3.40 only shows odd powers of L as the even powers of L are zero for charge distributions with cubic symmetry [145].

Q in Eq. 3.40 cannot be calculated directly for defects in crystalline materials [153]. Therefore in practise when using the MP scheme $E_{\mathrm{corr}}^{\mathrm{MP}}$ is usually not calculated but is estimated by fitting Eq. 3.40 to the formation energies calculated for defects with increased supercell size and then extrapolating to the infinite supercell limit. As already discussed, at high levels of theory such large systems may be computationally unfeasible. Furthermore, it has been shown that Eq. 3.40 does not always give a good fit to calculated defect formation energies, creating doubt regarding the predictive power of this scheme [149]. A number of alternative schemes have been proposed that do not require the use of increasing supercell sizes [152, 151, 154, 142, 149, 147]. Next some such schemes will be outlined.

The MP scheme [152] discussed above was developed for molecular systems and when calculating Q in Eq. 3.40 the part of the defect charge density due to the electronic screening from the host crystal is not included [153, 142]. However, it has been shown that Q is dominated by this contribution in crystalline solids [153]. The LZ scheme, as outlined in Ref. 142, was devised to resolve this situation when calculating the ICC for charged defects in crystalline solids. This method involves a practical approximation to Q that has been determined for supercells with cubic geometry and an isotropic dielectric response [145].

The LZ method firstly involves the assumption that bound charge is drawn uniformly from the host supercell. For this reason, the method depends on the material having an isotropic response. The polarisation of the bound charge is used to define Q. The LZ scheme effectively involves scaling the $MP1$ term as shown in

$$E_{\mathrm{ICC}}^{\mathrm{LZ}} = [1 + c_{\mathrm{sh}}(1 - \epsilon_{\mathrm{s}}^{-1})]E_{\mathrm{MP1}}, \tag{3.41}$$

where c_{sh} is the shape factor, which only depends on the shape of the supercell. The relation between the LZ and MP schemes (with only odd powers of L) suggests that the LZ methods also makes the assumption of a cubic supercell with zero charge density

for even powers of L [145]. In the LZ scheme the potential alignment correction is performed independently of the ICC.

The FNV scheme, as outlined in Ref. 149, differs from the LZ scheme in that it does not depend upon the shape of the supercell and does not involve a separate potential alignment step. In this approach, the defect-induced charge density is modelled as a Gaussian distribution. The electrostatic potential of the model system and the DFT calculation are aligned at regions far from the defect to account for extra polarisation effects when calculating the ICC.

A scheme proposed recently by Durrant et al [145] is quite closely related to the LZ scheme, but makes use of DFT charge density differences and therefore avoids the need of an approximate form for the defect-induced charge distribution. This scheme therefore does not depend on a supercell having cubic geometry or that the dielectric response of the host material is isotropic. The work also systematically decomposes the contributions to the potential alignment to decouple contributions to the potential alignment from those in the image-interaction correction. The study showed that the potential alignment correction was only partly accounted for by their ICC.

Band filling correction

The above correction methodologies require that the charge of the defect is localised within the supercell unit. However, this is not always the case. Large finite-size effects that converge slowly with increased supercell size have been observed for some defects, even in charge neutral states. This has been attributed to band filling effects from high defect concentrations in typical finite-size supercells [153, 155, 140]. This effect is typically more pronounced for shallower defects. Shallower defects typically have more delocalised wavefunctions associated with them, therefore increasing the likelihood of the defect wavefunction extending beyond the boundary of the supercell unit. Consequently, it is possible for even neutral defects to interact with defect-images in adjacent supercells.

Defect-defect interaction means that the defect-induced energy level may interact with that of its image to form a defect band with a dispersion in the band energies that would not be present for a distinct, localised defect level that would be expected for a defect in the dilute limit. In the case of a donor defect, the electrons may now occupy defect-induced energy levels in the defect band at higher energies than would be possible in the dilute limit due to the dispersion of the defect band. This could then

also lead to spurious hybridisation of defect bands with the host electron states, and the donor electrons can partly populate the host conduction bands, giving rise to band filling effects (Moss-Burstein shift) [153].

A correction step for such effects has been proposed [155, 153, 142] and is to be applied after performing the potential alignment step in the LZ scheme outlined above. To correct the total energy of the finite supercell due to the band-filling effects, the higher energy populations are subtracted [155]. For a given k-point set (weighted sum, w_k) and band occupations, $\eta_{n,k}$, the correction for a shallow donor is obtained from

$$E_{\mathrm{BF}} = -\sum_{n,k} w_k \eta_{n,k} [e_{n,k} - \tilde{e}_{\mathrm{c}}], \tag{3.42}$$

and for a shallow acceptor from

$$E_{\mathrm{BF}} = -\sum_{n,k} w_k (1 - \eta_{n,k}) [e_{n,k} - \tilde{e}_{\mathrm{v}}], \tag{3.43}$$

where $e_{n,k}$ are the band energies in the defect calculation, $\tilde{e}_{\mathrm{c}}$ and $\tilde{e}_{\mathrm{v}}$ are the CBM and VBM energies respectively of the pure host after performing the potential alignment step within the LZ scheme [140]. However, if the intention is to simulate defects in highly doped semiconductors, the corrections in Eq. 3.42 and 3.43 should be zero or at least smaller since the formation of defect bands with band dispersion and heavy band filling should be present in a system where defect-defect interactions are a correct physical representation [155].

3.4 Modelling imperfect solids: Extended antisite defects

In this section defects and disorder is considered on much larger scales than is computationally feasible from electronic structure calculations. Here, the fundamentals of utilising the Monte Carlo method to describe thermodynamic substitutional disorder are outlined. This is equivalent to investigating interacting extended antisite defects at higher defect concentrations than would be considered as the 'dilute', non-interacting limit. This method is applied to study Cu/Zn disorder in Cu_2ZnSnS_4 in chapter 4.

3.4.1 The Monte Carlo method for thermodynamic disorder

The Monte Carlo (MC) method allows for the simulation of systems with many degrees of freedom. Its name derives from its use of (pseudo-)random numbers to simulate statistical fluctuations in order to numerically generate probability distributions [156]. The MC method in statistical physics is a special case of the more general MC method. Starting from a model hamiltonian, the method can be used to calculate thermodynamic information about a system of N interacting ions represented on a 3D lattice by using classical statistics, considering only two-body forces and assuming that the potential field of an ion is spherically symmetric. If we know the positions of the N interacting ions on the lattice then the potential energy of the system can be calculated using

$$U = \frac{1}{2}\sum_{i=1}^{N} q_i \sum_{j=1}^{N(j\neq i)} \frac{1}{4\pi\epsilon_0}\frac{q_j}{d_{ij}}, \tag{3.44}$$

where d_{ij} is the minimum distance between ions i and j with charge q_i and q_j [157].

To calculate the properties of the system, the canonical ensemble is used where the temperature, number of ions and volume are all constant. In this ensemble, the equilibrium value for any quantity of interest, B, is given by

$$< B >= \frac{\sum_\alpha \mathrm{e}^{-\frac{E_\alpha}{k_\mathrm{B}T}} B_\alpha}{\sum_\alpha \mathrm{e}^{-\frac{E_\alpha}{k_\mathrm{B}T}}} = \frac{\sum_\alpha \mathrm{e}^{-\frac{E_\alpha}{k_\mathrm{B}T}} B_\alpha}{Z} = \sum_\alpha B_\alpha p_\alpha, \tag{3.45}$$

where E_α is the energy of the system when in state α and p_α is the probability of the system being in state α, which is given by

$$p_\alpha = \frac{\mathrm{e}^{-\frac{E_\alpha}{k_\mathrm{B}T}}}{\sum_\alpha \mathrm{e}^{-\frac{E_\alpha}{k_\mathrm{B}T}}} = \frac{\mathrm{e}^{-\frac{E_\alpha}{k_\mathrm{B}T}}}{Z}. \tag{3.46}$$

Z in Eq. 3.45 is called the partition function. For most systems calculating the value of the partition function requires the summation over a large number of states. When applying the Monte Carlo method to a system of particles, the summation over discrete states for Z is replaced by a set of integrals

$$< U >= \frac{\int \mathrm{e}^{-\frac{U(\boldsymbol{r}^N)}{k_\mathrm{B}T}} U(\boldsymbol{r}^N)\mathrm{d}\boldsymbol{r}^N}{\int \mathrm{e}^{-\frac{U(\boldsymbol{r}^N)}{k_\mathrm{B}T}} \mathrm{d}\boldsymbol{r}^N} = \frac{\int \mathrm{e}^{-\frac{U(\boldsymbol{r}^N)}{k_\mathrm{B}T}} U(\boldsymbol{r}^N)\mathrm{d}\boldsymbol{r}^N}{Z_{\mathrm{NVT}}}, \tag{3.47}$$

where $U(\mathbf{r}^N)$ is the potential energy of the system which depends upon the position, $\boldsymbol{r}$,

of the N interacting ions in the system and Z_{NVT} is the configurational integral [158]. The configurational integral is over the three coordinates of each ion

$$\mathrm{d}\boldsymbol{r}^N = \mathrm{d}x_1\mathrm{d}y_1\mathrm{d}z_1\mathrm{d}x_2\mathrm{d}y_2\mathrm{d}z_2...\mathrm{d}x_N\mathrm{d}y_N\mathrm{d}z_N. \tag{3.48}$$

There are therefore $3N$ coordinates that define all possible configurations of the system.

For a system containing several hundred ions this would be a several-hundred dimensional integral over the configuration space, which would be impractical to carry out by the usual numerical methods. The Monte Carlo method for many-dimensional integrals is used for this purpose [157]. It is conceptually easiest to think about this method for a one-dimensional integral. This method involves sampling a large number of random points within a region defined by the limits of the integral. The integrated function is then the fraction of points that fall below the curve of the function multiplied by the area of the sampled region. The value obtained becomes a better approximation to the actual value of the integral as the number of random numbers, called Monte Carlo steps (MCS), used to sample the integration region increases. [158].

Monte Carlo simulation with the Metropolis Algorithm

The Standard MC method for our system would involve placing each of the N ions at random positions in the lattice to define a random point in the $3N$-dimensional configuration space. The energy of the system would then be calculated using Eq. 3.44 and the configuration would then be weighted using $\mathrm{e}^{-\frac{U(\mathbf{r}^N)}{k_b T}}$ when obtaining the equilibrium value of U. However, many configurations are very improbable so performing this calculation for every possible configuration would be inefficient and unnecessary to sufficiently evaluate the ensemble. The custom MC code in this study makes use of the Metropolis modified MC scheme [157]. In this implementation of the MC method, instead of choosing configurations randomly and then weighting them, the Metropolis algorithm considers the relative probability of a system being in a new configuration, β, to that of being in the current configuration, α

$$\frac{p_\beta}{p_\alpha} = \frac{\mathrm{e}^{-\frac{E_\alpha}{k_\mathrm{B}T}}}{Z}\frac{Z}{\mathrm{e}^{-\frac{E_\alpha}{k_\mathrm{B}T}}} = \mathrm{e}^{-\frac{E_\beta - E_\alpha}{k_\mathrm{B}T}}, \tag{3.49}$$

where E_α is the energy of state α and E_β is the energy of state β. The relative probabilities of the two states are completely determined by the energy difference, such

that if

$$\Delta E = E_\beta - E_\alpha \leq 0 \quad then \quad \frac{p_\beta}{p_\alpha} \geq 1, \tag{3.50}$$

and if

$$\Delta E = E_\beta - E_\alpha > 0 \quad then \quad \frac{p_\beta}{p_\alpha} < 1. \tag{3.51}$$

The Metropolis algorithm creates a list of configurations through configuration space that has the correct probability distribution. This list is called a trajectory through configuration space. The approach involves making a trial move of the system to a new configuration. In the case of the study presented in section 4.3.2 [159] this would be a substitution between a Cu and a Zn ion in an on-lattice model of Cu_2ZnSnS_4. It is then decided if this new configuration should be added to the trajectory or not based on the probability of the new configuration relative to the current configuration. As shown above, the relative probabilities of two states are determined by their energy difference. In the case of the on-lattice model of Cu_2ZnSnS_4, the change in lattice energy before and after a proposed Cu/ Zn substitution is evaluated for every trial MC move. If the relative probability is ≥ 1, as shown in Eq. 3.50, then the move is accepted and added to the trajectory. However, if the relative probability is < 1 then the move will only be accepted if $e^{-\frac{\Delta E}{k_B T}} \geq$ a random number generated between 0 and 1 [158]. Provided a sufficiently large number of trial moves have been made, from this procedure it is possible to obtain equilibrium disordered configurations for the ions in Cu_2ZnSnS_4 at various simulation temperatures. The model developed for Cu_2ZnSnS_4 is discussed further in the section 4.3.1.

Chapter 4

Performance bottlenecks of Cu_2ZnSnS_4 solar cells

4.1 Motivations and challenges for Cu_2ZnSnS_4 solar cells

Thin-film PV technology is a desirable contender for making a major contribution to terawatt-scale renewable energy generation. Kesterite-structured Cu_2ZnSnS_4 (CZTS) stands out for its potential for large-scale deployment due to the abundance and non-toxicity of its elemental components, as well as sunlight-matched direct band gap of 1.5 eV [160]. In the following letter we outline the motivations for utilising kesterites as the absorber layer in a solar cell and compare the volume of research efforts directed towards this type of solar cell technology to that for hybrid halide perovskite solar cells. We then go on to discuss some of the most likely bottlenecks preventing the advancement of kesterite-based solar cells.

4.1.1 Publication: The steady rise of kesterite solar cells

Statement of Authorship

This declaration concerns the article entitled:									
The Steady Rise of Kesterite Solar Cells Pages 73-76 of thesis									
Publication status (tick one)									
draft manuscript		**Submitted**		**In review**		**Accepted**		**Published**	X
Publication details (reference)	Wallace, S., Mitzi, D. and Walsh, A. (2017). The Steady Rise of Kesterite Solar Cells. *ACS Energy Letters*, 2(4), pp.776-779.								
Candidate's contribution to the paper (detailed, and also given as a percentage).	*Formulation of ideas (50%):* The central idea of this letter (to compare research efforts directed towards kesterite solar cells to that for hybrid halide perovskites) was provided by A. Walsh. Ideas for further contents of the letter were a product of discussions between myself (S. Wallace) and A. Walsh. *Design of methodology (%):* N/A *Experimental work (%):* N/A *Presentation of data in journal format (60%):* Plots comparing numbers of publications of each technology were produced by A. Walsh. The body of the text providing a brief literature review and discussion of bottlenecks to the advancement of kesterites solar cells were mostly written by S. Wallace with support from D. Mitzi and A. Walsh.								
Statement from Candidate	This paper reports on original research I conducted during the period of my Higher Degree by Research candidature.								
Signed	S. Wallace				**Date**	04.12.18			

ACS Energy LETTERS

http://pubs.acs.org/journal/aelccp

VIEWPOINT

The Steady Rise of Kesterite Solar Cells

Could slow and steady win the race to sustainable energy generation? While perovskite solar cells are currently at the forefront of photovoltaic research activity, we argue in this Viewpoint that devices based on the mineral kesterite could be the dark horse of next-generation solar energy conversion. The most urgent research challenges for this technology are outlined.

Thin-film photovoltaic (PV) technologies offer an economically promising and flexible means to harness solar energy.[1] Compared to silicon, the use of materials that absorb sunlight strongly allows for less material to be used, lowering cost and opening up more possibilities for integrating the solar cell modules with buildings. Only a small number of commercial thin-film technologies have achieved power conversion efficiencies (PCEs) greater than 20%: CdTe and Cu(In,Ga)-$(S,Se)_2$ (CIGS) have champion device PCEs of 21%.[2] The toxicity of cadmium and competition in the supply of indium are limiting factors for the large-scale utilization of these technologies.

In the emerging thin-film PV market, hybrid halide perovskites such as methylammonium lead iodide ($CH_3NH_3PbI_3$) have received an immense amount of research interest, with over 3000 publications in relation to solar cells since 2009. The efficiency of laboratory-scale halide perovskite devices has risen sharply, especially over the course of the first 500 publications focused on the material (see Figure 1). The current record for a perovskite solar cell is 22.1%.[2] Progress in PCE with respect to the number of publications on this material is beginning to plateau. Furthermore, stability issues and concerns over the lead content of halide perovskites remain as challenges for the commercialization of this technology.[3]

Solar cells based on the kesterite mineral structure, including Cu_2ZnSnS_4 (CZTS), $Cu_2ZnSnSe_4$ (CZTSe), and their alloys $Cu_2ZnSn(S_xSe_{1-x})_4$ (CZTSSe), stand out from other thin-film PV candidates for being composed of earth-abundant and nontoxic elements. Since the first kesterite solar cell was fabricated in 1997, the PCE of the champion device has risen from 0.66%[4] to the current certified record of 12.6% set in 2013,[5] with a 13.8% small-area device reported in late 2016.[6] These efficiencies fall far below the 28% predicted for this technology from the Shockley–Queisser limit. However, kesterites have achieved relatively little attention, with fewer than 1000 publications to date related to photovoltaic applications. A directed focus in research effort may see this sustainable PV technology achieve PCEs approaching those of hybrid perovskites or commercial thin-film PV technologies, perhaps as well with much improved operational stability.

There are numerous synthetic routes to kesterite thin films, including both vacuum-based deposition and nonvacuum-based solution processing. Nonvacuum approaches are desirable for scalability and feasible industrial production, including electrodeposition,[7−10] nanocrystal dispersion,[11−13] hydrazine-based deposition,[14] and other pure-solution approaches.[15−17] The current champion CZTSSe solar cell was fabricated using the hydrazine-based solution method developed at the IBM T. J. Watson Research Center.[5] Most record devices since 1997 have been produced by solution-based film deposition approaches,[18] alluding to the potential for large-scale fabrication, which is required to support a terawatt PV industry.

The relatively low efficiency of kesterite-based solar cells is attributed to a large deficit in the open-circuit voltage (V_{OC}) relative to the band gap of the absorber layer. This is universal for high-performance kesterite devices, with the deficit being even larger for the pure sulfide material. While there is a consensus that the V_{OC} deficit is the key limiting factor for devices, the origin remains very much an open question.[19] There are a number of hypotheses to account for the V_{OC} deficit, which can be separated into three categories:

(i) A non-Ohmic back electrical contact, usually Mo/CZTS, which could result in a high recombination velocity;
(ii) A poorly optimized interface between CZTS and the CdS buffer layer, which could also result in rapid electron–hole recombination;
(iii) Large amounts of defects and disorder in the bulk of the absorber layer, limiting minority charge carrier lifetimes and enhancing recombination processes.

In the best devices, it has been shown that the back contact with Mo is Ohmic in nature.[20] The borrowed device architecture from CIGS solar cells involves the use of a CdS buffer layer, and analysis of the conduction band offset between CdS and CZTSSe also does not imply any major limitation on device performance.[21] This then leaves us with consideration of defects and disorder in the bulk of the absorber layer.

Advances in defect engineering, through modification of synthesis, deposition, and/or annealing procedures, enable a reduction in the impact of extended defects such as grain boundaries, passivation of surfaces, and production of pinhole-free thin films. However, point defects such as site vacancies and antisites will remain present even for carefully processed samples.[22] Devices fabricated from high-quality single crystals have demonstrated PCEs of 10%, with a V_{OC} deficit similar to that of thin-film solar cells.[23]

Kesterites are an example of a multinary semiconductor, with a zinc-blende-related structure (space group type $I\bar{4}$) and the general chemical formula of Cu_2-M^{II}-M^{IV}-X_4 (X = O, S, Se, Te). A consequence of the many components of the material is an increase in the number of possible lattice defects, with particular concern for cation disorder.[24] In CZTS, disorder among Cu and Zn metals would seem particularly likely because of the chemical similarity of the two species, which are neighbors in the periodic table. Indeed, first-principles calculations predict that the neutral defect pair [Cu_{Zn}^{-} + Zn_{Cu}^{+}] has a low formation energy,[25] implying a high equilibrium concentration, and there is a large body of experimental evidence for Cu/Zn disorder from neutron

Received: February 17, 2017
Accepted: March 3, 2017
Published: March 10, 2017

DOI: 10.1021/acsenergylett.7b00131
ACS Energy Lett. 2017, 2, 776−779

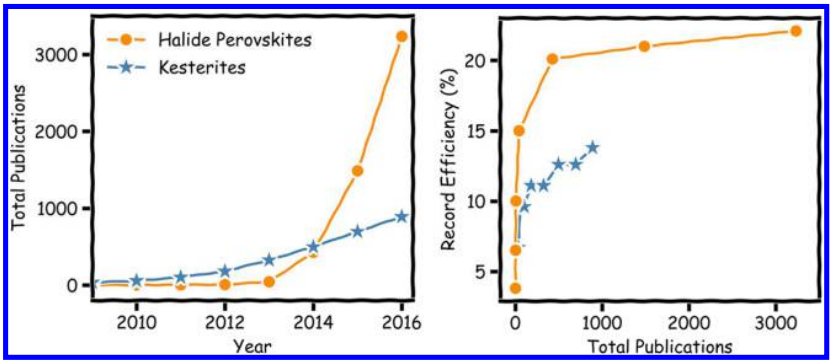

Figure 1. Comparison of the cumulative research output for $Cu_2ZnSn(S,Se)_4$ (kesterite) and $CH_3NH_3PbI_3$ (halide perovskite) related photovoltaic technologies against year and the record light-to-electricity conversion efficiency. The publication data has been generated from Web of Science (February 15, 2017) for kesterite (search terms: "kesterite OR stannite" AND "solar cell") and halide perovskite (search terms: "halide perovskite OR iodide perovskite OR hybrid perovskite" AND "solar cell") solar cells.

diffraction, synchrotron X-ray diffraction, and near-resonant Raman studies.[22] It is now universally accepted that Cu/Zn disorder will be present to a high degree even in high-quality thin films. However, the impact of this type of disorder on device performance is the subject of ongoing debate in the community.[19,26]

The open-circuit voltage of a PV device is limited by the band gap of the absorber material, but defects can modify the underlying electronic band structure (Figure 2). Lattice

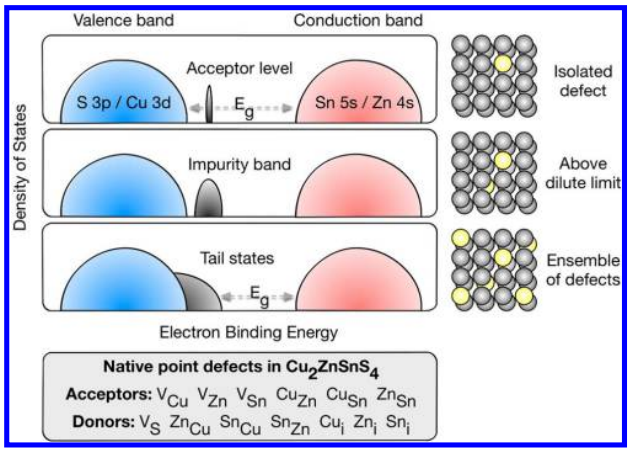

Figure 2. Acceptor defect-induced energy level within the band gap of a semiconductor, broadening to an impurity band with increased defect density until at sufficiently high defect concentrations the band merges with the valence band maximum, resulting in a reduced band gap. Such tail states would limit the open-circuit voltage accessible in a photovoltaic device and could explain the voltage deficit observed in kesterite-based solar cells. Also listed are the range of possible acceptor and donor defects in Cu_2ZnSnS_4; a large number of possible charge-neutral defect clusters can also be formed.

disorder can result in localized states near the top of the valence band or at the bottom of the conduction band. At sufficiently high concentrations, these interact to form an impurity band. As the density of defects increases, the tail states become more prevalent and penetrate further into the band gap. Localized states and associated band tailing in the electronic structure lead to band gap narrowing.[22,27] As such, peaks in the photoluminescence spectra are red-shifted to energies below those of the optical band gap obtained from internal quantum efficiency measurements (which reflects only extended electronic states).[28] Band tailing in CZTSSe devices is roughly twice as severe as that in CIGS devices, and it has been suggested that Cu/Zn disorder in CZTSSe is one contributing factor. In comparison, cation disorder in CIGS could be expected to be less prevalent because Cu is less chemically similar to Ga/In than Cu is to Zn, increasing the energy cost associated with making substitutions among any of these two species with Cu compared to that of Zn with Cu. Furthermore, it has been observed that band tailing is less severe in devices made from $Ag_2ZnSnSe_4$,[29] where cation disorder could be expected to be suppressed because of the greater ionic radii mismatch between Ag^+ and Zn^{2+} than Cu^+ and Zn^{2+}.

To our knowledge no direct connection between bulk disorder in the kesterite absorber layer and photovoltaic performance has yet been made. Postannealing treatments can be used to reduce the prevalence of Cu/Zn antisites.[30] Devices of varying degrees of Cu/Zn disorder in the absorber layer produced in this way demonstrated that the V_{OC} changes by the same amount as the optical band gap. The postannealing treatment therefore had no impact on V_{OC} deficit.[19] The lack of direct connection between Cu/Zn antisite concentration and photovoltaic performance could be because, despite reduction in Cu/Zn disorder, the antisite concentration is still high from the perspective of device performance. Alternatively, it could be because there are other defects that are more important for controlling device properties at the current performance level. It is worth noting that the primary factors limiting performance could differ considerably for devices produced using different absorber fabrication procedures or for different performance levels for samples produced using the same approach.

Beyond Cu/Zn antisite defects, another explanation for the V_{OC} deficit is the presence of defects with levels deep in the band gap that could be acting as centers for nonradiative recombination. In particular, defects involving Sn result in deeper charge transition states owing the higher charge and larger radius of Sn relative to Cu and Zn.[31] Deep-level defects in CZTS have been predicted to have a formation energy that is higher than those of the shallow defects;[16] therefore, it could be expected that they will be less prevalent. However, the presence of "killer centers"[32] even in low concentrations could be limiting device performance. It is possible that the formation energy of such centers may be reduced by the specific environmental conditions during synthesis and chemical potentials of the constituent elements.

DOI: 10.1021/acsenergylett.7b00131
ACS Energy Lett. 2017, 2, 776−779

To summarize, some key challenges and opportunities for kesterite solar cells include the following:

1. **Missing activation step**. For CdTe, a postdeposition chemical treatment of $CdCl_2$ or similar is required to "activate" the absorber layer[33] (e.g., passivate grain boundaries, enlarge grain size), while for CIGS a Cu-rich processing stage is needed during the 3-stage evaporation process.[34] Identifying a similar activation process for kesterites may enable a step-change in PV action.
2. **Accurate material and device measurements**. The wide variety of demonstrated growth processes and conditions makes comparison of reported physical properties challenging. Accurate and consistent measurements concerning carrier generation, transport, recombination, and collection for different absorbers would provide valuable insights to overcome device bottlenecks.
3. **Quantifying defects and disorder**. A number of different descriptors are being used in the field to quantify disorder, including Raman spectra, optical spectra, and neutron diffraction. However, the site disorder averaged over a macroscopic sample does not provide insights into the microscopic cation distribution that will interact with photogenerated electrons and holes. More accurate local structure techniques and materials simulations could provide valuable insights.
4. **Alternative device architectures**. Relatively little effort has been spent on looking at alternatives to the standard Mo/CZTS/CdS device configuration. Beyond simple component replacement (e.g., Mo for W or ZnS for CdS), other device configurations such as p−i−n could result in enhanced photovoltaic performance.

Two large research consortia have recently been funded to address some of these questions. One is *PVTEAM*, led by L. M. Peter at the University of Bath (U.K.) that links with the SPECIFIC Innovation and Knowledge Centre for scale-up, and *STARCELL*, led by E. Saucedo at IREC (Spain) that combines 13 partners across Europe, Japan, and the United States. At a time when further breakthroughs in perovskite solar cells will become increasingly difficult to achieve, a focused effort on kesterites and related materials could have major impacts. While this technology has been relatively slow to emerge, the combination of earth-abundant and nontoxic elements in a chemically stable compound is the solution that sustainable thin-film photovoltaics requires.

Suzanne K. Wallace[†,‡]
David B. Mitzi[§,∥]
Aron Walsh[‡,⊥]

[†]Centre for Sustainable Chemical Technologies, Department of Chemistry, University of Bath, Claverton Down, Bath BA2 7AY, United Kingdom
[‡]Department of Materials, Imperial College London, Exhibition Road, London SW7 2AZ, United Kingdom
[§]Department of Mechanical Engineering and Materials Science, Duke University, Durham, North Carolina 27708, United States
[∥]Department of Chemistry, Duke University, Durham, North Carolina 27708, United States
[⊥]Department of Materials Science and Engineering, Yonsei University, Seoul 03722, South Korea

AUTHOR INFORMATION

ORCID

Aron Walsh: 0000-0001-5460-7033

Notes

Views expressed in this Viewpoint are those of the authors and not necessarily the views of the ACS.
The authors declare no competing financial interest.

REFERENCES

(1) Polman, A.; Knight, M.; Garnett, E. C.; Ehrler, B.; Sinke, W. C. Photovoltaic materials − present efficiencies and future challenges. *Science* **2016**, *352*, aad4424.
(2) Green, M. A.; Emery, K.; Hishikawa, Y.; Warta, W.; Dunlop, E. D. Solar Cell Efficiency Tables (Version 49). *Prog. Photovoltaics* **2016**, *24*, 3.
(3) Park, N.-G.; Grätzel, M.; Miyasaka, T.; Zhu, K.; Emery, K. Towards stable and commercially available perovskite solar cells. *Nat. Energy* **2016**, *1*, 16152.
(4) Katagiri, H.; Sasaguchi, N.; Hando, S.; Hoshino, S.; Ohashi, J.; Yokota, T. Preparation and evaluation of Cu_2ZnSnS_4 thin films by sulfurization of E-B evaporated precursors. *Sol. Energy Mater. Sol. Cells* **1997**, *49*, 407.
(5) Wang, W.; Winkler, M. T.; Gunawan, O.; Gokmen, T.; Todorov, T. K.; Zhu, Y.; Mitzi, D. B. Device Characteristics of CZTSSe Thin-Film Solar Cells with 12.6% Efficiency. *Adv. Energy Mater.* **2014**, *4*, 1301465.
(6) Reported at PVSEC-36 by a research team led at DGIST in South Korea. A 0.181 cm^2 solar cell was certified at 13.80% by KIER.
(7) Jiang, F.; Ikeda, S.; Harada, T.; Matsumura, M. Pure Sulfide Cu_2ZnSnS_4 Thin Film Solar Cells Fabricated by Preheating an Electrodeposited Metallic Stack. *Adv. Energy Mater.* **2014**, *4*, 1301381.
(8) Guo, L.; Zhu, Y.; Gunawan, O.; Gokmen, T.; Deline, V. R.; Ahmed, S.; Romankiw, L. T.; Deligianni, H. Electrodeposited $Cu_2ZnSnSe_4$ Thin Film Solar Cell with 7% Power Conversion Efficiency. *Prog. Photovoltaics* **2014**, *22*, 58.
(9) Yao, L.; Ao, J.; Jeng, M.-J.; Bi, J.; Gao, S.; He, Q.; Zhou, Z.; Sun, G.; Sun, Y.; Chang, L.-B.; et al. CZTSe solar cells prepared by electrodeposition of Cu/Sn/Zn stack layer followed by selenization at low Se pressure. *Nanoscale Res. Lett.* **2014**, *9*, 678.
(10) Scragg, J. J.; Dale, P. J.; Peter, L. M. Synthesis and Characterization of Cu_2ZnSnS_4 Absorber Layers by an Electrodeposition-Annealing Route. *Thin Solid Films* **2009**, *517*, 2481.
(11) Larramona, G.; Bourdais, S.; Jacob, A.; Chone, C.; Muto, T.; Cuccaro, Y.; Delatouche, B.; Moisan, C.; Pere, D.; Dennler, G. 8.6% Efficient CZTSSe Solar Cells Sprayed from Water-Ethanol CZTS Colloidal Solutions. *J. Phys. Chem. Lett.* **2014**, *5*, 3763.
(12) Guo, Q.; Ford, G. M.; Yang, W.-C.; Walker, B. C.; Stach, E. A.; Hillhouse, H. W.; Agrawal, R. Fabrication of 7.2% Efficient CZTSSe Solar Cells Using CZTS Nanocrystals. *J. Am. Chem. Soc.* **2010**, *132*, 17384.
(13) Zhou, H.; Hsu, W.-C.; Duan, H.-S.; Bob, B.; Yang, W.; Song, T.-B.; Hsu, C.-J.; Yang, Y. CZTS nanocrystals: a promising approach for next generation thin film photovoltaics. *Energy Environ. Sci.* **2013**, *6*, 2822.
(14) Bag, S.; Gunawan, O.; Gokmen, T.; Zhu, Y.; Todorov, T. K.; Mitzi, D. B. Low band gap liquid-processed CZTSe solar cell with 10.1% efficiency. *Energy Environ. Sci.* **2012**, *5*, 7060.
(15) Xin, H.; Katahara, J. K.; Braly, I. L.; Hillhouse, H. W. 8% Efficient $Cu_2ZnSn(S,Se)_4$ Solar Cells from Redox Equilibrated Simple Precursors in DMSO. *Adv. Energy Mater.* **2014**, *4*, 1301823.
(16) Haass, S. G.; Diethelm, M.; Werner, M.; Bissig, B.; Romanyuk, Y. E.; Tiwari, A. N. 11.2% Efficient Solution Processed Kesterite Solar Cell with a Low Voltage Deficit. *Adv. Energy Mater.* **2015**, *5*, 1500712.
(17) Su, Z.; Sun, K.; Han, Z.; Cui, H.; Liu, F.; Lai, Y.; Li, J.; Hao, X.; Liu, Y.; Green, M. A. Fabrication of Cu_2ZnSnS_4 solar cells with 5.1% efficiency via thermal decomposition and reaction using a non-toxic sol−gel route. *J. Mater. Chem. A* **2014**, *2*, 500.

DOI: 10.1021/acsenergylett.7b00131
ACS Energy Lett. 2017, 2, 776−779

(18) Liu, X.; Feng, Y.; Cui, H.; Liu, F.; Hao, X.; Conibeer, G.; Mitzi, D. B.; Green, M. The current status and future prospects of kesterite solar cells: a brief review. *Prog. Photovoltaics* **2016**, *24*, 879.
(19) Bourdais, S.; Choné, C.; Delatouche, B.; Jacob, A.; Larramona, G.; Moisan, C.; Lafond, A.; Donatini, F.; Rey, G.; Siebentritt, S.; et al. Is the Cu/Zn disorder the main culprit for the voltage deficit in kesterite solar cells? *Adv. Energy Mater.* **2016**, *6*, 1502276.
(20) Gunawan, O.; Gokmen, T.; Mitzi, D. B. Suns-V_{OC} characteristics of high performance kesterite solar cells. *J. Appl. Phys.* **2014**, *116*, 084504.
(21) Gershon, T.; Gokmen, T.; Gunawan, O.; Haight, R.; Guha, S.; Shin, B. Understanding the relationship between $Cu_2ZnSn(S,Se)_4$ material properties and device performance. *MRS Commun.* **2014**, *4*, 159.
(22) Shin, D.; Saparov, B.; Mitzi, D. B. Defect Engineering in Multinary Earth-Abundant Chalcogenide Photovoltaic Materials. *Adv. Energy Mater.* **2017**, 1602366.
(23) Lloyd, M. A.; Bishop, D.; Gunawan, O.; Mccandless, B. Fabrication and performance limitations in single crystal $Cu_2ZnSnSe_4$ Solar Cells. *2016 IEEE 43rd Photovoltaic Specialists Conference (PVSC)* **2016**, 3636.
(24) Baranowski, L. L.; Zawadzki, P.; Lany, S.; Toberer, E. S.; Zakutayev, A. A review of defects and disorder in multinary tetrahedrally bonded semiconductors. *Semicond. Sci. Technol.* **2016**, *31*, 123004.
(25) Chen, S. Y.; Yang, J.-H. H.; Gong, X. G.; Walsh, A.; Wei, S.-H. H. Intrinsic point defects and complexes in the quaternary kesterite semiconductor Cu_2ZnSnS_4. *Phys. Rev. B: Condens. Matter Mater. Phys.* **2010**, *81*, 245204.
(26) Scragg, J. J. S.; Larsen, J. K.; Kumar, M.; Persson, C.; Sendler, J.; Siebentritt, S.; Platzer Björkman, C. Cu-Zn Disorder and Band Gap Fluctuations in $Cu_2ZnSn(S,Se)_4$: Theoretical and Experimental Investigations. *Phys. Status Solidi B* **2016**, *253*, 247.
(27) Van Mieghem, P. Theory of band tails in heavily doped semiconductors. *Rev. Mod. Phys.* **1992**, *64*, 755.
(28) Gokmen, T.; Gunawan, O.; Todorov, T. K.; Mitzi, D. B. Band tailing and efficiency limitation in kesterite solar cells. *Appl. Phys. Lett.* **2013**, *103*, 103506.
(29) Gershon, T.; Sardashti, K.; Gunawan, O.; Mankad, R.; Singh, S.; Lee, Y. S.; Ott, J. A.; Kummel, A.; Haight, R. Photovoltaic Device with over 5% Efficiency Based on an n-Type $Ag_2ZnSnSe_4$ Absorber. *Adv. Energy Mater.* **2016**, *6*, 1601182.
(30) Scragg, J. J. S.; Choubrac, L.; Lafond, A.; Ericson, T.; Platzer-Björkman, C. A low-temperature order-disorder transition in Cu_2ZnSnS_4 thin films. *Appl. Phys. Lett.* **2014**, *104*, 041911.
(31) Chen, S.; Walsh, A.; Gong, X.-G.; Wei, S.-H. Classification of lattice defects in the kesterite Cu_2ZnSnS_4 and $Cu_2ZnSnSe_4$ earth-abundant solar cell absorbers. *Adv. Mater.* **2013**, *25*, 1522.
(32) Stoneham, A. M. Non-radiative transitions in semiconductors. *Rep. Prog. Phys.* **1981**, *44*, 1251.
(33) Major, J. D.; Treharne, R. E.; Phillips, L. J.; Durose, K. A low-cost non-toxic post-growth activation step for CdTe solar cells. *Nature* **2014**, *511*, 334.
(34) Gabor, A. M.; Tuttle, J. R.; Albin, D. S.; Contreras, M. A.; Noufi, R.; Hermann, A. M. High-efficiency $CuIn_xGa_{1-x}Se_2$ Solar Cells Made From $(In_xGa_{1-x})_2Se_3$ Precursor Films. *Appl. Phys. Lett.* **1994**, *65*, 198.

DOI: 10.1021/acsenergylett.7b00131
ACS Energy Lett. 2017, 2, 776−779

4.2 Impact of defects on Cu_2ZnSnS_4 solar cells

Large amounts of defects and disorder in the bulk of the absorber layer was listed as one of the possible origins of the performance deficit of Cu_2ZnSnS_4 solar cells in the letter presented in the previous section. The low open circuit voltage (V_{OC}) relative to the band gap has been recognised as the key limiting factor on the performance of Cu_2ZnSnS_4 solar cells [75]. The measured current density-voltage ($J-V$) curve of a solar cell is used to determine the solar to electric power conversion efficiency (PCE), η. The PCE of a solar cell is the ratio of power output from the solar cell (P_{MP}) to the power input from the Sun (P_{in})

$$\eta = \frac{P_{\mathrm{MP}}}{P_{\mathrm{in}}}, \tag{4.1}$$

where P_{MP} is given in terms of the $\mathrm{V_{OC}}$ (the voltage from the $J-V$ curve of the solar cell at $J=0$) and the short-circuit current density, J_{SC}, (the current density on the $J-V$ curve at $V=0$)

$$P_{\mathrm{MP}} = FFV_{\mathrm{OC}}J_{\mathrm{SC}}. \tag{4.2}$$

For an efficient solar cell, it is desirable to have a high J_{SC}, a high V_{OC} and a FF that is as close to 1 as possible.

As can be seen from the position of CZTSSe devices on the plot in Fig. 4-1, the V_{OC} measured for these devices are considerably less than that of the higher-performing CIGS devices, which have a similar value for the band gap of the material. In general, the main cause of V_{OC} deficit in a PV device is the recombination of photogenerated charge carriers in the bulk material or at surfaces [75]. In Cu_2ZnSnS_4 one explanation that has been put forward is band tailing in the bulk [161].

Several photoluminescence (PL) studies have been performed on kesterite-structured samples of Cu_2ZnSnS_4, $Cu_2ZnSnSe_4$ and alloys of the two. PL measurements are able to pick up optical signatures of defects even if they are present at low concentrations with high resolution. In a PL experiment, photons with energies larger than that of the band gap excite electrons from the valence band to the conduction band. In addition, electrons can be excited from or relax to defect levels. When the excited electrons transition to lower energy levels, they can emit light to conserve energy, resulting in a peak in the PL spectrum. In a PL excitation experiment, the PL intensity is measured as a function of excitation photon energy. This gives an absorption profile for the defects. PL measurements alone however cannot be used to identify the character of a defect, here first-principles defect calculations can provide some insight [65].

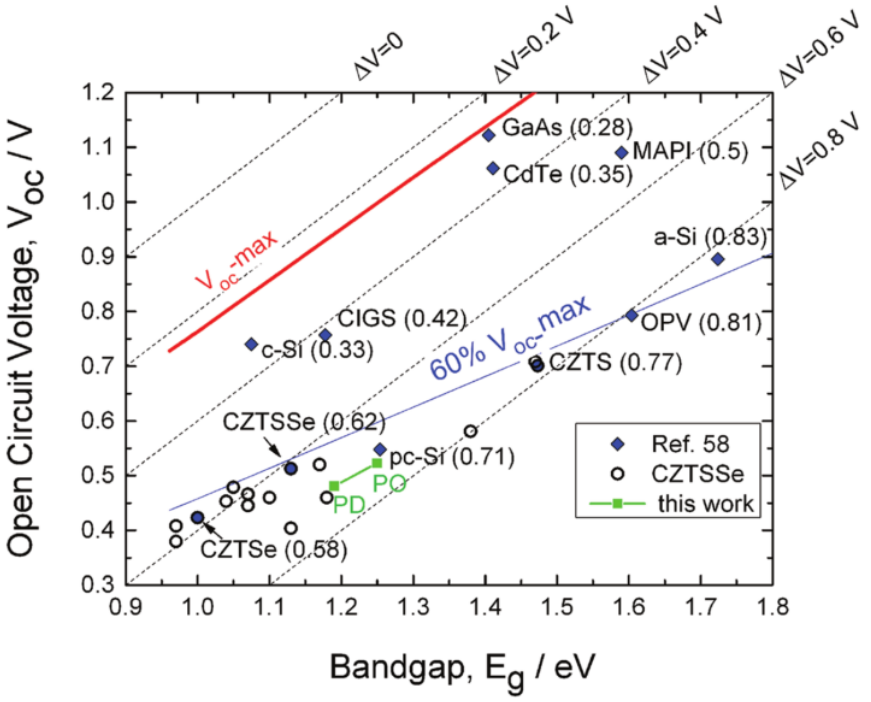

Figure 4-1: V_{OC} versus band gap of high performance CZTSSe devices (>9% efficiency) indicated by circles with best devices based on other photovoltaic materials shown for comparison by diamond symbols: Methyl-ammonium lead iodide (MAPI), amorphous silicon (a-Si), organic photovoltaic films (OPV), crystalline silicon (c-Si) and polycrystalline silicon (pc-Si). The oblique lines give a constant V_{OC} deficit from 0.8 V to 0 V. The green points correspond to CZTSSe films that are partially ordered (PO) or partially disordered (PD) due to disorder amongst Cu and Zn. Figure reproduced with permission from Ref. 75.

PL measurements have been performed on both full devices and polycrystalline thin-films [161, 162, 163, 164, 165, 166] and single crystals [167, 168, 169] of CZTS. Ref. 167 compares the PL spectra for varying compositions of the samples, whereas in Ref. 161 measurements on both CIGSSe and record-efficiency CZTSSe thin films are performed in an attempt to account for the difference in the performance of these two technologies by comparing their defect-influenced PL emission spectra. In thin-film photovoltaic devices, the absorber layers are most likely to be polycrystalline. However, comparison between measurements with single crystals and polycrystalline samples could enable the isolation of recombination at grain boundaries and interfaces from those due to defects in the bulk of the absorber layer. One feature common to all of the PL spectra from studies on kesterite samples is clear evidence of defects and disorder from the observed band tailing. Fig. 4-2 shows PL spectroscopy measurements performed on

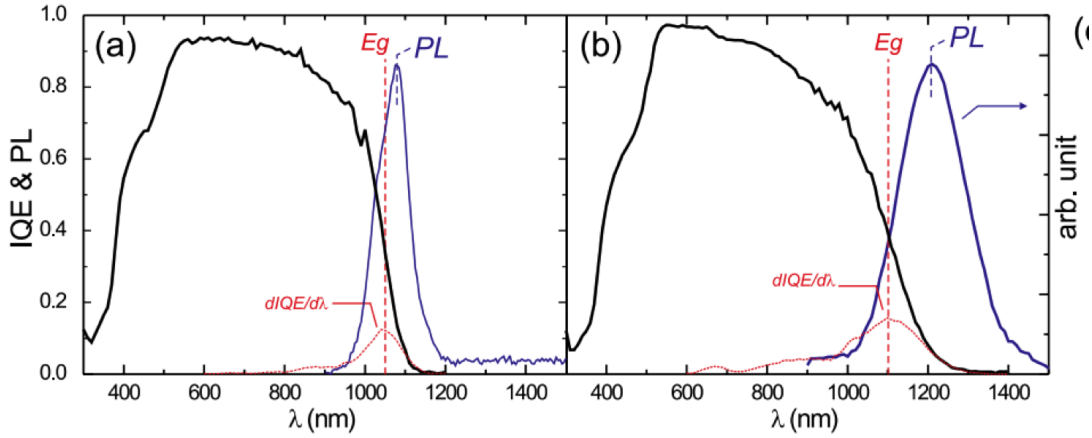

Figure 4-2: The internal quantum efficiency (IQE), band gap as determined from the IQE inflection point and the photoluminescence spectra of high performance devices with thin-film absorber layers of (a) CIGSSe (E_g = 1.19 eV) and (b) CZTSSe (E_g = 1.13 eV). Figure reproduced with permission from Ref. 161.

CZTSSe thin films by Gokmen et al [161]. The figure shows that there is a shift in the PL peak to lower energies (red-shifting), below the value of the band gap obtained from internal quantum efficiency (IQE) measurements performed on the same thin films. It is also noted in this study when comparing the PL spectra of CZTSSe films to that of CIGSSe films that the PL peak for CZTSSe thin films is broader and that the red-shifting was roughly twice as severe. This effect is referred to as the 'band-edge tailing', where photons of energies less than the band gap of the material are emitted following photoexcitation and subsequent relaxation back to the ground state. Measurements performed in Ref. 161 found the tailing in CZTSSe to be roughly twice as severe as that observed in higher-performing CIGSSe devices.

Theoretical predictions for the defect formation energy and defect transition levels in Cu_2ZnSnS_4 in Ref. 139 suggest that defects which would be expected to produce a deep defect level also have a high formation energy and hence would be expected to be less likely to form. However, a recent theoretical study has revisited the defect physics of Cu_2ZnSnS_4 to demonstrate possible mechanisms where defect-mediated recombination could occur without a charge transition level deep in the band gap of the material [170]. There is currently no experimental evidence on the nature of the defects that may be responsible for the latter, however, in Cu_2ZnSnS_4 the presence of a large extent of disorder amongst Cu and Zn, and hence high concentrations of Cu^{-}_{Zn} and Zn^{+}_{Cu} antisites, has been inferred from calculations of defect formation energy [139] and confirmed from several experimental studies [171, 172, 173]. Although these types of defects are not

predicted to produce a deep defect level or linked to the recombination mechanisms investigated in Ref. 170, it has been proposed that they may be linked to observed band tailing in Cu_2ZnSnS_4 due to the high-concentrations of the defects [161].

4.3 Defects beyond the dilute limit in Cu_2ZnSnS_4

Electronic structure calculations for the formation energies of point defects and point defect pairs in the dilute limit have already been calculated for Cu_2ZnSnS_4, where the $[Cu^-_{Zn} + Zn^+_{Cu}]$ defect pair was found to have a particularly low formation energy [139]. The calculations performed in Ref. 139 were performed using the GGA functional with a rigid shift applied to the defect levels to account for the band gap error at this level of theory [142]. In Ref. 139 one defect calculation was performed using a hybrid functional where it was found that the formation energy of the test defect differed by 0.1 eV. This section of the thesis is concerned with the possible role of Cu/Zn disorder in the performance deficit of Cu_2ZnSnS_4 solar cells. We therefore repeated the calculation of the formation energy for the defect pair of interest for our study.

For our calculation of the formation energy of the nearest-neighbour $[Cu^-_{Zn} + Zn^+_{Cu}]$ charge-neutral defect pair, we construct a 64-atom supercell from a $2 \times 2 \times 1$ expansion of the conventional unit cell of Cu_2ZnSnS_4. This was the most isotropic and largest supercell that could feasibly be used for our calculations at the level of theory desired. The HSE06 hybrid-functional [100] (described towards the end of section 3.1.2) was used for the exchange-correlation functional as implemented in the Vienna Ab-initio Simulation Package (VASP) [106] with an energy cut-off of 500 eV for the plane-wave basis set during relaxation of the defect-pair supercell. Calculations were initially performed at the gamma point (a $1 \times 1 \times 1$ k-point mesh) until forces on the ions converged to within 0.01 eV/Å. A single geometry step was then performed with a $2 \times 2 \times 2$ k-point mesh centred on the gamma point as these parameters were found to be sufficient for the total energy to converge to within <2 meV per atom with respect to increased plane-wave cut-off energy and for the external pressure to be <1 kbar. However, performing the full calculation with a $2 \times 2 \times 2$ k-point mesh was found to be too computationally expensive. As the defect pair is charge neutral, we were able to use Eq. 3.37 to calculate the formation energy. From our calculation, we predict a defect formation energy of 0.30 eV. While the value from a previous study using a GGA functional was approximately 30% less than this value at 0.21 eV [139].

When defect concentrations are less than 1%, it is usually assumed that the system is

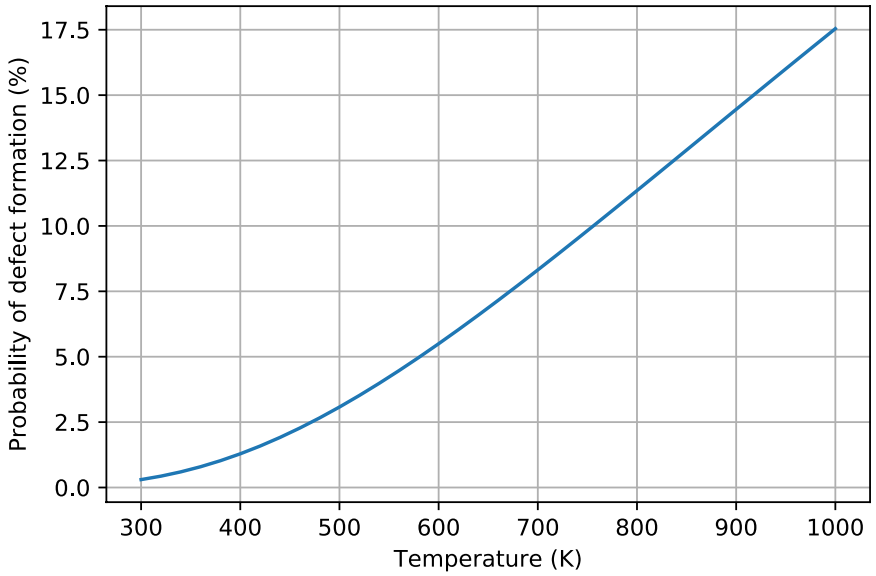

Figure 4-3: Probability of nearest neighbour [$Cu_{Zn}^{-} + Zn_{Cu}^{+}$] defect formation as a function of temperature based on the equilibrium defect concentration from classical thermodynamics.

in the dilute defect limit where defects can be considered to be non-interacting [174]. Using statistical thermodynamics for point defects, an expression for the equilibrium concentration of point defects, n, as a function of temperature can be obtained as [175]

$$n = N\mathrm{e}^{\frac{-\Delta H}{k_{\mathrm{B}}T}}, \tag{4.3}$$

where N is the number of sites, ΔH is the defect formation energy, k_{B} is the Boltzmann constant and T is the temperature of the system. This expression will be discussed further in section 6.2.3, but for now it is just applied to determine the regime of defect concentration we are dealing with for the present investigation.

The probability of defect formation as a function of temperature is given by the exponential expression in Eq. 4.3. The defect formation energy from the DFT calculations were halved to take an average of the formation energy per defect during the formation of an antisite pair before being inserted into this expression. This is plotted against temperature in Fig. 4-3. Even 'low-temperature' synthesis procedures for Cu_2ZnSnS_4 use annealing temperatures over 600 K [176]. It can be seen from Fig. 4-3 that the probability of defect formation even at 600 K is much higher than what would be considered as the 'dilute limit'. Furthermore, there is experimental evidence of high concentra-

tions of Cu/ Zn disorder [177, 178, 179, 171], indicating the likely formation of extended defect structures beyond point defects and pairs. To simulate such defect structures in Cu_2ZnSnS_4 a bespoke Monte Carlo model was developed. This will be outlined in the next section and is applied in the study presented in section 4.3.2 [159].

4.3.1 Monte Carlo model for Cu/Zn disorder in Cu_2ZnSnS_4

The general methodology for simulating thermodynamic substitutional disorder with the Metropolis Monte Carlo scheme was introduced in section 3.4. The on-lattice Monte Carlo model developed here to simulate thermodynamic Cu/ Zn disorder is analogous to the Ising model of a ferromagnet, descriptions of which can be found in many textbooks such as Ref. 180 and 181. The Ising model uses interactions between spins, whereas our model considers the Coulombic interaction between the bare formal charges of ions in the lattice of Cu_2ZnSnS_4. In the case of an Ising model, the trial moves in the Metropolis algorithm are spin flips, whereas in our model the trial moves are swaps between nearest-neighbour Cu and Zn ions. Typically, when performing simulations of an Ising model the calculated quantities of interest are the internal energy and average magnetisation of the system as a function of temperature obtained by summing over the distribution of atomic spins. In the case of our system, the quantities of interest are the spatial arrangement of the Cu and Zn ions due to thermodynamic substitutions between the two species and the resulting distribution of electrostatic potential across the system.

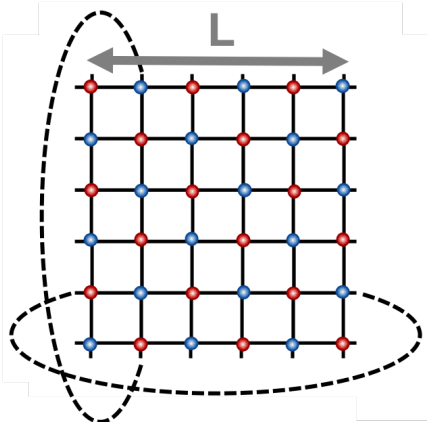

Figure 4-4: Typical periodic boundary conditions for the two-dimensional Ising model. Figure adapted from Ref. 181.

Before we attempt to extract any information on thermodynamic disorder, two impor-

tant considerations for our model will be: to determine if the disordered configuration we obtain is in fact the equilibrated configuration at the given simulation temperature and secondly if finite size effects are having an impact on the system properties we obtain from our simulations. As simulations are performed for finite lattices, to simulate a bulk system the edges or 'boundaries' of the system must be treated carefully. The boundaries can be effectively eliminated through the use of periodic boundary conditions (PBCs). In the case of an Ising model, this means that the first spin in a row interacts with the last spin in the row as if it were a nearest neighbour, and vice versa [181]. This principle is illustrated for a two-dimensional system in Fig. 4-4. Although this procedure effectively eliminates boundary effects, the system is still characterized by the finite lattice size, L, which limits the correlation length to $\frac{L}{2}$. Resultant properties of the simulated system may then differ from the bulk system. We therefore will need to perform simulations with increasing system size to look for any differences in the quantities of interest.

Determining if our system has reached equilibration at each temperature, however, may require a more complicated procedure. As the Monte Carlo method is stochastic, making use of sampling many times with random numbers to determine the minimum energy configuration of the system, the trajectory to reach this final configuration will by nature be random. Therefore, we can draw no conclusions about the properties of our system from evolved states until the final configuration at the particular temperature is reached.

In the case of the Ising model when, for example, determining the average magnetisation of a system at a given temperature, the simulation must be run for a suitably long time until the system has come to equilibrium at that temperature. This is referred to as the equilibration time. To gauge if a system has reached equilibrium, in the case of the Ising model, it is common practice to run the simulation for a large number of Monte Carlo steps (MCS) (where one MCS corresponds to attempting a trial spin-flip at all sites in the system once) and looking for how the value of a quantity of interest, such as the average magnetisation across the system, changes with increasing number of MCS as the simulation progresses. Equilibration is often considered as the point at which the value of a quantity of interest, which initially changes by a large amount, eventually converges to fluctuating about a steady average value. This is dependent upon the principle that a system in equilibrium spends the overwhelming majority of its time in a small subset of states in which its properties take a narrow range of values [180]. Provided the simulation has equilibrated, the final configuration for a given system at a given temperature should always be the same regardless of the initial configuration

of the simulation.

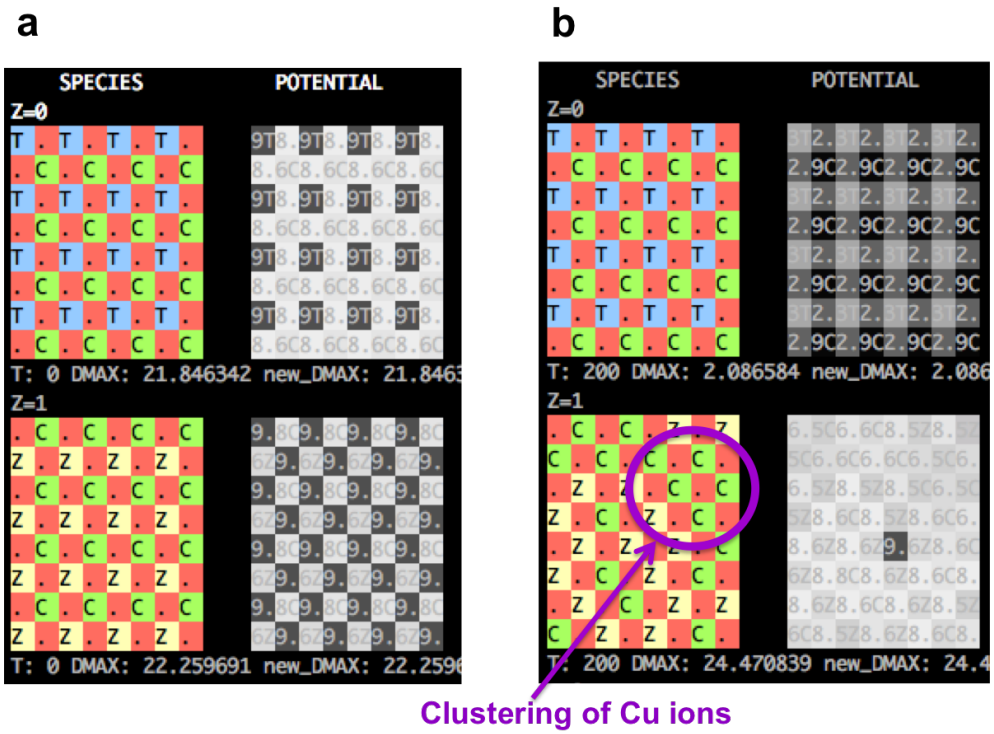

Figure 4-5: Example outputs of 2D slices of cation sub-lattice of Cu_2ZnSnS_4 from Eris Monte Carlo simulations of Cu-Zn disorder from an initially ordered lattice showing the top two layers of the lattice when simulations are performed at temperatures $T = 0\,\mathrm{K}$ (a) and at sufficiently high temperatures for Cu-Zn substitutions (b).

Using this principle, one way to determine if our system has reached its equilibrium configuration could be to use perfectly ordered or disordered initial lattice configurations. Both of these initial configurations, if the simulation is allowed to evolve over a suitable number of MCS, should eventually result in the same equilibrium system configuration. It would be difficult to distinguish differences in the atomic arrangement of one 3D lattice to another by eye, therefore comparisons of the pair correlation functions (PCFs) for each configuration as it evolves from either an ordered or disordered initial configuration can be made. Another method to check for equilibration involves looking for the point at which the value of a quantity of interest converges to fluctuating about a steady average value (as discussed above). In the case of our system, it is the distribution of on-site electrostatic potentials in the system that is of interest. As we fix Sn ions in our simulation, we calculate the on-site electrostatic potential for Sn ions to study how the chemical environment of these species is altered by Cu/ Zn disorder. To check for equilibration, we look for a point after which the variance of the distribution

of electrostatic potentials of Sn ions across the system has reached a steady value. Both of these methods were tested and are discussed in the study in section 4.3.2 [159].

Monte Carlo simulations of thermodynamic substitutions between Cu and Zn ions will be allowed to evolve until the equilibrium configuration in terms of the arrangement of Cu and Zn atoms at the given temperature is reached. Fig. 4-5 shows an example output from our simulations, where Fig. 4-5a shows a perfectly ordered system at T = 0 K and Fig. 4-5b shows spatial clustering of Cu and Zn ions as the system has been allowed to evolve at a finite temperature. The model is used to investigate and quantify thermodynamic Cu/Zn disorder in Cu_2ZnSnS_4 in the study presented in the next section.

4.3.2 Publication: Atomistic insights into the order-disorder transition in Cu_2ZnSnS_4 from Monte Carlo simulations

For Cu_2ZnSnS_4 a lot of attention in the literature has been paid to disorder amongst Cu and Zn cations with a large amount of experimental evidence for the presence of this disorder [171, 172, 173] and theoretical predictions for the low formation energy of the $[Cu^{-}_{Zn} + Zn^{+}_{Cu}]$ antisite pair [139]. Near resonant Raman spectroscopy has been used to examine thin films of Cu_2ZnSnS_4 prepared using different thermal treatments to determine if long post-annealing cooling times could produce films with a high level of order amongst Cu and Zn cations. In this study the authors postulate that achieving a very high level of order amongst Cu and Zn could require years [182]. This clearly would not be a practical treatment for a PV device and so it would seem that the presence of a fairly large amount of disorder amongst Cu and Zn, and hence Cu^{-}_{Zn} and Zn^{+}_{Cu} antisites, is inevitable in the material.

In the following paper, we have applied a bespoke Monte Carlo model to gain atomistic insights into the spatial distribution of thermodynamic disorder on Cu and Zn sites in the cation sublattice. Cation site disorder averaged over a macroscopic sample (as is probed from measurements) does not provide insights into the microscopic cation distribution that will interact with photogenerated electrons and holes. In this study we consider 2D Cu/ Zn disorder, involving just substitutions amongst the cations in Cu-Zn (001) planes, and 3D Cu/ Zn disorder, where Zn ions may also substitute onto Cu 2a sites in Cu-Sn (001) planes. Previous experimental studies have suggested that 2D Cu/ Zn disorder is the dominant disorder mechanism for the Cu/ Zn order-disorder transition (ODT) and that disorder on Cu 2a sites only occurs after the ODT [183]. However, more recent studies have suggested that this disorder mechanism is a part of

the ODT [184, 185]. We extract the critical temperatures, T_C, for the Cu/ Zn ODT for these two Cu/ Zn disorder mechanisms. We find that defects are less concentrated in Cu-Sn (001) planes but that Zn ions readily substitute into Cu-Sn planes even before the ODT and present spatial distributions of antisites from thermodynamic Cu/ Zn disorder in our model.

The following paper has been reproduced from Journal of Materials Chemistry A 7 (1), 312-321 (2019) with permission from the Royal Society of Chemistry. The supplemental material for this paper is included in Appendix A.1.

Statement of Authorship

This declaration concerns the article entitled:									
Atomistic insights into the order-disorder transition in Cu2ZnSnS4 solar cells from Monte Carlo simulations Pages 88 - 98 of thesis									
Publication status (tick one)									
draft manuscript		**Submitted**		**In review**		**Accepted**		**Published**	X
Publication details (reference)	Atomistic insights into the order-disorder transition in Cu2ZnSnS4 solar cells from Monte Carlo simulations SK Wallace, JM Frost, A Walsh Journal of Materials Chemistry A, 2019, DOI: 10.1039/C8TA04812F								
Candidate's contribution to the paper (detailed, and also given as a percentage).	*Formulation of ideas (50%):* The original code used in this work was provided by J. Frost and the idea to investigate Cu-Zn disorder in Cu2ZnSnS4 (CZTS) was provided by A. Walsh. Ideas for subsequent developments of the code and analysis of the data were mostly formulated and implemented by myself (S. Wallace) with support and discussions provided by J. Frost and A. Walsh throughout this study. *Design of methodology (50%):* The Bespoke Monte Carlo model, Eris, (doi: 10.5281/zenodo.1248445) developed for this publication is based on the Starry Night code (doi: 10.5281/zenodo.10543) written by J. Frost to simulate dipole-dipole interactions and ferroelectric domains in a hybrid organic-inorganic perovskite solar cell. Eris was originally adapted by J. Frost from Starry Night to simulate thermodynamic Cu-Zn disorder in CZTS. Developments of the Eris code by S. Wallace include writing routines for: • Lattice initialisation methods to ensure a stoichiometric CZTS crystal • Testing the convergence in the electrostatic summations for calculating the change in lattice energy when performing a Monte Carlo move • Developing and testing methods to check that the equilibrium disordered configuration was achieved for each simulation temperature • Additional outputs from the code including: data to compute an order parameter, tests for convergence when computing on-site electrostatic potentials and outputting lattice on-site electrostatic potentials in various forms for further analysis • Extending the model to include Cu/Zn disorder between the planes, i.e. allowing Zn from Cu-Zn layers to substitute onto Cu sites in the Cu-Sn planes *Experimental work (100%):* All data generated from the Eris code that was used in the publication was produced by S. Wallace. Contributions from implementation of the code include running simulations to test for finite size effects in the model, generating data and developing post-processing tools to quantify and visualise Cu-Zn disorder in the system. *Presentation of data in journal format (70%):* The first draft of the manuscript was prepared by S. Wallace and support was provided by the co-authors when finalising the manuscript for submission.								
Statement from Candidate	This paper reports on original research I conducted during the period of my Higher Degree by Research candidature.								
Signed	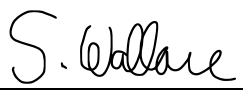			**Date**	05/12/18				

Journal of Materials Chemistry A

PAPER

View Article Online
View Journal

Cite this: DOI: 10.1039/c8ta04812f

Atomistic insights into the order–disorder transition in Cu_2ZnSnS_4 solar cells from Monte Carlo simulations†

Suzanne K. Wallace,[ab] Jarvist Moore Frost[c] and Aron Walsh*[bd]

Kesterite-structured Cu_2ZnSnS_4 (CZTS) is an earth-abundant and non-toxic semiconductor that is being studied for use as the absorber layer in thin-film solar cells. Currently, the power-conversion efficiencies of this technology fall short of the requirements for commercialisation. Disorder in the Cu–Zn sublattice has been observed and is proposed as one explanation for the shortcomings of CZTS solar cells. Cation site disorder averaged over a macroscopic sample does not provide insights into the microscopic cation distribution that will interact with photogenerated electrons and holes. To provide atomistic insight into Cu/Zn disorder, we have developed a Monte Carlo (MC) model based on pairwise electrostatic interactions. Substitutional disorder amongst Cu and Zn ions in Cu–Zn (001) planes on the 2c and 2d Wyckoff sites – 2D disorder – has been proposed as the dominant form of Cu/Zn disorder in near-stoichiometric crystals. We use our model to study the Cu/Zn order–disorder transition in 2D but also allow Zn to substitute onto the Cu 2a site – 3D disorder – including Cu–Sn (001) planes. We find that defects are less concentrated in Cu–Sn (001) planes but that Zn ions readily substitute onto the Cu 2a site and that the critical temperature is lowered for 3D disorder.

Received 23rd May 2018
Accepted 23rd November 2018

DOI: 10.1039/c8ta04812f

rsc.li/materials-a

1 Introduction

Amongst the semiconductors being developed for applications in thin-film photovoltaic (PV) devices, kesterite-structured Cu_2ZnSnS_4 (CZTS) stands out as being composed of low-cost, earth-abundant and non-toxic elements. While the material has many of the bulk properties required to be a high-efficiency photovoltaic absorber, such as a high absorption coefficient of 10^4 cm^{-1} and a direct band gap of 1.5 eV,[1] the power-conversion efficiencies (PCEs) of solar cells are considerably less than the theoretical maximum of 28% as predicted by the Shockley–Queisser limit[2] based on its sunlight-matched optical band gap. The current confirmed record PCE for the kesterite-based alloy $Cu_2ZnSn(S_xSe_{1-x})_4$ (CZTSSe) is at 12.6%,[3] while that of the pure sulfide material still lags behind at 11%,[4] both of which are far below that of the similar PV technology $Cu(In_{1-y}, Ga_y)Se_2$(CIGSe) with a record PCE of 22.6%.[5]

The low open-circuit voltage (compared to the optical band gap) limits achieved device efficiencies.[6,7] This is referred to as the V_{OC} deficit. It is possible that the efficiency of devices fabricated with absorber layers produced from different synthesis procedures may be limited by different factors, making it a difficult task to pinpoint a universal origin of the V_{OC} deficit in CZTS solar cells. Defects and bulk disorder in CZTS is one explanation for the V_{OC} deficit.[8–12] For record-efficiency devices, produced by the hydrazine-based solution method pioneered at the IBM T. J. Watson Research Center,[3,13] this has been attributed to fluctuations in electrostatic potential due to Cu–Zn disorder, and associated band tailing.[14] The origin of the V_{OC} deficit is still an on-going debate.[6]

Inhomogeneity within the cation sublattice of tetrahedrally bonded multinary semiconductors is a particularly likely form of disorder.[15] This can decisively alter the electronic properties of a material.[16] The Cu–Zn–Sn cation sublattice of Cu_2ZnSnS_4 is analogous to a metallic alloy. According to the works by Williams and Bragg,[17–19] an alloy is a system in dynamic equilibrium where atomic species are interchanged between different sites due to thermal agitation, but without destroying the crystalline structure of the phase. In CZTS, substitutional disorder between Cu^+ and Zn^{2+} ions has a low enthalpic cost due to the similar ionic radii and chemical character of the two species. Density functional theory (DFT) predicts a low formation energy for the $[Cu_{Zn}^{-} + Zn_{Cu}^{+}]$ antisite defect pair[20] and there is a large body of evidence for the presence of disorder amongst Cu^+ and Zn^{2+} ions in CZTS.[21–26] Furthermore, ref. 24–27 indicate

[a]Department of Chemistry, Centre for Sustainable Chemical Technologies, University of Bath, Claverton Down, Bath, BA2 7AY, UK
[b]Department of Materials, Imperial College London, Exhibition Road, London SW7 2AZ, UK. E-mail: a.walsh@imperial.ac.uk
[c]Department of Physics, King's College London, Strand, London WC2R 2LS, UK
[d]Department of Materials Science and Engineering, Yonsei University, Seoul 03722, Korea

† Electronic supplementary information (ESI) available. See DOI: 10.1039/c8ta04812f

a distinct order–disorder transition (ODT) attributed to Cu–Zn substitutional disorder.

During the high-temperature synthesis of CZTS disorder can be 'frozen in' to the material as it cools to room temperature. Studies have been conducted to determine if low temperature post-deposition annealing could improve device performance and some improvements were observed from such treatments.[28,29] However, in the latter study the authors postulate that a high level of order amongst the Cu^+ and Zn^{2+} ions would require years of this treatment.[29] It is unclear if the disorder is due to slow kinetics, which could be improved through optimising the processing conditions, or if the disorder is due to fundamental thermodynamic limitations for the material at room temperature.[30] In our study, we model only thermodynamic equilibrium disorder as a function of temperature. Therefore, our model could be used to isolate disorder due to equilibrium thermodynamics from kinetic limitations in experiments. Our model can be used to quantify the absolute limit on order in Cu_2ZnSnS_4 at experimentally relevant temperatures and to generate atomic configurations arising from the disorder process.

Devices made from CZTSSe make the highest performing devices.[3,13] In this study we focus on the pure sulfide. The V_{OC} deficit is worse in CZTS devices[6] and so potentially studying causes of the problem in this particular system could be more informative. Although ultimately the aim for this technology is to make thin-film devices from CZTS, in which the material is likely to be polycrystalline with grain boundaries, we focus on the bulk material. We are doing this for two reasons. Firstly, to improve the understanding of the fundamental material properties before attempting to understand a more complex system. Secondly, it has been proposed that the V_{OC} deficit in CZTSSe devices could be associated with properties of the bulk crystal.[31] It is believed that the most recent high-performance devices are not limited by interface recombination.[32,33] Furthermore, devices fabricated from single crystals have demonstrated a V_{OC} deficit of 530 mV, which equals that of the record thin-film devices, indicating that the deficit could largely be due to bulk disorder.[34]

Studies on various multinary semiconductors have indicated that it is not sufficient to consider only point defects to understand the defect physics of this type of compound due to the likely presence of structural disorder and extended antisite defects.[15,35] System sizes that avoid artificial periodic disorder and associated finite-size effects would be beyond computationally feasible limits for density functional theory (DFT) or other first-principles calculations. However, a number of studies have investigated substitutional disorder by utilising Metropolis Monte Carlo (MC) simulations. One study used DFT to calculate the energy of local structural motifs centred on the S-ions in CZTS (*i.e.* out to nearest-neighbour interactions) and then performed MC simulations for the redistribution of the motifs for systems of up to 1200 atoms.[36] This work indicated clear cation clustering in CZTS with increased temperature. However, the model did not account for any long-ranged interactions which may be important in systems with extended defect structures. Other MC studies have made use of cluster expansion models. In ref. 30 DFT calculations of clusters of interacting dimers and trimers were used to perform MC simulations of up to 512 atoms. This work also investigated the possibility of voltage loss from Cu/Zn disorder by performing DFT calculations to obtain the electronic band gap for selected disordered atomic configurations from their MC simulations. Ref. 37 used a cluster expansion model with clusters out to second-nearest neighbour cations and performed MC simulations for up to 64 000 atoms. Prior to the studies outlined above, there has been little work modelling disordered phases in CZTS, apart from one study where the choice of the disordered phase was arbitrary[38] and another investigating the configurational entropy of independent microstates in small systems of up to 64 atoms.[39]

In this study, we simulate substitutional disorder between Cu^+ and Zn^{2+} ions for system sizes of over 50 000 atoms and allow for Coulomb interactions between all pairs of ions in the system. We use on-lattice Metropolis MC simulation with an interaction model that has been parameterised with the dielectric constant of CZTS determined from first-principles[40] to calculate the changes in lattice energies when performing Cu/Zn substitutions. Our model allows us to freeze certain species in the system, we are therefore able to study separately thermodynamic disorder in 2D where substitutions are only in-plane between Cu and Zn ions on 2c and 2d sites and in 3D where Zn may also substitute on the Cu 2a sites. Cu/Zn disorder in 2D is believed to be the most prevalent type of substitutional disorder for near stoichiometric samples and that substitutions onto the Cu 2a sites occur only after the Cu/Zn ODT has occurred.[21,24,41] However, other studies have suggested that disorder on the 2a site plays an important role.[37,42] We therefore perform simulations to study the ODT for both cases. Simulations are performed in parallel over different temperatures using GNU parallel,[43] and the associated simulation codes have been made openly available.

2 Computational methodology

2.1 Lattice model of Cu_2ZnSnS_4

The crystal structure of Cu_2ZnSnS_4 can be described by two inter-penetrating face-centred cubic (FCC) lattices: one of metal cations and one of sulfur anions. This is shown in Fig. 1a, where green planes are a guide to the eye to distinguish the anion sub-lattice. The sulfur sub-lattice is implicit during the MC simulations but incorporated later in calculations of lattice electrostatics. The cation lattice can be described by alternating layers of Cu–Sn and Cu–Zn in (001) planes, as shown in Fig. 1b. Cu/Zn disorder in only the Cu–Zn (001) planes is referred to as '2D disorder' in this study, while full Cu/Zn disorder is referred to as '3D disorder'. In the case of the latter, Zn ions are able to substitute onto Cu 2a sites in the Cu–Sn (001) planes. For computational convenience, we map this FCC lattice onto a simple cubic (SC) lattice by introducing empty lattice sites.

The separation between lattice sites in our model is re-scaled using DFT (PBEsol functional) optimised lattice parameters of $a = b = 5.44$ Å.[45] Kesterite has a tetragonal lattice with $\frac{c}{2a}$ ratio

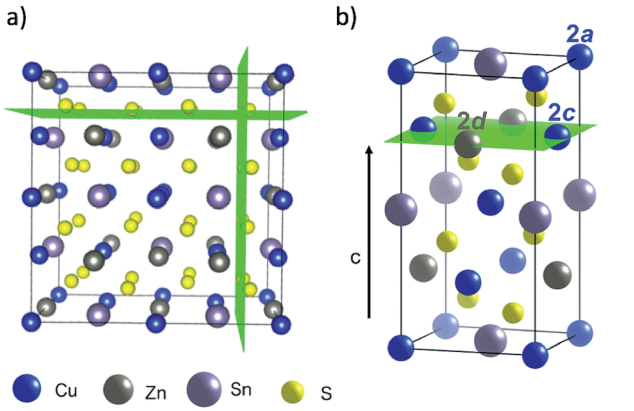

Fig. 1 Representations of the crystal structure of kesterite-structured Cu_2ZnSnS_4 where green planes are used as guides to the eye: (a) supercell indicating the two inter-penetrating anion and cation sub-lattices, (b) the conventional unit cell highlighting a Cu–Zn layer in the (001) planes along the *c*-axis. Visuals were produced using VESTA.[44]

close to 1 (0.998 from DFT/PBEsol-optimisation). We use a value of 1 in the MC simulations, which has a minor effect on the lattice energy as confirmed from explicit calculations using the General Utility Lattice Program (GULP).[46] Lattice energies of an ordered 64 atom supercell with the exact DFT/PBEsol-optimised lattice parameters and an equivalent supercell with the approximated lattice parameters differed by less than 2%.

In our model we fix the position of Sn ions. To simulate only nearest-neighbour Cu/Zn disorder within the Cu–Zn layers, we use a cut-off radius of 2 lattice units (to account for the empty sites between each cation, shown in Fig. 4). The cut-off radius in the *c*-direction is only 1 lattice unit so that substitutions may only occur with the plane above or below. The model does not account for strain effects during Cu–Zn substitutions as it is fixed on-lattice. It has been reported that there is a small change in the *c* lattice parameter with increased disorder;[47] however, due to the similar ionic radii of Cu and Zn we neglect this effect, but it could be incorporated into future models. Sn ions have the largest formal charge in the lattice and are fixed during the simulations.

2.2 Pair interaction model and metropolis Monte Carlo simulation of cation disorder

The MC method can be used to calculate thermodynamic information about a system of interacting ions, which we represent on a 3D lattice as described above. We assume that the potential field of an ion is spherically symmetric and consider two-body forces acting between all pairs of ions in this system. If we know the positions of the N interacting ions on the lattice then the potential energy of the system can be calculated using eqn (1), where d_{ij} is the minimum distance between ions i and j with charge q_i and q_j.[48]

$$U = \frac{1}{2}\sum_{i=1}^{N} q_i \sum_{j=1}^{N(j\neq i)} \frac{1}{4\pi\varepsilon_0}\frac{q_j}{d_{ij}} \quad (1)$$

To calculate the properties of the system, the canonical (NVT) ensemble is used where the number of ions, volume and temperature are all constant. The trial MC moves are swaps between nearest-neighbour Cu and Zn ions.

Using a standard MC method for our system would involve placing each of the N ions at random positions in the lattice to define a random point in the $3N$-dimensional configuration space. However, most configurations are improbable so performing this calculation for every possible configuration would be inefficient and unnecessary to sufficiently evaluate the ensemble. The custom MC code in this study makes use of the Metropolis modified MC scheme.[48] In this implementation of the MC method, instead of choosing configurations randomly and then weighting them, the Metropolis algorithm considers the relative probability of a system being in a new configuration, β, to that of being in the current configuration, α. This is shown in eqn (2), where E_α is the energy of state α, E_β is the energy of state β, and Z is the partition function. For most systems, calculating the value of the partition function requires the summation over a large number of states. However, in the expression for the probability of the trial within the Metropolis scheme, Z cancels out.

$$\frac{p_\beta}{p_\alpha} = \frac{e^{-\frac{E_\alpha}{k_b T}}}{Z}\frac{Z}{e^{-\frac{E_\alpha}{k_b T}}} = e^{-\frac{E_\beta - E_\alpha}{k_B T}} \quad (2)$$

The relative probabilities of the two states are completely determined by the energy difference, such that if:

$$\Delta E = E_\beta - E_\alpha \leq 0, \text{ then } \frac{p_\beta}{p_\alpha} \geq 1 \quad (3)$$

and if

$$\Delta E = E_\beta - E_\alpha > 0, \text{ then } \frac{p_\beta}{p_\alpha} < 1 \quad (4)$$

It is then decided if this new configuration should be added to the trajectory of the system (towards the minimum energy configuration), or not, based on the probability of the new configuration relative to the current configuration. If the relative probability is ≥ 1, as shown in eqn (3), then the move is accepted and added to the trajectory. However, if the relative probability is <1 then the move will only be accepted if $e^{-\frac{\Delta E}{k_B T}} \geq$ a random number generated between 0 and 1.

Lattice energy summations of the system were performed before and after a proposed Cu–Zn substitution out to a finite radius to obtain ΔE. Within periodic boundary conditions, the upper limit for the cut off radius is half the minimum dimension of the system. Details of the convergence in ΔE with respect to the cut off radius used in the lattice summations are given in the ESI.† Eqn (5) is used to calculate the electrostatic interaction between pairs of ions in the system, where q_1 and q_2 are the bare formal charges, r is the separation of the point charges, ε_r is the effective dielectric constant of the crystal and ε_0 is the permittivity of free space.

$$E_{\text{electrostatic}} = \frac{q_1 q_2}{4\pi\varepsilon_0\varepsilon_r} e^2 \frac{1}{r} = q_1 q_2 I_{\text{electrostatic}} \quad (5)$$

To define $I_{\text{electrostatic}}$, we use the separation of nearest-neighbour Cu–Zn ions for r (3.8 Å) and the calculated value for the static dielectric constant of 9.9.[40] This results in $I_{\text{electrostatic}} = -0.378$ eV.

3 Results and discussion

3.1 Equilibration

Due to the stochastic nature of the trajectory from an initial configuration in the MC method, we cannot draw any conclusions about the thermodynamic properties of that system at the given simulation temperature until equilibrium has been reached. The number of simulation steps required to reach this point is the 'equilibration time'. Equilibration is often considered as the point at which the value of a quantity of interest, which initially changes by a large amount, eventually converges to fluctuating about a steady average value. This is dependent upon the principle that a system in equilibrium spends the majority of time in a small subset of states in which the properties take a narrow range of values.[49]

Our MC model for Cu/Zn disorder is analogous to the Ising model of a ferromagnet and we describe the rationale for our equilibration procedure by referring to this common example. In the case of an Ising model, the trial moves in the Metropolis algorithm are spin flips, whereas in our model the trial moves are swaps between Cu and Zn ions. For the Ising model, one MC step corresponds to attempting a trial spin-flip at all sites in the system once. Similarly, for our model one MC step corresponds to sweeping across the entire lattice and attempting a near-neighbour Cu–Zn swap at each Cu and Zn site. In the case of the Ising model it is usually the average magnetisation of the system, or internal energy, as a function of temperature that are the quantities of interest. For our system, we are interested in the configuration of the ions (and extent of thermodynamic disorder) and the corresponding distribution of the electrostatic potential across the system, as this can be related to the observed band tailing. We now explore two methods to gauge when the system has reached the equilibrium disordered configuration at each simulation temperature: the pair correlation function (PCF) for information on the structural disorder and also the variance of the distribution of on-site electrostatic potentials of species in the system.

3.1.1 Pair correlation functions from ordered and disordered initial lattices. We first attempted two simulations for each temperature, one starting from an initial ordered lattice and one from an initial disordered lattice (produced by randomly 'shuffling' Cu and Zn ions in the ordered lattice), until both simulations converged to the same equilibrium configuration. To gauge the point at which this had been reached, we compare the pair correlation functions (PCFs) for each configuration, an example of this analysis is given in Fig. 2.

We found that systems initialised from a disordered lattice required a substantially larger number of MC steps to evolve away from the initial configuration. This can be seen in Fig. 2 from the Zn–Zn PCFs. The most noticeable feature when comparing the PCF for an ordered initial lattice to that of a disordered lattice is the emergence of a new nearest-neighbour Zn–Zn peak at $\sqrt{2}$ lattice units due to the clustering of Zn ions once Cu and Zn ions have been allowed to substitute. This point is discussed further in Section 3.2 as an order parameter, but for now we just remark that the peak is largest for the disordered initial lattice and decreases for the system evolved from this initial configuration at moderate simulation temperatures. After a large number of MC steps the peak for the two systems evolved from the ordered and disordered initial lattices were not of the same height. This observation may be explained by the entropic penalty in going from a disordered to a more ordered system, suggesting that this method may not be computationally efficient. We therefore adopted an alternative approach to check for equilibration, as outlined below.

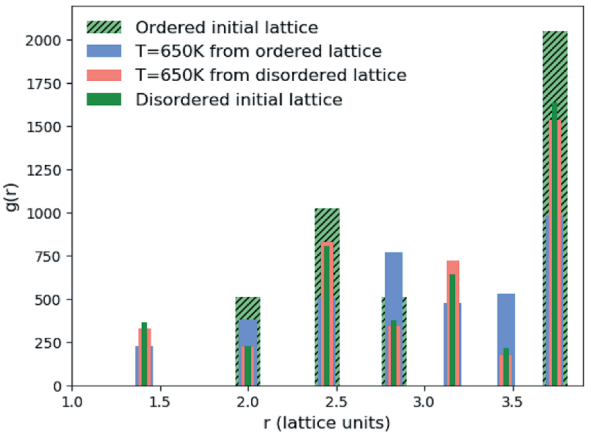

Fig. 2 Pair correlation function (PCF) between pairs of Zn ions in Cu_2ZnSnS_4. PCFs of an initial ordered lattice are plotted with that of a disordered initial lattice as reference points as well as systems that have been evolved from both of these initial configurations at T = 650 K. Widths of the bars plotted are arbitrarily chosen to ensure all data is visible.

3.1.2 Variance in the distribution of on-site electrostatic potentials. Our second method is analogous to using the point at which the average magnetisation fluctuates about a steady value in the Ising model, as discussed earlier. We check the number of MC steps required for the variance of the distribution of on-site electrostatic potentials of all Sn ions in the lattice to fluctuate about a steady value. We use Sn ions because we have fixed the locations of Sn ions in our simulations, making them stationary reference points. There is one crystallographically distinct Sn lattice site in Cu_2ZnSnS_4. We start from an ordered lattice and as all ions are on their correct lattice sites, there is only one unique chemical environment for Sn and the variance in electrostatic potential is zero. As the system evolves, and Cu and Zn ions are substituted, unique chemical environments emerge for the Sn ions in the system.

An example of a test to determine a suitable number of MC steps for equilibration (*i.e.* steps to run before collecting data on the system) is shown in Fig. 3 for 3D Cu/Zn disorder. The equivalent for 2D disorder is given in the ESI.† We perform this check

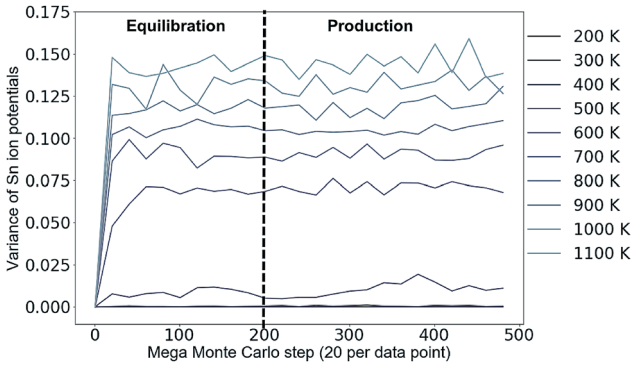

Fig. 3 Variance in the distribution of the on-site electrostatic potential of Sn ions in a 13 824 atom Cu_2ZnSnS_4 system across a range of simulation temperatures with 3D Cu/Zn disorder. Equivalent for 2D disorder can be found in the ESI.† Each mega Monte Carlo step corresponds to sweeping across the lattice and attempting 100 trial moves per lattice site.

for the largest system size in our study and the whole simulation temperature range we study. A larger system may require a considerably larger number of MC steps to equilibrate and we perform the check for each temperature because if there is a phase transition (as suggested in several works[24–27]), there could be 'critical slowing down' close to the transition temperature.

From Fig. 3, we take 200 mega MC steps as a suitable number of equilibration steps to ensure all simulation temperatures have reached their equilibrium configuration before we start collecting data. One mega MC step consists of attempting on average 100 trial Cu–Zn substitutions per site, *i.e.* 100 sweeps of the lattice per mega MC step. The absence of variance in Fig. 3 at low simulation temperatures is because the system remains ordered.

3.2 Order parameters

To quantify the extent of substitutional Cu–Zn disorder in our system, we consider two order parameters to enable us to investigate long- and short-ranged order.

3.2.1 Pair correlation functions. Pair correlation functions (PCFs) show the number of pairs of particular species with particular separations within the system. We generate reference PCFs of ordered and disordered systems (using equilibrated configurations at low and high temperatures, respectively) of the same size. The most noticeable feature in the PCFs of the system was the emergence of a new nearest-neighbour peak in the Zn–Zn PCF at $\sqrt{2}$. This can be explained using Fig. 4. In the ordered lattice the shortest Zn–Zn spacing is 2 lattice units. Once Cu and Zn begin to substitute a new shortest Zn–Zn spacing of $\sqrt{2}$ lattice units becomes possible. An increase in the intensity of this $\sqrt{2}$ peak indicates more clustering of Zn ions and so provides insights into the extent of short-ranged disorder in the system. The same analysis is not possible using the Cu–Cu PCF because a $\sqrt{2}$ Cu–Cu separation is present between the (001) planes in the ordered lattice.

3.2.2 Cation site occupancy. An order parameter used in experimental literature to quantify Cu–Zn disorder in kesterites is based on cation site occupancies.[24,25] In ordered CZTS, Cu ions occupy 2c sites in the Cu–Zn layers indicated in Fig. 1b and 2a sites in the Cu–Sn layers. Sn ions occupy the 2b sites and Zn ions occupy the 2d sites.[27] In completely disordered CZTS Cu and Zn are found evenly distributed over 2c and 2d sites, indicating disorder in the Cu–Zn layers. A measure of increasing order is when Cu shows a preference to occupy 2c sites and Zn to occupy 2d sites. For ordered CZTS, the parameter $S = 1$, corresponding to all Zn ions on 2d sites and all Cu ions on 2c sites. For fully disordered CZTS $S = 0$, corresponding to no preference for Cu or Zn to occupy their ideal crystallographic site.

$$S = \frac{[Cu_{2c} + Zn_{2d}] - [Zn_{2c} + Cu_{2d}]}{[Cu_{2c} + Zn_{2d}] + [Zn_{2c} + Cu_{2d}]} \quad (6)$$

However, it is possible that this metric may overestimate the extent of disorder in a system as locally ordered domains, displaced relative to the configuration of the initial lattice,

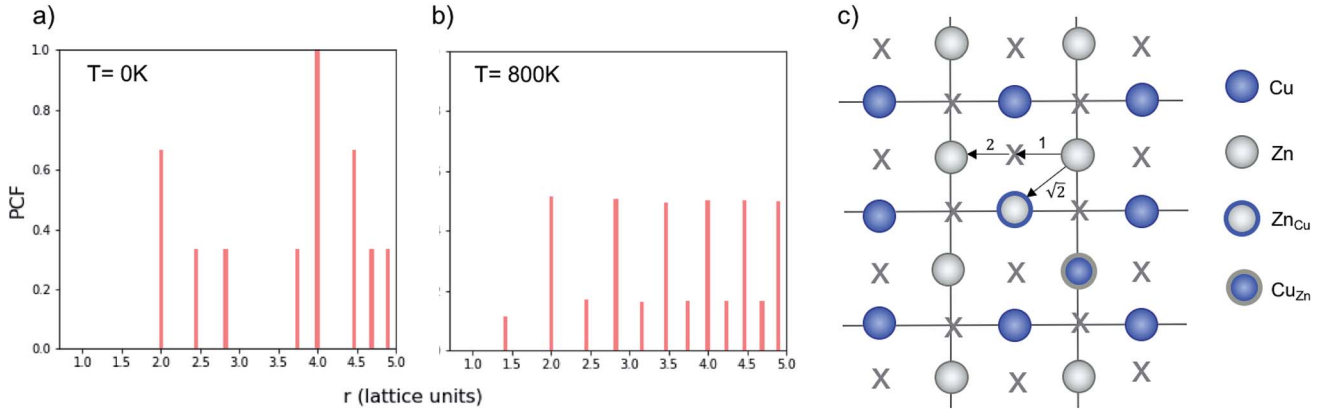

Fig. 4 Normalised Zn–Zn pair correlation functions (PCFs) at 0 K (a) and 800 K (b) for an (001) Cu–Zn plane in the cation sub-lattice of Cu_2ZnSnS_4 with structure shown in (c). Crosses denote the gap sites used in our lattice model to map an fcc lattice onto a sc lattice. Before a Cu–Zn swap, the nearest-neighbour Zn–Zn pair is 2 lattice units apart. After a Cu–Zn swap there is a Zn–Zn pair separated by $r = \sqrt{2}$. The 0 K PCF is for the ordered lattice before any Cu–Zn substitutions have occurred and shows a Zn–Zn PCF peak intensity of zero at $r = \sqrt{2}$. The 800 K PCF shows an increase in the peak intensity at $r = \sqrt{2}$, once Cu and Zn ions begin to substitute.

would be considered as disordered. We therefore compare the extent of order at each simulation temperature inferred from our PCF analysis to that suggested by the S parameter as we increase the system size to check for the formation of locally ordered domains. A decrease in S and an increase in Zn–Zn PCF $\sqrt{2}$ peak intensity correspond to a reduction in order in the system. For the case of locally ordered domains, a low S (suggesting large extents of Cu–Zn disorder) could coincide with a relatively small $\sqrt{2}$ Zn–Zn PCF peak, suggesting long-range disorder, but short range order within the Cu–Zn planes. It is also worth noting that the S order parameter only considers disorder on the 2c and 2d sites and hence neglects disorder on the Cu 2a site when 3D Cu/Zn disorder is present. However, the use of the first Zn–Zn PCF peak as an order parameter is still relevant when considering 3D disorder as substitutions of Zn onto the 2a can result in Zn ions being separated by $\sqrt{2}$ lattice units.

3.3 Finite size effects

To investigate finite size effects, we perform simulations for system sizes ranging from 12 × 12 × 12 (=1728 ions) to 32 × 32 × 32 (=32 768 ions). We investigate the disorder behaviour of the systems as a function of temperature using the two order parameters in Fig. 5. Fig. 5a shows the increase in the intensity of the Zn–Zn PCF at $r = \sqrt{2}$ with temperature (explained schematically in Fig. 4). Fig. 5b shows the decrease in S from 1 to 0 with increased simulation temperature. Both order parameters show approximately the same temperature-dependence for the disorder process. Our model shows clear signs of finite size effects for the smallest system (1728 ions), in the regime used in some previous studies. We consider a 24 × 24 × 24 size system (=13 824 ions) to give a converged disorder process with respect to system size and use this system size for all subsequent simulations.

3.4 Cu/Zn order–disorder transitions

In this section we use the order parameters introduced in Section 3.2 to characterise the Cu/Zn order–disorder transitions (ODTs) for 2D Cu/Zn disorder (when the only mechanism is substitutions between Cu and Zn ions on 2c and 2d sites) and for 3D Cu/Zn disorder (when Zn may also substitute onto the Cu 2a sites). To improve our statistics, we performed 11 independent Monte Carlo simulations, each using different random number seeds and perform simulations across smaller temperature increments at temperatures close to the ODT critical temperatures, T_C. Due to the possibility of critical slowing down when using temperature increments closer to T_C, we repeat equilibration checks to ensure data is still for equilibrated configurations.

Fig. 6 compares the S order parameter based on the cation occupancy of 2c and 2d sites obtained for simulations of both 2D and 3D Cu/Zn disorder to anomalous X-ray powder diffraction data for $Cu_2ZnSnSe_4$ from ref. 24. In the plot, experimental data has been shifted by 70 K to account for the difference in the order–disorder transition temperature for the pure sulfide and pure selenide reported in ref. 50. As our model considers only

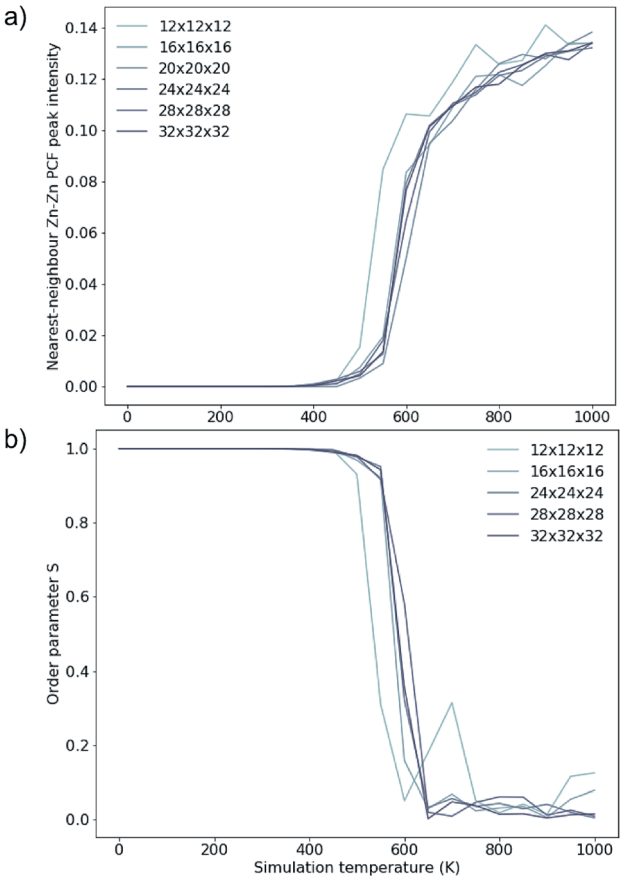

Fig. 5 Two order parameters to assess finite-size effects for 3D Cu/Zn disorder. Equivalent for 2D disorder can be found in the ESI.† (a) The nearest-neighbour ($r = \sqrt{2}$) Zn–Zn pair correlation function peak intensity for systems of various sizes at thermodynamic equilibrium across simulation temperatures ranging from 0 to 1000 K, indicating clustering of Zn ions and deviation from the perfectly ordered lattice with a $r = \sqrt{2}$ peak intensity greater than zero. (b) The S order parameter based on Cu and Zn site occupancies in Cu_2ZnSnS_4 as a function of simulation temperature. $S = 1$ corresponds to a fully ordered lattice and $S = 0$ corresponds to complete Cu–Zn disorder within the (001) plane (b).

thermodynamic disorder, the difference in the value of the S order parameter at comparable temperatures between our model and experiment, and the diverging gradients of the curves at lower temperatures, could be attributed to kinetic limitations on the ordering processes that will be present in the real system but not in our model.

Taking T_C to be the temperature at which $S = 0$ gives a T_C of approximately 750 K and 650 K for 2D and 3D Cu/Zn disorder, respectively, as shown in Fig. 6. T_C predicted from our 3D model based on the S order parameter is closer to the observed value of approximately 550 K. The overestimate in T_C could be due to the bulk (macroscopic) dielectric constant used in the interaction energy. In polycrystalline films, there may be additional contributions to dielectric polarisation from the presence of internal interfaces and inhomogeneity in the mechanical and electrical properties.[51]

As discussed in Section 3.2, S only accounts for Cu/Zn disorder on the 2c and 2d sites and therefore may not fully

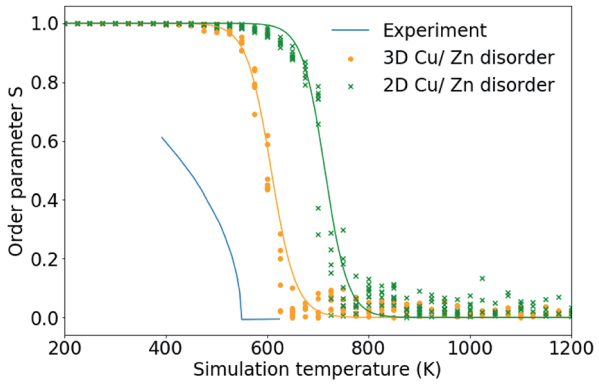

Fig. 6 The S order parameter based on Cu and Zn site occupancies in Cu_2ZnSnS_4 for 24 × 24 × 24 (=13 824 ions) from 11 independent Monte Carlo simulations for 2D Cu/Zn disorder and 3D Cu/Zn disorder plotted against anomalous X-ray powder diffraction data for Cu_2ZnSnS_4 from ref. 24. Experimental data has been shifted by 70 K to account for the difference in the order–disorder transition temperature for the pure sulfide and pure selenide reported in ref. 50.

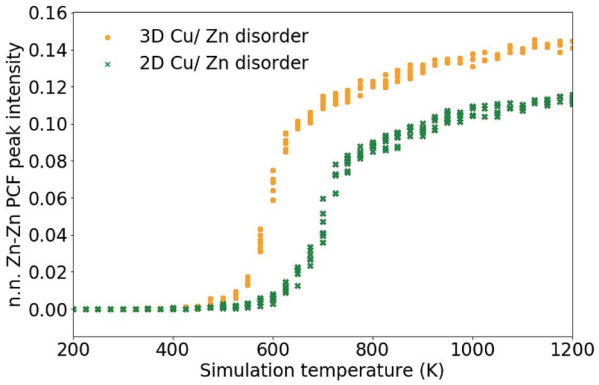

Fig. 7 Nearest-neighbour Zn–Zn pair correlation function peak intensity, which emerges due to the substitution of Zn ions onto nearest-neighbour Cu sites in Cu_2ZnSnS_4 as shown in Fig. 4. 11 independent Monte Carlo simulations are performed for 2D Cu/Zn disorder and 3D Cu/Zn disorder.

describe the 3D case. For this reason, the nearest Zn–Zn PCF peak order parameter is also used to compare the ODT for 2D and 3D Cu/Zn disorder. The S order parameter can be considered as a measure of the loss of order in the system, allowing for the sudden drop in the parameter with increasing temperature. The PCF peak order parameter on the other hand, can be considered as an increase in disorder in the system which gradually increases towards complete disorder at the infinite temperature limit. The high-temperature Zn–Zn nearest-neighbour PCF peaks shown in Fig. 7 can be understood as the Cu–Zn sub-lattice beginning to melt. Within the cation sub-lattice, there are 12 nearest neighbours. In the $S = 0$ disorder regime, Cu shows no preference to occupy the 2c sites and Zn to occupy the 2d sites, we can therefore expect the density of Zn–Zn nearest neighbours to converge towards 2/12 (approximately 0.167). However, we cannot expect the PCF peak at high-temperatures to reach a complete plateau at high-temperatures as is seen for the S order parameter due to the lower stoichiometric ratio of Zn relative to Cu in Cu_2ZnSnS_4. The larger PCF peak intensity for 3D Cu/Zn disorder than for 2D Cu/Zn disorder can be understood by the larger number of possible options for Zn to substitute onto nearest-neighbour Cu sites in the 3D case.

Fig. 8 and 9 show locations of Cu-on-Zn and Zn-on-Cu antisites in Cu–Zn and Cu–Sn (001) planes of the lattice model at various simulation temperatures for 2D and 3D Cu/Zn disorder respectively. In each case, the choice of planes used for the visualisation was chosen based on ones that showed the presence of disorder in the low-disorder temperature regime when disorder was not present in all layers of the lattice. Fig. 8a and b show two configurations of a Cu–Zn (001) plane at temperatures below T_C for the 2D Cu/Zn ODT with Fig. 8b showing the nucleation of a distinct disordered region in the lower left corner of the plane. Fig. 8c shows a configuration above T_C with a large extent of Cu/Zn disorder.

Fig. 9a and b show the location of a small number of Cu-on-Zn and Zn-on-Cu antisites in the Cu–Zn and Cu–Sn (001) planes

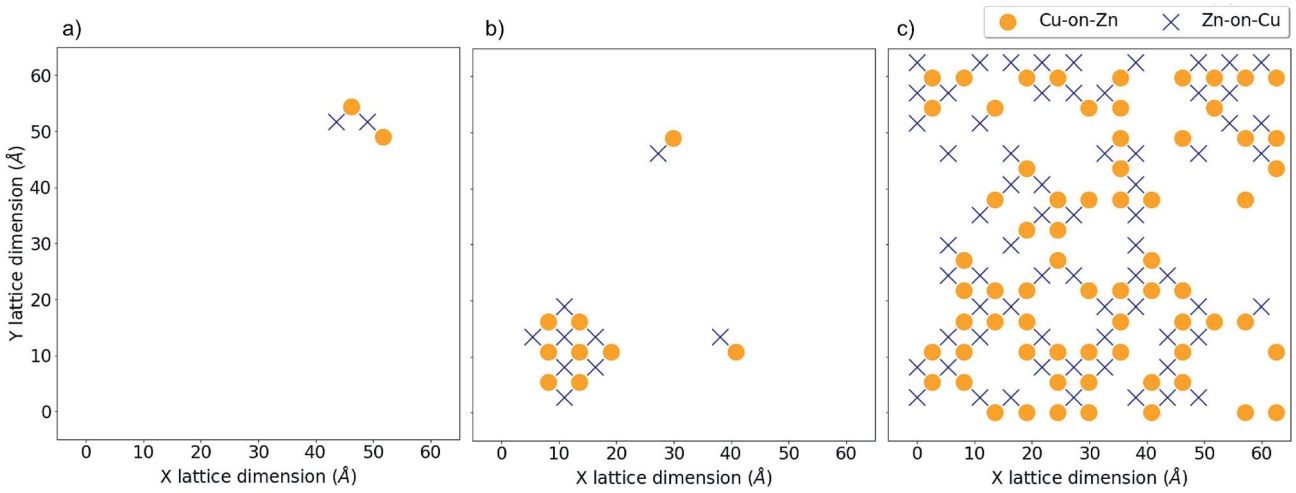

Fig. 8 2D Cu/Zn disorder in a 13 824 atom system. Critical temperature, T_C, for the order–disorder transition is approximately 750 K for this system. (a) Shows antisite locations at $T = 550$ K in a Cu–Zn plane, (b) shows the same plane at $T = 650$ K with the formation of a distinct disordered region and (c) shows the same plane above T_C at $T = 900$ K.

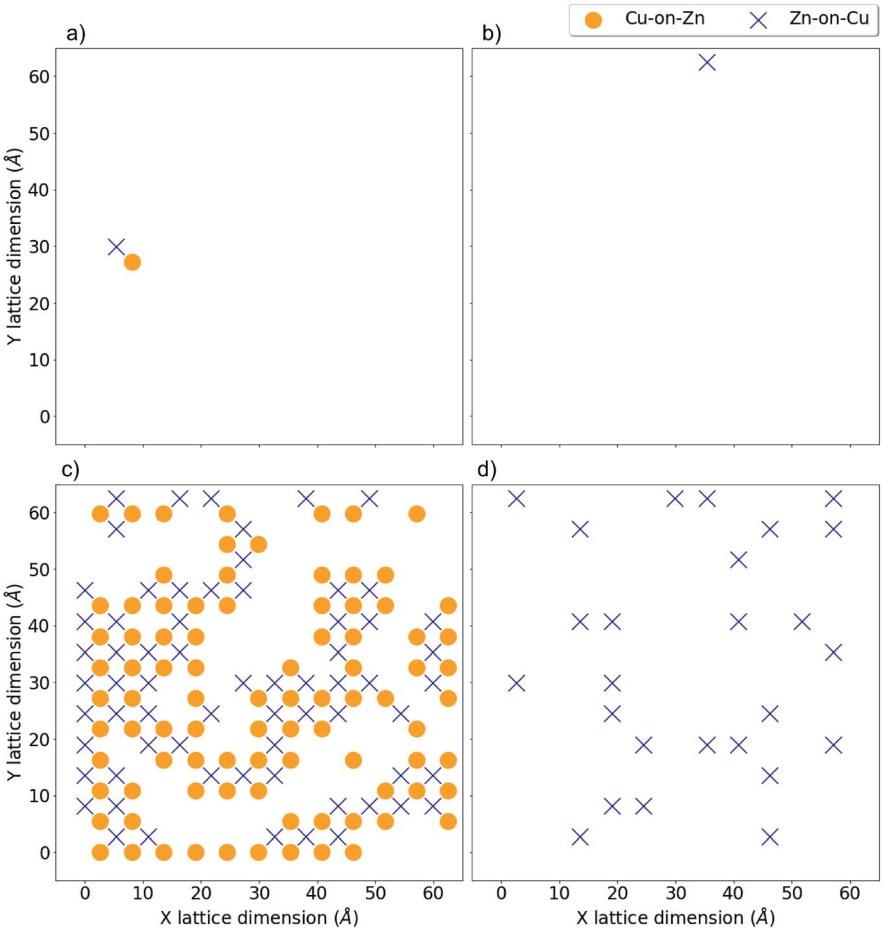

Fig. 9 3D Cu/Zn disorder in a 13 824 atom system. Critical temperature, T_C, for the order–disorder transition is approximately 650 K for this system. (a) and (b) show antisite locations at $T = 400$ K in a Cu–Zn and Cu–Sn plane respectively. (c) and (d) show the same for $T = 750$ K, *i.e.* above and below T_C respectively.

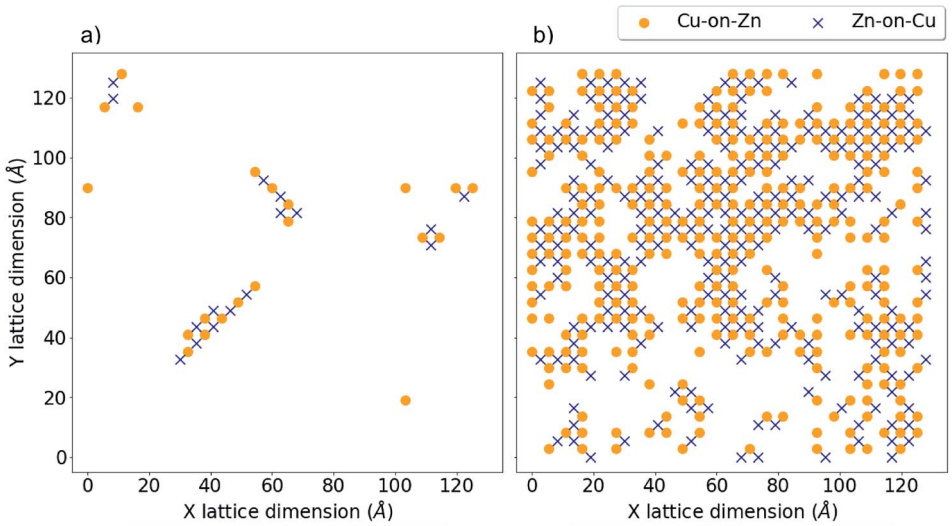

Fig. 10 3D Cu/Zn disorder in a 55 296 atom system. Critical temperature, T_C, for the order–disorder transition (ODT) is approximately 650 K for this system. (a) Antisite locations at in a Cu–Zn plane $T = 550$ K and (b) at $T = 650$ K, corresponding to low-disorder before the ODT and high-disorder after the ODT, respectively.

respectively at a simulation temperature below T_C for the 3D Cu/Zn ODT. It can be seen here that Zn readily substitutes onto the Cu 2a sites even in this low-disorder temperature regime. This is in agreement with results from cluster expansion MC simulations performed in ref. 30 where the temperature for the onset of Cu–Sn plane disorder was the same as that for Cu–Zn planes. This is also in agreement with cluster expansion MC simulations performed in ref. 37 which indicated that there is no intermediate 'partially disordered' phase where there is only disorder in the Cu–Zn planes. Fig. 9c and d show the antisite locations in the same planes at a simulation temperature above T_C for the 3D Cu/Zn ODT, which shows a similar spatial distribution of antisites in the Cu–Zn plane to that observed for 2D Cu/Zn disorder above T_C in Fig. 8c. We also note that in the high-temperature disorder regime the disorder is more dilute in the Cu–Sn planes, with Fig. 9d showing less than half the antisite concentrations of Fig. 9c. This is also in agreement with ref. 30, where the order parameter for the simulated Cu–Sn plane disorder reduced to a lesser extent with increasing temperature than that of the Cu–Zn planes. This observation may also explain why 2a site disorder is not always observed to be as prevalent as 2c and 2d site disorder experimentally. Fig. 10 shows antisite locations in a Cu–Zn plane that is twice as large as those in Fig. 8 and 9. Fig. 10a shows a plane in the low-disorder regime just before the ODT and Fig. 10b shows the same plane just above the ODT. The defect structures such as those shown in Fig. 10a indicate the presence of extended defect structures in Cu_2ZnSnS_4. The distribution of antisites above T_C for the larger system in Fig. 10b is similar to that in the system half the size in Fig. 9c.

4 Summary and further work

In summary, we have developed a Monte Carlo (MC) model to simulate Cu/Zn disorder in kesterite-structured Cu_2ZnSnS_4 (CZTS) based on electrostatic pairwise interactions. We simulate separately the cases of 2D and 3D Cu/Zn disorder. We find that the critical temperature for disordering is lowered when swaps between adjacent (001) planes are allowed. In line with recent work,[37,42] our model suggests that it is important to also consider Cu/Zn disorder on the Cu 2a sites; however, the concentration of defects in Cu–Zn planes is higher, which may explain why this is often thought to be the dominant mechanism in the order–disorder transition.

Extending the MC procedure to treat off-stoichiometric kesterites, as are often found to produce the highest-performing devices, could provide insights into the origin of the performance improvement. It has been observed that the critical temperature is not altered through tuning of the stoichiometry, but it has been suggested that stoichiometry influences the kinetics of cation ordering.[52] As our model considers only thermodynamic cation ordering, it could be used to isolate kinetic limitations for different stoichiometric CZTS compounds. Incorporating the effects of Cu/Zn disorder from our model on electron transport and recombination in kesterite solar cells will also be a valuable line for future research.

Data access statement

The Monte Carlo model is implemented in the code Eris, which is available from https://doi.org/10.5281/zenodo.1471439 under an MIT open-source license. Data from our Monte Carlo simulations is available from the online repository zenodo at https://doi.org/10.5281/zenodo.1481749.

Conflicts of interest

There are no conflicts to declare.

Acknowledgements

We thank Laurie Peter, Mark Weller, David Mitzi, Benjamin Morgan, Ji-Sang Park and Sunghyun Kim for useful discussions. This research has been funded by the EPSRC (Grant No. EP/L017792/1 and EP/K016288/1), as well as the EU Horizon 2020 Framework (STARCELL, Grant No. 720907). AW is supported by a Royal Society University Research Fellowship. We are grateful to the UK Materials and Molecular Modelling Hub for computational resources, which is partially funded by EPSRC (EP/P020194/1).

References

1 X. Liu, Y. Feng, H. Cui, F. Liu, X. Hao, G. Conibeer, D. B. Mitzi and M. Green, *Prog. Photovoltaics*, 2016, **24**, 879–898.
2 W. Shockley and H. J. Queisser, *J. Appl. Phys.*, 1961, **32**, 510.
3 W. Wang, M. T. Winkler, O. Gunawan, T. Gokmen, T. K. Todorov, Y. Zhu and D. B. Mitzi, *Adv. Energy Mater.*, 2013, **4**, 1301465.
4 C. Yan, J. Huang, K. Sun, S. Johnston, Y. Zhang, H. Sun, A. Pu, M. He, F. Liu, K. Eder, L. Yang, J. M. Cairney, N. J. Ekins-Daukes, Z. Hameiri, J. A. Stride, S. Chen, M. A. Green and X. Hao, *Nat. Energy*, 2018, **3**, 764–772.
5 P. Jackson, R. Wuerz, D. Hariskos, E. Lotter, W. Witte and M. Powalla, *Phys. Status Solidi RRL*, 2016, **10**, 583–586.
6 S. Bourdais, C. Choné, B. Delatouche, A. Jacob, G. Larramona, C. Moisan, A. Lafond, F. Donatini, G. Rey, S. Siebentritt, A. Walsh and G. Dennler, *Adv. Energy Mater.*, 2016, **6**, 1502276.
7 R. Aninat, L.-E. Quesada-Rubio, E. Sanchez-Cortezon and J.-M. Delgado-Sanchez, *Thin Solid Films*, 2017, **633**, 146–150.
8 S. K. Wallace, D. B. Mitzi and A. Walsh, *ACS Energy Lett.*, 2017, **2**, 776–779.
9 J. Li, D. Wang, X. Li, Y. Zeng and Y. Zhang, *Adv. Sci.*, 2018, 1700744.
10 J. S. Park, S. Kim, Z. Xie and A. Walsh, *Nat. Rev. Mater.*, 2018, **3**, 194–210.
11 S. Kim, J.-S. Park and A. Walsh, *ACS Energy Lett.*, 2018, **3**, 496–500.
12 J.-S. Park, S. Kim and A. Walsh, *Phys. Rev. Mater.*, 2018, **2**, 014602.
13 T. K. Todorov, K. B. Reuter and D. B. Mitzi, *Adv. Mater.*, 2010, **22**, E156–E159.

14 T. Gokmen, O. Gunawan, T. K. Todorov and D. B. Mitzi, *Appl. Phys. Lett.*, 2013, **103**, 103506.
15 L. L. Baranowski, P. Zawadzki, S. Lany, E. S. Toberer and A. Zakutayev, *Semicond. Sci. Technol.*, 2016, **31**, 123004.
16 S. Lany, A. N. Fioretti, P. P. Zawadzki, L. T. Schelhas, E. S. Toberer, A. Zakutayev and A. C. Tamboli, *Phys. Rev. Mater.*, 2017, **1**, 035401.
17 W. L. Bragg and E. J. Williams, *Proc. R. Soc. A*, 1934, **145**, 699–730.
18 W. L. Bragg and E. J. Williams, *Proc. R. Soc. A*, 1935, **151**, 540–566.
19 E. J. Williams, *Proc. R. Soc. A*, 1935, **152**, 231–252.
20 S. Chen, J.-H. Yang, X. G. Gong, A. Walsh and S.-H. Wei, *Phys. Rev. B: Condens. Matter Mater. Phys.*, 2010, **81**, 245204.
21 S. Schorr, *Sol. Energy Mater. Sol. Cells*, 2011, **95**, 1482–1488.
22 T. Washio, H. Nozaki, T. Fukano, T. Motohiro, K. Jimbo and H. Katagiri, *J. Appl. Phys.*, 2011, **110**, 074511.
23 B. G. Mendis, M. D. Shannon, M. C. Goodman, J. D. Major, R. Claridge, D. P. Halliday and K. Durose, *Prog. Photovoltaics*, 2012, **22**, 24–34.
24 D. M. Többens, G. Gurieva, S. Levcenko, T. Unold and S. Schorr, *Phys. Status Solidi B*, 2016, **253**, 1890–1897.
25 J. J. S. Scragg, L. Choubrac, A. Lafond, T. Ericson and C. Platzer-Björkman, *Appl. Phys. Lett.*, 2014, **104**, 041911.
26 G. Rey, A. Redinger, J. Sendler, T. P. Weiss, M. Thevenin, M. Guennou, B. E. Adib and S. Siebentritt, *Appl. Phys. Lett.*, 2014, **105**, 112106.
27 A. Ritscher, M. Hoelzel and M. Lerch, *J. Solid State Chem.*, 2016, **238**, 68–73.
28 G. Rey, T. Weiss, J. Sendler, A. Finger, C. Spindler, F. Werner, M. Melchiorre, M. Hála, M. Guennou and S. Siebentritt, *Sol. Energy Mater. Sol. Cells*, 2016, **151**, 131–138.
29 K. Rudisch, Y. Ren, C. Platzer-Björkman and J. Scragg, *Appl. Phys. Lett.*, 2016, **108**, 231902.
30 K. Yu and E. A. Carter, *Chem. Mater.*, 2016, **28**, 864–869.
31 A. Polizzotti, I. L. Repins, R. Noufi, S.-H. Wei and D. B. Mitzi, *Energy Environ. Sci.*, 2013, **6**, 3171.
32 S. Siebentritt, *Nat. Energy*, 2017, **2**, 840–841.
33 K. Sun, C. Yan, F. Liu, J. Huang, F. Zhou, J. A. Stride, M. Green and X. Hao, *Adv. Energy Mater.*, 2016, **6**, 1600046.
34 M. A. Lloyd, D. Bishop, O. Gunawan and B. McCandless, *2016, IEEE 43rd Photovoltaic Specialists Conference (PVSC)*, 2016.
35 P. Zawadzki, A. Zakutayev and S. Lany, *Phys. Rev. B: Condens. Matter Mater. Phys.*, 2015, **92**, 201204.
36 P. Zawadzki, A. Zakutayev and S. Lany, *Phys. Rev. Appl.*, 2015, **3**, 034007.
37 S. P. Ramkumar, A. Miglio, M. J. van Setten, D. Waroquiers, G. Hautier and G.-M. Rignanese, *Phys. Rev. Mater.*, 2018, **2**, 085403.
38 J. J. S. Scragg, J. K. Larsen, M. Kumar, C. Persson, J. Sendler, S. Siebentritt and C. P. Björkman, *Phys. Status Solidi B*, 2015, **253**, 247–254.
39 S. Shang, Y. Wang, G. Lindwall, N. R. Kelly, T. J. Anderson and Z.-K. Liu, *J. Phys. Chem. C*, 2014, **118**, 24884–24889.
40 B. Monserrat, J.-S. Park, S. Kim and A. Walsh, *Appl. Phys. Lett.*, 2018, **112**, 193903.
41 J. J. S. Scragg, J. K. Larsen, M. Kumar, C. Persson, J. Sendler, S. Siebentritt and C. P. Björkman, *Phys. Status Solidi B*, 2015, **253**, 247–254.
42 C. J. Bosson, M. T. Birch, D. P. Halliday, K. S. Knight, A. S. Gibbs and P. D. Hatton, *J. Mater. Chem. A*, 2017, **5**, 16672–16680.
43 O. Tange, *The USENIX Magazine*, 2011, 36, pp. 42–47.
44 K. Momma and F. Izumi, *J. Appl. Crystallogr.*, 2011, **44**, 1272–1276.
45 T. Shibuya, J. M. Skelton, A. J. Jackson, K. Yasuoka, A. Togo, I. Tanaka and A. Walsh, *APL Mater.*, 2016, **4**, 104809.
46 J. D. Gale and A. L. Rohl, *Mol. Simul.*, 2003, **29**, 291–341.
47 M. Quennet, A. Ritscher, M. Lerch and B. Paulus, *J. Solid State Chem.*, 2017, **250**, 140–144.
48 N. Metropolis, A. W. Rosenbluth, M. N. Rosenbluth, A. H. Teller and E. Teller, *J. Chem. Phys.*, 1953, **21**, 1087–1092.
49 M. E. J. Newman and G. T. Barkema, *The Ising Model and the Metropolis Algorithm*, Oxford University Press, 1999.
50 T. Gershon, D. Bishop, P. Antunez, S. Singh, K. W. Brew, Y. S. Lee, O. Gunawan, T. Gokmen, T. Todorov and R. Haight, *Curr. Opin. Green Sustain. Chem.*, 2017, **4**, 29–36.
51 E. I. Parkhomenko, *Piezoelectric and Pyroelectric Effects in Minerals*, Springer US, 1971.
52 K. Rudisch, A. Davydova, C. Platzer-Björkman and J. Scragg, *J. Appl. Phys.*, 2018, **123**, 161558.

4.4 Electronic band tailing in Cu_2ZnSnS_4

Electronic band tailing was introduced in section 2.4.2 and is associated with a high concentration of disorder and inhomogeneity in an absorber layer. It can be caused by either spatial band gap variations or electrostatic potential fluctuations in the material [161] indicated in Fig. 4-6a and 4-6b respectively. In the case of the former, for example, an impurity atom of a different size to the atoms of the host lattice can result in a local mechanical strain, which results in a deformation potential. Local strains can alter the separation of atoms in the crystal and the atomic separation within a crystal has a significant impact on the band structure [72]. Additionally, due to the narrow region of phase stability for Cu_2ZnSnS_4, it is also possible there may be compositional inhomogeneity and secondary phases present [186], which could also produce local band gap fluctuations.

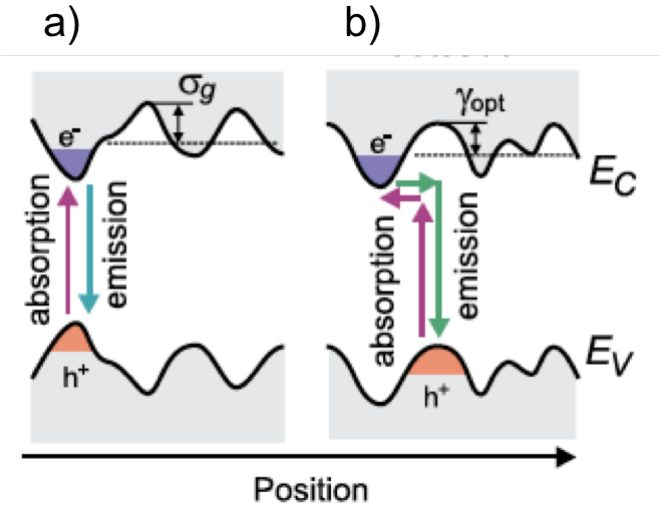

Figure 4-6: Schematic of band gap fluctuations (a) and electrostatic potential fluctuations (b) where the band gap is only maintained in the case of (b). Figure reproduced with permission from Ref. 161.

In the case of electrostatic potential fluctuations, it is the inhomogeneous distribution of ionised defects that cause the fluctuations. An ionised donor exerts an attractive force on conduction electrons and a repulsive force on valence holes. As the defects are distributed randomly, the local interaction varies depending on the crowding of the defects. In this case the energy gap between the valence band and conduction band is maintained, as shown in Fig. 4-6b, and the states of each tail are spatially separated [72]. The broadening of the PL peak measured for Cu_2ZnSnS_4 has been attributed to

spatially fluctuating electrostatic potential in the material [173].

4.4.1 Fluctuations in electrostatic potential from Monte Carlo simulations of Cu/Zn disorder

Disordered lattice configurations generated from the study presented in section 4.3.2 [159] could be used to infer the possible contribution to electronic band tailing in Cu_2ZnSnS_4 from potential fluctuations caused by high concentrations of charged Cu_{Zn}^{-} and Zn_{Cu}^{+} antisite defects. It is worth noting that fluctuations in electrostatic potential are not the only possible contribution to band tailing, as discussed in the previous section, and that our model cannot account for any strain effects on the band gap because it is fixed on-lattice. However, there are differing views in the literature as to whether it is electrostatic potential fluctuations or band gap fluctuations from Cu/ Zn disorder that is the main contribution to the observed band tailing and the performance deficit of Cu_2ZnSnS_4 solar cells, or, if Cu/Zn disorder is the main bottleneck to improving device efficiencies at all [75, 187, 161]. As our model considers only one contribution, we would be able to isolate the possible impact of this specific contribution.

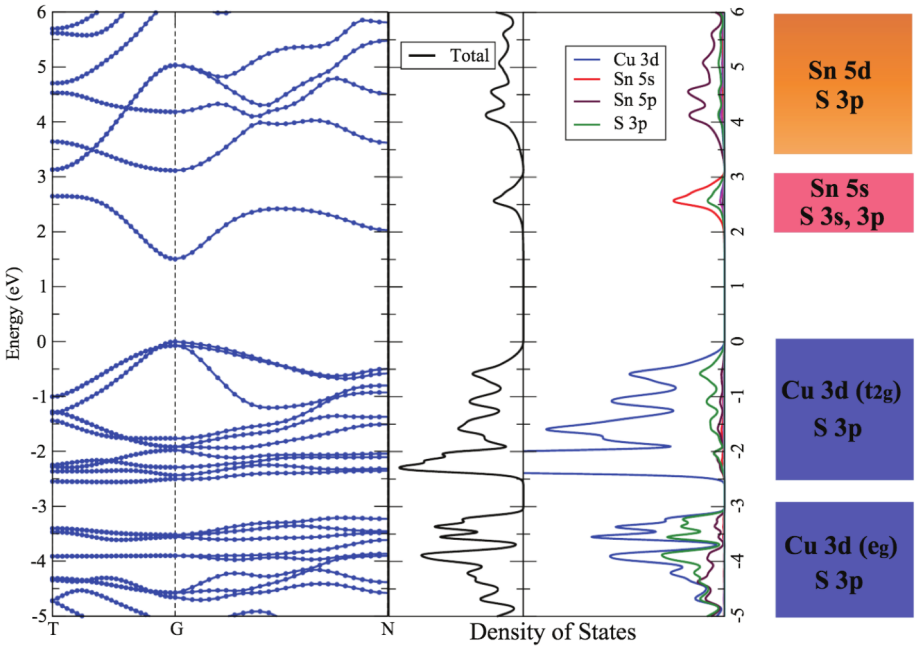

Figure 4-7: Electronic band structure of Cu_2ZnSnS_4 calculated with the HSE06 hybrid-DFT functional, total and partial density of states, and schematic plot of the band components. Figure reproduced with permission from Ref. 67.

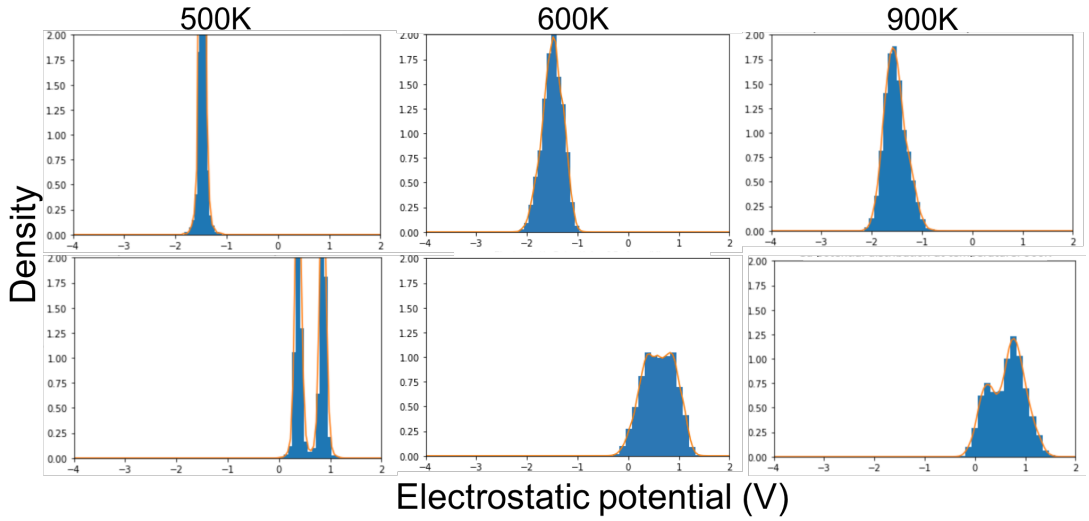

Figure 4-8: Distributions of on-site electrostatic potentials of Sn (top panels) and Cu (bottom panels) with increasing simulation temperature (left to right). The distribution broadens from one delta function for Sn ions at $T = 0\,\mathrm{K}$ (corresponding to one crystallographically distinct Sn site) and broadens from two delta functions for Cu at $T = 0\,\mathrm{K}$ corresponding to the Cu $2a$ and $2c$ sites in Cu_2ZnSnS_4.

To quantify the contribution to electronic band tailing from fluctuations in electrostatic potential caused by $[Cu^{-}_{Zn} + Zn^{+}_{Cu}]$ antisites, the distribution of on-site electrostatic potentials of species in the disordered lattice configurations obtained from our Monte Carlo model could be used to infer perturbations to the band edges compared to the perfect, bulk material. In the study presented in section 4.3.2 [159], we showed that 3D Cu/ Zn disorder was an important mechanism in the Cu/ Zn ODT, we therefore would use configurations generated from our Monte Carlo model with 3D Cu/ Zn disorder. The electronic band structure of Cu_2ZnSnS_4 and composition of the frontier orbitals is shown in Fig. 4-7. The VBM of Cu_2ZnSnS_4 is formed from the hybridisation of Cu-3d and S-3p orbitals, while the CBM is formed from the hybridisation of Sn-5s orbitals with S-3p and 3s [67]. Due to the composition of the frontier orbitals of Cu_2ZnSnS_4, the potential distribution of Cu and Sn ions from our model could be used to infer band tailing of the VBM and CBM respectively from fluctuations in electrostatic potential.

Fig. 4-8 shows the impact of increased Cu/ Zn disorder on the distribution electrostatic potentials of Sn and Cu ions in the disordered lattice configurations obtained from our model. On-site electrostatic potentials are calculated by a summation over pairwise electrostatic interactions in the lattice using the bulk dielectric constant of Cu_2ZnSnS_4 calculated in Ref. [188] to account for screening of the bare formal charges of ions by the

surrounding material. The top panel of Fig. 4-8 shows the change in the distribution of Sn potentials with increased simulation temperature from left to right and the bottom panel shows the same for Cu ions. In the case of Sn, the distribution broadens from a single delta function for the one crystallographically distinct Sn site in perfect kesterite Cu_2ZnSnS_4, while the lower panel for Cu shows the broadening of two delta functions with disorder for the Cu $2a$ and $2c$ sites in Cu_2ZnSnS_4.

Fig. 4-9 shows the on-site electrostatic potentials of Cu and Sn in a (001) Cu-Sn plane minus the average on-site potential for each species within the same plane in our Cu_2ZnSnS_4 lattice model for complete ($S = 0$) equilibrium thermodynamic Cu/Zn disorder at 950K. In Fig. 4-9a, a region with a clustering of Zn^{+}_{Cu} antisites is indicated and Fig. 4-9b shows a corresponding increase in the local electrostatic potential of neighbouring Sn ions in the same plane. This is consistent with observations of clusters of Zn^{+}_{Cu} antisites from scanning transmission electron microscopy with associated band bending from local increases in the electrostatic potential in Ref. 173, implying qualitative agreement between our model and experimental observations.

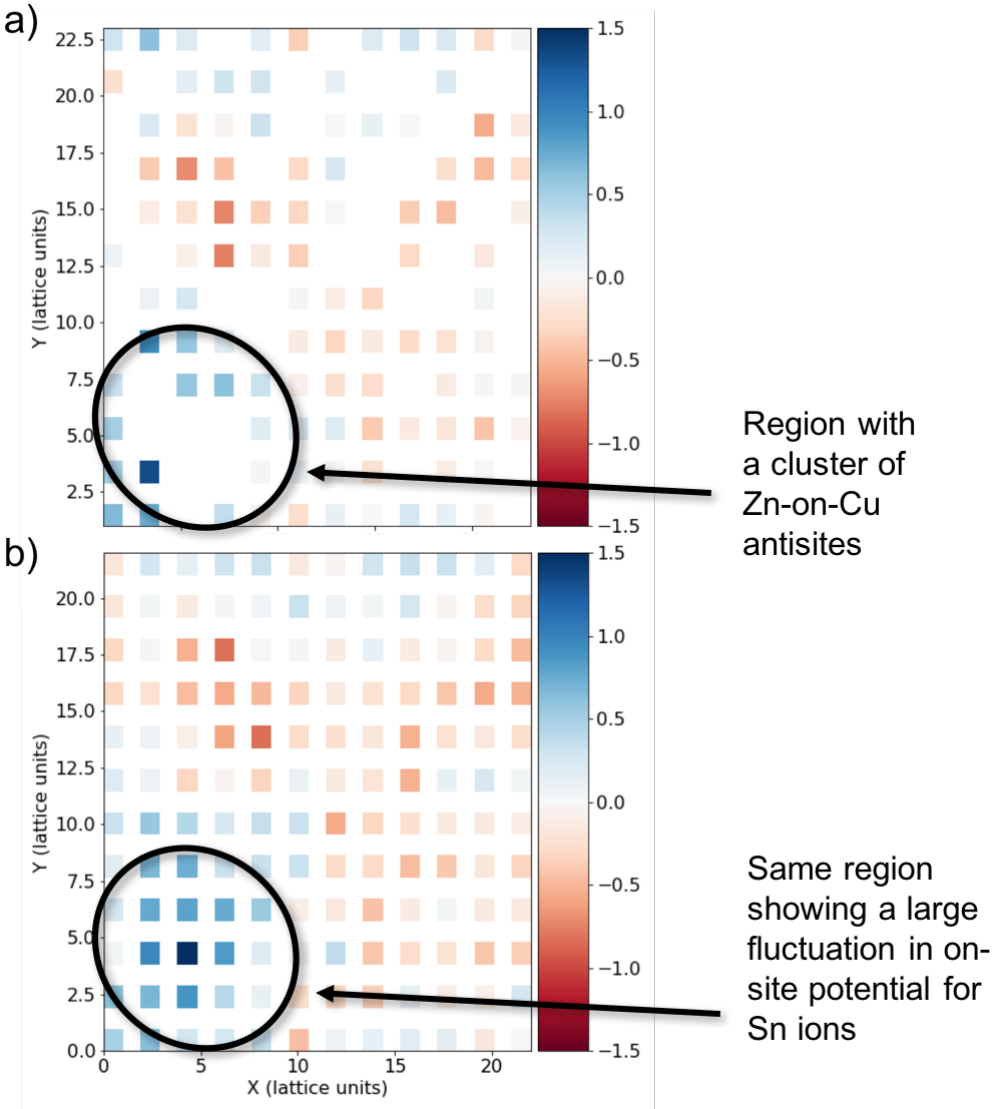

Figure 4-9: 2D histograms showing on-site electrostatic potentials in units of V for Cu (a) and Sn (b) in a (001) Cu-Sn plane minus the average on-site potential for each species within the same plane in our Cu_2ZnSnS_4 lattice model for complete ($S = 0$) equilibrium thermodynamic Cu/ Zn disorder at 950 K. Any deviation from 0 potential demonstrates the spatial fluctuation in electrostatic potential across the plane and empty sites in (a) show where Zn ions have substituted onto Cu 2a sites.

Chapter 5

Screening for candidate photoferroic solar absorbers

In the previous chapter, Cu/Zn disorder in the solar absorber material Cu_2ZnSnS_4 and the contribution of electrostatic potential fluctuations from this type of disorder to the observed electronic band tailing was discussed. The focus of this chapter is searching for alternative solar absorber materials. The motivation of this study was to identify candidate 'photoferroic' or photoactive ferroelectric materials. The mechanisms behind such phenomena (discussed next) are not yet fully understood, however it may be possible to achieve improvements in solar cell performance from enhanced local carrier separation from the internal electric fields of polar crystals, possibly providing new pathways to achieving high-performance devices.

5.1 Observed phenomena in photoactive ferroelectric materials

A ferroelectric material possesses a spontaneous electric polarisation that can be switched between two or more states using an electric field [189]. Many interesting PV phenomena have been observed in ferroelectric (FE) materials such as the bulk photovoltaic effect (BPE) and the anomalous photovoltaic effect (APE) [190]. The BPE was first recorded in 1956 in $BaTiO_3$ [191], where photovoltages were measured in un-doped single crystals [190]. The BPE is distinctly different from the typical PV effect in semiconductor p-n junctions outlined in section 2.2.2 as the driving force for the pho-

tocurrent is provided by the internal electric polarisation of the crystal [192]. The APE was first observed in PbS films in 1946 [193] and has since been reported in polycrystalline CdTe, ZnTe, InP [194, 195, 196], where photovoltages output along the polarisation direction can be significantly larger than the band gap of the material [192], which is usually the limit for a semiconductor PV material [190]. The Shockley-Queisser limit [15], which prevents any single p-n junction solar cell from converting more than 33.7% of the incident light into electricity, has not been predicted to apply for these photovoltaic phenomena. An upper limit for the theoretical power conversion efficiency (PCE) from this PV mechanism seems to still be an open question [197, 198], although an ultimate maximum efficiency of any single-band gap absorber of 44% has been set by thermodynamic considerations [15].

The identification, understanding and utilisation of such phenomena discussed above may open up the possibility of more efficient PV devices constructed from photoactive-ferroelectric, i.e. 'photoferroic', materials. In addition to the above novel PV effects, it has been proposed that the presence of electric polarisation in a PV absorber material may allow for efficient polarisation-driven charge carrier separation [199, 200] and also that ferroelectric materials in solar cells may allow for control over the internal electric fields and carrier injection barriers, which play a central role in the PV mechanism [197]. However, most of the commonly used ferroelectric materials such as $LiNbO_3$ and $BaTiO_3$ have band gaps larger than 3 eV and can therefore only absorb sunlight in the UV range to convert into electricity, which accounts for only around 3.5% of the solar spectrum.

Research efforts have sought to adjust the optical absorption of ferroelectric materials without influencing the ferroelectric properties through chemical doping or alloying [192]. In $Bi_4Ti_3O_{12}$ the optical band gap has been tuned in such a way, resulting in a decrease from 3.6 eV to 2.7 eV [201], although this is still considerably larger than the optimal range for a PV absorber material, as discussed in section 2.3. A recent study has demonstrated a more substantial reduction in the optical band gap of $BaTiO_3$ to 1.66 eV, whilst maintaining 70% of the original polarisation [200], however the PV performance of the modified material was not demonstrated in this study. This then leads on to the second component of this study: to identify new candidate solar absorber materials that may exhibit ferroelectricity and have band gaps within the optimal range for the absorption of sunlight.

5.2 Publication: Candidate photoferroic absorber materials for thin-film solar cells from naturally occurring minerals: enargite, stephanite, and bournonite

The screening criteria used to identify the candidate solar absorber layers enargite (Cu_3AsS_4), stephanite (Ag_5SbS_4) and bournonite ($CuPbSbS_3$) is outlined further in the study presented below, but the basic principles are as follows: by starting from a dataset of naturally occurring minerals, it could be assumed that all candidates are likely to be thermodynamically stable. Secondly, necessary (although not sufficient) conditions are used to screen for candidate photoferroic materials. Materials satisfying these conditions are not guaranteed to be photoferroic, but all photoferroic materials also have these properties. Therefore, the following screening criteria can be used to reduce the search space to materials that are more likely to be photoferroic. A dark streak colour for the mineral implies that the magnitude of the optical band gap may be somewhere within the visible spectrum and therefore within the ideal range for a PV absorber layer. A polar space group is a necessary, but again not sufficient, condition for a material to exhibit ferroelectricity. Even in the absence of switchable ferroelectric states, the internal crystal polarisation may be beneficial for a PV material, as mentioned at the start of this chapter.

In the following study, the optoelectronic properties of the candidate materials are calculated to further assess the likely performance of solar cells made from these absorber materials to determine those worthy of further experimental study. The identification of stable materials with a large polarisation and strong optical absorption could provide more test systems for further experimental investigation and, ideally, the development of control of the novel PV phenomena outlined in the previous section.

 The supplemental material for this paper is included in Appendix A.2.

Statement of Authorship

This declaration concerns the article entitled:									
Candidate photoferroic absorber materials for thin-film solar cells from naturally occurring minerals: enargite, stephanite, and bournonite Pages 107-118 of thesis									
Publication status (tick one)									
draft manuscript		**Submitted**		**In review**		**Accepted**		**Published**	X
Publication details (reference)	Wallace, S., Svane, K., Huhn, W., Zhu, T., Mitzi, D., Blum, V. and Walsh, A. (2017). Candidate photoferroic absorber materials for thin-film solar cells from naturally occurring minerals: enargite, stephanite, and bournonite. *Sustainable Energy & Fuels*, 1(6), pp.1339-1350.								
Candidate's contribution to the paper (detailed, and also given as a percentage).	*Formulation of ideas (50%):* The original idea for the criteria used in this study to screen minerals for candidate photoactive ferroelectrics for photovoltaic (PV) applications (dark streak colour and polar space group) was provided by A. Walsh. The dataset of minerals was also provided by A. Walsh. Ideas for further investigations into the properties of the candidates for PV applications were from myself (S. Wallace) with support when performing the electronic structure calculations with FHI-aims provided by V. Blum, W. P Huhn and T. Zhu. *Design of methodology (50%):* As this study involved a small dataset (<200 minerals) novel screening techniques were not required. After identifying the candidate materials subsequent electronic structure calculations were primarily conducted during a collaboration visit to Duke University with developers of the FHI-aims electronic structure software package. Spin-orbit coupling was incorporated into routines used in this study to calculate the optical dielectric constant by T. Zhu. Before applying this methodology, S. Wallace assisted in testing and benchmarking the modified routines. Otherwise, existing routines in the FHI-aims software package were utilised in this study. *Experimental work (75%):* The screening process was conducted by S. Wallace. Most calculations in the work were performed by S. Wallace, the only exceptions being those of electron localisation functions (presented in the supplemental material) and spontaneous lattice polarisations (presented in the main body of the paper and the supplemental material) which were performed by K. Svane at the University of Bath using the VASP electronic structure software package. The Python script used to obtain fits to the band extrema to compute charge carrier effective masses with band structures in the format outputted by FHI-aims was written by T. Zhu and used with permission. *Presentation of data in journal format (75%):* The first draft of the manuscript was written by S. Wallace. Discussions were provided by all co-authors throughout the study and all helped with proof-reading and preparing the manuscript for submission.								
Statement from Candidate	This paper reports on original research I conducted during the period of my Higher Degree by Research candidature.								
Signed	S. Wallace			**Date**	01.11.18				

Sustainable Energy & Fuels

PAPER

View Article Online
View Journal | View Issue

Cite this: *Sustainable Energy Fuels*, 2017, **1**, 1339

Candidate photoferroic absorber materials for thin-film solar cells from naturally occurring minerals: enargite, stephanite, and bournonite†

Suzanne K. Wallace,[ab] Katrine L. Svane,[a] William P. Huhn,[c] Tong Zhu,[c] David B. Mitzi,[cd] Volker Blum[cd] and Aron Walsh*[be]

To build on the success of other mineral systems employed in solar cells, including kesterites (Cu_2ZnSnS_4) and herzenbergite (SnS), as well as mineral-inspired systems such as lead halide perovskites ($CH_3NH_3PbI_3$), we have searched for photoactive minerals with the additional constraint that a polar crystal structure is adopted. Macroscopic electric fields provide a driving force to separate electrons and holes in semiconductor devices, while spontaneous lattice polarisation in polar semiconductors can facilitate microscopic photo-carrier separation to enhance carrier stability and lifetimes. We identify enargite (Cu_3AsS_4), stephanite (Ag_5SbS_4), and bournonite ($CuPbSbS_3$) as candidate materials and explore their chemical bonding and physical properties using a first-principles quantum mechanical approach.

Received 5th June 2017
Accepted 28th June 2017

DOI: 10.1039/c7se00277g

rsc.li/sustainable-energy

1 Introduction

A key component of the pathway towards terawatt-scale solar power generation is the continued reduction in cost, whilst also improving the performance of solar modules.[1] The search for candidate 'thin-film' photovoltaic (PV) materials that are able to absorb sunlight more strongly than silicon is an active area of research to enable the fabrication of cost-effective and highly-efficient solar cell devices.[2] Common ways to screen for such materials include looking for systems with an optical band gap that is direct and well-matched to the solar spectrum[3] and with an abrupt onset in the absorption spectrum.[4]

Interest in this field has intensified in recent years with the remarkable power conversion efficiencies (PCEs) achieved with lead halide perovskites. PCEs of around 20% (ref. 5 and 6) have been achieved over a much shorter period of development than has been needed for many other PV technologies to achieve the same level of performance.[7] Lead halide perovskites currently out-perform many other materials that also meet the aforementioned screening criteria, such as $Cu_2ZnSn(S,Se)_4$ (ref. 8) and SnS.[9] Of this class of materials, methylammonium lead iodide ($CH_3NH_3PbI_3$ or $MAPbI_3$) particularly stands out for its champion device efficiencies.[6]

The long minority-carrier lifetimes of 280 ns (ref. 10) and diffusion lengths up to 175 microns (ref. 11) demonstrated by $MAPbI_3$-based devices are comparable with the best single-crystal semiconductors,[12] even with low-cost solution processing fabrication methods from which one would usually expect to produce a lower-quality defective material. In contrast, other candidate thin-film PV materials such as $Cu_2ZnSn(S,Se)_4$ (ref. 8) and SnS[9] suffer from short minority carrier lifetimes and diffusion lengths and, ultimately, large open-circuit voltage deficits in photovoltaic devices. The difference in behaviour can be attributed to 'defect tolerance'. Either the formation of detrimental defects are avoided (*e.g.* due to high formation energies) or their effects are minimised (due to their shallow nature within the band gap or to effective dielectric screening). It has also been suggested that the presence of polar domains in $MAPbI_3$ could contribute to the low recombination rate (and hence long carrier lifetimes) due to the enhanced spatial separation of carriers.[13] The presence of macroscopic ferroelectricity in hybrid perovskites remains a matter of research and debate, but there is growing evidence supporting polar domains at room temperature.[14–16]

In this study we consider only naturally occurring minerals, and so one could expect that the materials would not suffer from the same instability issues observed for lead halide perovskites.[17] We start from a small dataset[18] of ~200 known, naturally occurring minerals and aim to identify materials that possess many of the desirable properties for an efficient material for solar energy conversion, using screening criteria discussed in the next section. We then investigate the chemical and physical properties of three candidate systems using a first-

[a]*Department of Chemistry, Centre for Sustainable Chemical Technologies, University of Bath, Claverton Down, Bath, BA2 7AY, UK*
[b]*Department of Materials, Imperial College London, Exhibition Road, London SW7 2AZ, UK. E-mail: a.walsh@imperial.ac.uk*
[c]*Department of Mechanical Engineering and Materials Science, Duke University, Durham, North Carolina 27708, USA*
[d]*Department of Chemistry, Duke University, Durham, North Carolina 27708, USA*
[e]*Global E[3] Institute, Department of Materials Science and Engineering, Yonsei University, Seoul 03722, Korea*

† Electronic supplementary information (ESI) available. See DOI: 10.1039/c7se00277g

principles quantum mechanical approach to assess if these materials are likely to be capable of producing efficient photovoltaic devices.

2 Search for light absorbing polar minerals

2.1 Mineral screening criteria

Our screening criteria is outlined in the Venn diagram shown in Fig. 1 and the rationale behind our screening procedure is outlined below. The candidate materials we identified from a dataset of 193 naturally occurring multi-component minerals[18] are those that could both absorb light within the energy range that makes up the majority of the solar spectrum and possibly exhibit ferroelectricity. The combination of light absorption, semiconductivity, and ferroelectricity in a single material can give rise to novel photoferroic effects.[19]

The most fundamental property to consider for an efficient PV material is an optical band gap that is direct with a magnitude within a range that is well-matched to the solar spectrum. The optimal energy range for the optical band gap of single-junction solar cells is approximately 1.0 to 1.7 eV.[20] The streak colour of a mineral can be indicative of visible light absorption. The streak colour is that of the crushed powder, usually identified by producing a streak across a porcelain tile. While the observed colour of a mineral in massive form can vary considerably between different samples, the colour of the streak remains consistent. A mineral with a dark streak colour implies, but does not guarantee, that it will possess a band gap within the optimal range for the absorption of sunlight. We obtained information on the streak colour of the minerals from ref. 18 and this formed our first screening criterion, reducing the dataset from 193 to 36 minerals.

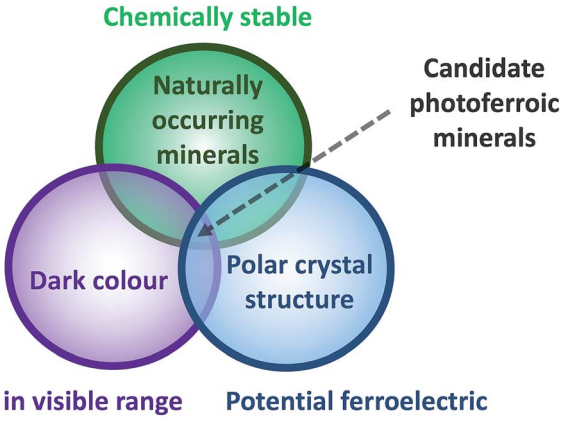

Fig. 1 Venn diagram outlining our screening criteria used to extract candidate photoferroic materials from a sample of 193 naturally occurring minerals, which we could expect to be thermodynamically stable compounds. A mineral with a dark streak colour suggests that it will possess a band gap within the energy range of visible light. Similarly, a polar crystal structure is a necessary, but not sufficient, condition for a material to exhibit ferroelectricity.

Our second screening criterion is the potential to exhibit ferroelectricity. A ferroelectric material is one that exhibits a spontaneous electric dipole moment within the unit cell, and so this is present even without the application of an electric field, but the direction of polarisation can be changed when an external electric field is applied. To identify candidate ferroelectric materials, we screen the space groups of materials to search for those that adopt crystal structures with a polar point group. This screening criterion then limited our dataset from 36 to 4. However, we discounted ZnS from our study because it is known to be a wide band gap semiconductor when prepared in pure form.

A polar point group is a necessary but not sufficient property for a material to exhibit ferroelectricity and so acts as a good starting point for further study of the materials. Desirable effects could be obtained with local polarisation alone, once the correlation length of spontaneous polarisation is sufficient to interact with electron and hole carriers (typically tens of nm). Furthermore, polar structures lack a centre of inversion symmetry and so they are not bound by the same optical selection rules, which could reduce the likelihood of dipole-disallowed transitions[21] and the associated reduction in the strength of the onset of absorption for direct gap materials as outlined by Yu and Zunger in their spectroscopically limited maximum efficiency (SLME) metric.[4]

2.2 Photoferroics for PV devices

Ferroelectric materials typically display large dielectric constants due to low-energy polarisation mechanisms.[22] This can have a number of implications for carrier transport and lifetimes in PV materials, such as a reduction in the electrostatic force between an electron–hole pair (low exciton binding energies), potentially leading to a reduced rate of electron–hole recombination in the material,[23] provided the nuclear subsystem is able to respond on a fast enough time scale. Also, the capture cross-section for charge carriers by a charged defect can be reduced by the charge screening in a dielectric material, possibly allowing for more defect-tolerant carrier transport.[12]

In addition to the desirable properties that could be expected for ferroelectric materials, there are a number of novel phenomena that have been observed in photoactive polar semiconductors that are outlined in ref. 24, which could open up new pathways to highly efficient PV devices. The potential of utilising ferroelectric crystals for solar cells was first highlighted in the work of V. M. Fridkin,[25,26] but the observation of novel photovoltaic phenomena in polar crystals dates back even earlier. The bulk photovoltaic effect (BPE) was first recorded in 1956 in $BaTiO_3$,[27] where photovoltages were measured in un-doped single crystals.[24] The BPE effect is distinct from the typical PV effect in a solar cell where the electric fields that drive photo-carrier separation are typically associated with a 'p–n' or 'p–i–n' junction. In the BPE it is the internal electric fields arising from spontaneous polarisation of the lattice that drive the photocurrent. It is therefore possible for charge-carrier generation and separation to occur simultaneously in the bulk material. It has recently been demonstrated experimentally in ferroelectric single crystals of $BaTiO_3$ that electron–hole recombination is inhibited by the presence of the internal

fields, with recombination being rapidly accelerated after the ferroelectric dipole was switched off.[28]

The anomalous photovoltaic effect (APE) was first observed in PbS films in 1946 (ref. 29) and has since been reported in polycrystalline CdTe, ZnTe and InP,[30–32] where photovoltages output along the polarisation direction can be significantly larger than the band gap of the material,[33] which is usually the upper limit for a semiconductor PV material.[24] The Shockley–Queisser limit,[3] which prevents any single p–n junction solar cell from converting more than one third of the incident light into electricity, can in principle be surpassed by exploiting such phenomena.[34]

Most of the commonly studied ferroelectric materials such as $LiNbO_3$ and $BaTiO_3$ have band gaps larger than 3 eV and can therefore only absorb sunlight in the UV range, which accounts for only around 3.5% of the solar spectrum.[33] The efficiency of PV devices made from these materials is therefore severely limited by the large band gaps. Research efforts have gone into adjusting the optical absorption of ferroelectric materials without influencing the ferroelectric properties of the material through chemical doping or alloying.[33] In $Bi_3Ti_3O_{12}$ the optical band gap has been tuned in such a way, resulting in a decrease from 3.6 eV to 2.7 eV,[35] although this is still considerably larger than the optimal range for a PV absorber material. There are some known ferroelectric materials with band gaps closer to the optimal range. Ferroelectricity in SbSI was studied extensively in the 1960's and has a value of approximately 2 eV for the band gap, which can be tuned by varying the chalcogen and halide.[36] The Curie temperature for the phase transition from a polar to paraelectric phase for this material has been measured to be around room temperature.[37] With typical operating temperatures of solar cell devices approaching 50 °C,[38] it could prove difficult to exploit the ferroelectricity of this material in a working device. As the set of materials we screened are all naturally-occurring minerals with polar structures, they may retain their polar crystal structure under typical operating conditions of a solar cell.

2.3 Candidate minerals

From our screening process, we identified three sulfosalt minerals: enargite (Cu_3AsS_4), stephanite (Ag_5SbS_4), and bournonite ($CuPbSbS_3$), which are shown in Fig. 2. A basic sulfosalt mineral can be defined as a ternary compound $A_xB_yC_z$, which is the case for enargite (Cu_3AsS_4) and stephanite (Ag_5SbS_4). Options for species A include: Cu, Ag, Pb, Sn, Mn, amongst others. Species B can be either: As, Sb or Bi. Options for species C includes: S, Se and Te. It is also possible to form quaternary sulfosalt compounds from isoelectronic substitution of additional transition metals, as in the case of bournonite ($CuPbSbS_3$). The occurrence of these materials in nature under ambient conditions indicates thermodynamic stability.[39] Although these materials are naturally occurring minerals, knowledge of their optoelectronic properties is scarce.

A very recent experimental study assessed the band gaps and photovoltaic response of six sulfide minerals, which included the three sulfosalt minerals we investigate in this study.[40] However, the potential of sulfosalt minerals for PV applications was first highlighted by Dittrich *et al.* in 2007.[39] This work and ref. 41 provide overviews of crystal growth and thin-film deposition methods that have been developed for synthesising sulfosalt layers. There are works in the literature referring to synthetic samples of enargite[42] and stephanite.[43] A recent study on bournonite[44] also details a procedure for synthesising this material.

The possibility of using low temperature thin-film deposition conditions for sulfosalt solar cells has been highlighted.[39] Such an approach could enable the use of a wide variety of substrates or to reduce the interaction with the back contact during deposition, which is believed to be detrimental in Cu_2ZnSnS_4 devices with the Mo back contact reacting with the absorber layer to form MoS_2.[45] However, it is worth noting that the mineral class of 'sulfosalts' contains materials with a diverse range of crystal structures; therefore the extent of the similarity of physical properties of different sulfosalt materials is not clear.

3 Computational details

3.1 Density functional theory

The electronic structure of the three candidate photoferroic materials was calculated using the FHI-aims[46–48] all-electron

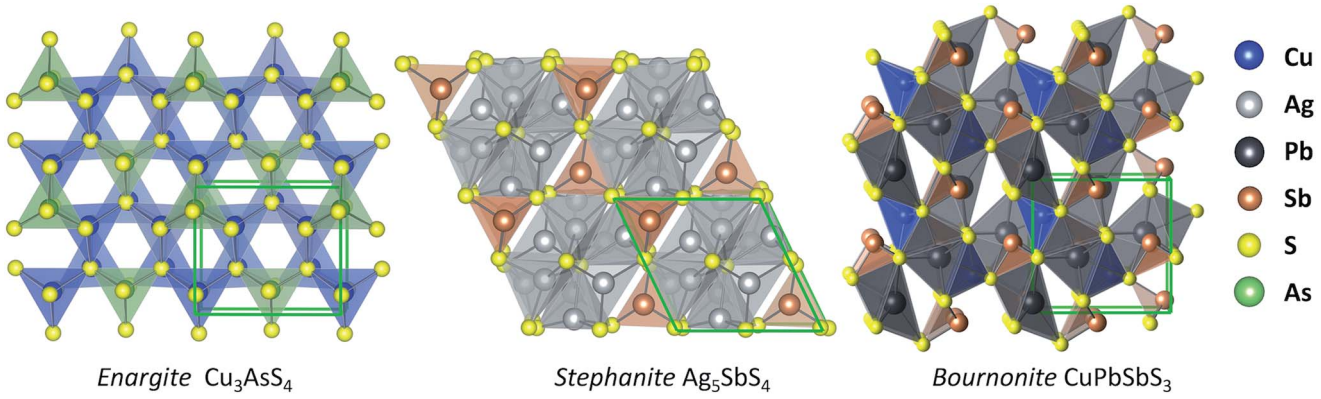

Fig. 2 Illustrations of the crystal structures of candidate solar minerals: enargite (space group $Pmn2_1$), stephanite (space group $Cmc2_1$), and bournonite (space group $Pmn2_1$).

electronic structure code, which is an implementation of density functional theory (DFT) based on numeric atom-centered orbital basis sets with a linear-scaling approach to hybrid functionals.[49,50] We use the short-range screened hybrid exchange–correlation HSE06 functional[51] and spin–orbit coupling (SOC)[52] is included. Hybrid DFT functionals have been found to correct for the underestimation of the optical band gap inherent in the generalized gradient and local density approximations.[53,54]

The FHI-aims default 'tight' numerical settings are used for all calculations, which specifies the basis sets, integration grids, and Hartree potential. Structural optimization was performed with the Broyden–Fletcher–Goldfarb–Shanno algorithm. We fix the lattice parameters of the unit cell to room temperature X-ray diffraction data values from the Inorganic Crystal Structure Database (ICSD)[55] and optimize the internal coordinates with a tolerance of 10^{-3} eV Å^{-1}. A Γ-centred $4 \times 4 \times 4$ k-point grid is used to sample the electronic Brillouin zone for structural optimization, but a more dense k-point grid of $8 \times 8 \times 8$ was required for convergence for band structure calculations. Convergence tests for the calculation settings are given in the ESI.† All visuals of atomic and electronic structure are produced using VESTA.[56]

3.2 Carrier effective masses

To assess the semiconducting potential of these materials, we obtain values for the carrier effective masses (m^*) at the band extrema of the electronic band structures. We use a fitting procedure for the three independent components of the m^* tensor for an orthorhombic crystal structure, shown in eqn (1), where the three components are in three directions parallel to crystallographic directions a, b and c ($\|a$, $\|b$ and $\|c$), respectively.

$$\frac{1}{m^*} = \frac{1}{\hbar^2}\begin{bmatrix} a & 0 & 0 \\ 0 & b & 0 \\ 0 & 0 & c \end{bmatrix} \quad (1)$$

Once the location of the band extrema has been determined from our calculated electronic band structures, we recalculate the band structure over a restricted data range close to the band extrema along the three axes. We then obtain expressions for the three components of m^* at the upper valence and lower conduction bands by numerical parabolic fits to the calculated restricted band structures within a fitting range of $k_0 \pm 0.01$ bohr^{-1}, using eqn (2), where k_0 denotes the location of the band extremum in k-space.

$$E(k) = E_0 + \frac{\hbar^2}{2m^*}(k - k_0)^2 \quad (2)$$

3.3 Optical response function

The linear macroscopic dielectric tensor as a function of photon frequency, $\varepsilon^{ij}(\omega)$, of each material is calculated within the random phase approximation as implemented in FHI-aims, following the derivation in ref. 57. We use this to predict the high-frequency dielectric response of the semiconductor to incident sunlight, *i.e.* the response of the electron density. Inter- and intra-band contributions to the dielectric function are computed, but the former dominate the optical spectra of semiconducting materials. Indirect (phonon assisted) transitions are not accounted for, and generally have weaker intensity, but may make a substantial contribution to the optical properties of materials with strongly indirect band structures.

A k-point grid of $8 \times 8 \times 8$ was required to reach convergence in the calculated dielectric function for bournonite ($CuPbSbS_3$), whereas a more dense k-point grid of $10 \times 10 \times 10$ was required for both enargite (Cu_3AsS_4) and stephanite (Ag_5SbS_4). Data for convergence tests are included in the ESI.†

We obtain the frequency-dependent absorption coefficient in units of cm^{-1} for each material from the real and imaginary components of the dielectric function using eqn (3). The derivation for the units of the absorption coefficient is given in the ESI.†

$$\alpha(\omega) = \frac{4\pi}{hc}\omega\sqrt{\frac{-\mathrm{Re}\varepsilon(\omega) + \sqrt{\mathrm{Re}^2\varepsilon(\omega) + \mathrm{Im}^2\varepsilon(\omega)}}{2}} \quad (3)$$

3.4 Spontaneous polarisation

To investigate the strength of polarity, calculations of the spontaneous electric polarisation, P_s, of each material were performed using the Berry-phase formalism[58] with the methodology outlined in ref. 59. Only differences in polarisation are physically meaningful; we therefore optimise the structure with polarisation $+P_s$ and invert this structure to get the opposite polarisation, $-P_s$. The polarisation difference between those two structures, $2P_s$, is calculated. We verify that the change in polarisation is continuous by considering the polarisation for a number of configurations connecting the two structures, with their coordinates $\mathbf{r}$ obtained from eqn (4), where λ is a number between 0 and 1.

$$\mathbf{r} = \lambda\mathbf{r}_{P_s} + (1 - \lambda)\mathbf{r}_{-P_s} \quad (4)$$

These calculations were performed in VASP[60,61] using the HSE06 functional,[51] projector augmented wave core potentials[62] and a 500 eV plane wave cutoff energy, without including SOC. Sampling of the electronic Brillouin zone using a $2 \times 2 \times 2$ grid of k-points was found to be converged with respect to the calculated polarisation values. Further details of the polarisation calculations are included in the ESI.†

4 Results and discussion

In the following sections we assess the predicted optoelectronic properties of each material in turn. As discussed in the introduction, an effective PV material must absorb light and transport charge. In addition to the band gap and carrier effective masses, we consider the dielectric function, and the associated optical absorption spectra. We finish with an assessment of

spontaneous electric polarisation to determine the strength of the polarity in the materials and the effect on the electronic band structure.

4.1 Enargite (Cu_3AsS_4)

The potential of the sulfosalt mineral enargite (Cu_3AsS_4) for PV applications was suggested by Pauporté and Lincot in 1995.[42] It received little scientific interest until Yu and Zunger's high-throughput study based on their SLME metric, where they calculate a theoretical power conversion efficiency of 25.5% for the material.[4] A recent experimental work has emerged assessing the photovoltaic response of six minerals, including enargite.[40]

The crystallographic unit cell (as shown in Fig. 2) has orthorhombic symmetry with space group $Pmn2_1$ and tetrahedral coordination for all atoms.[63] It has recently been proposed that tetrahedrally bonded multinary semiconductors may be more prone to cation disorder, and the associated extended antisite defect pairs, than lower dimensional multinary compounds.[64] However, compared to materials such as $Cu_2ZnSn(S,Se)_4$ that are known to suffer from mixing of Cu and Zn cations,[65–67] the cations in enargite are more dissimilar in terms of charge and radius. It has been shown that replacing cations with species further apart on the periodic table can reduce this type of disorder.[68–71] We therefore expect cation disorder to be reduced in this compound, as has been found to be the case when substituting Cu with Ag[70] or Zn with Ba[68,69] in $Cu_2ZnSn(S,Se)_4$.

Enargite is a mineral semiconductor of type $A^{I}_3B^{V}C^{II}_4$. Natural samples of enargite are frequently found as an impurity in copper ores.[72] Natural samples have been found to exhibit the electrical properties of a p-type doped semiconductor with a conductivity of 0.0014 S m^{-1} (from the stated value of approximately 7 Ω cm for the resistivity at 295 K).[42] The main impurities in natural enargite are Sb and Fe, but Pb and Ag are also known to be present.[72] In a recent study on natural sulfide minerals,[40] the authors detected <1% of Sb impurities in the natural samples of enargite, which show a clear p-type photoconductivity. The p-type response could either be due to intrinsic acceptor defects or due to defects introduced by the Sb impurities. In 1995, Pauporté and Lincot measured two optical transitions in enargite: an indirect one at 1.19 eV and a direct one at 1.44 eV. However more recent studies have reported values of 1.28 eV (ref. 41) and 1.36 eV (ref. 40) for a direct band gap, with some photocurrent due to band tailing further in the IR region for the latter, which the authors attribute to lattice disorder or impurity states in the band gap. G_0W_0 calculations based on wavefunctions generated from the hybrid functional HSE06 (ref. 51) predicted a value of 1.32 eV for the band gap.[73] Although a number of different values have been reported for the band gap of enargite, all values fit within the optimal range for a solar absorber material.[20]

4.1.1 Enargite: electronic structure. The chemical formula Cu_3AsS_4 suggests the presence of closed-shell Cu(I) and As(V) ions. It has been proposed that a number of the beneficial properties of lead halide perovskites are linked to the presence of lone pairs of electrons and that other materials with post-transition metals with an ns^2 electronic configuration may also exhibit similar properties.[21] While As(III) has a $4s^2$ electronic configuration, for As(V) as present here, the s orbitals are formally empty. We have further confirmed the charge state as As(V) using electron localisation functions (ELFs)[75] calculated with VASP; however, we note the complications of assigning oxidation states from first principles.[76] The ELF gives the probability of finding an electron near a reference electron, and thus highlights the presence of bonds and lone pairs; further details are given in the ESI.†

For enargite, we predict a direct band gap at the Γ point with a magnitude of 1.24 eV, which is close to the reported G_0W_0@HSE06 value of 1.32 eV.[73] The calculated band structure is shown in Fig. 3a. The conduction band minimum (CBM) is dispersive, indicating the potential for high carrier mobility at the band edge. This is confirmed by the estimates for the minority carrier effective masses of electrons in the conduction band, m_c, presented in Table 1, which also indicates that the effective masses from $\Gamma \rightarrow X, Y, Z$ are almost isotropic. However, the estimated values for effective masses in Table 1 indicate that holes are heavier along the $\Gamma \rightarrow Y, Z$ directions in enargite.

It has been suggested for other semiconducting materials that the defect-tolerance of optoelectronic properties, to a certain extent, can be associated with an electronic structure where the VBM possesses predominantly antibonding character.[12,77,78] $CuInSe_2$ is an example of another thin-film PV technology that is defect tolerant with shallow defects[78] and benign grain boundaries.[79,80] The electronic density of states (DOS) at the top of the valence band in enargite, which is shown in Fig. 4, shares some common features with that of $CuInSe_2$. In the case of $CuInSe_2$ the upper valence bands consist of the hybridized Cu d-states and Se p-states, whereas for enargite it is instead S p-states hybridized with Cu d-states. The p–d repulsion is large in $CuInSe_2$ and appears to be even larger in enargite. In $CuInSe_2$, the p–d repulsion gap separates the bonding p–d states below and the antibonding p–d states above, yielding antibonding states for the upper valence bands.

To assess further if enargite possesses an upper valence band with antibonding character we visualize the electron

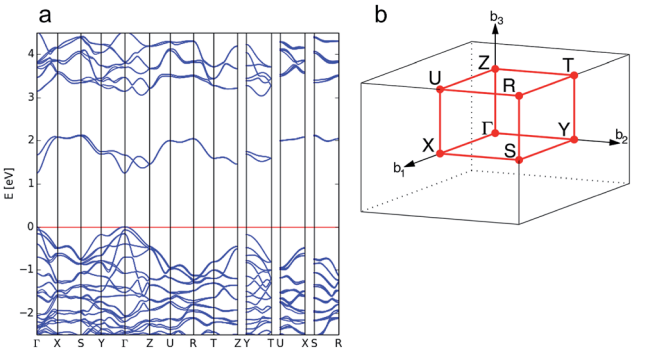

Fig. 3 Calculated electronic band structure of enargite (Cu_3AsS_4) (a) and the reciprocal space k-path for the structure determined by the Aflow-online utility[74] (b).

Table 1 Effective masses of electrons at the conduction band minimum, m_c, and holes at the valence band maximum, m_h, of enargite (Cu_3AsS_4), stephanite (Ag_5SbS_4) and bournonite ($CuPbSbS_3$) in units of the free electron mass m_e, determined by parabolic fits to the calculated band structures at the band extrema. The optical dielectric constants, ε_∞, calculated within the random phase approximation are also reported

Enargite (Cu_3AsS_4)					Stephanite (Ag_5SbS_4)					Bournonite ($CuPbSbS_3$)				
Direction	m_e	m_h	ε		Direction	m_e	m_h	ε		Direction	m_e	m_h	ε	
$\|a$	0.20	0.22	${\varepsilon_\infty}^{xx}$	5.70	$\|a$	0.37	0.60	${\varepsilon_\infty}^{xx}$	6.01	$\|a$	0.52	0.99	${\varepsilon_\infty}^{xx}$	7.16
$\|b$	0.23	1.20	${\varepsilon_\infty}^{yy}$	5.89	$\|b$	0.40	1.94	${\varepsilon_\infty}^{yy}$	5.86	$\|b$	0.37	0.97	${\varepsilon_\infty}^{yy}$	7.24
$\|c$	0.22	1.35	${\varepsilon_\infty}^{zz}$	5.91	$\|c$	0.26	0.77	${\varepsilon_\infty}^{zz}$	5.83	$\|c$	0.50	0.86	${\varepsilon_\infty}^{zz}$	7.55

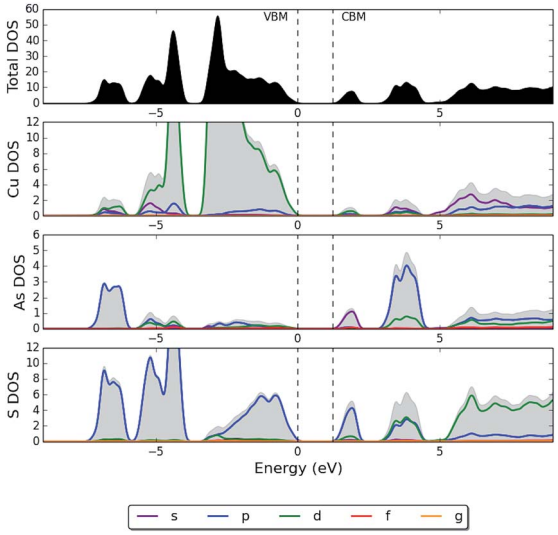

Fig. 4 HSE06 + SOC partial electronic density of states (pDOS) of enargite (Cu_3AsS_4), where the top of the valence band has been set to 0 eV.

wavefunction of the highest occupied state, as is shown in Fig. 5a. From this, the opposite parity of neighbouring S p-orbitals and Cu d-orbitals indicates antibonding character at the valence band maximum, which could suggest that acceptor defects are more likely to produce shallow defect levels with respect to the band edges. Enargite may therefore have defect-tolerant optoelectronic properties, which has been suggested in some recent studies. Firstly, the photocurrent conversion efficiency of a natural enargite sample was found to be greater than that of a natural kesterite sample.[40] Secondly, the photocurrent density measured for enargite nanocrystals had a 10-fold improvement to that of Cu_3SbS_4 nanocrystals,[81] both of which could be expected to possess highly-defective nanocrystalline structures.

4.1.2 Enargite: optical properties. The optical properties of enargite are anisotropic, with the *xx*, *yy* and *zz* components of the optical dielectric tensor, $\varepsilon^{ij}(\omega)$, differing considerably, as shown in Fig. 6. We predict values of just under 6 for the static limit ($\omega \rightarrow 0$) of the optical dielectric constants ${\varepsilon_\infty}^{ij}$ (given in Table 1), obtained from the *y*-intercept of the real components of $\varepsilon^{ij}(\omega)$. This is very similar to values of ${\varepsilon_\infty}^{ij}$ calculated for the perovskite $MAPbI_3$ of approximately 5.6 to 6.5.[83]

In Fig. 7 we plot the isotropic average of the optical absorption coefficient, $\alpha(\omega)$, of enargite, with comparison to GaAs and $MAPbI_3$, as known strong PV absorber materials, and crystalline Si (c-Si) as a material that is known to have weak absorption. Enargite has a comparable strength of absorption to the strong absorber materials GaAs and $MAPbI_3$, and considerably stronger than c-Si, within the region for the onset of absorption (incident photon energy of approximately $\omega = 1$–3 eV).

4.2 Stephanite (Ag_5SbS_4)

The unit cell of the second candidate, stephanite (Ag_5SbS_4), also has an orthorhombic crystal structure but with space group $Cmc2_1$ (Fig. 2). The chemical formula suggests formal

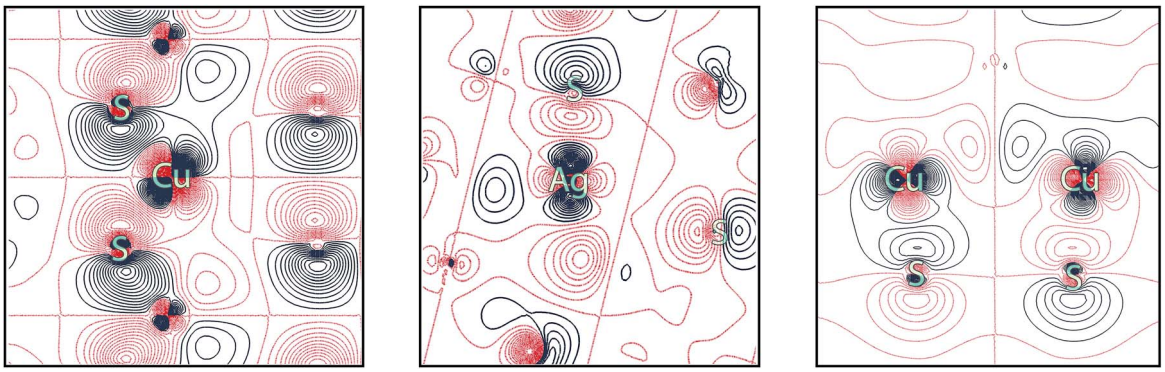

Fig. 5 The real component of the electron wavefunction of the highest occupied state in (left panel) enargite (Cu_3AsS_4), (centre panel) stephanite (Ag_5SbS_4) and (right panel) bournonite ($CuPbSbS_3$), showing sulfur p-orbitals and copper d-orbital in enargite and bournonite and silver d-orbitals in stephanite. The difference in colour indicates the different parity of the wavefunctions and the position of the ions are indicated on the plot.

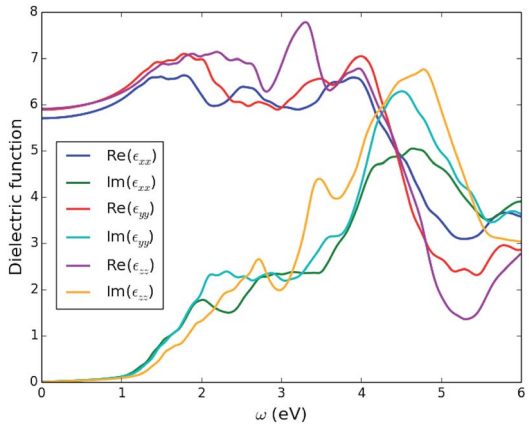

Fig. 6 Three independent components of the calculated optical dielectric tensor, $\varepsilon(\omega)$, as a function of incident photon energy, ω, for enargite (Cu_3AsS_4).

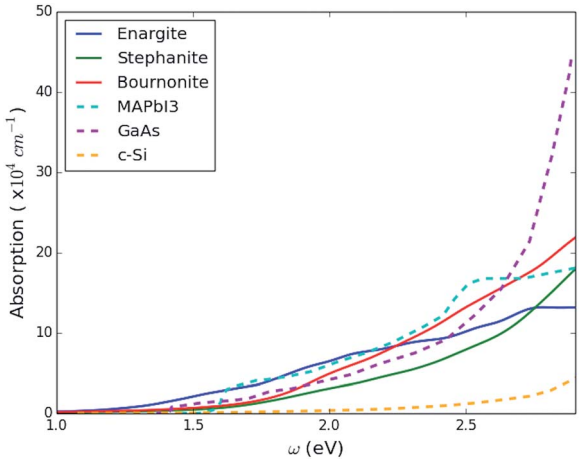

Fig. 7 Isotropic average of the optical absorption coefficient for three sulfosalt materials enargite (Cu_3AsS_4), stephanite (Ag_5SbS_4) and bournonite ($CuPbSbS_3$) plotted in comparison to the same parameter for other important photovoltaic materials over the onset energy range (1–3 eV). The comparison photovoltaic materials include: the strong direct-gap absorber material GaAs, the weaker indirect-gap absorber crystalline-Si and the hybrid perovskite $MAPbI_3$, where data for these latter compounds was taken from ref. 82.

oxidations states of Ag(I) and Sb(III), which are associated with $4d^{10}$ and $5s^2$ valence electronic configurations. The structure consists of SbS_3 trigonal pyramids layered along the *c*-axis that are connected with Ag atoms that form triangular and near tetrahedral structures with S atoms.[40] As was discussed for enargite, the components in stephanite are dissimilar in terms of charge and size, so it could be expected that cation disorder will not be prevalent in this compound.

There is limited literature on the optical or electrical properties of stephanite apart from a work in 1973 (ref. 43) showing the electrical resistivity of a synthetic sample of stephanite as a function of temperature. They report a resistivity of approximately 9 Ω cm at 110 °C, which corresponds to a conductivity of 0.0011 S m^{-1}. It has been reported that stephanite has a band gap of 1.62 eV (ref. 41) and a recent study on a natural sample of stephanite has measured a band gap of 1.67 eV and p-type conductivity.[40] Chemical analysis indicated that there was no detectable level of impurities present.[40] This could suggest that the p-type conductivity of the crystal is due to the presence of acceptor intrinsic defects in stephanite (*e.g.* V_{Ag}^-). The work[40] also comments on the possibility of high Ag ion conductivity. Ion transport has been suggested as a cause of current–voltage hysteresis in lead halide perovskites;[84] but it can also contribute to 'self-healing' of detrimental extended defects as ions can redistribute over time.

There has been some speculation in the literature on the possibility of ferroelectric behaviour in stephanite due to the presence of polar phases at low temperatures in pyrargyrite (Ag_3SbS_3), proustite (Ag_3AsS_3), and stibnite (Sb_2S_3), which are crystallochemically related to stephanite.[85] The same study notes that similar displacive structural changes occur in stephanite to those in proustite and pyrargyrite that are responsible for the ferroelectric properties.

4.2.1 Stephanite: electronic structure. For stephanite, we predict a direct band gap of 1.59 eV at the Γ point of the Brillouin zone, which is in good agreement with the literature experimental values.[40,41] Similar to enargite, Fig. 8a shows that the dispersion of the lower conduction band is greater than the upper valence band; this is reflected in the effective masses calculated for electrons and holes, shown in Table 1. The electronic pDOS of stephanite (Fig. 9) indicates that the valence band is mainly composed of hybridized Ag d-states and S p-states, while contributions from Sb s-states only appear at higher binding energy. In Fig. 5b we visualize the electron wavefunction of the highest occupied state in stephanite, which again displays anti-bonding character between the Ag d and neighbouring S p.

4.2.2 Stephanite: optical properties. The optical properties of stephanite, as shown in Fig. 10, are more isotropic than those of enargite. This could be due to the crystal structure of enargite more closely resembling stacked two-dimensional planes than that of stephanite. The value of the optical dielectric constant for stephanite is similar to enargite, at just under 6 (Table 1). The strength in the onset of absorption predicted for stephanite

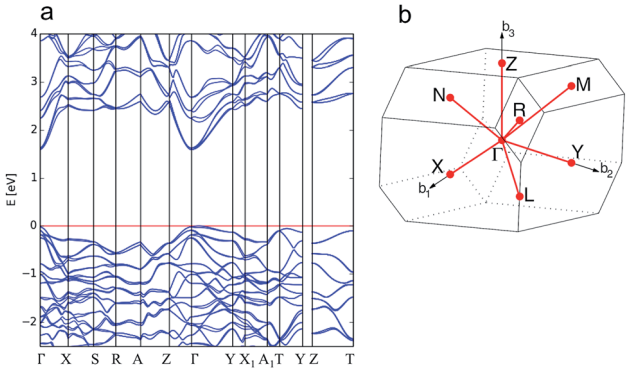

Fig. 8 Calculated electronic band structure of stephanite (Ag_5SbS_4) (a) and the reciprocal space *k*-path for the structure determined by the Aflow-online utility[74] (b).

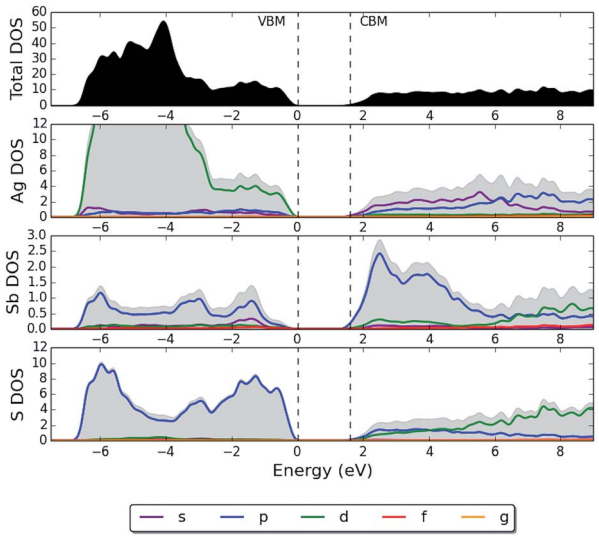

Fig. 9 HSE06 + SOC partial electronic density of states (pDOS) of stephanite (Ag_5SbS_4), where the top of the valence band has been set to 0 eV.

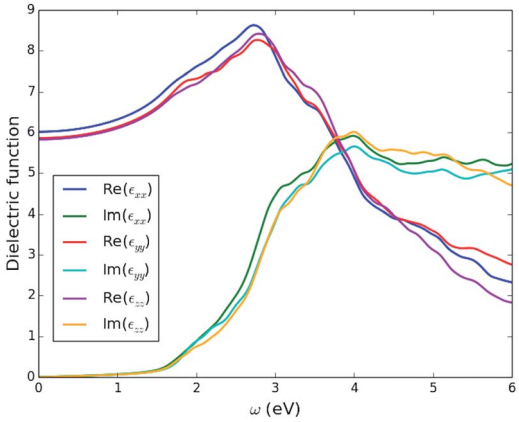

Fig. 10 Three components of the calculated dielectric function, $\varepsilon(\omega)$, as a function of incident photon energy, ω, for stephanite (Ag_5SbS_4).

shown in Fig. 7 is less than that of the high-performance absorbers GaAs and $MAPbI_3$, but still considerably stronger than that of crystalline Si.

4.3 Bournonite ($CuPbSbS_3$)

Bournonite ($CuPbSbS_3$) again adopts an orthorhombic crystal structure and the same space group as enargite, $Pmn2_1$. The unit cell of bournonite is shown in Fig. 2. The structure is derived from stibnite (Sb_2S_3), where Pb(II) atoms alternatively occupy the Sb(III) sites and Cu(I) atoms form tetrahedra to compensate for the charge.[40]

Measured values of 1.23 eV (ref. 41) and 1.31 eV (ref. 86) have been reported for the band gap, which are both within the optimal range for a solar absorber material. Recently, this material has received increasing scientific interest for thermoelectric and rewriteable data storage applications due to a low thermal conductivity, which has been attributed to the distorted environments of the Pb(II) and Sb(III) atoms from the stereochemically active lone-pair s^2 electrons.[44] Consequently, works on the synthesis of bournonite are beginning to emerge.[86] A study of two natural samples of bournonite[40] reported n-type conductivity, a direct gap of 1.29 eV, and an indirect band gap of 1.17 eV in one sample, and the same direct band gap and a lower indirect band gap of 1.01 eV in another.

4.3.1 Bournonite: electronic structure. For bournonite, we predict an indirect band gap in the Γ–Y direction with a magnitude of 1.37 eV and the smallest direct gap is predicted to be only slightly larger at 1.41 eV. The indirect gap is in quite good agreement with experimental values.[41,86] The conduction band minimum features a spin splitting due to SOC, which can be seen from comparing the plots of results before and after the inclusion of SOC along the Γ–Y, shown in Fig. 11a. The effective masses at the conduction band of bournonite (Table 1) are not as light or isotropic as in enargite; however, both the hole and electron masses remain below 1 m_e.

The upper valence band of bournonite is formed primarily of hybridized Cu d-states and S p-states (Fig. 12), although there does not appear to be a pronounced p–d repulsion as was shown in the pDOS plot for enargite. Contributions from Sb and Pb s-states at the VBM appear to be minor. In Fig. 5c we visualize the electron wavefunction of the highest occupied state in bournonite to determine the bonding characteristics. As for the previous two materials, the opposite parity of the electron wavefunctions for the anion and cation show antibonding character, which could support defect tolerance.

4.3.2 Bournonite: optical properties. The optical properties of the final candidate absorber material (Fig. 13) are more anisotropic than stephanite but less than enargite. The optical dielectric constant (7.1–7.6) of bournonite is larger than that of enargite and stephanite (5.7–6.0). The larger value could be due to the presence of the Pb ion in bournonite, which is larger and more polarisable than the cations in enargite and stephanite. Again bournonite has a comparable onset of absorption to that of established PV absorber materials (see Fig. 7).

4.4 Polarisation and Rashba splitting

The results presented above have shown the three candidate materials have electronic and optical properties suitable for

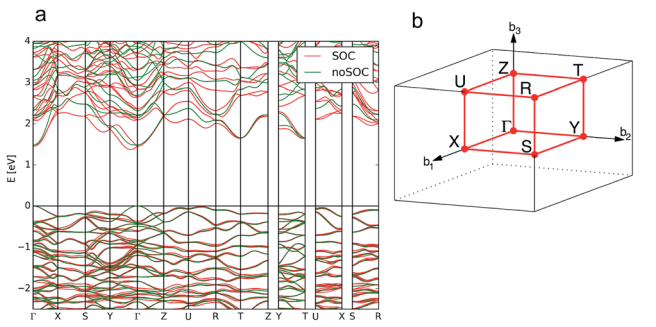

Fig. 11 Calculated band structure of bournonite ($CuPbSbS_3$) showing the result without the inclusion of spin–orbit coupling (SOC) in green and the calculation including SOC in red (a) and the reciprocal space k-path for the structure determined by the Aflow-online utility[74] (b).

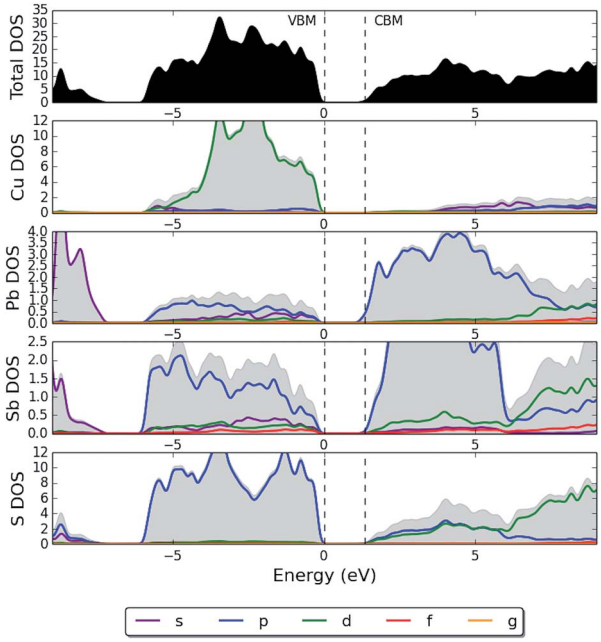

Fig. 12 HSE06 + SOC partial electronic density of states (pDOS) of bournonite ($CuPbSbS_3$), where the top of the valence band has been set to 0 eV.

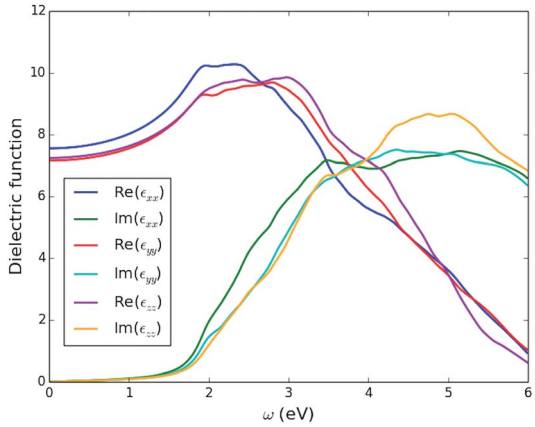

Fig. 13 Three components of the calculated dielectric function, $\varepsilon(\omega)$, as a function of incident photon energy, ω, for bournonite ($CuPbSbS_3$).

solar energy harvesting. An additional criterion for our search is that the materials adopt a polar space group.

4.4.1 Lattice polarisation. We have quantified the strength of polarity within the modern theory of polarisation. Spontaneous polarisations of 67.8, 31.9 and 1.83 μC cm^{-2} are found in enargite, stephanite and bournonite, respectively (see Fig. 14). Table 2 also shows the values of spontaneous polarisation calculated for the materials in this study, along with measured and some calculated values for known ferroelectric materials. Whether a material will exhibit the ferroelectric–photovoltaic phenomena outlined in Section 2.2 is dependent upon a large number of factors, which are discussed in ref. 87. One parameter however is the magnitude of the polarisation[88] and we show here that the calculated spontaneous polarisation for both enargite and stephanite is high and comparable to those of standard ferroelectric materials $BaTiO_3$ and $PbTiO_3$.

It is worth noting that for the materials in this study the switching from one polarisation to the other requires a significant rearrangement of the atoms. We estimate the switching barrier from the energy change along the paths used to calculate the spontaneous lattice polarisation, but note that this estimate is an upper limit for the switching barrier as the intermediate structures have not been relaxed to their minimum energy configuration (further details included in the ESI†). We estimate the upper limit for the switching barrier to be 19.7, 12.5 and 21.8 eV per unit cell for enargite, stephanite and bournonite; which are orders of magnitude larger than barriers calculated for $BaTiO_3$.[89] Thus, the direction of polarisation of the materials is unlikely to be easy to switch, making them unsuitable for switchable memory applications. However, the local electric fields could still be beneficial for enhanced charge separation in solar energy applications.

4.4.2 Relativistic Rashba splitting. The presence of macroscopic polarisation may have a direct effect on the transport and collection of photogenerated charge carriers in the direction of the associated internal electric field. There is an additional effect on the electronic structure: the combination of heavy elements with non-centrosymmetric crystal structures leads to a relativistic spin-splitting of the bands. For cases where the orbital components of the valence and conduction bands are different, the so-called Rashba/Dresselhaus splitting can turn a direct band material indirect. This was shown to be the case for bournonite in Fig. 11. This effect has been associated with slow electron–hole recombination in lead halide perovskites.[93–95]

The spin–orbit interaction varies with the square of the atomic mass, yielding an expected splitting size ordering of Pb ≫ Sb > As; however, this is also influenced by the local electric field around the metal centre. From our calculations, we predict

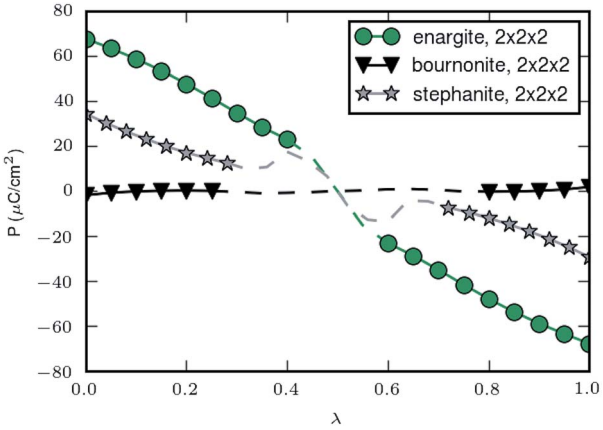

Fig. 14 Spontaneous polarisation along a path connecting the structures with $+P_s$ and $-P_s$ for enargite (Cu_3AsS_4), stephanite (Ag_5SbS_4) and bournonite ($CuPbSbS_3$). The markers indicate points calculated with 2 × 2 × 2 k-points and the dashed line is the path obtained using 1 × 1 × 1 k-points. The curves are set to pass through 0 for $\lambda = 0.5$. See ESI† for further details.

Table 2 Calculated spontaneous polarisation for enargite (Cu_3AsS_4), stephanite (Ag_5SbS_4) and bournonite ($CuPbSbS_3$) compared to values of known ferroelectric crystals

	Method	Ref.	P_s ($\mu C\ cm^{-2}$)
Enargite	DFT (HSE06)	This work	67.8
Stephanite	DFT (HSE06)	This work	31.9
Bournonite	DFT (HSE06)	This work	1.83
$BaTiO_3$	DFT (HSE06)	90	40.7
$BaTiO_3$	Expt.	91	26
$PbTiO_3$	DFT (LDA)	92	88
$PbTiO_3$	Expt.	91	57
SbSI	Expt.	91	25

that only bournonite will exhibit Rashba splitting, despite the considerably weaker spontaneous polarisation we predict for this material. Bournonite is the only one of the three material that contains Pb, which suggests that the atomic mass of the heavy element is the more dominant factor than the strength of spontaneous polarisation for the Rashba effect. The splitting needs to be sufficient so that for a given temperature and light intensity that the Rashba pockets are partially filled; above this threshold direct band gap behaviour is recovered. For bournonite, we measure an energy difference in the CBM between direct and indirect recombination of approximately 80 meV, whereas k_BT at typical solar cell operating temperature of 50 °C is 28 meV, indicating that this indirect behaviour should play a role in an operating solar cell.

5 Conclusions and outlook

We have used a first-principles quantum mechanical approach to assess the optoelectronic properties of the three candidate photoferroic materials: enargite (Cu_3AsS_4), stephanite (Ag_5SbS_4) and bournonite ($CuPbSbS_3$). We predicted a direct band gap of 1.24 eV, a direct band gap of 1.59 eV and a slightly indirect band gap of 1.37 eV for enargite, stephanite and bournonite respectively, within the optimal range for a single junction solar cell. We also observe similar features (spin–orbit splitting) in the band structure of bournonite to those associated with the high-performance of hybrid perovskites.[93] We predict low electron effective masses for all three materials and heavier holes (see Table 1). We also predict optical dielectric constants, ε_∞, again comparable to hybrid perovskites.[83]

We have calculated the spontaneous polarisation density for all three materials and from this we predict that enargite and stephanite will have considerable spontaneous polarisations, comparable to that of standard ferroelectric materials $BaTiO_3$ and $PbTiO_3$. This could suggest that it may be possible to combine a near-optimal band gap (for AM1.5 solar radiation) with ferroelectric–photovoltaic phenomena such as the bulk photovoltaic effect or anomalous photovoltaic effect within these materials. With the upper limit for the power conversion efficiency from these novel PV phenomena still being an open question, these materials could allow for new routes to high efficiency devices.

Our study has shown that the three minerals merit deeper investigation. In addition to further experimental work on synthesis, characterisation and optimisation, the extension of theoretical investigations to include analysis of the defect tolerance of the bulk (beyond the speculation made in this study based on the bonding character of the VBM), and identifying compatible interfaces for high-efficiency devices could help to accelerate the development of these new technologies.

Data access statement

The optimised crystal structures of the three minerals studied are available at https://github.com/wmd-group/crystal_structures. The input and output files for the DFT calculations are available from the online repository NOMAD at http://dx.doi.org/10.17172/nomad/2017.05.16-1.

Acknowledgements

This work has been supported by the EPSRC grant no. EP/L016354/1 and EP/K016288/1 (SKW) and by the ERC programme grant no. 277757 (KLS). Part of this work was also supported by the National Science Foundation under Grant No. 1511737 (WPH, TZ, DBM, VB). AW is supported by a Royal Society University Research Fellowship. This work benefited from access to ARCHER, the UK's national high-performance computing service, which is funded by the Office of Science and Technology through EPSRC's High End Computing Programme (Grant no. EP/L000202). We also acknowledge use of Hartree Centre resources in this work through the Energy Materials: Computational Solutions EPSRC project (EP/K016288/1). In particular the author's would like to acknowledge the computational support of Alin Marin Elena. We thank Jarvist M. Frost and Keith T. Butler for fruitful discussions, and Mark Weller, Oliver Weber and Chris Bowen for support and discussions during early stages of the project.

References

1 N. M. Haegel, R. Margolis, T. Buonassisi, D. Feldman, A. Froitzheim, R. Garabedian, M. Green, S. Glunz, H.-M. Henning, B. Holder, I. Kaizuka, B. Kroposki, K. Matsubara, S. Niki, K. Sakurai, R. A. Schindler, W. Tumas, E. R. Weber, G. Wilson, M. Woodhouse and S. Kurtz, *Science*, 2017, **356**, 141–143.
2 A. Polman, M. Knight, E. C. Garnett, B. Ehrler and W. C. Sinke, *Science*, 2016, **352**, aad4424.
3 W. Shockley and H. J. Queisser, *J. Appl. Phys.*, 1961, **32**, 510.
4 L. Yu and A. Zunger, *Phys. Rev. Lett.*, 2012, **108**, 068701.
5 S. S. Shin, E. J. Yeom, W. S. Yang, S. Hur, M. G. Kim, J. Im, J. Seo, J. H. Noh and S. I. Seok, *Science*, 2017, **356**, 167–171.
6 M. A. Green, A. Ho-Baillie and H. J. Snaith, *Nat. Photonics*, 2014, **8**, 506–514.
7 S. K. Wallace, D. B. Mitzi and A. Walsh, *ACS Energy Lett.*, 2017, **2**, 776–779.
8 I. L. Repins, H. Moutinho, S. G. Choi, A. Kanevce, D. Kuciauskas, P. Dippo, C. L. Beall, J. Carapella,

C. DeHart, B. Huang and S. H. Wei, *J. Appl. Phys.*, 2013, **114**, 084507.
9 N. M. Mangan, R. E. Brandt, V. Steinmann, R. Jaramillo, J. V. Li, J. R. Poindexter, K. Hartman, L. Sun, R. G. Gordon and T. Buonassisi, *2014 IEEE 40th Photovoltaic Specialist Conference (PVSC)*, 2014.
10 S. D. Stranks, G. E. Eperon, G. Grancini, C. Menelaou, M. J. P. Alcocer, T. Leijtens, L. M. Herz, A. Petrozza and H. J. Snaith, *Science*, 2013, **342**, 341–344.
11 Q. Dong, Y. Fang, Y. Shao, P. Mulligan, J. Qiu, L. Cao and J. Huang, *Science*, 2015, **347**, 967–970.
12 R. E. Brandt, V. Stevanović, D. S. Ginley and T. Buonassisi, *MRS Commun.*, 2015, **5**, 265–275.
13 J. M. Frost, K. T. Butler, F. Brivio, C. H. Hendon, M. van Schilfgaarde and A. Walsh, *Nano Lett.*, 2014, **14**, 2584–2590.
14 H. Guo, P. Liu, S. Zheng, S. Zeng, N. Liu and S. Hong, *Curr. Appl. Phys.*, 2016, **16**, 1603–1606.
15 P. Wang, J. Zhao, L. Wei, Q. Zhu, S. Xie, J. Liu, X. Meng and J. Li, *Nanoscale*, 2017, **9**, 3806–3817.
16 Y. Rakita, O. Bar-Elli, E. Meirzadeh, H. Kaslasi, Y. Peleg, G. Hodes, I. Lubomirsky, D. Oron, D. Ehre and D. Cahen, *Proc. Natl. Acad. Sci. U. S. A.*, 2017, 201702429.
17 E. I. Parkhomenko, *Piezoelectric and Pyroelectric Effects in Minerals*, Springer, US, 1971.
18 R. L. Bonewitz, *Rocks and Minerals*, Dorling Kindersley, Ltd, 2012.
19 V. M. Fridkin, *Ferroelectric Semiconductors*, Consultants Bureau, 1980.
20 S. Adachi, *Earth-Abundant Materials for Solar Cells: Cu2-II-IV-VI4 Semiconductors*, Wiley, 2015.
21 A. M. Ganose, C. N. Savory and D. O. Scanlon, *Chem. Commun.*, 2017, **53**, 20–44.
22 R. E. Newnham, *Properties of Materials*, Oxford University Press, 2005.
23 T. L. Bahers, M. Rérat and P. Sautet, *J. Phys. Chem. C*, 2014, **118**, 5997–6008.
24 K. T. Butler, J. M. Frost and A. Walsh, *Energy Environ. Sci.*, 2015, **8**, 838–848.
25 V. M. Fridkin, *Photoferroelectrics*, Springer-Verlag, Berlin, Heidelberg, 1979.
26 B. I. Sturman and V. M. Fridkin, *Photovoltaic and Photo-refractive Effects in Noncentrosymmetric Materials*, Gordon and Breach Science Publishers, 1992.
27 A. G. Chynoweth, *Phys. Rev.*, 1956, **102**, 705–714.
28 M. R. Morris, S. R. Pendlebury, J. Hong, S. Dunn and J. R. Durrant, *Adv. Mater.*, 2016, **28**, 7123–7128.
29 J. Starkiewicz, L. Sosnowski and O. Simpson, *Nature*, 1946, **158**, 28.
30 H. R. Johnson, R. H. Williams and C. H. B. Mee, *J. Phys. D: Appl. Phys.*, 1975, **8**, 1530–1541.
31 B. Goldstein and L. Pensak, *J. Appl. Phys.*, 1959, **30**, 155–161.
32 M. D. Uspenskii, N. G. Ivanova and I. E. Malkis, *Sov. Phys. Semicond.*, 1968, 1059.
33 Y. Yuan, Z. Xiao, B. Yang and J. Huang, *J. Mater. Chem. A*, 2014, **2**, 6027–6041.
34 C. Paillard, X. Bai, I. C. Infante, M. Guennou, G. Geneste, M. Alexe, J. Kreisel and B. Dkhil, *Adv. Mater.*, 2016, **28**, 5153–5168.
35 W. S. Choi, M. F. Chisholm, D. J. Singh, T. Choi, G. E. Jellison and H. N. Lee, *Nat. Commun.*, 2012, **3**, 689.
36 K. T. Butler, S. McKechnie, P. Azarhoosh, M. van Schilfgaarde, D. O. Scanlon and A. Walsh, *Appl. Phys. Lett.*, 2016, **108**, 112103.
37 E. Fatuzzo, G. Harbeke, W. J. Merz, R. Nitsche, H. Roetschi and W. Ruppel, *Phys. Rev.*, 1962, **127**, 2036–2037.
38 M. A. García and J. Balenzategui, *Renewable Energy*, 2004, **29**, 1997–2010.
39 H. Dittrich, A. Bieniok, U. Brendel, M. Grodzicki and D. Topa, *Thin Solid Films*, 2007, **515**, 5745–5750.
40 B. Durant and B. A. Parkinson, *2016 IEEE 43rd Photovoltaic Specialists Conference (PVSC)*, 2016.
41 H. Dittrich, A. Stadler, D. Topa, H.-J. Schimper and A. Basch, *Phys. Status Solidi A*, 2009, **206**, 1034–1041.
42 T. Pauporté and D. Lincot, *Adv. Mater. Opt. Electron.*, 1995, **5**, 289–298.
43 N. I. Butsko, I. D. Zhezhnich and M. M. Pidorya, *Russ. Phys. J.*, 1973, **16**, 223–224.
44 Y. Dong, A. R. Khabibullin, K. Wei, J. R. Salvador, G. S. Nolas and L. M. Woods, *ChemPhysChem*, 2015, **16**, 3264–3270.
45 J. J. Scragg, J. T. Wätjen, M. Edoff, T. Ericson, T. Kubart and C. Platzer-Björkman, *J. Am. Chem. Soc.*, 2012, **134**, 19330–19333.
46 V. Blum, R. Gehrke, F. Hanke, P. Havu, V. Havu, X. Ren, K. Reuter and M. Scheffler, *Comput. Phys. Commun.*, 2009, **180**, 2175–2196.
47 X. Ren, P. Rinke, V. Blum, J. Wieferink, A. Tkatchenko, A. Sanfilippo, K. Reuter and M. Scheffler, *New J. Phys.*, 2012, **14**, 053020.
48 V. Havu, V. Blum, P. Havu and M. Scheffler, *J. Comput. Phys.*, 2009, **228**, 8367–8379.
49 S. V. Levchenko, X. Ren, J. Wieferink, R. Johanni, P. Rinke, V. Blum and M. Scheffler, *Comput. Phys. Commun.*, 2015, **192**, 60–69.
50 A. C. Ihrig, J. Wieferink, I. Y. Zhang, M. Ropo, X. Ren, P. Rinke, M. Scheffler and V. Blum, *New J. Phys.*, 2015, **17**, 093020.
51 J. Heyd, G. E. Scuseria and M. Ernzerhof, *J. Chem. Phys.*, 2003, **118**, 8207–8215.
52 W. P. Huhn and V. Blum, arXiv preprint: 1705.01804, 2017.
53 E. N. Brothers, A. F. Izmaylov, J. O. Normand, V. Barone and G. E. Scuseria, *J. Chem. Phys.*, 2008, **129**, 011102.
54 A. J. Garza and G. E. Scuseria, *J. Phys. Chem. Lett.*, 2016, **7**, 4165–4170.
55 G. Bergerhoff and I. Brown, *Crystallographic Databases*, 1987.
56 K. Momma and F. Izumi, *J. Appl. Crystallogr.*, 2011, **44**, 1272–1276.
57 C. Ambrosch-Draxl and J. O. Sofo, *Comput. Phys. Commun.*, 2006, **175**, 1–14.
58 N. A. Spaldin, *J. Solid State Chem.*, 2012, **195**, 2–10.
59 K. L. Svane and A. Walsh, *J. Phys. Chem. C*, 2016, **121**, 421–429.

60 G. Kresse and J. Furthmüller, *Comput. Mater. Sci.*, 1996, **6**, 15–50.
61 G. Kresse and J. Furthmüller, *Phys. Rev. B: Condens. Matter Mater. Phys.*, 1996, **54**, 11169–11186.
62 P. E. Blöchl, *Phys. Rev. B: Condens. Matter Mater. Phys.*, 1994, **50**, 17953–17979.
63 R. Shuey, *Semiconducting Ore Minerals*, Elsevier, 2012.
64 L. L. Baranowski, P. Zawadzki, S. Lany, E. S. Toberer and A. Zakutayev, *Semicond. Sci. Technol.*, 2016, **31**, 123004.
65 F. J. Espinosa-Faller, D. R. Conradson, S. C. Riha, M. B. Martucci, S. J. Fredrick, S. Vogel, A. L. Prieto and S. D. Conradson, *J. Phys. Chem. C*, 2014, **118**, 26292–26303.
66 S. Schorr, H.-J. Hoebler and M. Tovar, *Eur. J. Mineral.*, 2007, **19**, 65–73.
67 J. J. S. Scragg, L. Choubrac, A. Lafond, T. Ericson and C. Platzer-Björkman, *Appl. Phys. Lett.*, 2014, **104**, 041911.
68 D. Shin, B. Saparov, T. Zhu, W. P. Huhn, V. Blum and D. B. Mitzi, *Chem. Mater.*, 2016, **28**, 4771–4780.
69 Z. Xiao, W. Meng, J. V. Li and Y. Yan, *ACS Energy Lett.*, 2017, **2**, 29–35.
70 T. Gershon, K. Sardashti, O. Gunawan, R. Mankad, S. Singh, Y. S. Lee, J. A. Ott, A. Kummel and R. Haight, *Adv. Energy Mater.*, 2016, **6**, 1601182.
71 D. Shin, B. Saparov and D. B. Mitzi, *Adv. Energy Mater.*, 2017, 1602366.
72 P. Velásquez, D. Leinen, J. Pascual, J. Ramos-Barrado, R. Cordova, H. Gómez and R. Schrebler, *J. Electroanal. Chem.*, 2000, **494**, 87–95.
73 L. Yu, R. S. Kokenyesi, D. A. Keszler and A. Zunger, *Adv. Energy Mater.*, 2013, **3**, 43–48.
74 S. Curtarolo, W. Setyawan, G. L. Hart, M. Jahnatek, R. V. Chepulskii, R. H. Taylor, S. Wang, J. Xue, K. Yang, O. Levy, M. J. Mehl, H. T. Stokes, D. O. Demchenko and D. Morgan, *Comput. Mater. Sci.*, 2012, **58**, 218–226.
75 B. Silvi and A. Savin, *Nature*, 1994, **371**, 683–686.
76 A. Walsh, A. A. Sokol, J. Buckeridge, D. O. Scanlon and C. R. A. Catlow, *J. Phys. Chem. Lett.*, 2017, **8**, 2074–2075.
77 A. Zakutayev, C. M. Caskey, A. N. Fioretti, D. S. Ginley, J. Vidal, V. Stevanovic, E. Tea and S. Lany, *J. Phys. Chem. Lett.*, 2014, **5**, 1117–1125.
78 S. B. Zhang, S.-H. Wei, A. Zunger and H. Katayama-Yoshida, *Phys. Rev. B: Condens. Matter Mater. Phys.*, 1998, **57**, 9642–9656.
79 C. Persson and A. Zunger, *Phys. Rev. Lett.*, 2003, **91**, 266401.
80 C. Persson and A. Zunger, *Appl. Phys. Lett.*, 2005, **87**, 211904.
81 R. B. Balow, C. K. Miskin, M. M. Abu-Omar and R. Agrawal, *Chem. Mater.*, 2017, **29**, 573–578.
82 S. D. Wolf, J. Holovsky, S.-J. Moon, P. Löper, B. Niesen, M. Ledinsky, F.-J. Haug, J.-H. Yum and C. Ballif, *J. Phys. Chem. Lett.*, 2014, **5**, 1035–1039.
83 F. Brivio, A. B. Walker and A. Walsh, *APL Mater.*, 2013, **1**, 042111.
84 C. Eames, J. M. Frost, P. R. F. Barnes, B. C. O'Regan, A. Walsh and M. S. Islam, *Nat. Commun.*, 2015, **6**, 7497.
85 A. Y. Orlova, R. R. Gainov, A. V. Dooglav, I. N. Pen'kov and E. A. Korolev, *JETP Lett.*, 2012, **96**, 370–374.
86 K. Wei, J. Martin, J. R. Salvador and G. S. Nolas, *Cryst. Growth Des.*, 2015, **15**, 3762–3766.
87 R. Pandeya, G. Vatsc, J. Yund, C. R. Bowen, A. W. Y. Ho-Baillied and J. Seidel, arXiv preprint: 1705.05529, 2017.
88 P. S. Brody, *Appl. Phys. Lett.*, 1981, **38**, 153–155.
89 H.-Y. Huang, M. Wu and L.-J. Qiao, *Comput. Mater. Sci.*, 2014, **82**, 1–4.
90 R. Wahl, D. Vogtenhuber and G. Kresse, *Phys. Rev. B: Condens. Matter Mater. Phys.*, 2008, **78**, 104116.
91 Y. Xu, *Ferroelectric Materials and Their Applications*, North-Holland, 1991.
92 I. Grinberg and A. M. Rappe, *Phys. Rev. B: Condens. Matter Mater. Phys.*, 2004, **70**, 220101.
93 P. Azarhoosh, S. McKechnie, J. M. Frost, A. Walsh and M. van Schilfgaarde, *APL Mater.*, 2016, **4**, 091501.
94 F. Zheng, L. Z. Tan, S. Liu and A. M. Rappe, *Nano Lett.*, 2015, **15**, 7794–7800.
95 L. D. Whalley, J. M. Frost, Y.-K. Jung and A. Walsh, *J. Chem. Phys.*, 2017, **146**, 220901.

5.3 Outlook: High-throughput screening for candidate photoferroics

In the study in the previous section, three candidate photoferroic materials were identified from the dataset of approximately 200 naturally occurring minerals. This choice of initial dataset was motivated by the high stability that could be expected for naturally occurring minerals. However, the availability of various materials properties databases [202, 203, 204, 205, 206, 207] and utilisation of high-throughput density functional theory (DFT) calculations [208, 209, 210] is opening up new avenues for materials discovery for various technologies [211] such as energy-generation with thermoelectrics [212, 213, 214] and photovoltaics [215, 216, 217, 218, 219]. Consequently, there are much larger search spaces for materials discovery and it may be possible to identify better materials from such a resource. For this reason, an ongoing study is being conducted in collaboration with Lee A. Burton to perform a similar screening procedure to that in the previous section but instead using the Materials Project [202] database. All screening of the Materials Project and subsequent calculations are being conducted by L. Burton. Therefore, here just the motivations and modified screening criteria are outlined as this is my main contribution to the study.

As we do not start from a dataset of naturally occurring minerals in this extension, we limit our search space to only stable materials by considering only compounds with energies less than 24 meV above the thermodynamic convex hull. We also only consider compounds composed of 4 or less elements to avoid materials that are likely to be particularly challenging to synthesise. Otherwise, we apply similar screening criteria to the previous project. We also screen by polar space group but as opposed to using the streak colour as an indication that the band gap is likely to be within the visible range, we use the calculated band gaps for the compounds contained in the Materials Project database. DFT calculations for the material properties contained in the Materials Project database are performed at the GGA level of theory. The underestimation of the band gaps in the Materials Project database is stated to be approximately 40% [220, 208]. With the optimal range for a PV absorber being approximately 1.1 eV to 1.7 eV, we use 0 eV to 1.5 eV as the range of band gap for our candidates to account for the typical underestimation of the band gap.

Effective masses were calculated for the three candidate photoferroic minerals in the previous study by fits to the extrema of the calculated electronic band structures. In this study, charge-carrier transport properties for the compounds from the initial screening procedure will be determined by solving the Boltzmann transport equations

using calculated band structures from the Materials Project and the BoltzTraP code [221]. In the calculations, the temperature will be set to the typical operating temperature of a solar cell and carrier concentration will assumed to be in the ideal range, as this is a property than could be tuned experimentally for the most promising candidates through doping, subject to the doping limits of the material [55]. With the substantially larger number of candidate photoferroic materials from this study, we will be able to be more stringent in our standards for charge carrier effective masses. We will first screen by the isotropic average and then by components of the effective mass tensor so that we are left with candidates satisfying the necessary condition for isotropic high carrier mobility for both electrons and holes at the CBM and VBM respectively.

Chapter 6

Theoretical insights for new solar absorbers

In chapter 5 three candidate photoferroic materials were identified and necessary optoelectronic properties for an absorber layer to form a high-performance solar cell were predicted from electronic structure calculations. The focus of this chapter is to use further predicted material properties, as well as insights from previous studies on more mature PV technologies, to further assess the likely performance of the candidate absorber layers in PV devices and, where possible, to provide guidance to optimise performance.

6.1 Development of new solar cell device architectures

To develop a high-performance solar cell device, the full device architecture must be optimised for the specific absorber layer. This optimisation process can be a barrier to the utilisation of new solar cell technologies. It is often the case that device architectures optimised for different absorber materials are used for new PV absorbers, which are not necessarily optimal, resulting in reduced device performance. Examples include the use of a typical architecture optimised for Cu(In,Ga)Se_2 (CIGS) solar cell technologies for $CuSbS_2$ [222] and also for one of the candidate absorber layers in this study, Cu_3AsS_4 [223].

6.1.1 Publication: Finding a junction partner for candidate solar cell absorbers enargite and bournonite from electronic band and lattice matching

The study presented here aims to use theory to accelerate device optimisation for two of the candidate absorber layers identified in chapter 5 by providing suggestions for suitable solar cell heterojunction partners. Although it may be possible to achieve photovoltaic energy conversion without a solar cell junction for photoferroic absorbers, as described in section 5.1, a solar cell junction is likely to still be beneficial to provide a global driving force for carrier separation with internal electric fields allowing for improved local carrier separation. The following work is a data mining procedure to determine suitable junction partners for two of the candidate absorber materials from chapter 5. Insights for optimal electronic band offsets for a solar cell heterojunction are based on studies performed for PV absorbers CdTe [224], CIGS [225] and $ZnSnN_2$ [226].

The following paper has been reproduced with permission from AIP Publishing. The supplemental material for this work is included in Appendix A.3.

Statement of Authorship

This declaration concerns the article entitled:									
Finding a junction partner for candidate solar cell absorbers enargite and bournonite from electronic band and lattice matching Pages 124 - 131 of thesis									
Publication status (tick one)									
draft manuscript		**Submitted**		**In review**	X	**Accepted**		**Published**	
Publication details (reference)	Finding a junction partner for candidate solar cell absorbers enargite and bournonite from electronic band and lattice matching SK Wallace, KT Butler, Y Hinuma, A Walsh								
Candidate's contribution to the paper (detailed, and also given as a percentage).	*Formulation of ideas (70%):* The dataset of candidate junction partners was collated by K. Butler and the ElectronLatticeMatch python libraries were also developed by K. T. Butler. The idea to use this existing tool to look for junction partners with specific band offsets (cliff- or spike-like) for the absorber materials identified in chapter 5 of this thesis was from myself (S. Wallace) where the screening criteria used in the study was chosen by S. Wallace and informed by previous works in the literature on other absorber materials (CdTe, ZnSnN2 and CIGS). *Design of methodology (50%):* As mentioned in the previous section, this work made use of a python library developed by K. Butler (ElectronLatticeMatch). This was incorporated into an interactive workflow by S. Wallace to screen for candidate junction partners in this study with screening criteria chosen by S. Wallace. Non-polar, symmetric slab models used for the calculations of ionisation potential in this study were cut by Y. Hinuma using methodology developed by Y. Hinuma. Ionisation potentials of the slab models were calculated using existing MacroDensity python libraries. *Experimental work (70%):* For this study, S. Wallace performed electronic structure calculations with the VASP software package for the volume relaxation of bulk unit cells from which Y. Hinuma generated slab models. S. Wallace also performed electronic structure calculations for the slab models and processed outputs from the electronic structure calculations with the MacroDensity and ElectronLatticeMatch python libraries. Throughout this work, support and discussions were provided by K. T. Butler for utilising the python libraries and performing electronic structure calculations for the slab models. *Presentation of data in journal format (70%):* The first draft of the manuscript was prepared by S. Wallace and all co-authors provided support when finalising the manuscript for submission.								
Statement from Candidate	This paper reports on original research I conducted during the period of my Higher Degree by Research candidature.								
Signed	S. Wallace			**Date**	06/12/18				

Journal of Applied Physics ARTICLE scitation.org/journal/jap

Finding a junction partner for candidate solar cell absorbers enargite and bournonite from electronic band and lattice matching

Cite as: J. Appl. Phys. **125**, 055703 (2019); doi: 10.1063/1.5079485
Submitted: 31 October 2018 · Accepted: 7 January 2019 ·
Published Online: 6 February 2019

View Online Export Citation CrossMark

Suzanne K. Wallace,[1,2] Keith T. Butler,[3] Yoyo Hinuma,[4,5] and Aron Walsh[2,6,a)]

AFFILIATIONS

[1]Department of Chemistry, Centre for Sustainable Chemical Technologies, University of Bath, Claverton Down, Bath BA2 7AY, United Kingdom
[2]Department of Materials, Imperial College London, Exhibition Road, London SW7 2AZ, United Kingdom
[3]ISIS Neutron and Muon Source, Rutherford Appleton Laboratories, Didcot, Oxfordshire OX11 0QX, United Kingdom
[4]Center for Frontier Science, Chiba University, Chiba 263-8522, Japan
[5]Center for Materials Research by Information Integration, Research and Services Division of Materials Data and Integrated System, National Institute for Materials Science, Tsukuba 305-0047, Japan
[6]Department of Materials Science and Engineering, Yonsei University, Seoul 03722, South Korea

[a)]a.walsh@imperial.ac.uk

ABSTRACT

An essential step in the development of a new photovoltaic (PV) technology is choosing appropriate electron and hole extraction layers to make an efficient device. We recently proposed the minerals enargite (Cu_3AsS_4) and bournonite ($CuPbSbS_3$) as materials that are chemically stable with desirable optoelectronic properties for use as the absorber layer in a thin-film PV device. For these compounds, spontaneous lattice polarization with internal electric fields—and potential ferroelectricity—may allow for enhanced carrier separation and novel photophysical effects. In this work, we calculate the ionization potentials for non-polar surface terminations and propose suitable partners for forming solar cell heterojunctions by matching the electronic band edges to a set of candidate electrical materials. We then further screen these candidates by matching the lattice constants and identify those that are likely to minimise strain and achieve epitaxy. This two-step screening procedure identified a range of unconventional candidate junction partners including SnS_2, ZnTe, WO_3, and Bi_2O_3.

I. INTRODUCTION

Solar power is an attractive source of sustainable electricity. Technological breakthroughs to enable high-efficiency photovoltaic (PV) devices without the need to use scarce material components and with low manufacturing costs would secure solar power as a future power source. Exploiting non-centrosymmetry and lattice polarization in "photoferroic" materials could provide new pathways to high-efficiency PV devices. Phenomena referred to as "anomalous" and "bulk" PV effects in polar materials have demonstrated photovoltages' orders of magnitude greater than the optical bandgap and photocurrents in bulk, single-crystal absorbers in the absence of a typical p-n junction for carrier separation.[1–3] On-going research efforts are exploring the theory behind these observed phenomena.[4–7]

We recently identified three naturally-ocurring minerals as candidate photoferroic materials based on their optical bandgaps and polar crystal structures,[8] including enargite (Cu_3AsS_4) and bournonite ($CuPbSbS_3$). To our knowledge, to date, only one study has made solar cells out of any of these materials. In Ref. 9, solar cells were made from solution processed enargite using a device architecture developed for Cu(In, Ga)Se_2 (CIGS) solar cell technology. In this study, the authors list non-optimal band alignment of the absorber layer with the device architecture as

a likely limitation of the current solar cell performance. This is also the case for $CuSbS_2$ solar cells using device architecture optimised for CIGS absorber layers.[10] Mature technologies, such as CIGS-based devices, are still being optimised through improved band alignment with the n-type buffer layer,[11] and non-optimal band alignment is also being considered as a limiting factor on the performance of $Cu_2ZnSn(S, Se)_4$-based solar cells.[12] The optimization of device architecture for a new solar cell technology is a challenging and time-consuming process.

For many of the materials being studied for use as absorber layers in thin-film solar cells, such as chalcogenide semiconductors, it is not possible, or is very difficult, to achieve ambipolar doping. Therefore, to achieve a p-n junction for many thin-film PV devices, it is necessary to form an interface between materials with different optical bandgaps, lattice constants, and even crystal structures.[15] In the extreme case when the two materials are poorly matched, differences in lattice constant and crystal structure at a heterojunction interface can introduce a large strain, resulting in poor epitaxy.[16] Even for less extreme differences, small lattice mismatch at an interface generally introduces intra-bandgap defect states, which enhances Shockley-Read-Hall recombination, increasing dark currents, and reducing the open-circuit voltage of the device.[17]

In this work, we aim to accelerate the optimisation of solar cell device architectures for enargite (Cu_3AsS_4) and bournonite ($CuPbSbS_3$) by screening for candidate junction partners that could have optimal electronic band offsets and crystal lattices well-matched to minimise strain at the interface. The principles behind our screening criteria for optimal band offsets are outlined in Sec. II. Where there is no literature consensus as to whether the material is likely to be more easily doped p-type or n-type, we screen for candidate junction partners based on the relevant band offset for forming a solar cell junction for both cases.

II. BAND OFFSETS FOR SOLAR CELL HETEROJUNCTIONS

The band alignment at a solar cell junction is crucial to facilitate the separation of photo-excited electrons and holes to allow for extraction of the charge carriers before recombination can occur.[18] Although internal electric fields in the materials in this study may allow for a bulk photovoltaic effect for thin films (where the electrical asymmetry at a junction is not required for a photocurrent to be generated), a heterojunction would provide a global driving force for carrier collection at electrodes, while internal electric fields from the polar crystal structure could enhance carrier separation locally.

Semiconductor junctions are classified as type I, II, or III based on the band alignment; however, only type I and type II are of interest for PV applications. A type II "staggered" junction can also be referred to as a "cliff-like" offset, and a type I "straddling" junction can also be referred to as a "spike-like" offset, as illustrated schematically in Fig. 1. For a p-type absorber layer, the minority carriers are electrons promoted into the conduction band (CB) of the absorber. Therefore, the transport of electrons from the CB of the p-type absorber to the junction partner is important for determining device performance. The parameter of interest here is the conduction band offset (CBO) between the two materials. However, for

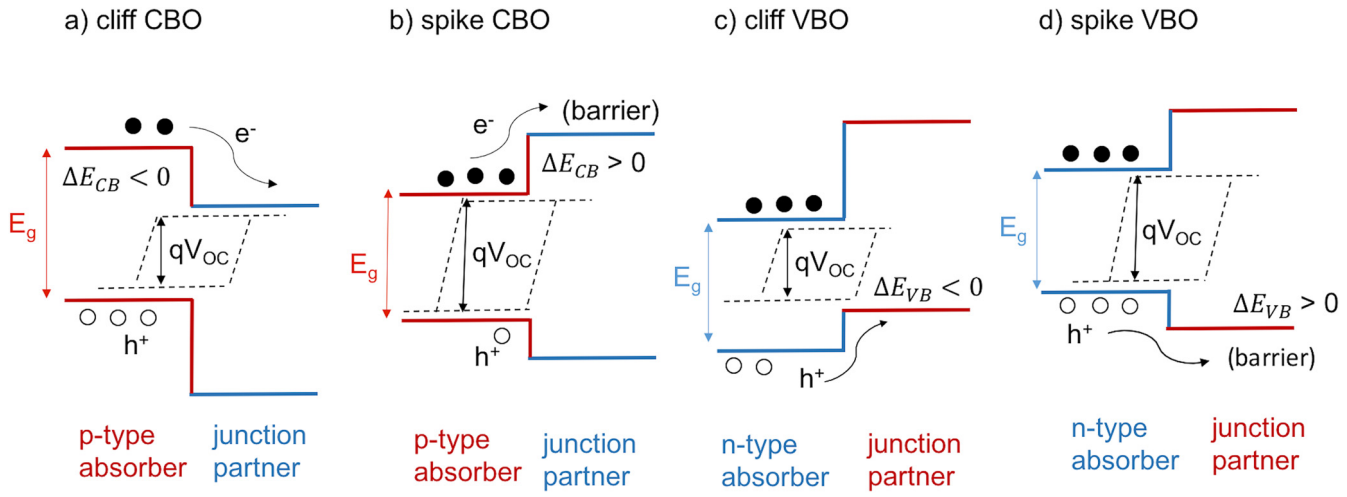

FIG. 1. Illustration of four possible junctions present in a solar cell. (a) A type II heterojunction between a p-type absorber and an n-type material where photoelectrons flow across the interface with no barrier at the negative "cliff" conduction band offset (CBO). The open-circuit voltage is reduced relative to the absorber bandgap if the cliff is large. (b) A type I heterojunction between a p-type absorber layer and an n-type material with a small positive ("spike") CBO. If the spike is sufficiently small, electrons can tunnel through the barrier and across the interface. Holes are repelled from the interface region. (c) A type II heterojunction between an n-type absorber and a p-type material where photoelectrons flow across the interface with no barrier at the negative "cliff" valence band offset (VBO). The open-circuit voltage is reduced relative to the absorber bandgap if the cliff is large. (d) A type I heterojunction between an n-type absorber layer and a p-type material with a small positive ("spike") VBO. If the spike is too large, this barrier will impede transport across the interface. The schematics follow those presented in Refs. 13 and 14.

n-type absorbers, it is photoexcited holes that are the minority carriers and so it is the magnitude of the valence band offset (VBO) between the n-type absorber and the junction partner that is important for charge extraction.

It has been observed that for the p-type absorbers CIGS and CdTe, a spike offset (CBO within the range 0.1–0.3 eV), as shown in Fig. 1(a), gives better device performance.[13,21] Here, a small positive spike CBO creates an absorber inversion layer, resulting in a large hole barrier at the interface.[13] The modest barrier to electron transfer means that electrons may still tunnel across the interface or have sufficient thermal energy to overcome the barrier and be collected.[17] Electron-hole recombination at an interface with high defect densities is then thought to be suppressed due to an insufficient hole supply. In contrast, for a cliff offset where the CBO is negative, as shown in Fig. 1(b), there may be high concentrations of holes in the vicinity of the interface to assist interface recombination, thereby reducing the open-circuit voltage.[13]

For the n-type absorber $ZnSnN_2$, the opposite trend has been observed, where a spike VBO is expected to give a poorer performance.[14] Here, a spike offset limits transport across the interface due to the larger effective mass of minority-carrier holes (compared to CIGS and CdTe[22]) and associated lower hole mobility.[14] For $ZnSnN_2$, a small cliff is thought to be optimal. In this study, we use calculated effective masses to inform our choice of optimal band offsets for forming solar cell heterojunctions.

III. METHODOLOGY

A. Electronic band and lattice matching

Screening for candidate heterojunction partners based on electronic band offsets and minimum lattice strain is conducted using the methodology and dataset of tabulated ionization potentials (IPs) and electron affinities (EAs) for candidate junction partners in Ref. 16 and ElectronLatticeMatch libraries.[23] This dataset currently contains the electronic band gaps, IPs, and EAs of 173 candidate heterojunction partners obtained either from experimental measurements or electronic structure calculations.

For p-type (n-type) absorbers, we screen for candidate junction partners based on the CBO (VBO). We look for a small cliff offset by selecting a band offset in the range 0 to −0.3 eV. However, for cases where the minority carrier effective mass calculated in Ref. 8 is less than $0.5m_e$, we also look for a small spike offset in the range +0.1 to +0.3 eV. For CIGS, +0.2 eV has been reported to be optimal[21] and +0.3 eV for CdTe.[13]

We further limit our search to candidate junction partners where an interface with in-plane lattice strain less than 4% in both the x- and y-directions is obtained. We consider no defect states at the interface and allow no chemical intermixing, which is known to be present to a large extent at the CdTe:CdS interface.[24,25] For final candidate junction partners, we estimate the likely extent of interface intermixing based on the chemical similarities of the components of the two materials forming the heterojunction.

B. Band alignment

The alignment of the valence band energy to a common vacuum level, i.e., the ionization potential (IP), can be performed using techniques such as photoelectron spectroscopy or Kelvin probe microscopy and can be computed using first-principles calculations of surface slab models.[26] The electron affinity (χ) is the conduction band energy with respect to the vacuum level, which can be obtained by adding the value of the electronic bandgap onto the IP of a material. Results from two decades of photoelectron spectroscopy experiments on CdTe and CIGS thin-film solar cells have been compared to density functional theory (DFT) calculations,[15] where it was found that the energy band alignments for many interfaces were in good agreement. Theoretically predicted band alignments are usually the "intrinsic" or "natural" alignment for a particular combination of materials forming an interface,[15] i.e., in the absence of defects, interfacial reconstructions, or thermal effects.[27] This ideal band alignment therefore acts as a starting point to limit the search space for suitable junction partners.

The model used to predict the energy band alignment at solar cell heterojunctions in this study is the electron affinity rule (also known as Anderson's rule) where energies are aligned through the vacuum level.[28,29] The vacuum level of the two materials on either side of the heterojunction are aligned to the same energy, and the difference between the distance between the CBM and the vacuum (χ) of each material is used to predict the CBO, as shown in Eq. (1).

We take semiconductor 2 to be the absorber with a bandgap ($E_{g,abs}$) within the visible range (approximately 1.1–1.7 eV) and semiconductor 1 to be the transparent junction partner with a wider $E_{g,jp}$ in the range of 2–3 eV. The conduction band offset is defined as

$$\Delta E_c = \chi_{abs} - \chi_{jp}. \tag{1}$$

Similarly, the valence band offset is determined through the difference in the ionization potentials ($IP = \chi + E_g$)

$$\Delta E_v = IP_{jp} - IP_{abs}. \tag{2}$$

A negative ΔE_c or ΔE_v corresponds to a cliff CBO or cliff VBO, respectively; this is then a "staggered gap." These different cases are illustrated in Fig. 2.

C. Computational details

1. Surface slab models

Band energies are dependent upon the surface terminations of a crystal. We therefore construct slab models for all possible non-polar surface terminations of the materials using the algorithm described in Ref. 30. Symmetric slab models are then cut from relaxed unit cells; visualisations of the slab structures are given in the supplementary material.

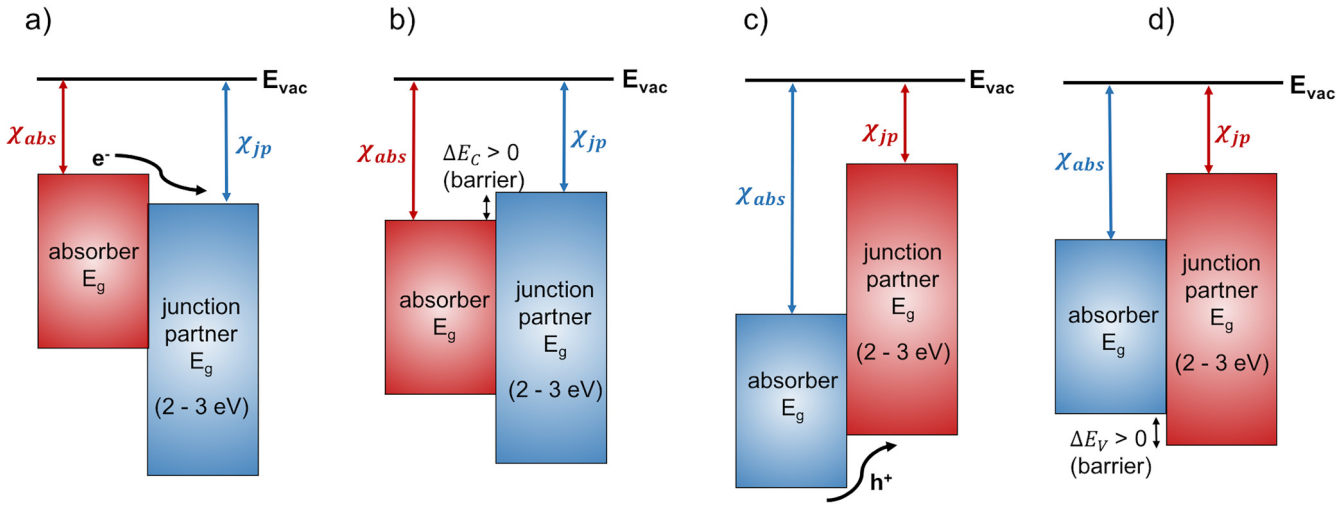

FIG. 2. Heterojunction alignments for solar cells with respect to the external vacuum level, E_{vac}, based on the electron affinity (conduction band energy), χ_{abs}. (a) Type II "staggered" offset with a p-type absorber and no barrier to minority photocarrier transport across the junction. (b) Type I "straddling" offset with a p-type absorber and a small barrier (positive ΔE_c) to minority carrier transport. (c) Type II "staggered" offset with an n-type absorber and no barrier to minority photocarrier transport. (d) Type I "straddling" offset with an n-type absorber and a small barrier (postive ΔE_v) to minority carrier transport. The schematics follow those presented in Refs. 19 and 20.

For the relaxation of the ion positions and volume of the unit cells, calculations are performed in VASP[31,32] using the PBEsol functional,[33] projector augmented wave core potentials,[34] without including spin-orbit coupling (SOC) and with symmetry fixed until forces on the atoms are converged to within 0.005 eV per Å. A plane wave cutoff energy of 350 eV is used, and k-grid densities of $6 \times 6 \times 6$ and $4 \times 4 \times 4$ were used to sample the electronic Brillouin zone for a 16 atom unit cell of enargite (Cu_3AsS_4) and a 24 atom unit cell of bournonite ($CuPbSbS_3$), respectively.

To inform our later discussion for which candidate junction partners are likely to be the most important for devices, we calculate the surface energies for the slab models using Eq. (3), where E_{bulk} is the total energy of the bulk crystal per formula unit, n is the number of formula units in the surface slab, and A is the area of surface, of which there are two per slab model:

$$\gamma = \frac{E_{surf} - nE_{bulk}}{2A}. \quad (3)$$

2. Ionization potential and electron affinity

Calculations for planar averaged electrostatic potential of the slab models are also performed in VASP but using the HSE06 functional[35] with SOC and a single k-point is used to sample the slab along the finite dimension. To calculate the ionization potentials of the surface slab models, a macroscopic average technique is used.[26] The difference between the macroscopic average of the vacuum potential and the bulk-like region of the surface slab is used to obtain the surface dipole shift, D_s. The ionization potential is then calculated using the eigenvalue of the valence band maximum (ϵ_{VBM}) for the bulk crystal

$$IP = D_s - \epsilon_{VBM}. \quad (4)$$

Electron affinities, χ, are then calculated from the IP using the electronic bandgap calculated with the HSE06 functional.

IV. RESULTS AND DISCUSSION

A. Electronic matching of junction partners

The band energies calculated for the low-index, non-polar surfaces for each material are summarised in Table I,

TABLE I. Calculated ionization potentials (IPs), electron affinities (χ), DFT/HSE06 bandgaps (E_g) all in units of eV and unrelaxed surface energies (γ) in units of eV per Å^2 for symmetric and non-polar slab models of enargite (Cu_3AsS_4) and bournonite ($CuPbSbS_3$).

Absorber	Termination	E_g	IP	χ	γ
Enargite (Cu_3AsS_4)	(100)	1.32	4.97	3.64	0.050
	(010)a	1.32	5.21	3.89	0.025
	(010)b	1.32	6.23	4.91	0.120
	(110)	1.32	4.95	3.63	0.070
Bournonite ($CuPbSbS_3$)	(100)	1.68	5.61	3.93	0.042
	(010)a	1.68	5.20	3.52	0.150
	(010)b	1.68	5.21	3.53	0.106
	(110)a	1.68	6.50	4.82	0.090
	(110)b	1.68	6.04	4.36	0.037

where the labels a and b refer to different surface cuts along the same [*hkl*]. Visuals of the slab models are contained in the supplementary material. We find a notable variation in the IP for different surface terminations of the same material, which may have implications for the simplicity of the junction fabrication, especially as the low energy surface terminations have significantly different IPs. From inspection of the slab geometries (shown in the supplementary material), slab models with larger IPs have denser surface structures with anion-rich terminations that could be associated with a larger double layer.[36]

Experimental data for enargite suggest that the material exhibits native p-type conductivity.[37,38] For bournonite, there is variation in the literature between experimental measurements on natural samples measuring n-type conductivity[38] and theoretical prediction of the defect physics suggesting the material will be intrinsically p-type and difficult to dope n-type.[39] Junction partners for enargite are screened based on the CBO only, while for bournonite, the CBO and VBO are considered in turn to provide options for a p-type or a n-type absorber layer. We screen for both cliff and spike CBO for a p-type bournonite, but only for a cliff VBO for a n-type bournonite due to calculated heavy hole effective mass ($m_h > 0.5m_e$)[8] in line with our earlier discussion. In all cases, we search for junction partners with bandgaps in the range 2–3 eV.

B. Low strain junctions

Candidates passing the electronic matching stage were screened for those with less than 4% in-plane lattice strain at the interface in both the x- and y-directions. Candidates containing Fe were not considered further as Fe is often associated with fast non-radiative recombination in solar cells due to possible excitations and recombination channels from a half occupied *d*-shell (d^5 for Fe^{3+} and d^6 for Fe^{2+}). Where multiple structure files for the candidates were available on the Materials Project database,[41] unit cells for the most stable structures were preferentially selected for this lattice matching step, based on the energy above the thermodynamic convex hull. All candidates considered in this second screening stage, including the materials project ID for the corresponding structure file, can be found in the supplementary material.

Each surface slab termination was screened individually starting from the tabulated data for 173 candidate heterojunction partners. The remaining candidates after the two-step screening process for each surface model are listed in Tables II and III for bournonite and enargite, respectively. Averaged in-plane interface strain for all low-strain electronically-matched candidate junction partners is also reported. A selection of band alignment plots are shown in Figs. 3 and 4; all other slab terminations are included in the supplementary material. In each case, the candidate junction partner with the lowest interface strain is highlighted.

TABLE II. Finding a partner for five surface terminations of bournonite ($CuPbSbS_3$). Low strain terminations and in-plane averaged interface strain (%) of heterojunction partners after electronic band and lattice matching for all surface models of bournonite allowing for the absorber to be either p-type (through electronic matching of conduction bands via the CBO) or n-type (through matching of the valence bands via the VBO).

	Spike conduction band offset			Cliff conduction band offset			Cliff valence band offset		
Surface	Candidate	(*hkl*)	Strain (%)	Candidate	(*hkl*)	Strain (%)	Candidate	(*hkl*)	Strain (%)
				Ce_2O_3	(011), (101), (110)	1.23			
				GaP	(011), (101), (110)	1.01			
(100)				SiC	(010), (100)	0.73			
				SnS_2	(110)	0.67			
				ZnSe	(001), (010), (100)	0.83			
	La_2S_3	(110)	0.71	Ce_2S_3	(001)	1.71	AlP	(011), (101), (110)	0.71
(010)a	Nd_2S_3	(001)	0.10	Cu_2O	(011), (101), (110)	0.81	MoO_3	(100)	0.23
	Sm_2S_3	(001)	2.28	Gd_2S_3	(011)	0.71	CuI	(110)	2.73
	WO_3	(110)	0.49	ZnTe	(001), (010), (100)	0.75			
	La_2S_3	(110)	0.71	Ce_2S_3	(001)	1.71	AlP	(011), (101), (110)	0.71
(010)b	Nd_2S_3	(001)	0.10	Cu_2O	(011), (101), (110)	0.81	MoO_3	(100)	0.23
	Sm_2S_3	(001)	2.28	Gd_2S_3	(011)	0.71	CuI	(110)	2.73
	WO_3	(110)	0.49	ZnTe	(001), (010), (100)	0.75			
	As_2S_3	(101)	0.90				Ce_2O_3	(011), (101), (110)	0.68
	Bi_2O_3	(100)	1.60				GaP	(011), (101), (110)	1.35
(110)a	$CoTiO_3$	(110)	1.03				SnS_2	(010), (100)	0.94
	$NiTiO_3$	(110)	1.08				WO_3	(010)	1.00
							$Zn_3In_2S_6$	(110)	0.09
							Dy_2S_3	(110)	1.47
							SiC	(110)	1.47
	GaP	(011), (101), (110)	1.35	As_2S_3	(101)	0.90	Nd_2S_3	(110)	0.64
	SnS_2	(101), (100)	0.94	Bi_2O_3	(100)	1.60	Sm_2S_3	(110)	0.70
(110)b				CdS	(110)	2.17	Tb_2S_3	(110)	1.71
				$CoTiO_3$	(110)	1.03	ZnTe	(011), (101), (110)	0.43
				PbO	(110)	1.67			

TABLE III. Finding a partner for five surface terminations of enargite (Cu_3AsS_4). Identified low-strain terminations and in-plane averaged interface strain (%) after electronic band and lattice matching. CBO refers to the conduction band offset for electron extraction.

Surface	Candidate	(*hkl*)	Strain (%)
(100) spike CBO	Dy_2S_3	(001)	0.81
	Sm_2S_3	(001)	1.43
	Tb_2S_3	(001)	1.10
	ZnTe	(011), (101), (110)	1.01
(010)a spike CBO	Ce_2S_3	(001)	1.05
	$Zn_3In_2S_6$	(110)	1.19
(010)a cliff CBO	Ce_2O_3	(001), (010), (100)	0.20
	GaP	(001), (010), (100)	0.83
	SiC	(010), (100)	1.33
	ZnSe	(001), (010), (100)	2.02
(010)b spike CBO	Bi_2O_3	(101)	0.75
(110) spike CBO	Dy_2S_3	(011), (101)	0.68
	Sm_2S_3	(001)	1.15
	Tb_2S_3	(011), (101)	0.98
	WO_3	(011)	0.33
	ZnTe	(011), (101), (110)	0.19

1. Junction partners for bournonite

The lowest energy surfaces for bournonite were for the (100) and (110)b terminations (see Table I). For the bournonite (100) surface, we were only able to find low-strain partners for a CBO cliff, which is relevant for bournonite as a p-type absorber. Table II and Fig. 3(a) show several options for junction partners. SnS_2 is found to be the minimum strain candidate for the (100) surface. A further consideration is the simplicity of junction fabrication. Candidate junction partners able to produce a low-strain interface for multiple facets of the junction partner may imply more robust synthesis. For this reason, GaP and Ce_2O_3 are highlighted as alternative options.

For bournonite (110)b, we identified candidate junction partners for a spike CBO, cliff CBO, and cliff VBO. Candidate junction partners containing rare-earth elements such as Sm, Tb, or Dy are less desirable for practical devices. SnS_2 again emerges as a promising option for a spike CBO, Bi_2O_3 for a low-toxicity cliff CBO, and ZnTe for a cliff VBO for bournonite as an n-type absorber.

Overall, SnS_2 appears to be a promising junction partner for bournonite as a p-type absorber and ZnTe for bournonite as an n-type absorber. It is possible that there could be significant intermixing between a S containing absorber and a Te containing junction partner, as has been observed at the CdTe:CdS interface,[24] which would require careful processing and may change the nature of the band offsets.

2. Junction partners for enargite

For enargite, the (010)a termination is the lowest energy with the next being the (100) and (110) terminations with similar energies (see Table I). We note that although CdS is in our database of candidate junction partners, it did not make it through the screening process. This is likely a contributing factor to the low open-circuit voltage of enargite solar cells fabricated with CdS as the junction partner in Ref. 9.

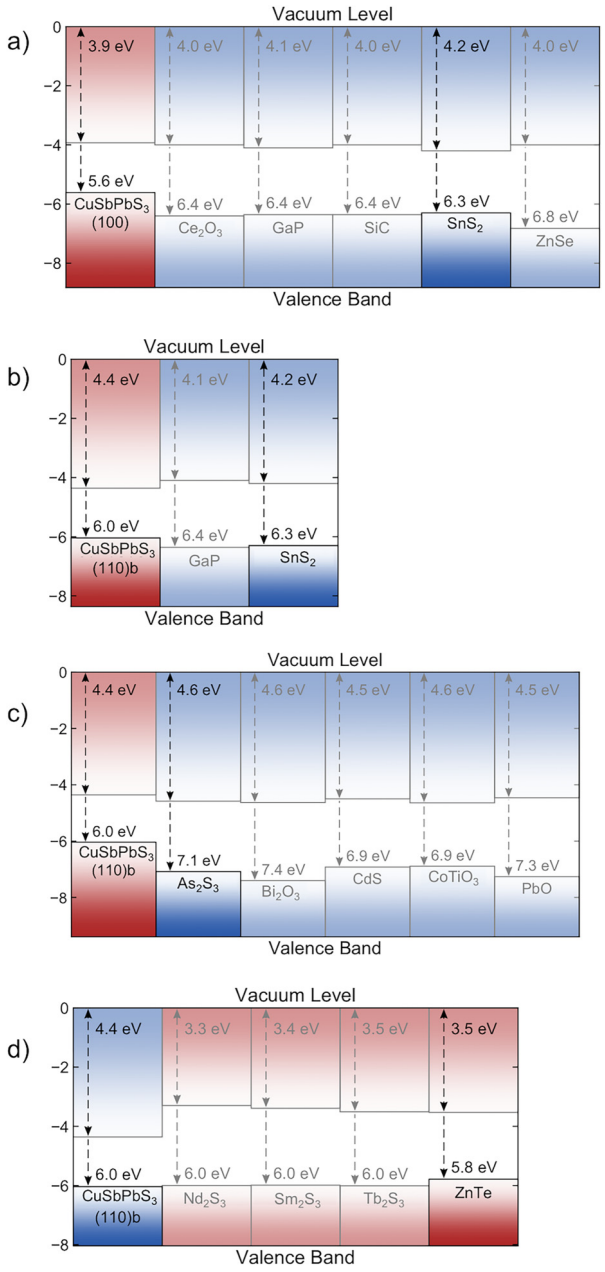

FIG. 3. Candidate junction partners for p-type bournonite ($CuPbSbS_3$) absorber layer termination (100) for (a) a cliff conduction band offset (CBO), (b) (110)b termination for a spike CBO, (c) cliff CBO, and (d) cliff valence band offset for n-type bournonite absorber. Low strain junction partner is shown in bold. Band alignment plots are produced using the bapt package.[40]

For the minimum energy (010)a termination of enargite, junction partners with low strain were found for both a cliff and a spike CBO (Table III). For this termination, Ce_2O_3 and Ce_2S_3 produced the lowest strain interfaces for a cliff and

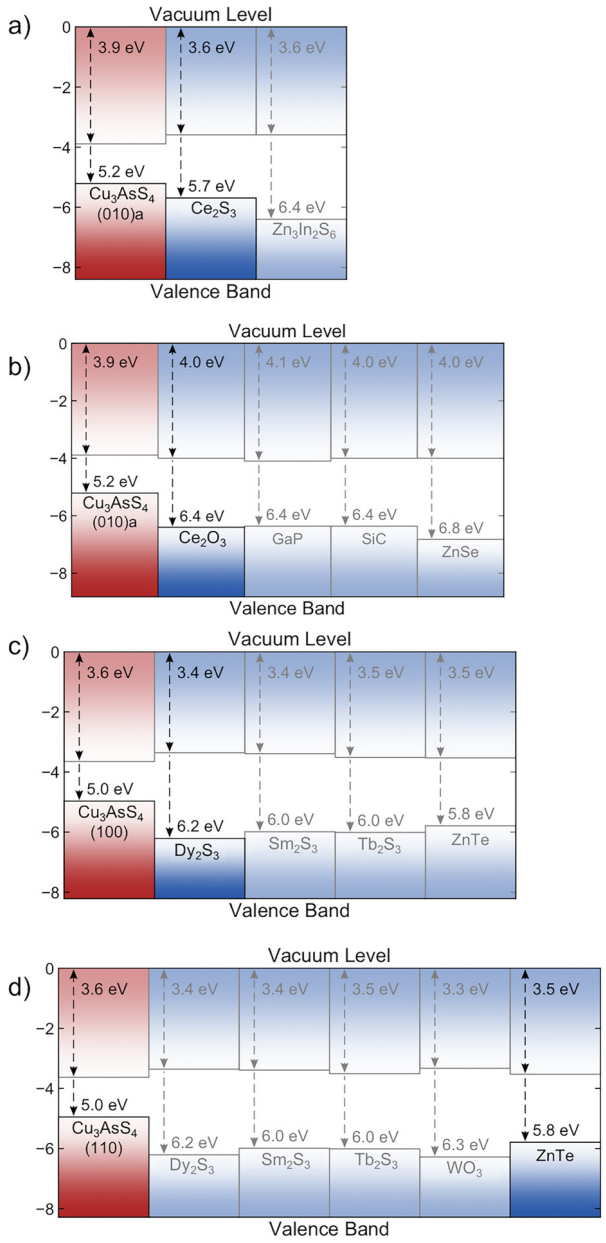

FIG. 4. Candidate junction partners for p-type enargite (Cu_3AsS_4) absorber layer termination (010)a for (a) spike conduction band offset (CBO), (b) cliff CBO, (c) spike CBO for (100) termination, and (d) spike CBO for (110) termination. A low strain junction partner is highlighted in each case. Band alignment plots produced using the bapt package.[40]

spike CBO, respectively. For the (100) and (110) terminations of enargite, only low-strain candidates were found for a spike CBO, but both terminations had a similar list of candidate junction partners. Dy_2S_3 produced the lowest strain interface with the enargite (100) surface. However, due to the rarity of Dy, Sm, and Tb, we regard candidates containing these elements as less desirable. ZnTe is a more promising candidate for the (100) termination. For the (110) surface, ZnTe is the minimum strain candidate, with WO_3 being another viable option. ZnTe is likely to be the most robust choice owing to the similar matching to the (100) and (110) surface of enargite, again providing that significant interface mixing or defect formation does not occur.

V. CONCLUSIONS

The aim of this study has been to provide a route forward for the development of solar cell technologies based on enargite and bournonite. By using a combination of data-mining and first-principles calculations, we have identified promising photovoltaic heterojunction partners for low-index surface terminations of Cu_3AsS_4 and $CuPbSbS_3$. The candidate partner materials include SnS_2, ZnTe, WO_3, and Bi_2O_3. Charge carrier effective masses and optical dielectric constants for Cu_3AsS_4 and $CuPbSbS_3$ were calculated in Ref. 8, and calculations for the defect properties of $CuPbSbS_3$ have been performed in Ref. 39.

One aspect not covered in this report is the potential photoferroic nature of these absorber materials and devices. Internal electric fields in polar semiconductors may suppress electron-hole recombination by enhanced local carrier separation[7] to provide a means of achieving high-efficiency solar cells. The orientation of electric polarization may influence the direction of charge transport and collection—as has been explored in photoanodes for photoelectrochemical water splitting applications.[42] These factors could determine the optimal growth and orientations for maximizing solar conversion efficiencies. Further work is required in this direction both in terms of atomistic and device modeling for non-conventional photovoltaic architectures.

SUPPLEMENTARY MATERIAL

See supplementary material for visuals of surface slab models, plots of electrostatic potentials across the slab models (used to calculate the ionisation potentials), materials project IDs for structure files of junction partners, and the full set of band alignment plots for all slab models in this work.

ACKNOWLEDGMENTS

We thank Jake Bowers, Elisabetta Arca, Ji-Sang Park, and Lee Burton for useful discussions. This work has been supported by the Engineering and Physical Sciences Research Council (EPSRC) (Grant Nos. EP/L016354/1 and EP/K016288/1). This work benefited from access to ARCHER, the UK's national high-performance computing service, which is funded by the Office of Science and Technology through EPSRC's High End Computing Programme (No. EP/L000202). This work was also supported by a National Research Foundation of Korea (NRF) grant funded by the Korean government (MSIT) (No. 2018R1C1B6008728).

This study used the MacroDensity[43] and ElectronLatticeMatch[23] python libraries. The workflow used in this study can also be obtained from the git repository at https://github.com/keeeto/ElectronicLatticeMatch. The input and output files for the DFT calculations are available from the NOMAD repository at https://dx.doi.org/10.17172/NOMAD/2018.10.25-1.

REFERENCES

[1]V. M. Fridkin and B. N. Popov, Soviet Phys. Usp. **21**, 981 (1978).
[2]W. Ruppel, R. V. Baltz, and P. Wurfel, Ferroelectrics **43**, 109 (1982).
[3]K. T. Butler, J. M. Frost, and A. Walsh, Energy Environ. Sci. **8**, 838 (2015).
[4]S. M. Young and A. M. Rappe, Phys. Rev. Lett. **109**, 116601 (2012).
[5]H. Heyszenau, Phys. Rev. B **18**, 1586 (1978).
[6]F. Wang and A. M. Rappe, Phys. Rev. B **91**, 165124 (2015).
[7]P. Lopez-Varo, L. Bertoluzzi, J. Bisquert, M. Alexe, M. Coll, J. Huang, J. A. Jimenez-Tejada, T. Kirchartz, R. Nechache, F. Rosei, and Y. Yuan, Phys. Rep. **653**, 1 (2016).
[8]S. K. Wallace, K. L. Svane, W. P. Huhn, T. Zhu, D. B. Mitzi, V. Blum, and A. Walsh, Sustain. Energy Fuels **1**, 1339 (2017).
[9]S. A. McClary, J. Andler, C. A. Handwerker, and R. Agrawal, J. Mater. Chem. C **5**, 6913 (2017).
[10]T. J. Whittles, T. D. Veal, C. N. Savory, A. W. Welch, F. W. de Souza Lucas, J. T. Gibbon, M. Birkett, R. J. Potter, D. O. Scanlon, A. Zakutayev, and V. R. Dhanak, ACS Appl. Mater. Interfaces **9**, 41916 (2017).
[11]F. Larsson, N. S. Nilsson, J. Keller, C. Frisk, V. Kosyak, M. Edoff, and T. Törndahl, Prog. Photovoltaics Res. Appl. **25**, 755 (2017).
[12]A. Crovetto and O. Hansen, Solar Energy Mater. Solar Cells **169**, 177 (2017).
[13]T. Song, A. Kanevce, and J. R. Sites, J. Appl. Phys. **119**, 233104 (2016).
[14]E. Arca, A. Fioretti, S. Lany, A. C. Tamboli, G. Teeter, C. Melamed, J. Pan, K. N. Wood, E. Toberer, and A. Zakutayev, IEEE J. Photovoltaics **8**, 110 (2018).
[15]A. Klein, J. Phys. Condens. Matter **27**, 134201 (2015).
[16]K. T. Butler, Y. Kumagai, F. Oba, and A. Walsh, J. Mater. Chem. C **4**, 1149 (2016).
[17]J. Nelson, *The Physics of Solar Cells* (Imperial College Press, 2003), Chap. 8
[18]A. J. Heeger, Adv. Mater. **26**, 10 (2013).
[19]R. Hoffman and J. Wager, Thin Solid Films **436**, 286 (2003).
[20]S. Oktyabrsky, see https://albany.edu/~soktyabr/NNSE618/NNSE618-L21-heterojunctions.pdf for "L21-heterojunctions"; accessed 21 June 2018.
[21]M. Gloeckler and J. Sites, Thin Solid Films **480–481**, 241 (2005).
[22]D. T. F. Marple, Phys. Rev. **129**, 2466 (1963).
[23]K. T. Butler, see https://github.com/keeeto/ElectronicLatticeMatch for "ElectronicLatticeMatch"; accessed 12 October 2018.
[24]K. Ohata, J. Saraie, and T. Tanaka, Jpn. J. Appl. Phys. **12**, 1641 (1973).
[25]J.-S. Park, J.-H. Yang, T. Barnes, and S.-H. Wei, Appl. Phys. Lett. **109**, 042105 (2016).
[26]Y. Kumagai, K. T. Butler, A. Walsh, and F. Oba, Phys. Rev. B **95** (2017).
[27]B. Monserrat, J.-S. Park, S. Kim, and A. Walsh, Appl. Phys. Lett. **112**, 193903 (2018).
[28]R. L. Anderson, IBM J. Res. Dev. **4**, 283 (1960).
[29]K. T. Butler, Y. Kumagai, F. Oba, and A. Walsh, J. Mater. Chem. C **4**, 1149 (2016).
[30]Y. Hinuma, Y. Kumagai, F. Oba, and I. Tanaka, Comput. Mater. Sci. **113**, 221 (2016).
[31]G. Kresse and J. Furthmüller, Comput. Mater. Sci. **6**, 15 (1996).
[32]G. Kresse and J. Furthmüller, Phys. Rev. B **54**, 11169 (1996).
[33]G. I. Csonka, J. P. Perdew, A. Ruzsinszky, P. H. T. Philipsen, S. Lebègue, J. Paier, O. A. Vydrov, and J. G. Ángyán, Phys. Rev. B **79**, 155107 (2009).
[34]P. E. Blöchl, Phys. Rev. B **50**, 17953 (1994).
[35]J. Heyd, G. E. Scuseria, and M. Ernzerhof, J. Chem. Phys. **118**, 8207 (2003).
[36]J. Bardeen, Phys. Rev. **49**, 653 (1936).
[37]T. Pauporte and D. Lincot, Adv. Mater. Optics Electron. **5**, 289 (1995).
[38]B. Durant and B. A. Parkinson, in *2016 IEEE 43rd Photovoltaic Specialists Conference* (PVSC) (IEEE, 2016).
[39]A. Faghaninia, G. Yu, U. Aydemir, M. Wood, W. Chen, G.-M. Rignanese, G. J. Snyder, G. Hautier, and A. Jain, Phys. Chem. Chem. Phys. **19**, 6743 (2017).
[40]A. Ganose, see https://github.com/utf/bapt for "Band alignment plotting tool"; accessed 24 September 2018.
[41]A. Jain, S. P. Ong, G. Hautier, W. Chen, W. D. Richards, S. Dacek, S. Cholia, D. Gunter, D. Skinner, G. Ceder, and K. A. Persson, APL Mater. **1**, 011002 (2013).
[42]W. Yang, Y. Yu, M. B. Starr, X. Yin, Z. Li, A. Kvit, S. Wang, P. Zhao, and X. Wang, Nano Lett. **15**, 7574 (2015).
[43]K. T. Butler, J. M. Frost, A. J. Jackson, and A. Walsh, see https://zenodo.org/record/884521 for "wmd-group/macrodensity."

6.2 Predicting and tuning the impact of absorber layer defects

Although cation disorder could be less prevalent in the multi-component absorber materials identified in chapter 5 than Cu/Zn disorder in Cu_2ZnSnS_4 (which was the topic of chapter 4) due to less chemical similarity of the components, this does not rule out other origins of performance limitation for these materials. For example, there is the possibility of other types of defects and non-optimal device architectures, which could have a detrimental impact on solar cell performance. For the latter, the work in the previous section proposed solar cell heterojunction partners for Cu_3AsS_4 and $CuPbSbS_3$ as a contribution towards an optimised device architecture for these absorber layers. This section focuses on the defect physics of solar cell absorber layers and the possibility of using knowledge gained from studies of more mature PV technologies to infer the likely impact of defects on the PV performance of new absorber layers. Although chapter 4 dealt with large-scale extended antisite defects in Cu_2ZnSnS_4, for new absorber materials an important foundation for understanding the defect physics is to first consider point defects as, essentially, larger-scale disordered structures are formed from these smaller units. In this section, hypotheses for predicting the impact of defects on PV performance are discussed and results are presented for some calculated defect properties of Cu_3AsS_4.

6.2.1 Tunability of equilibrium defect concentrations

Calculating the formation energy, $\Delta H_{D,q}$ of various types of defects in the absorber material can provide valuable insights for determining the performance of a solar cell made from the absorber. The impact of defects in high and low concentrations on solar cell performance were discussed in section 2.4. When a defect forms, there is a trade-off in the cost of breaking bonds and the gain in configurational entropy, S. The resulting crystal configuration will be that which minimises the Gibbs free energy

$$G = H - TS, \tag{6.1}$$

where H is the enthalpy.

The trade-off between H and TS results in an equilibrium defect concentration, n, where

$$n = N\mathrm{e}^{\frac{-\Delta H_{D,q}}{k_\mathrm{B}T}}, \tag{6.2}$$

which depends on the formation energy of the defect, $\Delta H_{D,q}$, and the number of lattice sites, N. As shown in Eq. 3.37 and 3.38 in section 3.3, $\Delta H_{D,q}$ directly depends on the chemical potential of the species involved in the creation of the defect, μ_i. μ_i can be tuned experimentally as it is a function of temperature and pressure [227]. Consequently, this allows for some tunability in the concentrations of particular defects in an absorber material through the synthesis conditions.

6.2.2 Predicting the impact of point defects

Point defect calculations

As mentioned in the previous section, the formation energy of defects depends upon the chemical potential of the species and, as shown in Eq. 3.38 for charged defects in section 3.3, the formation energy of a defect may change as a function of the Fermi energy, i.e. the electron chemical potential. Fig. 6-1 from Ref. [67] shows an example analysis of the defect physics of Cu_2ZnSnS_4. The figure shows the formation energies of various intrinsic defects in Cu_2ZnSnS_4 for one particular point in the chemical potential space for phase-pure Cu_2ZnSnS_4 as a function of the Fermi energy. The Fermi energy is initially referenced to the VBM of the perfect host and set to zero and then tuned out to the other extreme in the electron chemical potential (the CBM of the host) to determine the transition levels between different charge states of an ionised defect. The ionisation levels of intrinsic defects in Cu_2ZnSnS_4 from Ref. 67 were shown early in this thesis in Fig. 2-10. The transition or ionisation levels can be determined from the turning points between different charge transition states in Fig. 6-1. The depth of defect transition levels can be used to determine if low energy defects can produce free carriers to contribute to electrical conductivity (for instance, if the defect-induced energy levels are within $k_{\mathrm{B}}T$ of the band edges to allow for thermal excitation of the charge carrier into the bands), or if the defects are likely to be a centre for Shockley-Read-Hall recombination (if levels are deep in the band gap) [66].

Further insights can be gained from plots such as Fig. 6-1. For each value of the Fermi energy, only the formation energy of the defect in its lowest formation energy charge state is shown. The charge state of the defect can be inferred from the gradient of the line in Fig. 6-1. A flat line corresponds to a neutral defect, as its formation energy is independent of the Fermi energy, the gradient is positive for a donor defect and negative for an acceptor defect. If the defect is doubly charged, the slope will be twice as steep. A plot showing formation energies for all likely defects in a material can be

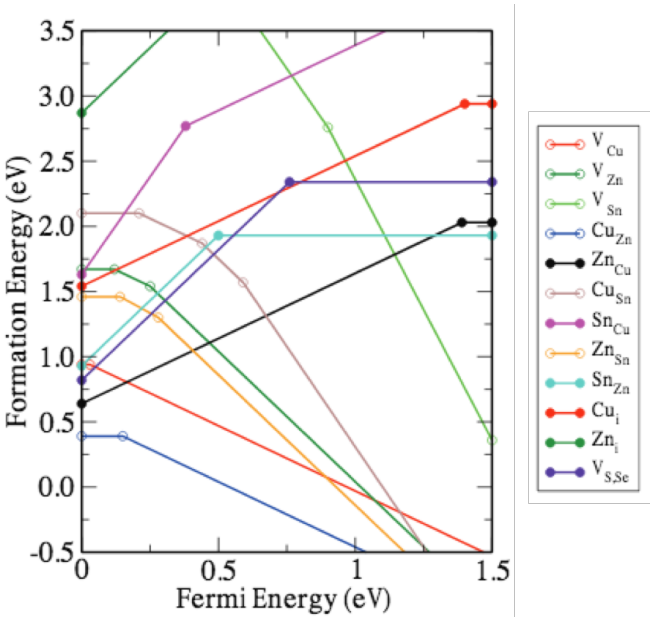

Figure 6-1: The change of the defect formation energy, $\Delta H_{D,q}$, in Cu_2ZnSnS_4 as a function of the Fermi energy at one point in the chemical potential for phase-stable Cu_2ZnSnS_4. The most stable charge state is plotted for a given Fermi energy. Figure reproduced with permission from Ref. 67.

used to determine if the material is likely to exhibit n-type or p-type conductivity from the relative formation energy of acceptor and donor defects. Plots such as Fig. 6-1 can also be used to determine if Fermi level pinning (limiting quasi fermi level splitting in a solar cell) could occur in a material based on the point defects. This can be inferred from any point defect formation energies becoming spontaneous for certain values of the Fermi energy or from crossing points between acceptor and donor defects, indicating approximately the Fermi energy at which compensation will happen in either direction.

Hypotheses for predicting the defect physics of Cu_3AsS_4

As discussed in the previous sections, a wealth of information on the defect properties of an absorber material, the implications for its performance as a solar cell and the tunability of the optoelectronic properties can be obtained from electronic structure calculations of point defects. A fuller understanding of the defect properties is likely to require considerations of defect pairs and extended defect structures such as grain boundaries in the multi-component, polycrystalline materials that are usually used in thin-film solar cells. However, the analysis of even just point defects from electronic structure calculations is a very computationally demanding process. In multinary semi-

conductors, there is a large number of different possible defects resulting in a large set of calculations to perform with large supercells to minimise finite-size effects (discussed in section 3.3). This section highlights some hypotheses from the literature for inferring the defect physics of a material without performing electronic structure calculations for all possible defect structures in a material. Hypotheses that could be tested with this case study for Cu_3AsS_4 are outlined.

The ability to determine if the performance of a material in a solar cell is likely to be severely hindered by the presence of defects, before performing any electronic structure calculations or synthesising the material, would clearly be a very powerful tool in high-throughput searches for new absorber materials for high-performance solar cells. Research efforts have sought to determine descriptors for 'defect-tolerance' by analogy to lead halide perovskites [228] due to the remarkable resilience of the observed optoelectronic properties of the absorber in highly defective, solution-processed solar cells [229, 230]. However, inferring any universal trends and design principles that are applicable across all material classes is very challenging. The defect physics of a material is typically a very idiosyncratic property of the material with the interplay of many subtle effects.

One of the material properties of the lead halide perovskites that has been related to the observed defect-tolerance is the particularly large static (low-frequency) dielectric constant, ϵ_s [228]. Consequently, ϵ_s has been proposed as one metric for determining how defect-tolerant a solar absorber is likely to be. A material with a larger ϵ_s is capable of more substantial charge screening, resulting in smaller defect charge-capture cross-sections and inhibiting radiative electron-hole recombination [231]. A number of works have hypothesised that the bonding character at the band extrema of a material may be related to the depth of defect levels [230, 232, 228, 230]. It has been proposed that antibonding states at the VBM imply shallower defects. The real component of the electron wavefunction of the highest occupied state in Cu_3AsS_4 from the paper presented in section 5.2 [233] is shown again in Fig. 6-2a with the partial electronic density of states (pDOS) of Cu_3AsS_4 shown in Fig. 6-2b. The opposite parity of neighbouring S p-orbitals and Cu d-orbitals in Fig. 6-2a indicates antibonding character at the VBM of Cu_3AsS_4.

General trends between the bonding character at the band extrema of different materials and their defect physics are yet to be confirmed, however, in a number of multinary Cu-based materials, Cu vacancies are found to be shallow with low formation energy. This has been shown to be the case in Cu_2ZnSnS_4 [67] and $CuInSe_2$ [234] and the p-type conductivity of $CuInSe_2$ is attributed to this intrinsic defect. For Cu_2ZnSnS_4,

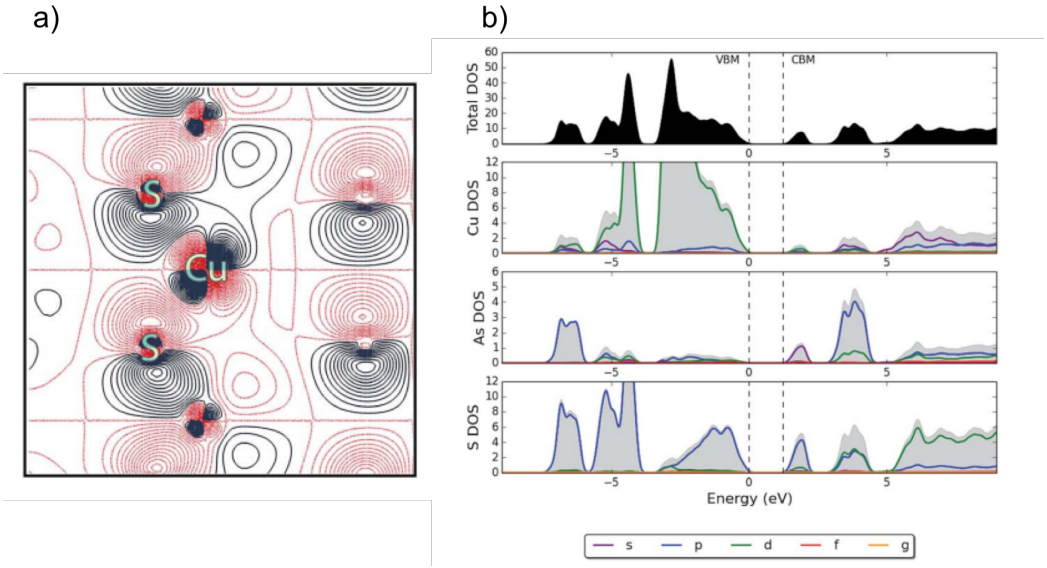

Figure 6-2: a) The real component of the electron wavefunction of the highest occupied state in Cu_3AsS_4. b) Partial electronic density of states (pDOS) of Cu_3AsS_4, where the top of the valence band has been set to 0 eV. Figure reproduced with permission from Ref. 233.

this observation has been rationalised in Ref. 235 as follows: 'Bonds in Cu-based quaternaries are weaker than in group-IV, III-V or II-VI binaries, the former have Cu-d-S/Se-p antibonding states (+sp3) while latter have purely sp3 which are stronger bonds'. From the bonding character shown at the VBM of Cu_3AsS_4 in Fig. 6-2b, we may also expect shallow Cu vacancies with low formation energies in this material, to possibly provide further confirmation of this trend. Additionally, available experimental data for Cu_3AsS_4 suggests that this material will also exhibit p-type conductivity [236, 237]. This observation implies shallow acceptor defects with low formation energies in Cu_3AsS_4 either from instrinsic defects, such as Cu vacancies, or due to the presence of impurities.

6.2.3 Defect physics of enargite, Cu_3AsS_4

Construction of defect supercells

Electronic structure calculations to predict the formation energy of isolated point defects in Cu_3AsS_4 are performed using the methodology outlined in section 3.3 using the supercell method with the all-electron electronic structure code FHI-aims. A $2 \times 2 \times 2$ supercell of the enargite unit cell was constructed (shown in Fig. 6-3b and

6-3a respectively). The $2 \times 2 \times 2$ supercell contains 128 atoms with dimensions of $14.86 \times 12.91 \times 12.33 \text{Å}^3$. This is the largest and most isotropic system for the desired level of theory. As mentioned in the methodology section, standard DFT methodology often results in underestimation of the electronic band gap, which can lead to inaccurate defect calculations [142, 143]. For this reason, calculations are performed using the HSE06 hybrid-DFT functional, also outlined in the methodology section.

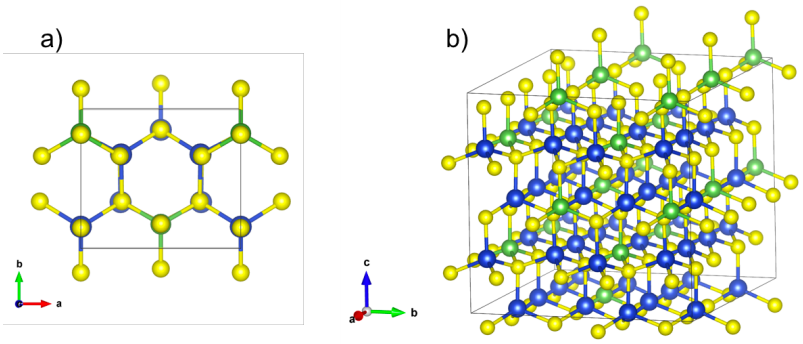

Figure 6-3: a) Unit cell of enargite (Cu_3AsS_4) and b) $2 \times 2 \times 2$ supercell containing 128 atoms with dimensions $14.86 \times 12.91 \times 12.33 \text{Å}^3$.

The supercell is constructed from a unit cell where the volume has been relaxed with a tolerance of with the HSE06 functional, including spin-orbit coupling (SOC), a $4 \times 4 \times 4$ k-grid and tabulated 'tight' basis set species defaults for the FHI-aims software package. It is important that the unit cell volume is relaxed before constructing the defect supercells as even slight differences in the lattice parameters for the given functional relative to the experimental values used in the study in section 5.2 could result in spurius ionic relaxations once a defect has been introduced into the supercell to compensate for the strain. To generate the supercell structures for all symmetrically inequivalent on site vacancy defects in Cu_3AsS_4, Transformer python libraries [238] (which utilise spglib crystal symmetry python libraries [239]) were used.

For the relaxation of the defect supercells, however, the lattice parameters are fixed and only internal atomic coordinates are relaxed. Allowing lattice parameters to relax in the defective supercells could result in excessive defect-induced relaxation which would be expected for a higher defect density than for isolated point defects in the dilute limit, which is being simulated here. Relaxations of the defect supercells are also performed using HSE06+SOC. The structures are first pre-relaxed with the 'light' species defaults, this is often recommended when using FHI-aims to reduce the number of geometry steps required at the 'tight' level of accuracy. The resulting structures are then relaxed with tight basis set species defaults. Relaxation is performed at the

gamma point and then a single-shot calculation is performed with a $2 \times 2 \times 2$ k-grid and including SOC.

Construction of phase diagram

As discussed in section 3.3, to obtain the formation energy of a defect it is necessary to know the chemical potentials of species added to or removed from the system when a defect is formed. We therefore need to know the range of chemical potentials for the synthesis of phase-pure material. For this, the total energies of the constitutent elements and formation energies of all competing secondary phases needed to be computed at the same level of theory as used for the defect calculations.

The range of chemical potentials must satisfy certain thermodynamic conditions for the desired compound to be thermodynamically stable without coexistence of unwanted secondary phases. Firstly, the sum of chemical potentials of the component elements should be at equilibrium with the formation energy of the compound. Secondly, the formation of the secondary compounds should be avoided. Lastly, all component elements should favour the formation of the compound, as opposed to pure elemental phases [139]. Examples of such conditions for enargite are shown in Eq. 6.3, 6.4 and 6.5, where As_2S_3 is an example of an unwanted competing phase and ΔH_f is the formation energy of a compound.

$$3\mu_{Cu} + \mu_{As} + 4\mu_S = \Delta H_f(Cu_3AsS_4). \tag{6.3}$$

$$2\mu_{As} + 3\mu_S < \Delta H_f(As_2S_3). \tag{6.4}$$

$$\mu_{Cu}, \mu_{As}, \mu_S < 0. \tag{6.5}$$

To determine the range of chemical potentials satisfying conditions such as those shown above, the CPLAP software package is used [240].

To determine all competing secondary phases for Cu_3AsS_4, the Materials Project [202] database was searched for all compounds containing Cu, As and S that were stable or with formation energy up to 0.1 eV per atom above the thermodynamic convex hull. The volume of the unit cell for each compound were relaxed with the HSE06 functional and including SOC. The light species defaults were used for the relaxation followed by a single-shot calculation with tight species defaults to ensure the level of theory matched

that of the defect calculations of Cu_3AsS_4. k-grid densities were set for a total number of k-points of 2000/(no. of atoms in unit cell) for insulators but a more dense setting of 10,000/(no. of atoms in unit cell) was used for metals.

Element	Total energy (eV)	No. atoms in unit cell	Energy per atom (eV)
Cu	-180982.234	4	-45245.558
As	-371370.779	6	-61895.130
S	-348162.585	32	-10880.081

Table 6.1: Elemental energies of components in enargite (Cu_3AsS_4) in their standard states calculated with the HSE06 functional and including SOC.

Calculated total energies of relaxed structures for the secondary compounds and elemental components in their standard states were used to determine the formation energies, ΔH_f, of the compounds. The energy of the elemental species were obtained as the total energy of the structure in the standard state divided by the number of atoms in the unit cell. The formation energies of the compounds were determined by the difference in energy between reactants and products by dividing the total energy of the compound by the number of formula units in the unit cell and subtracting the energies of the elemental components. Elemental energies are given in Table 6.2.3, formation energies of competing phases computed from these elemental values are are given in Table 6.2 for stable compounds and in Table 6.3 for unstable competing phases with formation energy of up to 0.1 eV per atom above the convex hull, as listed on the Materials Project database.

The phase diagram for enargite is shown in Fig. 6-4 with a, b and c corresponding to fixed chemical potential for Cu, S and As respectively. The grey region in each

Compound	Total energy (eV)	F.U. in unit cell	ΔH_f (eV)
Cu_3AsS_4	-482309.063	2	-2.403
As_2S_3	-625725.232	4	-0.806
AsS	-1164408.821	16	-0.341
$Cu_{12}As_4S_{13}$	-1863952.980	2	-8.219
$Cu_6As_4S_9$	-1233959.866	2	-5.336
Cu_7S_4	-1440968.101	4	-2.793
CuS_2	-134011.919	2	-0.240
CuAsS	-472086.216	4	-0.785
CuS	-336756.853	6	-0.503

Table 6.2: Formation energies of stable secondary phases for the phase diagram of Cu_3AsS_4 calculated with the HSE06 functional and including SOC.

Compound	Energy above hull (eV per atom)	Total energy (eV)	F.U. in unit cell	ΔH_f (eV)
As_4S_3	0.004	-1120887.027	4	-0.995
As_4S_5	0.003	-603964.775	2	-1.464
As_8S_9	0.003	-1186169.186	2	-2.827
$Cu_{18}S_{11}$	0.076	-934107.329	1	-6.389
Cu_2As	0.02	-304772.545	2	-0.026
Cu_2S	0.01	-608229.920	6	-0.456
Cu_3As	0.019	-1581055.864	8	-0.178
Cu_3AsS_3	0.032	-921094.597	4	-1.602
Cu_5As_2	0.05	-700036.355	2	-0.125
Cu_9S_5	0.045	-923227.266	2	-3.203
CuAs	0.052	-214280.966	2	0.205
$CuAs_2$	0.081	-338070.681	2	0.478

Table 6.3: Formation energies of unstable secondary phases with formation energy as listed on the Materials Project database of up to 0.1 eV per atom above the convex hull for the phase diagram of Cu_3AsS_4 calculated with the HSE06 functional and including SOC.

Int. point	μ_{Cu}	μ_{As}	μ_S
1	-0.563	-0.216	-0.125
2	-0.667	-0.403	0.000
3	-0.347	0.000	-0.341
4	0.000	-0.544	-0.465
5	-0.182	0.000	-0.465
6	0.000	-2.403	0.000
7	-0.478	-0.216	-0.188
8	-0.551	-0.403	-0.087
9	-0.316	0.000	-0.364
10	0.000	-2.055	-0.087

Table 6.4: Intersection points in chemical potential space from the phase diagram for enargite (Cu_3AsS_4) shown in Fig. 6-4, where μ_i is referenced to the total energy of the element phase in its standard state.

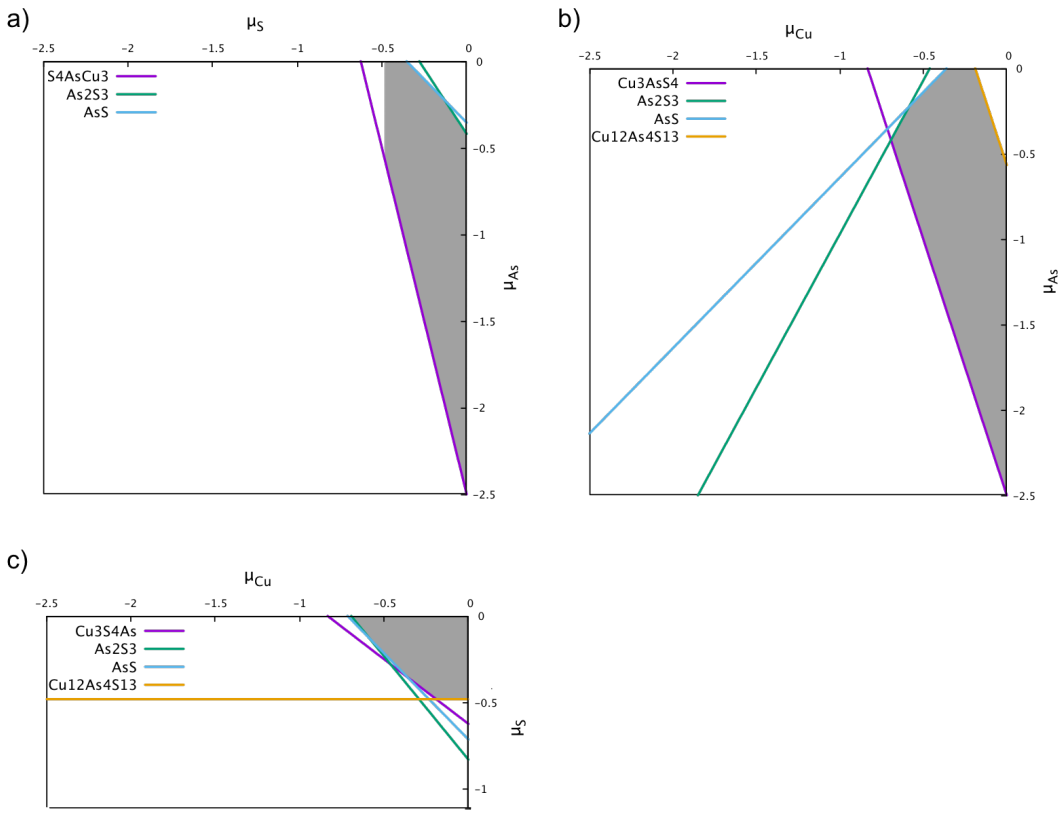

Figure 6-4: Phase diagram for enargite (Cu_3AsS_4) calculated with the HSE06 functional and including spin-orbit coupling. Plot generated using the CPLAP software package [240].

plot shows the region of phase stability for Cu_3AsS_4. This therefore determines the maximum range that the atomic chemical potentials could be tuned to influence the defect physics of Cu_3AsS_4 whilst allowing for the synthesis of phase-pure material. The intersection points in chemical potential space from the Cu_3AsS_4 phase diagram are given in Table 6.4.

Calculation of static dielectric constant

As outlined in section 3.3, the static (low frequency) dielectric constant, ϵ_s, is required to implement existing finite-size correction schemes for periodic electronic structure calculations of charged defects with the supercell method. Additionally, as outlined at the start of this section, a large ϵ_s has been proposed as a metric for predicting if a PV material is likely to be 'defect-tolerant' [228]. Therefore this is an important material property of Cu_3AsS_4 to calculate to gain further insights into the defect physics of this

absorber.

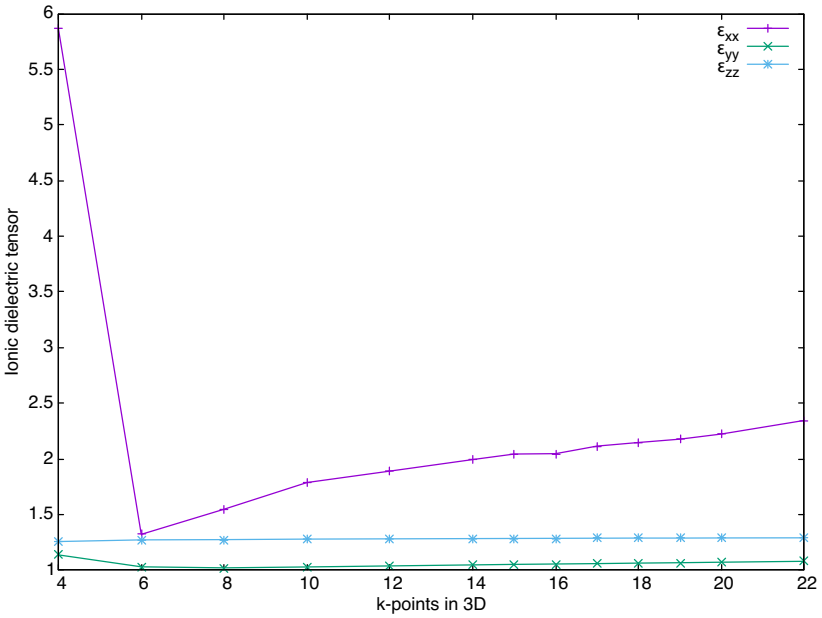

Figure 6-5: Ionic dielectric constant of enargite (Cu_3AsS_4) calculated from density functional perturbation theory with the PBEsol functional with increasing k-grid density.

In a solid in the absence of free dipole rotations, the dielectric response to a static perturbing electric field, such as that from a charged defect within the host lattice, is described by the electronic and ionic components of the static dielectric constant of the solid

$$\epsilon_{\mathrm{s}} = \epsilon_{\infty} + \epsilon_{\mathrm{ionic}}. \tag{6.6}$$

The static limit of the electronic component (ϵ_{∞}) is taken, i.e. $\epsilon_{\infty}(\omega \to 0)$, from the optical dielectric function calculated using the random phase approximation as implemented in FHI-aims for Cu_3AsS_4 in the study presented in section 5.2 [233]. The ionic dielectric constant is calculated with density functional perturbation theory (DFPT) with the PBEsol functional as implemented in the VASP [106] software package. The volume of the unit cell is first relaxed with VASP with the PBEsol functional with a k-grid density of $6 \times 6 \times 6$ and a plane wave cut off energy of 500 eV. Before computing the ionic dielectric constant it is important to have a well-optimised relaxed structure for the unit cell, for this reason strict relaxation criteria are used. The allowed error in total energy (i.e. the exit criteria for the electronic scf cycle) is reduced from the default value of 10^{-4} to 10^{-8} and ionic relaxation is performed until forces converge to within $0.001\,\mathrm{eV\AA^{-1}}$. The ionic dielectric constant is then computed with DFPT for

this relaxed unit cell with increasing k-grid density. This is shown in Fig. 6-5.

$10\times10\times10$ k-points is taken as sufficient for convergence in the ionic dielectric constant although, as shown in Fig. 6-5, the xx component showed poor convergence. The value calculated with $20\times20\times20$ k-points is 1.24 times larger than the value at $10\times10\times10$ k-points. Combining the ionic dielectric constant with data for the electronic dielectric constant from the study presented in section 5.2, gives the total static dielectric constant tensor

$$\epsilon_{\mathrm{s}} = \begin{bmatrix} 7.49 & 0 & 0 \\ 0 & 6.92 & 0 \\ 0 & 0 & 7.19 \end{bmatrix}. \tag{6.7}$$

The electronic contributions to the dielectric tensor of Cu_3AsS_4 (calculated in the study presented in section 5.2 [233]) of approximately 6 are comparable to those of other well-studied solar absorber materials such as CdTe and methylammonium lead iodide (MAPI) [241]. However, the ionic contributions shown in Fig. 6-5 are very modest, especially compared to the exceptionally large values of up to approximately 30 along some crystallographic directions for MAPI as calculated in Ref. 241. This could imply that, compared to the remarkable defect-tolerance of the observed optoelectronic properties of MAPI, more defect-induced charge-carrier scattering and recombination could be expected in Cu_3AsS_4.

Charge neutral vacancies in Cu_3AsS_4

To calculate the formation energy of charge neutral defects, Eq. 3.37 from section 3.3 is used with the total energies of the relaxed defect supercells, the total energy of an equivalent perfect host supercell and the total energy per atom in the standard states for elements added to or removed from the host are taken from Table 6.2.3. All ten intersection points in the chemical potential space from Table 6.4 are used. The intention here is to determine the values for the species chemical potentials that increase the formation energy of the defects, especially any that may be found to be detrimental to device performance.

Calculated defect formation energies of charge neutral vacancies in Cu_3AsS_4 are presented in Table 6.5. Here we focus only on site vacancies, which are defects that are likely to form in abundance. Future work could consider interstitials and antisites in all possible charge states, but owing to the low symmetry of Cu_3AsS_4 (space group 31), there are many possible configurations for defects. Table 6.5 shows that there are many points in the chemical potential space where formation energies of neutral Cu

Defect	E_{tot} (eV)	$\Delta H_{D,q=0}$ at all 10 intersection points for μ_i (eV)									
		1	2	3	4	5	6	7	8	9	10
$V_{S,q=0}$, sg1	-3847591.66	0.78	0.90	0.56	0.44	0.44	0.90	0.71	0.82	0.54	0.82
$V_{S,q=0}$, sg6, s1	-3847591.62	0.81	0.94	0.60	0.47	0.47	0.94	0.75	0.85	0.57	0.85
$V_{S,q=0}$, sg6, s2	-3847591.81	0.62	0.75	0.41	0.28	0.28	0.75	0.56	0.66	0.39	0.66
$V_{Cu,q=0}$, sg1	-3813225.74	0.77	0.67	0.99	1.34	1.16	1.34	0.86	0.79	1.02	1.34
$V_{Cu,q=0}$, sg6	-3813225.75	0.77	0.66	0.98	1.33	1.15	1.33	0.85	0.78	1.01	1.33
$V_{As,q=0}$, sg6	-3796572.40	4.89	4.71	5.11	4.57	5.11	2.71	4.89	4.71	5.11	3.06

Table 6.5: Formation energies, $\Delta H_{D,q=0}$ of charge neutral vacancies in enargite (Cu_3AsS_4) at all 10 intersection points in the chemical potential space for enargite from Table 6.4. E_{tot} are total energies of the defective supercells and defects are labelled according to their spacegroup (sg) and unique structure (s) as identified by crystal symmetry using Transformer libraries [238].

and S vacancies are less than 1 eV, implying appreciable concentrations of these defects. Firstly, this implies that Cu_3AsS_4 may fit the trend of low formation energies for Cu vacancies observed for Cu_2ZnSnS_4 and $CuInSe_2$, as discussed earlier in this section. Secondly, the low formation energies of S vacancies implies that sulfur partial pressure should be carefully controlled during the synthesis of Cu_3AsS_4. A number of studies on the synthesis of Cu_2ZnSnS_4 thin-films for solar cells have found that device performance is very sensitive to sulfur vapour pressure during the synthesis of the absorber [242, 243, 244].

Chapter 7

Closing remarks

The subject of this PhD thesis has been to investigate current performance limitations of metal sulfide solar cells. This study is motivated by the possibility of using these technologies to contribute towards achieving the goal of terawatt-scale power production from renewable energy resources. There were two major components to this study. Firstly, to investigate possible origins of the performance deficit of solar cells based on the earth-abundant and non-toxic candidate absorber material Cu_2ZnSnS_4. This was the subject of chapter 4. The second major component of this work has been to identify and assess the likely photovoltaic (PV) performance of candidate photoactive ferroelectric ('photoferroic') absorber materials to enable the exploration of possible alternative pathways to high-performance solar cells. This was the subject of chapter 5 and chapter 6.

7.1 Cu/ Zn disorder in Cu_2ZnSnS_4 solar cells

In chapter 4, various possible origins for the open circuit voltage (V_{OC}) deficit, and hence performance deficit, of Cu_2ZnSnS_4 solar cells were discussed and a computational model was developed to investigate one of the possible origins. The bespoke Monte Carlo model developed to simulate thermodynamic Cu/Zn disorder in Cu_2ZnSnS_4 enabled atomistic insights into the Cu/ Zn order-disorder transition. Our model indicated that this disorder process involved substitutions onto the Cu $2a$ sites as well as the Cu $2c$ sites. We were able to investigate the spatial distribution of Cu^{-}_{Zn} and Zn^{+}_{Cu} antisites at various simulation temperatures and generate disordered lattice configurations.

Electronic band tailing has been observed in all Cu_2ZnSnS_4 solar cells and has been linked to the V_{OC} deficit. A further investigation that could be conducted with the lattice configurations generated by our model, as introduced at the end of chapter 4, would be to calculate on-site electrostatic potentials in the lattice to explore the possible connection between Cu/ Zn disorder in Cu_2ZnSnS_4 and electronic band tailing from fluctuations in electrostatic potential. Confirming a link between high concentrations of cation disorder in materials with very chemically similar components and electronic band tailing would provide a general design principle for improving the efficiency of PV absorbers. A number of studies are already exploring substituting Cu and Zn with less chemically similar species in an attempt to suppress cation disorder to reduce band tailing [245, 246, 247].

An extension of our Monte Carlo model that could provide valuable insights into the performance deficit of Cu_2ZnSnS_4 solar cells would be to investigate if cation disorder is suppressed in off-stoichiometric Cu_2ZnSnS_4 types [248, 249]. Another extension could be to investigate Sn related defects and, specifically, if the presence of extended Cu/ Zn defect structures could lower the formation energy of such defects (which are thought to have the largest impact on the band-edges [187]), relative to the formation energies predicted for Sn related defects in a perfect host lattice in the dilute limit as performed in Ref. 67.

7.2 Candidate photoferroic absorbers in solar cells

A number of exciting PV phenomena have been observed in ferroelectric materials, as outlined in section 5.1, which could provide alternative pathways to achieving high-performance solar cells with enhanced local carrier separation from the internal electric fields of polar crystals and the possibility of increased photovoltages. Most known ferroelectric materials have band gaps that are considerably larger than the ideal range for solar absorption. The aim of chapter 5 was to identify candidate photoferroic absorbers with band gaps that are well-matched to the solar spectrum. However, at this stage it is unclear if these novel materials will provide new pathways to high-performance or result in additional complexity in solar cell fabrication, such as depolarisation fields at device interfaces [197] and if static ferroelectric domains could act as internal diodes to hinder charge-carrier transport. Experimental studies or device modelling of these absorber materials may be able to provide further insights here.

The aim of chapter 6 was to provide insights that may accelerate the optimisation of

solar cells made from these absorbers to enable the investigation of possible novel PV effects in these materials. In section 6.1.1 we provide suggestions for junction partners for two of the candidates identified in chapter 5, including options for 'spike-like' offsets in certain cases which are thought to result in more defect-tolerant heterojunctions in CdTe and CIGS solar cells [224, 225]. Further investigations for an optimal device architecture could be to explore candidates for the back contact of the solar cells. In section 6.2.3, we present the formation energies of neutral vacancy defects in Cu_3AsS_4 and relate this to the defect physics of more mature PV technologies and implications for optimal processing conditions for the material. Future work for predicting the defect physics of Cu_3AsS_4 would be to calculate the formation energies of all possible intrinsic defects, including antisites and interstitials, in all possible charge states and to predict the depth of defect levels in the band gap of the absorber.

7.3 Future of theory and simulation for photovoltaic materials

With the availability of high performance computing resources and advances in materials simulation techniques, we are in an exciting era for computational materials science. Electronic structure theory has advanced to a level that is able to achieve good quantitative agreement with experiment [39] and the development of materials properties databases now provide a valuable source of information for identifying materials with the potential for high-performance in various applications, such as PV energy generation. However, many of the materials that are of current technological interest for PV pose challenges both for synthesis as well as for the theory and simulation of these materials.

Many current research efforts are focused on multi-component materials, such as the candidate PV absorber Cu_2ZnSnS_4. Exploring more possible combinations of materials from binary, to ternary and quaternary allows material properties to be tuned to suit the specific application. However, the cost of such tunability is often the ease of synthesis, such as the very narrow region of the phase-diagram of Cu_2ZnSnS_4 to achieve phase-pure material [186] and larger numbers of possible detrimental secondary phases. Multi-component materials also allow for a vast range of possible defects. While not all defects are necessarily detrimental to performance [66], this poses a challenge for simulation due to the large variety of possible defect structures to consider. The formation of larger, extended defect structures are also more likely in multi-component

systems, such as those resulting from Cu/ Zn disorder in the study presented in section 4.3.2 [159]. Furthermore, thin-film solar cell technologies are usually based on polycrystalline materials with many grain boundaries and internal structures which deviate substantially from models of perfect, periodic crystals and much more so than would be expected for monocrystalline materials.

To accurately predict the optoelectronic properties of materials with large structural features, which could be expected in polycrystalline, multi-component materials, typically requires the accuracy of quantum-mechanical models with electronic structure calculations. However, performing such calculations for many possible configurations of large structures can become prohibitively computationally demanding. Materials of current technological interest highlight a need to combine different simulation techniques with the aim of allowing for the accuracy of quantum-mechanical models with the computational efficiency of less demanding approaches. Machine learning techniques are increasingly being utilised in materials science [250, 251]. One such example is recent developments of machine learning interatomic potentials [252, 253]. This data-driven approach constructs interatomic potentials using machine learning techniques with data from electronic structure calculations and aims to allow simulations to go far beyond the time- and length-scale regimes that are presently accessible using quantum-mechanical methods [254]. This is still a developing field with key challenges such as the development of optimal representations of atomic structures to use in the training procedure and systematic methods for producing the dataset of electronic structure calculations the model is trained on to ensure that it is sufficiently diverse and representative of the system [252]. However, such techniques could enable a deeper understanding of many of the multi-component candidate absorber materials for thin-film solar cells.

Bibliography

[1] F. Creutzig, P. Agoston, J. C. Goldschmidt, G. Luderer, G. Nemet, and R. C. Pietzcker, "The underestimated potential of solar energy to mitigate climate change," *Nature Energy*, vol. 2, no. 9, p. 17140, 2017.

[2] European Photovoltaic Industry Association, "Global market outlook for photovoltaics 2014-2018," 2014.

[3] J. Jean, P. R. Brown, R. L. Jaffe, T. Buonassisi, and V. Bulovic, "Pathways for Solar Photovoltaics," *Energy Environ. Sci.*, 2015.

[4] Massachusetts Institute of Technology, "The future of solar energy." http://mitei.mit.edu/system/files/MIT%20Future%20of%20Solar%20Energy%20Study_compressed.pdf. Accessed: 2018-03-28.

[5] BP p.l.c., "Solar energy." https://bp.com/en/global/corporate/energy-economics/statistical-review-of-world-energy/renewable-energy/solar-energy.html. Accessed: 2018-11-03.

[6] S. J. C. Irvine, *Materials Challenges: Inorganic Photovoltaic Solar Energy*. RSC Energy and Environment Series, 2014.

[7] A. Polman, M. Knight, E. C. Garnett, B. Ehrler, and W. C. Sinke, "Photovoltaic materials: Present efficiencies and future challenges," *Science*, vol. 352, no. 6283, 2016.

[8] University of Oregon Investment Group, "First solar, inc." http://uoinvestmentgroup.org/wp-content/uploads/2011/01/FSLR.pdf. Accessed: 2018-03-28.

[9] The German Energy Society, "Planning and installing photovoltaic systems," ch. Introduction and the history of photovoltaics, Routledge, 2013.

[10] D. W. Lane, K. J. Hutchings, R. McCracken, and I. Forbes, "Materials challenges: Inorganic photovoltaic solar energy," ch. New Chalcogenide Materials for Thin Film Solar Cells, The Royal Society of Chemistry, 2015.

[11] Fraunhofer Institute for Solar Energy Systems, ISE, "Photovoltaics report." https://www.ise.fraunhofer.de/content/dam/ise/de/documents/publications/studies/Photovoltaics-Report.pdf. Accessed: 2019-03-30.

[12] J. E. Girard, *Principles of Environmental Chemistry.* Jones & Bartlett Learning, LLC, 2014.

[13] M. A. Green, Y. Hishikawa, E. D. Dunlop, D. H. Levi, J. Hohl-Ebinger, M. Yoshita, and A. W. Ho-Baillie, "Solar cell efficiency tables (version 53)," *Progress in Photovoltaics: Research and Applications*, vol. 27, pp. 3–12, dec 2018.

[14] T. Saga, "Advances in crystalline silicon solar cell technology for industrial mass production," *NPG Asia Mater.*, vol. 2, no. 3, pp. 96–102, 2010.

[15] W. Shockley and H. J. Queisser, "Detailed balance limit of efficiency of pn junction solar cells," *Journal of Applied Physics*, vol. 32, no. 3, 1961.

[16] Tom Veeken, "S-q charts." http://www.lmpv.nl/sq/. Accessed: 2019-04-05.

[17] US Department of Energy, "Energy efficiency and renewable energy: 2008 solar technologies market report," 2010.

[18] W. Hermes, D. Waldmann, M. Agari, K. Schierle-Arndt, and P. Erk, "Emerging Thin-Film Photovoltaic Technologies," *Chemie Ingenieur Technik*, vol. 87, no. 4, pp. 376–389, 2015.

[19] H. W. Schock *Adv. Solid State Phys.*, p. 147, 1994.

[20] K. R. et al *Prog. Photovolt. Res. Appl.*, 2003.

[21] C. Persson and A. Zunger, "Anomalous Grain Boundary Physics in Polycrystalline $CuInSe_2$: The Existence of a Hole Barrier," *Phys. Rev. Lett.*, vol. 91, p. 266401, 2003.

[22] C. Persson and A. Zunger, "Compositionally induced valence-band offset at the grain boundary of polycrystalline chalcopyrites creates a hole barrier," *Appl. Phys. Lett.*, vol. 87, no. 21, p. 211904, 2005.

[23] J. Yan and B. R. Saunders, "Third-generation solar cells: a review and comparison of polymer:fullerene, hybrid polymer and perovskite solar cells," *RSC Adv.*, vol. 4, pp. 43286–43314, 2014.

[24] Y. Yan, W.-J. Yin, T. Shi, F. Hong, J. Ge, Y. Yue, W. Ke, D. Zhao, and A. Cimaroli, "Theoretical and experimental study of earth-abundant solar cell materials," in *2015 22nd International Workshop on Active-Matrix Flatpanel Displays and Devices (AM-FPD)*, IEEE, 2015.

[25] V. Fthenakis, "Sustainability of photovoltaics: The case for thin-film solar cells," *Renewable and Sustainable Energy Reviews*, vol. 13, no. 9, pp. 2746 – 2750, 2009.

[26] S. Adachi, *Earth-Abundant Materials for Solar Cells: Cu2-II-IV-VI4 Semiconductors*. Wiley, 2015.

[27] M. Parenteau and C. Carlone, "Influence of temperature and pressure on the electronic transitions in SnS and SnSe semiconductors," *Phys. Rev. B*, vol. 41, pp. 5227–5234, 1990.

[28] J. M. Chamberlain, P. M. Nikolic, M. Merdan, and P. Mihailovic, "Far-infrared optical properties of sns," *Journal of Physics C: Solid State Physics*, vol. 9, no. 22, p. L637, 1976.

[29] R. Jaramillo, V. Steinmann, C. Yang, K. Hartman, R. Chakraborty, J. R. Poindexter, M. L. Castillo, R. Gordon, and T. Buonassisi, "Making record-efficiency SnS solar cells by thermal evaporation and atomic layer deposition," *Journal of Visualized Experiments*, no. 99, 2015.

[30] Y. Kumagai, L. A. Burton, A. Walsh, and F. Oba, "Electronic Structure and Defect Physics of Tin Sulfides: SnS, Sn_2S_3, and SnS_2," *Phys. Rev. Applied*, vol. 6, p. 014009, 2016.

[31] T. J. Whittles, L. A. Burton, J. M. Skelton, A. Walsh, T. D. Veal, and V. R. Dhanak, "Band Alignments, Valence Bands, and Core Levels in the Tin Sulfides SnS, SnS2, and Sn2S3: Experiment and Theory," *Chemistry of Materials*, vol. 28, no. 11, pp. 3718–3726, 2016.

[32] L. A. Burton and A. Walsh, "Phase Stability of the Earth-Abundant Tin Sulfides SnS, SnS2, and Sn2S3," *The Journal of Physical Chemistry C*, vol. 116, no. 45, pp. 24262–24267, 2012.

[33] H. Zhao and C. Persson, "Optical properties of $Cu(In, Ga)Se_2$ and $Cu_2ZnSn(S, Se)_4$," *Thin Solid Films*, vol. 519, no. 21, pp. 7508 – 7512, 2011. Proceedings of the EMRS 2010 Spring Meeting Symposium M: Thin Film Chalcogenide Photovoltaic Materials.

[34] J.-S. Seol, S.-Y. Lee, J.-C. Lee, H.-D. Nam, and K.-H. Kim, "Electrical and optical properties of Cu_2ZnSnS_4 thin films prepared by rf magnetron sputtering process," *Solar Energy Materials and Solar Cells*, vol. 75, no. 12, pp. 155 – 162, 2003. PVSEC 12 Part II.

[35] W. Wang, M. T. Winkler, O. Gunawan, T. Gokmen, T. K. Todorov, Y. Zhu, and D. B. Mitzi, "Device characteristics of CZTSSe thin-film solar cells with 12.6% efficiency," *Advanced Energy Materials*, vol. 4, no. 7, p. 1301465, 2013.

[36] S. Tajima, M. Umehara, M. Hasegawa, T. Mise, and T. Itoh, "Cu2ZnSnS4 photovoltaic cell with improved efficiency fabricated by high-temperature annealing after CdS buffer-layer deposition," *Progress in Photovoltaics: Research and Applications*, vol. 25, no. 1, pp. 14–22, 2016.

[37] S. Curtarolo, G. L. W. Hart, M. B. Nardelli, N. Mingo, S. Sanvito, and O. Levy, "The high-throughput highway to computational materials design.," *Nat. Mater.*, vol. 12, no. 3, pp. 191–201, 2013.

[38] K. T. Butler, J. M. Frost, J. M. Skelton, K. L. Svane, and A. Walsh, "Computational materials design of crystalline solids," *Chem. Soc. Rev.*, vol. 45, pp. 6138–6146, 2016.

[39] R. M. Martin, "Electronic structure: Basic theory and practical methods," ch. Introduction, Cambridge University Press, 2004.

[40] N. Ashcroft and N. Mermin, "Solid state physics," ch. Crystal Lattices, Saunders College Publishing, 1976.

[41] J. Piprek, *Semiconductor Optoelectronic Devices: Introduction to Physics and Simulation*. Elsevier Science, 2003.

[42] J. Nelson, "The physics of solar cells," ch. Electrons and Holes in Semiconductors, Imperial College Press, 2003.

[43] R. J. D. Tilley, "Colour and the optical properties of materialss," ch. Colour in Metals, Semiconductors and Insulators, John Wiley & Sons, Ltd, 2011.

[44] A. K. Jonscher, "Solid semiconductors," ch. The Electronic Structure of Solids, Routledge & Kegan Paul Ltd., 1965.

[45] P. Y. Yu and M. Cardona, "Fundamentals of semiconductors," ch. Electronic Band Structures, Springer-Verlag Berlin Heidelberg, 2010.

[46] A. K. Jonscher, "Solid semiconductors," ch. The Imperfect Solid, Routledge & Kegan Paul Ltd., 1965.

[47] R. Hoffmann, "How chemistry and physics meet in the solid state," *Angewandte Chemie International Edition in English*, vol. 26, pp. 846–878, Sept. 1987.

[48] M. Bokalič and M. Topič, *Spatially Resolved Characterization in Thin-Film Photovoltaics.*

[49] J. Nelson, "The physics of solar cells," ch. Introduction, Imperial College Press, 2003.

[50] J. Nelson, "The physics of solar cells," ch. Junctions, Imperial College Press, 2003.

[51] A. Luque and S. Hegedus, *Handbook of Photovoltaic Science and Engineering.* John Wiely & Sons, Ltd, 2003.

[52] A. Kahn, "Fermi level, work function and vacuum level," *Mater. Horiz.*, vol. 3, pp. 7–10, 2016.

[53] J. Nelson, "The physics of solar cells," ch. Analysis of the p-n Junction, Imperial College Press, 2003.

[54] A. Klein, "Energy band alignment in chalcogenide thin film solar cells from photoelectron spectroscopy," *Journal of Physics: Condensed Matter*, vol. 27, no. 13, p. 134201, 2015.

[55] S. B. Zhang, "The microscopic origin of the doping limits in semiconductors and wide-gap materials and recent developments in overcoming these limits: a review," *Journal of Physics: Condensed Matter*, vol. 14, no. 34, p. 881, 2002.

[56] J. Nelson, "The physics of solar cells," ch. Photons In, Electrons Out: Basic Principles of PV, Imperial College Press, 2003.

[57] C. S. Wang and B. M. Klein, "First-principles electronic structure of si, ge, GaP, GaAs, ZnS, and ZnSe. i. self-consistent energy bands, charge densities, and effective masses," *Physical Review B*, vol. 24, pp. 3393–3416, sep 1981.

[58] M. Grundmann, *The Physics of Semiconductors*. Springer, 2006.

[59] S. D. Wolf, J. Holovsky, S.-J. Moon, P. Löper, B. Niesen, M. Ledinsky, F.-J. Haug, J.-H. Yum, and C. Ballif, "Organometallic halide perovskites: Sharp optical absorption edge and its relation to photovoltaic performance," *The Journal of Physical Chemistry Letters*, vol. 5, pp. 1035–1039, mar 2014.

[60] S. S. Li, *Semiconductor Physical Electronics*. Plenum Press, New York, 1993.

[61] H. Zimmermann, *Integrated Silicon Optoelectronics*. Springer, 2010.

[62] T. L. Bahers, M. Rérat, and P. Sautet, "Semiconductors used in photovoltaic and photocatalytic devices: Assessing fundamental properties from DFT," *The Journal of Physical Chemistry C*, vol. 118, no. 12, pp. 5997–6008, 2014.

[63] B. Kolb and A. M. Kolpak, "First-Principles Design and Analysis of an Efficient, Pb-Free Ferroelectric Photovoltaic Absorber Derived from $ZnSnO_3$," *Chem. Mater.*, vol. 27, no. 17, pp. 5899–5906, 2015.

[64] N. Ashcroft and N. Mermin, *Solid State Physics*. Saunders College Publishing, 1976.

[65] A. Alkauskas, M. D. McCluskey, and C. G. V. de Walle, "Tutorial: Defects in semiconductors—combining experiment and theory," *Journal of Applied Physics*, vol. 119, no. 18, p. 181101, 2016.

[66] A. Walsh and A. Zunger, "Instilling defect tolerance in new compounds," *Nature Materials*, vol. 16, no. 10, pp. 964–967, 2017.

[67] S. Chen, A. Walsh, X.-G. Gong, and S.-H. Wei, "Classification of Lattice Defects in the Kesterite Cu2ZnSnS4and Cu2ZnSnSe4 Earth-Abundant Solar Cell Absorbers," *Advanced Materials*, vol. 25, no. 11, pp. 1522–1539, 2013.

[68] A. M. Stoneham, "Non-radiative transitions in semiconductors," *Reports on Progress in Physics*, vol. 44, no. 12, p. 1251, 1981.

[69] W. Shockley and W. T. Read, "Statistics of the recombinations of holes and electrons," *Phys. Rev.*, vol. 87, pp. 835–842, 1952.

[70] J. Nelson, "The physics of solar cells," ch. Generation and Recombination, Imperial College Press, 2003.

[71] K. W. Böer, *Handbook of the Physics of Thin-Film Solar Cells*. Springer, 2013.

[72] J. I. Pankove, *Optical Processes in Semiconductors*. Dover Publications, Inc, 1971.

[73] I. Lifshitz, "The energy spectrum of disordered systems," *Advances in Physics*, vol. 13, no. 52, pp. 483–536, 1964.

[74] F. Urbach, "The long-wavelength edge of photographic sensitivity and of the electronic absorption of solids," *Phys. Rev.*, vol. 92, pp. 1324–1324, 1953.

[75] S. Bourdais, C. Choné, B. Delatouche, A. Jacob, G. Larramona, C. Moisan, A. Lafond, F. Donatini, G. Rey, S. Siebentritt, A. Walsh, and G. Dennler, "Is the Cu/Zn Disorder the Main Culprit for the Voltage Deficit in Kesterite Solar Cells?," *Adv. Energy Mater.*, 2016.

[76] S. D. Wolf, J. Holovsky, S.-J. Moon, P. Lper, B. Niesen, M. Ledinsky, F.-J. Haug, J.-H. Yum, and C. Ballif, "Organometallic halide perovskites: Sharp optical absorption edge and its relation to photovoltaic performance," *The Journal of Physical Chemistry Letters*, vol. 5, no. 6, pp. 1035–1039, 2014.

[77] L.-V. de Broglie, "On the Theory of Quanta." http://aflb.ensmp.fr/LDB-oeuvres/De$_B roglie_K racklauer.pdf. Accessed : 2019 - 04 - 05$.

[78] P. Weinberger, "Revisiting louis de broglies famous 1924 paper in thePhilosophical magazine," *Philosophical Magazine Letters*, vol. 86, pp. 405–410, jul 2006.

[79] C. J. Davisson and L. H. Germer, "Reflection of electrons by a crystal of nickel," *Proceedings of the National Academy of Sciences*, vol. 14, pp. 317–322, apr 1928.

[80] J. Polkinghorne, *Quantum Theory: A Very Short Introduction*. Oxford University Press, 2002.

[81] R. Prasad, "Electronic structure of materials," ch. Quantum Description of Materials, Taylor Francis Group, LLC, 2014.

[82] R. Lesar, "Introduction to computational materials science," ch. Electronic Structure Methods, Cambridge University Press, 2014.

[83] R. Prasad, "Electronic structure of materials," ch. Introduction, Taylor Francis Group, LLC, 2014.

[84] R. Prasad, "Electronic structure of materials," ch. Density Functional Theory, Taylor Francis Group, LLC, 2014.

[85] L. H. Thomas, "The calculation of atomic fields," *Mathematical Proceedings of the Cambridge Philosophical Society*, vol. 23, no. 5, pp. 542–548, 1927.

[86] E. Fermi, "Un metodo statistico per la determinazione di alcune priopriet dellatomo," *Endiconti: Accademia Nazionale dei Lincei*, vol. 6, 1927.

[87] R. M. Martin, "Electronic structure: Basic theory and practical methods," ch. Density functional theory: foundations, Cambridge University Press, 2004.

[88] P. Hohenberg and W. Kohn, "Inhomogeneous electron gas," *Phys. Rev.*, vol. 136, pp. 864–871, 1964.

[89] W. Kohn and L. J. Sham, "Self-consistent equations including exchange and correlation effects," *Phys. Rev.*, vol. 140, pp. 1133–1138, 1965.

[90] R. M. Martin, "Electronic structure: Basic theory and practical methods," ch. The Kohn-Sham ansatz, Cambridge University Press, 2004.

[91] R. M. Martin, "Electronic structure: Basic theory and practical methods," ch. Functionals for exchange and correlation, Cambridge University Press, 2004.

[92] D. M. Ceperley and B. J. Alder, "Ground state of the electron gas by a stochastic method," *Phys. Rev. Lett.*, vol. 45, pp. 566–569, 1980.

[93] J. P. Perdew, K. Burke, and M. Ernzerhof, "Generalized gradient approximation made simple," *Phys. Rev. Lett.*, vol. 77, pp. 3865–3868, 1996.

[94] J. P. Perdew, A. Ruzsinszky, G. I. Csonka, O. A. Vydrov, G. E. Scuseria, L. A. Constantin, X. Zhou, and K. Burke, "Restoring the density-gradient expansion for exchange in solids and surfaces," *Phys. Rev. Lett.*, vol. 100, p. 136406, 2008.

[95] J. P. Perdew, "Density functional theory and the band gap problem," *International Journal of Quantum Chemistry*, vol. 28, no. S19, pp. 497–523.

[96] J. P. Perdew, M. Ernzerhof, A. Zupan, and K. Burke, "Nonlocality of the density functional for exchange and correlation: Physical origins and chemical consequences," *The Journal of Chemical Physics*, vol. 108, no. 4, pp. 1522–1531, 1998.

[97] A. V. Krukau, O. A. Vydrov, A. F. Izmaylov, and G. E. Scuseria, "Influence of the exchange screening parameter on the performance of screened hybrid functionals," *The Journal of Chemical Physics*, vol. 125, no. 22, 2006.

[98] L. Schimka, J. Harl, and G. Kresse, "Improved hybrid functional for solids: The HSEsol functional," *The Journal of Chemical Physics*, vol. 134, no. 2, p. 024116, 2011.

[99] W. Kohn, "Density functional theory for systems of very many atoms," *International Journal of Quantum Chemistry*, vol. 56, no. 4, pp. 229–232.

[100] J. Heyd, G. E. Scuseria, and M. Ernzerhof, "Hybrid functionals based on a screened Coulomb potential," *J. Chem. Phys.*, vol. 118, no. 18, pp. 8207–8215, 2003.

[101] J. E. Moussa, P. A. Schultz, and J. R. Chelikowsky, "Analysis of the Heyd-Scuseria-Ernzerhof density functional parameter space," *The Journal of Chemical Physics*, vol. 136, no. 20, p. 204117, 2012.

[102] C. W. M. Castleton, A. Hglund, and S. Mirbt, "Density functional theory calculations of defect energies using supercells," *Modelling and Simulation in Materials Science and Engineering*, vol. 17, no. 8, p. 084003, 2009.

[103] R. M. Martin, "Electronic structure: Basic theory and practical methods," ch. Electronic structure of atoms, Cambridge University Press, 2004.

[104] R. M. Martin, "Electronic structure: Basic theory and practical methods," ch. Pseudopotentials, Cambridge University Press, 2004.

[105] V. Blum, R. Gehrke, F. Hanke, P. Havu, V. Havu, X. Ren, K. Reuter, and M. Scheffler, "Ab initio molecular simulations with numeric atom-centered orbitals," *Computer Physics Communications*, vol. 180, no. 11, pp. 2175 – 2196, 2009.

[106] G. Kresse and J. Furthmüller, "Efficiency of ab-initio total energy calculations for metals and semiconductors using a plane-wave basis set," *Computational Materials Science*, vol. 6, no. 1, pp. 15 – 50, 1996.

[107] P. H. Acioli and D. M. Ceperley, "Generation of pseudopotentials from correlated wave functions," *The Journal of Chemical Physics*, vol. 100, pp. 8169–8177, jun 1994.

[108] V. Blum, "The nuts and bolts of electronic structure theory: Technical foundations and numerical methods." https://th.fhi-berlin.mpg.de/sitesub/meetings/dft-workshop-2015/uploads/Meeting/July-15_T05_Blum.pdf. Accessed: 2018-08-24.

[109] J. Ghosh, "2.1 band structure calculation methods in semiconductors." http://www.iue.tuwien.ac.at/phd/ghosh/diss_htmse6.html. Accessed: 2018-08-31.

[110] R. Prasad, "Electronic structure of materials," ch. Methods of Electronic Structure Calculations I, Taylor Francis Group, LLC, 2014.

[111] P. E. Blöchl, "Projector augmented-wave method," *Phys. Rev. B*, vol. 50, pp. 17953–17979, 1994.

[112] G. Kresse and D. Joubert, "From ultrasoft pseudopotentials to the projector augmented-wave method," *Phys. Rev. B*, vol. 59, pp. 1758–1775, 1999.

[113] G. Kresse, "Pseudopotentials (Part I)." https://www.vasp.at/vasp-workshop/slides/pseudopp1.pdf. Accessed: 2018-08-31.

[114] O. K. Andersen, "Linear methods in band theory," *Phys. Rev. B*, vol. 12, pp. 3060–3083, 1975.

[115] D. Vanderbilt, "Soft self-consistent pseudopotentials in a generalized eigenvalue formalism," *Phys. Rev. B*, vol. 41, pp. 7892–7895, 1990.

[116] G. Kresse and J. Hafner, "Norm-conserving and ultrasoft pseudopotentials for first-row and transition elements," *Journal of Physics: Condensed Matter*, vol. 6, no. 40, p. 8245, 1994.

[117] Vaspwiki, "PAW method." https://cms.mpi.univie.ac.at/wiki/index.php/PAW_method. Accessed: 2018-08-31.

[118] K. Lejaeghere et al, "Reproducibility in density functional theory calculations of solids," *Science*, vol. 351, no. 6280, 2016.

[119] R. M. Martin, "Electronic structure: Basic theory and practical methods," ch. Solving Kohn-Sham equations, Cambridge University Press, 2004.

[120] N. Mousseau and P. Derreumaux, "Exploring energy landscapes of protein folding and aggregation." https://www.bioscience.org/2008/v13/af/3019/fulltext.php?bframe=PDFII. Accessed: 2018-08-30.

[121] B. Lange, "Practical Implementations: The Nuts and Bolts of DFT Part II." https://th.fhi-berlin.mpg.de/sitesub/meetings/dft-workshop-2015/uploads/Meeting/July-15_T06_Lange.pdf. Accessed: 2018-08-24.

[122] R. Prasad, "Electronic structure of materials," ch. Methods of Electronic Structure Calculations II, Taylor Francis Group, LLC, 2014.

[123] FHI-aims team, "Fritz Haber Institute ab initio molecular simulations: A Users' Guide." January 4 2018.

[124] A. Eichler, "Sampling the brillouin zone." https://www.vasp.at/vasp-workshop/slides/k-points.pdf. Accessed: 2018-08-31.

[125] H. J. Monkhorst and J. D. Pack, "Special points for brillouin-zone integrations," *Phys. Rev. B*, vol. 13, pp. 5188–5192, 1976.

[126] A. Kahn, "Fermi level, work function and vacuum level," *Materials Horizons*, vol. 3, no. 1, pp. 7–10, 2016.

[127] P. W. Tasker, "The stability of ionic crystal surfaces," *Journal of Physics C: Solid State Physics*, vol. 12, no. 22, p. 4977, 1979.

[128] K. T. Butler, J. M. Frost, A. J. Jackson, and A. Walsh, "Wmd-group/macrodensity." https://zenodo.org/record/884521.

[129] Y. Kumagai, K. T. Butler, A. Walsh, and F. Oba, "Theory of ionization potentials of nonmetallic solids," *Physical Review B*, vol. 95, no. 12, 2017.

[130] M. Peressi, N. Binggeli, and A. Baldereschi, "Band engineering at interfaces: theory and numerical experiments," *Journal of Physics D: Applied Physics*, vol. 31, no. 11, pp. 1273–1299, 1998.

[131] R. L. Anderson, "Germanium-gallium arsenide heterojunctions [letter to the editor]," *IBM Journal of Research and Development*, vol. 4, no. 3, pp. 283–287, 1960.

[132] K. T. Butler, Y. Kumagai, F. Oba, and A. Walsh, "Screening procedure for structurally and electronically matched contact layers for high-performance solar cells: hybrid perovskites," *J. Mater. Chem. C*, vol. 4, no. 6, pp. 1149–1158, 2016.

[133] B. Monserrat, J.-S. Park, S. Kim, and A. Walsh, "Role of electron-phonon coupling and thermal expansion on band gaps, carrier mobility, and interfacial offsets in kesterite thin-film solar cells," *Applied Physics Letters*, vol. 112, no. 19, p. 193903, 2018.

[134] J. Corish and P. Jacobs, "Ionic conductivity of silver chloride single crystals," *Journal of Physics and Chemistry of Solids*, vol. 33, no. 7-9, pp. 1799–1818, 1972.

[135] R. A. Jackson, J. E. Huntingdon, and R. G. J. Ball, "Defect calculations in solids beyond the dilute limit," *Journal of Materials Chemistry*, vol. 1, no. 6, p. 1079, 1991.

[136] C. Freysoldt, B. Grabowski, T. Hickel, J. Neugebauer, G. Kresse, A. Janotti, and C. G. V. de Walle, "First-principles calculations for point defects in solids," *Reviews of Modern Physics*, vol. 86, no. 1, pp. 253–305, 2014.

[137] S. B. Zhang and J. E. Northrup, "Chemical potential dependence of defect formation energies in GaAs: Application to Ga self-diffusion," *Phys. Rev. Lett.*, vol. 67, pp. 2339–2342, 1991.

[138] R. Baierlein, "The elusive chemical potential," *American Journal of Physics*, vol. 69, no. 4, pp. 423–434, 2001.

[139] S. Chen, J.-H. Yang, X. G. Gong, A. Walsh, and S.-H. Wei, "Intrinsic point defects and complexes in the quaternary kesterite semiconductor Cu_2ZnSnS_4," *Physical Review B*, vol. 81, no. 24, p. 245204, 2010.

[140] A. Goyal, P. Gorai, H. Peng, S. Lany, and V. Stevanović, "A computational framework for automation of point defect calculations," *Computational Materials Science*, vol. 130, pp. 1–9, 2017.

[141] C. W. M. Castleton, A. Höglund, and S. Mirbt, "Managing the supercell approximation for charged defects in semiconductors: Finite-size scaling, charge correction factors, the band-gap problem, and the ab initio dielectric constant," *Phys. Rev. B*, vol. 73, p. 035215, 2006.

[142] S. Lany and A. Zunger, "Accurate prediction of defect properties in density functional supercell calculations," *Model. Simul. Mater. Sci. Eng.*, vol. 17, no. 8, p. 084002, 2009.

[143] G. Petretto and F. Bruneval, "Systematic defect donor levels in III-V and II-VI semiconductors revealed by hybrid functional density-functional theory," *Physical Review B*, vol. 92, no. 22, 2015.

[144] H.-P. Komsa, T. T. Rantala, and A. Pasquarello, "Finite-size supercell correction schemes for charged defect calculations," *Physical Review B*, vol. 86, no. 4, 2012.

[145] T. R. Durrant, S. T. Murphy, M. B. Watkins, and A. L. Shluger, "Relation between image charge and potential alignment corrections for charged defects in periodic boundary conditions," *The Journal of Chemical Physics*, vol. 149, no. 2, p. 024103, 2018.

[146] A. M. Ganose, S. Matsumoto, J. Buckeridge, and D. O. Scanlon, "Defect engineering of earth-abundant solar absorbers BiSI and BiSeI," *Chemistry of Materials*, vol. 30, no. 11, pp. 3827–3835, 2018.

[147] Y. Kumagai and F. Oba, "Electrostatics-based finite-size corrections for first-principles point defect calculations," *Phys. Rev. B*, vol. 89, p. 195205, 2014.

[148] L. Kleinman, "Comment on the average potential of a Wigner solid," *Phys. Rev. B*, vol. 24, pp. 7412–7414, 1981.

[149] C. Freysoldt, J. Neugebauer, and C. G. Van de Walle, "Fully ab initio finite-size corrections for charged-defect supercell calculations," *Phys. Rev. Lett.*, vol. 102, p. 016402, 2009.

[150] Q. Wang, K. Birod, C. Angioni, S. Grösch, T. Geppert, P. Schneider, M. Rupp, and G. Schneider, "Spherical harmonics coefficients for ligand-based virtual screening of cyclooxygenase inhibitors," *PLoS ONE*, vol. 6, p. e21554, jul 2011.

[151] M. Leslie and N. J. Gillan, "The energy and elastic dipole tensor of defects in ionic crystals calculated by the supercell method," *Journal of Physics C: Solid State Physics*, vol. 18, no. 5, p. 973, 1985.

[152] G. Makov and M. C. Payne, "Periodic boundary conditions in ab initio calculations," *Phys. Rev. B*, vol. 51, pp. 4014–4022, 1995.

[153] S. Lany and A. Zunger, "Assessment of correction methods for the band-gap problem and for finite-size effects in supercell defect calculations: Case studies for ZnO and GaAs," *Phys. Rev. B*, vol. 78, p. 235104, 2008.

[154] P. A. Schultz, "Charged local defects in extended systems," *Phys. Rev. Lett.*, vol. 84, pp. 1942–1945, 2000.

[155] C. Persson, Y.-J. Zhao, S. Lany, and A. Zunger, "n-type doping of CuInSe2 and CuGaSe2," *Physical Review B*, vol. 72, no. 3, 2005.

[156] K. Binder, *Topics in Current Physics: Monte Carlo Methods in Statistical Physics*. Springer-Verlag, 1979.

[157] N. Metropolis, A. W. Rosenbluth, M. N. Rosenbluth, A. H. Teller, and E. Teller, "Equation of State Calculations by Fast Computing Machines," *J. Chem. Phys.*, vol. 21, no. 6, pp. 1087–1092, 1953.

[158] R. Lesar, "Introduction to computational materials science," ch. The Monte Carlo Method, Cambridge University Press, 2014.

[159] S. K. Wallace, J. M. Frost, and A. Walsh, "Atomistic insights into the order-disorder transition in Cu2ZnSnS4 solar cells from Monte Carlo simulations," *Journal of Materials Chemistry A*, 2018. DOI: 10.1039/C8TA04812F.

[160] X. Liu, Y. Feng, H. Cui, F. Liu, X. Hao, G. Conibeer, D. B. Mitzi, and M. Green, "The current status and future prospects of kesterite solar cells: a brief review," *Progress in Photovoltaics: Research and Applications*, vol. 24, no. 6, pp. 879–898, 2016.

[161] T. Gokmen, O. Gunawan, T. K. Todorov, and D. B. Mitzi, "Band tailing and efficiency limitation in kesterite solar cells," *Applied Physics Letters*, vol. 103, no. 10, 2013.

[162] T. Gershon, B. Shin, T. Gokmen, S. Lu, N. Bojarczuk, and S. Guha, "Relationship between Cu_2ZnSnS_4 quasi donor-acceptor pair density and solar cell efficiency," *Appl. Phys. Lett.*, vol. 103, pp. 2012–2015, 2013.

[163] T. Gershon, B. Shin, N. Bojarczuk, T. Gokmen, S. Lu, and S. Guha, "Photoluminescence characterization of a high-efficiency Cu_2ZnSnS_4 device," *J. Appl. Phys.*, vol. 114, no. 15, p. 154905, 2013.

[164] M. J. Romero, H. Du, G. Teeter, Y. Yan, and M. M. Al-Jassim, "Comparative study of the luminescence and intrinsic point defects in the kesterite Cu_2ZnSnS_4 and chalcopyrite $Cu(In,Ga)Se_2$," *Phys. Rev. B*, vol. 84, no. 16, p. 165324, 2011.

[165] Y. Miyamoto, K. Tanaka, M. Oonuki, N. Moritake, and H. Uchiki, "Optical Properties of Cu_2ZnSnS_4 Thin Films Prepared by SolGel and Sulfurization Method," *Jpn. J. Appl. Phys.*, vol. 47, no. 1, pp. 596–597, 2008.

[166] T. Unold, S. Kretzschmar, J. Just, O. Zander, B. Schubert, B. Marsen, and H.-W. Schock, "Correlation between composition and photovoltaic properties of Cu_2ZnSnS_4 thin film solar cells," *Photovolt. Spec. Conf. (PVSC), 2011 37th IEEE*, pp. 2820–2823, 2011.

[167] D. P. Halliday, R. Claridge, M. C. Goodman, B. G. Mendis, K. Durose, and J. D. Major, "Luminescence of Cu_2ZnSnS_4 polycrystals described by the fluctuating potential model," *J. Appl. Phys.*, vol. 113, no. 22, p. 2013, 2013.

[168] S. Levcenko, V. E. Tezlevan, E. Arushanov, S. Schorr, and T. Unold, "Free-to-bound recombination in near stoichiometric Cu_2ZnSnS_4 single crystals," *Phys. Rev. B*, vol. 86, no. 4, p. 045206, 2012.

[169] K. Hönes, E. Zscherpel, J. Scragg, and S. Siebentritt, "Shallow defects in Cu_2ZnSnS_4," *Phys. B Condens. Matter*, vol. 404, no. 23-24, pp. 4949–4952, 2009.

[170] S. Kim, J.-S. Park, and A. Walsh, "Identification of killer defects in kesterite thin-film solar cells," *ACS Energy Letters*, vol. 3, no. 2, pp. 496–500, 2018.

[171] S. Schorr, "The crystal structure of kesterite type compounds: A neutron and x-ray diffraction study," *Solar Energy Materials and Solar Cells*, vol. 95, no. 6, pp. 1482 – 1488, 2011.

[172] T. Washio, H. Nozaki, T. Fukano, T. Motohiro, K. Jimbo, and H. Katagiri, "Analysis of lattice site occupancy in kesterite structure of cu_2znsns_4 films using synchrotron radiation x-ray diffraction," *J. Appl. Phys.*, vol. 110, p. 074511, 2011.

[173] B. G. Mendis, M. D. Shannon, M. C. Goodman, J. D. Major, R. Claridge, D. P. Halliday, and K. Durose, "Direct observation of cu, zn cation disorder in cu_2znsns_4 solar cell absorber material using aberration corrected scanning transmission electron microscopy," *Progress in Photovoltaics: Research and Applications*, vol. 22, no. 1, pp. 24–34, 2014.

[174] A. M. Stoneham, *Ionic Solids at High Temperatures*. World Scientific, 1989.

[175] P. Varotsos and K. Alexopoulos, *Thermodynamics of Point Defects and Their Relation with Bulk Properties*. 1986.

[176] Y. Hou, H. Azimi, N. Gasparini, M. Salvador, W. Chen, L. S. Khanzada, M. Brandl, R. Hock, and C. J. Brabec, "Low-temperature solution-processed kesterite solar cell based on in situ deposition of ultrathin absorber layer," *ACS Applied Materials & Interfaces*, vol. 7, no. 38, pp. 21100–21106, 2015.

[177] J. Scragg, L. Choubrac, A. Lafond, T. Ericson, and C. Platzer-Björkman, "A low-temperature order-disorder transition in Cu_2ZnSnS_4 thin films," *Appl. Phys. Lett.*, vol. 104, no. 4, p. 041911, 2014.

[178] S. Schorr, H.-J. Hoebler, and M. Tovar, "A neutron diffraction study of the stannite-kesterite solid solution series," *Eur. J. Miner.*, vol. 19, no. 65, pp. 65–73, 2007.

[179] F. Espinosa-Faller, "Neutron Diffraction and Xray Absorption Fine Structure Evidence for Local Lattice Distortions and Aperiodic Antisite Substitution in Cu_2ZnSnS_4 Nanoparticles," *The Journal of Physical Chemistry C*, vol. 118, pp. 26292–26303, 2014.

[180] M. E. J. Newman and G. T. Barkema, "Monte carlo methods in statistical physics," ch. The Ising Model and the Metropolis Algorithm, Oxford University Press, 1999.

[181] D. P. Landau and K. Binder, *A Guide to Monte Carlo Simulations in Statistical Physics*. Cambridge University Press, 2015.

[182] K. Rudisch, Y. Ren, C. Platzer-Björkman, and J. Scragg, "Order-disorder transition in B-type Cu_2ZnSnS_4 and limitations of ordering through thermal treatments," *Applied Physics Letters*, vol. 108, p. 231902, 2016.

[183] D. M. Többens, G. Gurieva, S. Levcenko, T. Unold, and S. Schorr, "Temperature dependency of Cu/Zn ordering in CZTSe kesterites determined by anomalous diffraction," *physica status solidi (b)*, vol. 253, no. 10, pp. 1890–1897, 2016.

[184] C. J. Bosson, M. T. Birch, D. P. Halliday, K. S. Knight, A. S. Gibbs, and P. D. Hatton, "Cation disorder and phase transitions in the structurally complex solar cell material Cu2ZnSnS4," *Journal of Materials Chemistry A*, vol. 5, no. 32, pp. 16672–16680, 2017.

[185] S. P. Ramkumar, A. Miglio, M. J. van Setten, D. Waroquiers, G. Hautier, and G.-M. Rignanese, "Insights into cation disorder and phase transitions in CZTS from a first-principles approach," *Phys. Rev. Materials*, vol. 2, p. 085403, 2018.

[186] S. Siebentritt and S. Schorr, "Kesterites - a challenging material for solar cells," *Prog. Photovoltaics Res. Appl.*, vol. 20, pp. 512–519, 2012.

[187] G. Rey, G. Larramona, S. Bourdais, C. Chon, B. Delatouche, A. Jacob, G. Dennler, and S. Siebentritt, "On the origin of band-tails in kesterite," *Solar Energy Materials and Solar Cells*, vol. 179, pp. 142 – 151, 2018.

[188] B. Monserrat, J.-S. Park, S. Kim, and A. Walsh, "Role of electron-phonon coupling and thermal expansion on band gaps, carrier mobility, and interfacial offsets in kesterite thin-film solar cells," *Applied Physics Letters*, vol. 112, no. 19, p. 193903, 2018.

[189] M. E. Lines and A. M. Glass, *Principles and Applications of Ferroelectrics and Related Materials*. Oxford University Press, 1977.

[190] K. T. Butler, J. M. Frost, and A. Walsh, "Ferroelectric materials for solar energy conversion: photoferroics revisited," *Energy & Environmental Science*, vol. 8, no. 3, pp. 838–848, 2015.

[191] A. G. Chynoweth, "Surface space-charge layers in barium titanate," *Phys. Rev.*, vol. 102, pp. 705–714, 1956.

[192] Y. Yuan, Z. Xiao, B. Yang, and J. Huang, "Arising applications of ferroelectric materials in photovoltaic devices," *J. Mater. Chem. A*, vol. 2, no. 17, p. 6027, 2014.

[193] J. Starkiewicz, L. Sosnowski, and O. Simpson *Nature*, vol. 158, 1946.

[194] H. R. Johnson, R. H. Williams, and C. H. B. Mee, "The anomalous photovoltaic effect in cadmium telluride," *Journal of Physics D: Applied Physics*, vol. 8, no. 13, p. 1530, 1975.

[195] B. Goldstein and L. Pensak *J. Appl. Phys.*, vol. 155, 1959.

[196] M. D. Uspenskii, N. G. Ivanova, and M. I. E *Sov. Phys.- Semicond*, p. 1059, 1968.

[197] P. Lopez-Varo, L. Bertoluzzi, J. Bisquert, M. Alexe, M. Coll, J. Huang, J. A. Jimenez-Tejada, T. Kirchartz, R. Nechache, F. Rosei, and Y. Yuan, "Physical aspects of ferroelectric semiconductors for photovoltaic solar energy conversion," *Physics Reports*, vol. 653, pp. 1 – 40, 2016.

[198] C. Paillard, X. Bai, I. C. Infante, M. Guennou, G. Geneste, M. Alexe, J. Kreisel, and B. Dkhil, "Photovoltaics with Ferroelectrics: Current Status and Beyond," *Adv. Mater.*, 2016.

[199] J. M. Frost, K. T. Butler, F. Brivio, C. H. Hendon, M. van Schilfgaarde, and A. Walsh, "Atomistic origins of high-performance in hybrid halide perovskite solar cells.," *Nano Lett.*, vol. 14, no. 5, pp. 2584–90, 2014.

[200] S. Das, S. Ghara, P. Mahadevan, A. Sundaresan, J. Gopalakrishnan, and D. D. Sarma, "Designing a lower band gap bulk ferroelectric material with a sizable polarization at room temperature," *ACS Energy Letters*, vol. 3, no. 5, pp. 1176–1182, 2018.

[201] W. S. Choi, M. F. Chisholm, D. J. Singh, T. Choi, G. E. Jellison, and H. N. Lee, "Wide bandgap tunability in complex transition metal oxides by site-specific substitution," *Nature Communications*, vol. 3, jan 2012.

[202] A. Jain, S. P. Ong, G. Hautier, W. Chen, W. D. Richards, S. Dacek, S. Cholia, D. Gunter, D. Skinner, G. Ceder, and K. a. Persson, "The Materials Project: A materials genome approach to accelerating materials innovation," *APL Materials*, vol. 1, no. 1, p. 011002, 2013.

[203] C. E. Calderon, J. J. Plata, C. Toher, C. Oses, O. Levy, M. Fornari, A. Natan, M. J. Mehl, G. Hart, M. B. Nardelli, and S. Curtarolo, "The AFLOW standard for high-throughput materials science calculations," *Computational Materials Science*, vol. 108, pp. 233–238, 2015.

[204] V. Stevanović, S. Lany, X. Zhang, and A. Zunger, "Correcting density functional theory for accurate predictions of compound enthalpies of formation: Fitted elemental-phase reference energies," *Physical Review B*, vol. 85, no. 11, 2012.

[205] P. Gorai, D. Gao, B. Ortiz, S. Miller, S. A. Barnett, T. Mason, Q. Lv, V. Stevanović, and E. S. Toberer, "TE design lab: A virtual laboratory for thermoelectric material design," *Computational Materials Science*, vol. 112, pp. 368–376, 2016.

[206] "Computational Materials Repository." cmr.fysik.dtu.dk. Accessed: 2018-10-19.

[207] "The NOMAD Laboratory A European Centre of Excellence." nomad-repository.eu. Accessed: 2018-10-19.

[208] A. Jain, G. Hautier, C. J. Moore, S. P. Ong, C. C. Fischer, T. Mueller, K. A. Persson, and G. Ceder, "A high-throughput infrastructure for density functional theory calculations," *Computational Materials Science*, vol. 50, no. 8, pp. 2295 – 2310, 2011.

[209] A. van Roekeghem, J. Carrete, C. Oses, S. Curtarolo, and N. Mingo, "High-throughput computation of thermal conductivity of high-temperature solid phases: The case of oxide and fluoride perovskites," *Physical Review X*, vol. 6, no. 4, 2016.

[210] O. Isayev, C. Oses, C. Toher, E. Gossett, S. Curtarolo, and A. Tropsha, "Universal fragment descriptors for predicting properties of inorganic crystals," *Nature Communications*, vol. 8, p. 15679, 2017.

[211] K. Alberi et al, "The 2019 materials by design roadmap," *Journal of Physics D: Applied Physics*, vol. 52, no. 1, p. 013001, 2018.

[212] P. Gorai, V. Stevanović, and E. S. Toberer, "Computationally guided discovery of thermoelectric materials," *Nature Reviews Materials*, vol. 2, no. 9, p. 17053, 2017.

[213] W. Chen, J.-H. Pöhls, G. Hautier, D. Broberg, S. Bajaj, U. Aydemir, Z. M. Gibbs, H. Zhu, M. Asta, G. J. Snyder, B. Meredig, M. A. White, K. Persson, and A. Jain, "Understanding thermoelectric properties from high-throughput calculations: trends, insights, and comparisons with experiment," *Journal of Materials Chemistry C*, vol. 4, no. 20, pp. 4414–4426, 2016.

[214] J. Carrete, N. Mingo, S. Wang, and S. Curtarolo, "Nanograined half-heusler semiconductors as advanced thermoelectrics: An ab initio high-throughput statistical study," *Advanced Functional Materials*, vol. 24, no. 47, pp. 7427–7432, 2014.

[215] L. Yu and A. Zunger, "Identification of potential photovoltaic absorbers based on first-principles spectroscopic screening of materials," *Physical Review Letters*, vol. 108, no. 6, 2012.

[216] S. Chakraborty, W. Xie, N. Mathews, M. Sherburne, R. Ahuja, M. Asta, and S. G. Mhaisalkar, "Rational design: A high-throughput computational screening and experimental validation methodology for lead-free and emergent hybrid perovskites," *ACS Energy Letters*, vol. 2, no. 4, pp. 837–845, 2017.

[217] S. Chakraborty, W. Xie, N. Mathews, M. Sherburne, R. Ahuja, M. Asta, and S. G. Mhaisalkar, "Rational design: A high-throughput computational screening and experimental validation methodology for lead-free and emergent hybrid perovskites," *ACS Energy Letters*, vol. 2, no. 4, pp. 837–845, 2017.

[218] S. Körbel, M. A. L. Marques, and S. Botti, "Stability and electronic properties of new inorganic perovskites from high-throughput ab initio calculations," *Journal of Materials Chemistry C*, vol. 4, no. 15, pp. 3157–3167, 2016.

[219] J. Hachmann, R. Olivares-Amaya, A. Jinich, A. L. Appleton, M. A. Blood-Forsythe, L. R. Seress, C. Román-Salgado, K. Trepte, S. Atahan-Evrenk, S. Er, S. Shrestha, R. Mondal, A. Sokolov, Z. Bao, and A. Aspuru-Guzik, "Lead candidates for high-performance organic photovoltaics from high-throughput quantum chemistry – the harvard clean energy project," *Energy Environ. Sci.*, vol. 7, no. 2, pp. 698–704, 2014.

[220] A. Jain, S. P. Ong, G. Hautier, and C. Moore, "Calculations guide." https://materialsproject.org/docs/calculations. Accessed: 2018-09-03.

[221] G. K. Madsen and D. J. Singh, "Boltztrap. a code for calculating band-structure dependent quantities," *Computer Physics Communications*, vol. 175, no. 1, pp. 67 – 71, 2006.

[222] T. J. Whittles, T. D. Veal, C. N. Savory, A. W. Welch, F. W. de Souza Lucas, J. T. Gibbon, M. Birkett, R. J. Potter, D. O. Scanlon, A. Zakutayev, and V. R. Dhanak, "Core-levels, band alignments, and valence band states in CuSbS2 for solar cell applications," *ACS Applied Materials & Interfaces*, 2017.

[223] S. A. McClary, J. Andler, C. A. Handwerker, and R. Agrawal, "Solution-processed copper arsenic sulfide thin films for photovoltaic applications," *J. Mater. Chem. C*, vol. 5, no. 28, pp. 6913–6916, 2017.

[224] T. Song, A. Kanevce, and J. R. Sites, "Emitter/absorber interface of CdTe solar cells," *Journal of Applied Physics*, vol. 119, no. 23, p. 233104, 2016.

[225] M. Gloeckler and J. Sites, "Efficiency limitations for wide-band-gap chalcopyrite solar cells," *Thin Solid Films*, vol. 480-481, no. Supplement C, pp. 241 – 245, 2005. EMRS 2004.

[226] E. Arca, A. Fioretti, S. Lany, A. C. Tamboli, G. Teeter, C. Melamed, J. Pan, K. N. Wood, E. Toberer, and A. Zakutayev, "Band edge positions and their impact on the simulated device performance of znsnn2-based solar cells," *IEEE Journal of Photovoltaics*, vol. 8, no. 1, pp. 110–117, 2018.

[227] A. J. Jackson, D. Tiana, and A. Walsh, "A universal chemical potential for sulfur vapours," *Chem. Sci.*, vol. 7, pp. 1082–1092, 2016.

[228] R. E. Brandt, J. R. Poindexter, P. Gorai, R. C. Kurchin, R. L. Z. Hoye, L. Nienhaus, M. W. B. Wilson, J. A. Polizzotti, R. Sereika, R. Žaltauskas, L. C. Lee, J. L. MacManus-Driscoll, M. Bawendi, V. Stevanović, and T. Buonassisi, "Searching for "defect-tolerant" photovoltaic materials: Combined theoretical and experimental screening," *Chemistry of Materials*, vol. 29, no. 11, pp. 4667–4674, 2017.

[229] K. X. Steirer, P. Schulz, G. Teeter, V. Stevanovic, M. Yang, K. Zhu, and J. J. Berry, "Defect tolerance in methylammonium lead triiodide perovskite," *ACS Energy Letters*, vol. 1, no. 2, pp. 360–366, 2016.

[230] W.-J. Yin, T. Shi, and Y. Yan, "Unusual defect physics in CH3NH3PbI3 perovskite solar cell absorber," *Applied Physics Letters*, vol. 104, no. 6, p. 063903, 2014.

[231] A. M. Ganose, C. N. Savory, and D. O. Scanlon, "Beyond methylammonium lead iodide: prospects for the emergent field of ns2 containing solar absorbers," *Chemical Communications*, vol. 53, no. 1, pp. 20–44, 2017.

[232] A. Zakutayev, C. M. Caskey, A. N. Fioretti, D. S. Ginley, J. Vidal, V. Stevanovic, E. Tea, and S. Lany, "Defect tolerant semiconductors for solar energy conversion," *The Journal of Physical Chemistry Letters*, vol. 5, no. 7, pp. 1117–1125, 2014.

[233] S. K. Wallace, K. L. Svane, W. P. Huhn, T. Zhu, D. B. Mitzi, V. Blum, and A. Walsh, "Candidate photoferroic absorber materials for thin-film solar cells from naturally occurring minerals: enargite, stephanite, and bournonite," *Sustainable Energy & Fuels*, vol. 1, no. 6, pp. 1339–1350, 2017.

[234] S. B. Zhang, S.-H. Wei, A. Zunger, and H. Katayama-Yoshida, "Defect physics of the CuInSe2 chalcopyrite semiconductor," *Physical Review B*, vol. 57, no. 16, pp. 9642–9656, 1998.

[235] C. Persson, R. Chen, H. Zhao, M. Kumar, and D. Huang, "Copper zinc tin sulfide-based thin-film solar cells," ch. Electronic Structure and Optical Properties from First-Principles Modeling, pp. 75–105, John Wiley & Sons Ltd, 2015.

[236] T. Pauporte and D. Lincot, "Electrical, Optical and Photoelectrochemical Properties of Natural Enargite, Cu3AsS4," *Advanced Materials for Optics and Electronics*, vol. 5, pp. 289–298, 1995.

[237] B. Durant and B. A. Parkinson, "Photovoltaic response of naturally occurring semiconducting sulfide minerals," in *2016 IEEE 43rd Photovoltaic Specialists Conference (PVSC)*, IEEE, 2016.

[238] J. M. Skelton, "Transformer." https://github.com/JMSkelton/Transformer. Accessed: 2018-10-11.

[239] A. Togo, "Spglib." https://atztogo.github.io/spglib. Accessed: 2018-11-12.

[240] J. Buckeridge, "Chemical potential limits analysis program." https://github.com/jbuckeridge/cplap. Accessed: 2018-10-05.

[241] F. Brivio, A. B. Walker, and A. Walsh, "Structural and electronic properties of hybrid perovskites for high-efficiency thin-film photovoltaics from first-principles," *APL Mater.*, vol. 1, no. 4, p. 042111, 2013.

[242] W. Wang, G. Wang, G. Chen, S. Chen, and Z. Huang, "The effect of sulfur vapor pressure on Cu2ZnSnS4 thin film growth for solar cells," *Solar Energy*, vol. 148, pp. 12–16, 2017.

[243] A. Khalkar, K.-S. Lim, S.-M. Yu, D.-W. Shin, T.-S. Oh, and J.-B. Yoo, "Effects of sulfurization pressure on the conversion efficiency of co-sputtered Cu2ZnSnS4 thin film solar cells," *International Journal of Photoenergy*, vol. 2015, pp. 1–7, 2015.

[244] Y. Ren, N. Ross, J. K. Larsen, K. Rudisch, J. J. S. Scragg, and C. Platzer-Björkman, "Evolution of Cu2ZnSnS4 during non-equilibrium annealing with quasi-in situ monitoring of sulfur partial pressure," *Chemistry of Materials*, vol. 29, no. 8, pp. 3713–3722, 2017.

[245] T. Gershon, K. Sardashti, O. Gunawan, R. Mankad, S. Singh, Y. S. Lee, J. A. Ott, A. Kummel, and R. Haight, "Photovoltaic device with over 5% efficiency based on an n-type ag2 ZnSnSe4 absorber," *Advanced Energy Materials*, vol. 6, no. 22, p. 1601182, 2016.

[246] Z. Xiao, W. Meng, J. V. Li, and Y. Yan, "Distant-atom mutation for better earth-abundant light absorbers: A case study of cu2basnse4," *ACS Energy Letters*, vol. 2, no. 1, pp. 29–35, 2017.

[247] D. Shin, B. Saparov, T. Zhu, W. P. Huhn, V. Blum, and D. B. Mitzi, "BaCu2Sn(S,Se)4: Earth-Abundant Chalcogenides for Thin-Film Photovoltaics," *Chemistry of Materials*, vol. 28, no. 13, pp. 4771–4780, 2016.

[248] L. E. V. Rios, K. Neldner, G. Gurieva, and S. Schorr, "Existence of off-stoichiometric single phase kesterite," *Journal of Alloys and Compounds*, vol. 657, pp. 408 – 413, 2016.

[249] G. Gurieva, L. E. V. Rios, A. Franz, P. Whitfield, and S. Schorr, "Intrinsic point defects in off-stoichiometric Cu2ZnSnSe4: A neutron diffraction study," *Journal of Applied Physics*, vol. 123, no. 16, p. 161519, 2018.

[250] T. Mueller, A. G. Kusne, and R. Ramprasad, "Machine learning in materials science," in *Reviews in Computational Chemistry*, pp. 186–273, John Wiley & Sons, Inc, may 2016.

[251] K. T. Butler, D. W. Davies, H. Cartwright, O. Isayev, and A. Walsh, "Machine learning for molecular and materials science," *Nature*, vol. 559, pp. 547–555, jul 2018.

[252] A. V. Shapeev, "Chapter 3. applications of machine learning for representing interatomic interactions," in *Computational Materials Discovery*, pp. 66–86, Royal Society of Chemistry.

[253] J. Behler, "Constructing high-dimensional neural network potentials: A tutorial review," *International Journal of Quantum Chemistry*, vol. 115, pp. 1032–1050, mar 2015.

[254] V. Botu and R. Ramprasad, "Learning scheme to predict atomic forces and accelerate materials simulations," *Physical Review B*, vol. 92, sep 2015.

Appendix A

Appendix

A.1 Supplemental material for: 'Atomistic insights into the order-disorder transition in Cu_2ZnSnS_4 solar cells from Monte Carlo simulations'

Electronic Supplementary Material (ESI) for Journal of Materials Chemistry A.

Supplemental material for: 'Atomistic insights into the order-disorder transition in Cu_2ZnSnS_4 solar cells from Monte Carlo simulations'

Suzanne K. Wallace[a,b], Jarvist Moore Frost [c], and Aron Walsh[*b,d]

[a] *Department of Chemistry, Centre for Sustainable Chemical Technologies, University of Bath, Claverton Down, Bath, BA2 7AY, UK*

[b] *Department of Materials, Imperial College London, Exhibition Road, London SW7 2AZ, UK. Email: a.walsh@imperial.ac.uk*

[c] *Department of Physics, King's College London, Strand, London WC2R 2LS, UK*

[d] *Department of Materials Science and Engineering, Yonsei University, Seoul 03722, Korea*

1 Convergence of change in lattice energy with cut-off radius for Monte Carlo moves

In the Monte Carlo (MC) simulations of CZTS, we use the change in lattice energy, dE, of the system before and after performing an MC move (nearest-neighbour Cu-Zn substitution) to determine if the move should be accepted or rejected.

In a simple model of ionic crystals, it is assumed that the lattice energy is given entirely by the potential energy of classical ions of charge Z at their equilibrium positions [1]. Two oppositely charged ions separated by a distance r experience an attractive Coulomb force, F, shown in equation 1. Their Coulombic potential energy, U, is then given by equation 2 [2].

$$F = \frac{e^2 Z_+ Z_-}{4\pi\epsilon_0 r^2} \tag{1}$$

$$U = \int_{\infty}^{r} F dr = -\frac{e^2 Z_+ Z_-}{4\pi\epsilon_0 r} \tag{2}$$

Considering nearest neighbouring ions, next-nearest neighbours, etc. out to a particular cut-off and summing over pairwise contributions to the electrostatic potential gives the dominant term in the expression for the lattice energy. Here, we are neglecting short-range forces including van der Waals interactions.

For computational efficiency when performing large numbers of MC moves, we use a finite cutoff radius for the lattice energy summation. To ensure that we use a suitable r_{cutoff} for our lattice summations when calculating dE for each MC move, we calculate dE for the same move with increasing r_{cutoff}, as shown in Fig. 1. From this, we have taken 5 lattice units as a suitable value for r_{cutoff}. We use the same volume for

the lattice summation before and after performing the nearest-neighbour Cu-Zn substitution to compute dE (we called this our 'site_energy_stencil' method in the Eris source code). This method was found to be better for achieving convergence in dE when using a finite cutoff radius for the lattice energy summation.

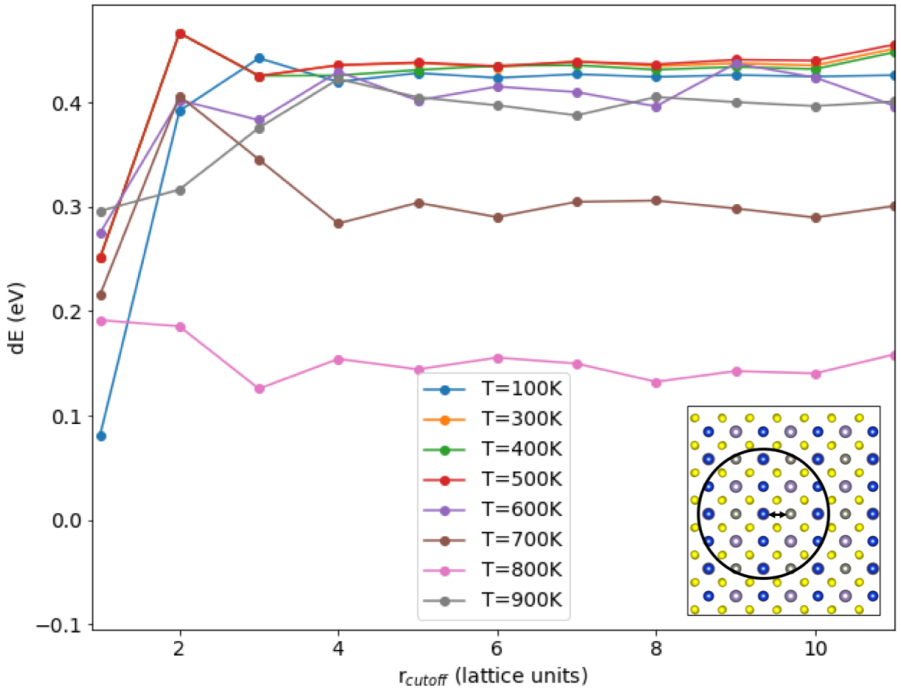

Figure 1: Convergence in the change in lattice energy (dE) for 3D Cu/ Zn disorder with respect to the cut-off radius (r_{cutoff}) for the lattice summations. The schematic shows a proposed swap between a Cu (blue) and Zn (steel grey) ion, and the circle is used to demonstrate a cut-off radius used for the lattice energy summation to obtain dE between the system before and after the proposed Monte Carlo move.

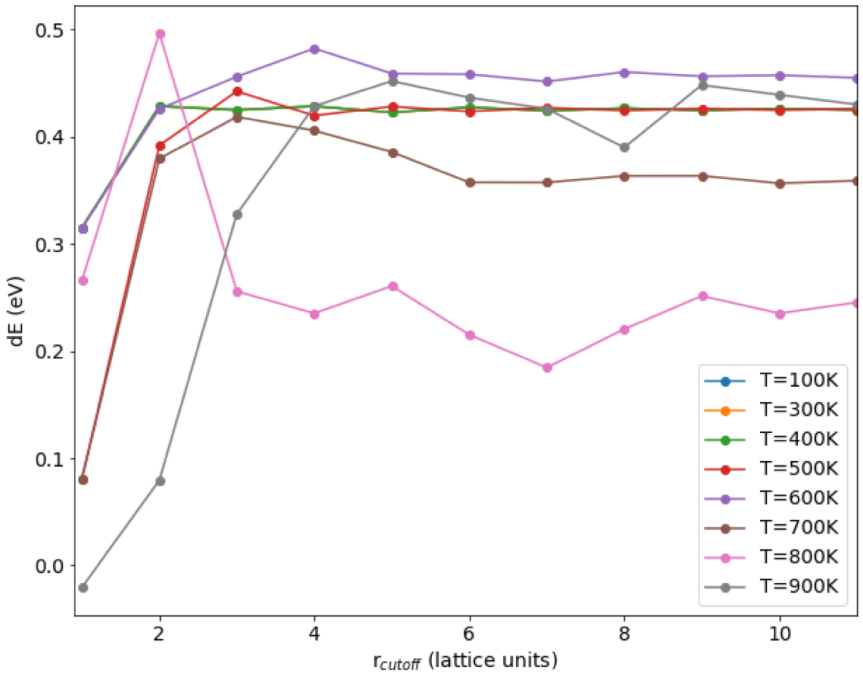

Figure 2: Convergence in the change in lattice energy (dE) for 2D Cu/ Zn disorder with respect to the cut-off radius (r_{cutoff}) for the lattice summations.

2 Equilibration check for 2D Cu/ Zn disorder

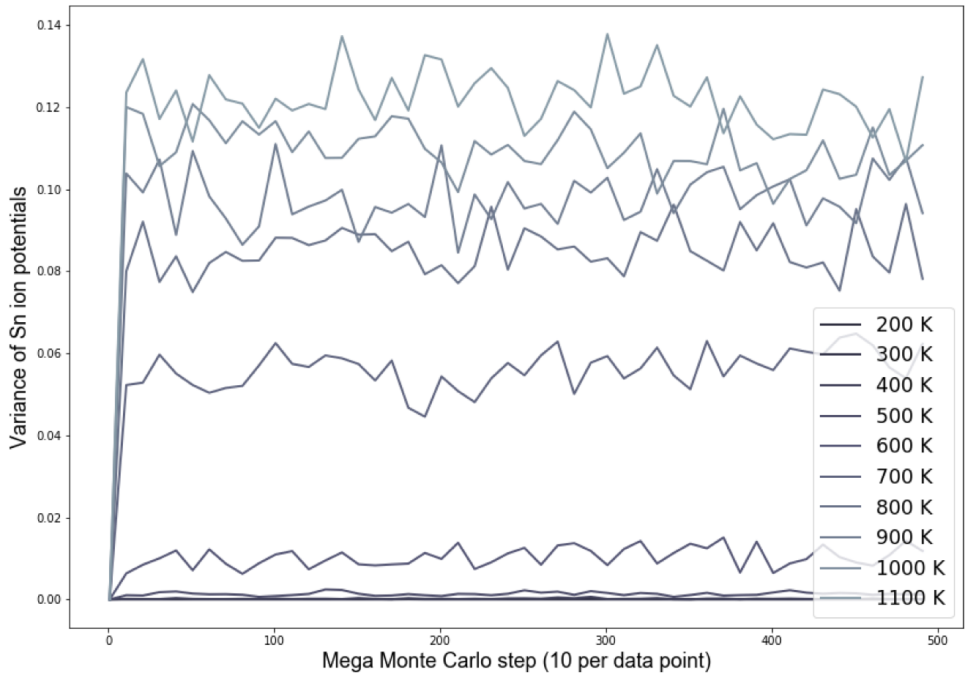

Figure 3: Variance in the distribution of the on-site electrostatic potential of Sn ions in a 24×24×24 Cu_2ZnSnS_4 system (containing 13,824 ions in total) across a range of simulation temperatures with 3D Cu/ Zn disorder. Each mega Monte Carlo step corresponds to sweeping across the lattice and attempting 100 trial moves per lattice site.

3 Finite-size check for 2D Cu/ Zn disorder

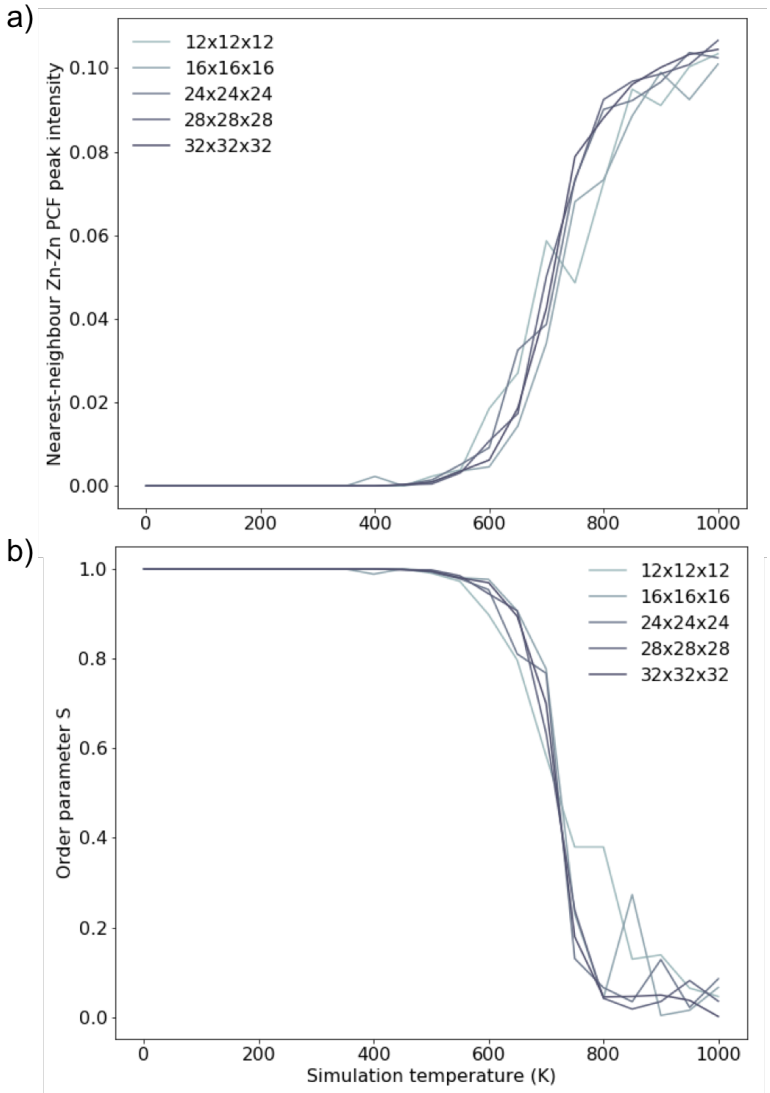

Figure 4: Two order parameters to assess finite-size effects for 2D Cu/ Zn disorder. Order parameters discussed further in the manuscript.

References

[1] N. Ashcroft and N. Mermin. *Solid State Physics*. Saunders College Publishing, 1976.

[2] A. West. *Bonding in Solids*. John Wiley & Sons, Ltd., 1999.

A.2 Supplemental material for: 'Candidate photoferroic absorber materials for thin-film solar cells from naturally occurring minerals: enargite, stephanite and bournonite'

Supplemental Material for: 'Candidate photoferroic absorber materials for thin-film solar cells from naturally occurring minerals: enargite, stephanite, and bournonite'

Suzanne K. Wallace[a,b], Katrine L. Svane[a], William P. Huhn[c], Tong Zhu[c], David B. Mitzi[c,d], Volker Blum[c], and Aron Walsh*[b,e]

[a] *Department of Chemistry, Centre for Sustainable Chemical Technologies, University of Bath, Claverton Down, Bath, BA2 7AY, UK*

[b] *Department of Materials, Imperial College London, Exhibition Road, London SW7 2AZ, UK. Email: a.walsh@imperial.ac.uk*

[c] *Department of Mechanical Engineering and Materials Science, Duke University, Durham, North Carolina 27708, USA*

[d] *Department of Chemistry, Duke University, Durham, North Carolina 27708, USA*

[e] *Global E^3 Institute and Department of Materials Science and Engineering, Yonsei University, Seoul 03722, Korea*

1 Total energy convergence for geometry optimization

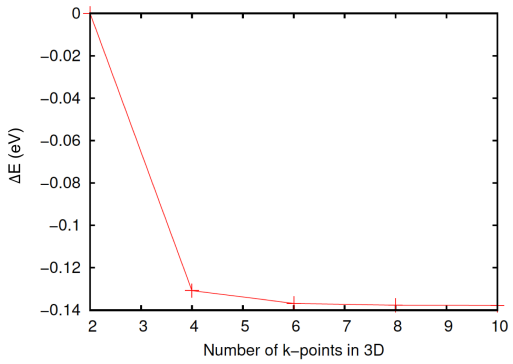

Figure 1: Convergence of the change in calculated total energy for enargite (Cu_3AsS_4) with respect to the number of k-points, calculated using the PBE functional.

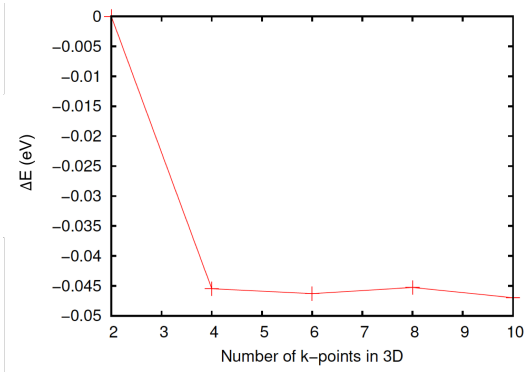

Figure 2: Convergence of the change in calculated total energy for bournonite ($CuPbSbS_3$) with respect to the number of k-points, calculated using the PBE functional.

2 Convergence of band structure

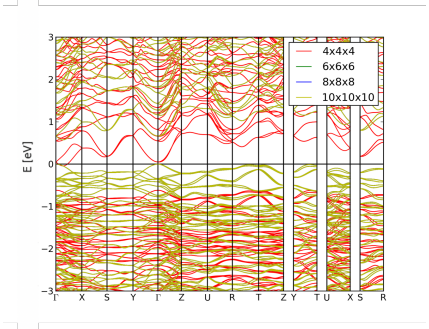

Figure 3: Convergence of bournonite band structure with increased density of k-points using a tight basis set calculated using PBE+SOC. Note that these calculations were performed for a different orientation of the unit cell as in the main body of the paper.

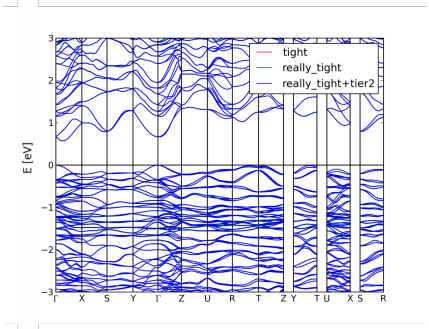

Figure 4: Convergence of bournonite band structure with increased basis set using an $8 \times 8 \times 8$ k-grid calculated using PBE+SOC. Note that these calculations were performed for a different orientation of the unit cell as in the main body of the paper.

3 Convergence of DOS

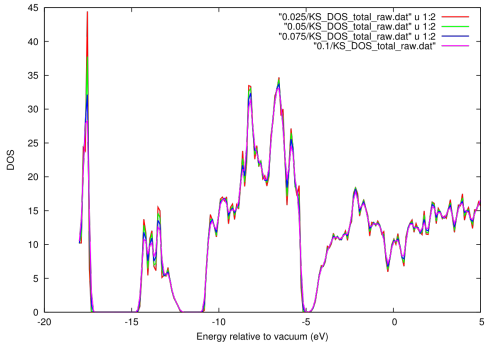

Figure 5: Convergence of bournonite density of states (DOS) with respect to Gaussian broadening applied to obtain a smooth density of states based on the peaks produced by individual states. Calculations were performed with an $8 \times 8 \times 8$ k-grid using PBE+SOC.

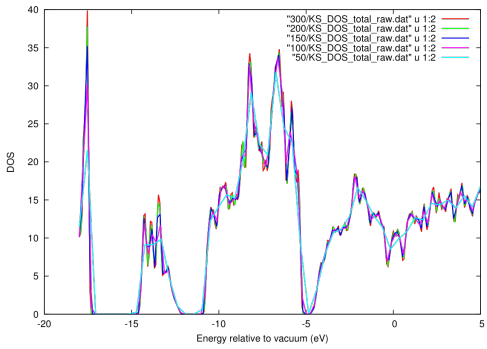

Figure 6: Convergence of bournonite density of states (DOS) with respect to the number of energy data points for which the DOS is given. Calculations were performed with an $8 \times 8 \times 8$ k-grid using PBE+SOC.

4 Fits to band extrema for effective mass calculation

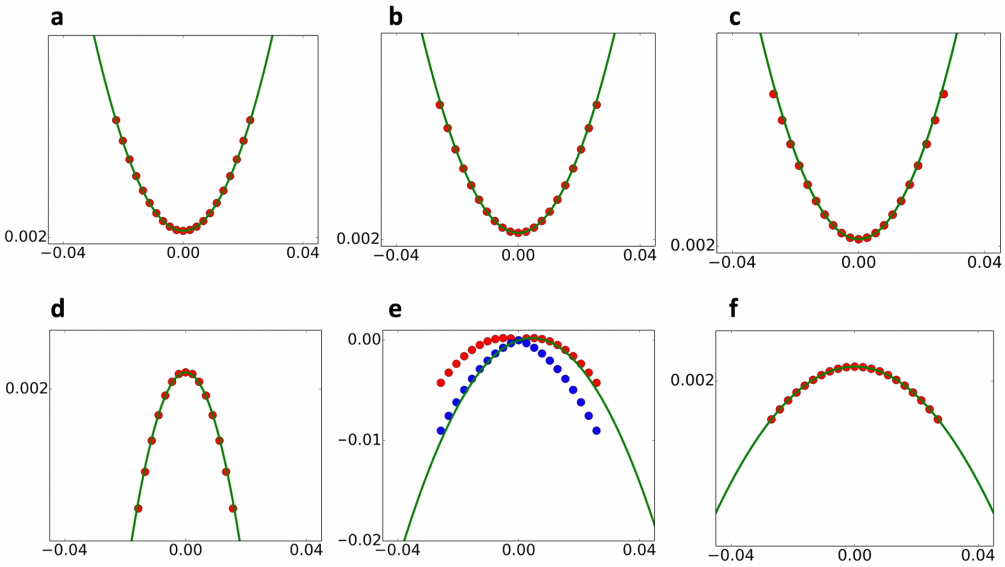

Figure 7: Parabolic fits to the band extrema of enargite (Cu_3AsS_4), where a-c correspond to the conduction band minimum (CBM) in directions ||a, ||b and ||c respectively and d-f correspond to the valence band maximum (VBM) in directions ||a, ||b and ||c respectively. Red dots are the band energies or eigenvalues, ϵ(k), green continuous curves are parabolic fits to these values, E(k). For the VBM in ||b direction, the extrema of the parabola did not coincide with the VBM for the data points. In this case we allow the fitting procedure to locate the position of the VBM and corresponding k-points. To check the extrapolated fitting curve, the DFT-HSE06+SOC ϵ(k) of the lower band (blue dots) are also shown for the VBM in the ||b direction.

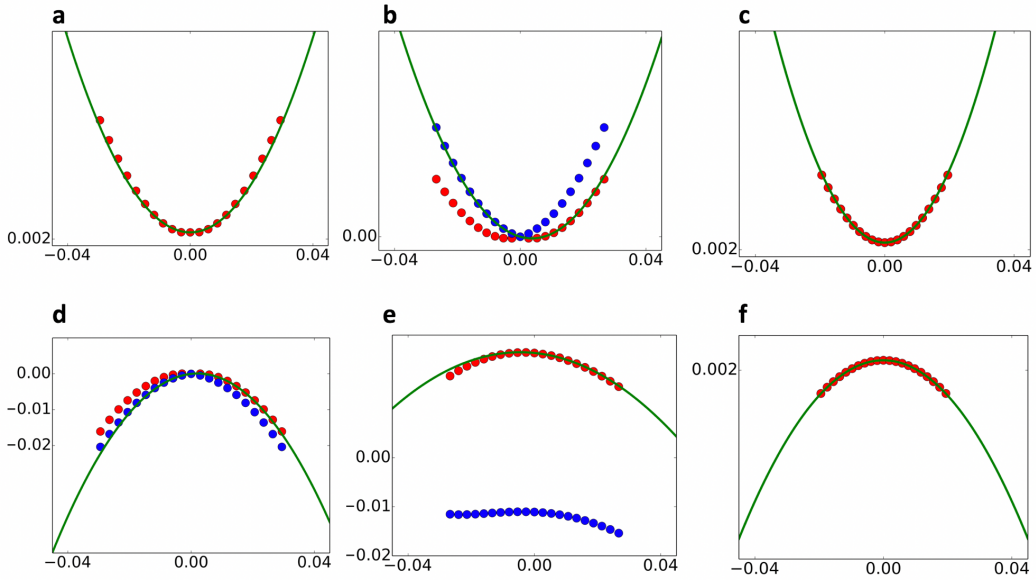

Figure 8: Parabolic fits to the band extrema of stephanite (Ag_5SbS_4), where a-c correspond to the conduction band minimum (CBM) in directions ||a, ||b and ||c respectively and d-f correspond to the valence band maximum (VBM) in directions ||a, ||b and ||c respectively. Red dots are the band energies or eigenvalues, ϵ(k), green continuous curves are parabolic fits to these values, E(k). For the VBM in ||a and ||b directions, the extrema of the parabola did not coincide with the VBM for the data points. In this case we allow the fitting procedure to locate the position of the VBM and corresponding k-points. To check the extrapolated fitting curve, the DFT-HSE06+SOC ϵ(k) of the lower band (blue dots) are also plotted. Similarly, for the CBM in the ||b direction the extrema of the parabola did not coincide with the CBM for the data points. We again allow the fitting procedure to locate the position of the CBM and corresponding k-points. To check the extrapolated fitting curve, the DFT-HSE06+SOC ϵ(k) of the lower band (blue dots) are also plotted.

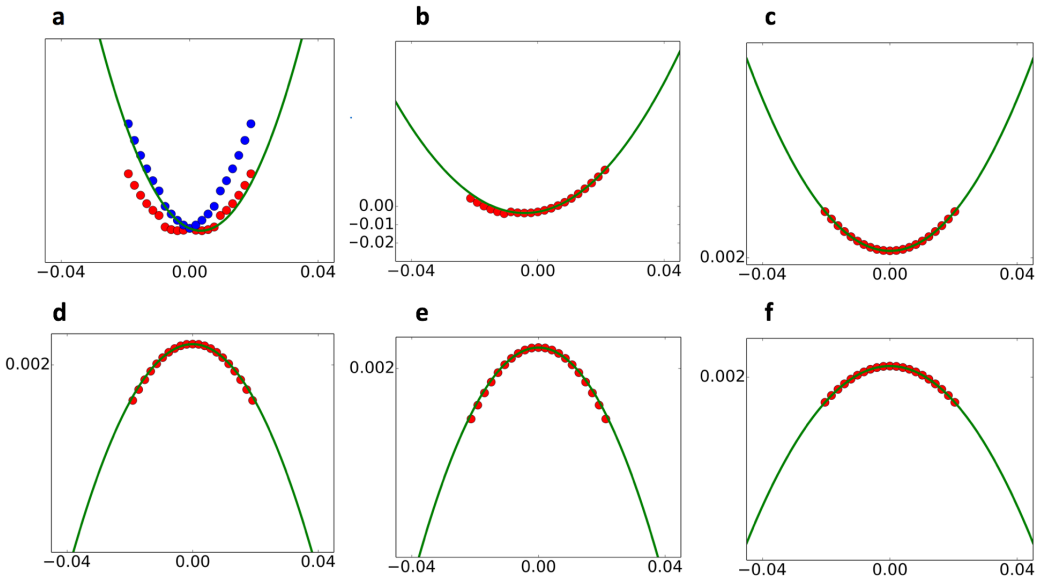

Figure 9: Parabolic fits to the band extrema of bournonite ($CuPbSbS_3$), where a-c correspond to the conduction band minimum (CBM) in directions ||a, ||b and ||c respectively and d-f correspond to the valence band maximum (VBM) in directions ||a, ||b and ||c respectively. Red dots are the band energies or eigenvalues, ϵ(k), green continuous curves are parabolic fits to these values, E(k). For the CBM in ||a direction, the extrema of the parabola did not coincide with the CBM for the data points. In this case we allow the fitting procedure to locate the position of the CBM and corresponding k-points. To check the extrapolated fitting curve, the DFT-HSE06+SOC ϵ(k) of the upper band (blue dots) are also shown for the CBM in the ||a direction.

5 Convergence of dielectric functions

We perform a convergence test for the optical dielectric function of bournonite ($CuPbSbS_3$) using the PBE functional. It was only possible to carry out the convergence test with PBE for bournonite, as both stephanite and enargite do not possess a band gap at this level of theory. From this we find the dielectric function of bournonite to converge with a k-point grid of density 8x8x8, as shown in figure 10. However, the smaller unit cells and lower valence band DOS of enargite and stephanite could indicate that these materials may require a more dense k-point grid than for bournonite. Therefore for enargite and stephanite a subsequent convergence test was carried out at the HSE level of accuracy, as shown in figures 11 and 12, where it was found that both materials required a 10x10x10 k-point grid for a converged dielectric function. All calculations for the optical dielectric function were performed using the FHI-aims software package.

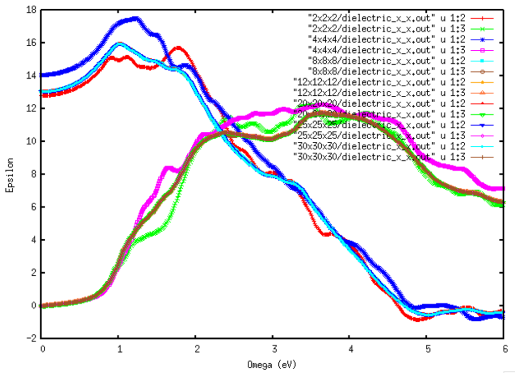

Figure 10: Convergence of the calculated dielectric function of bournonite ($CuPbSbS_3$), calculated with the PBE functional and SOC, with respect to the density of the k-point grid.

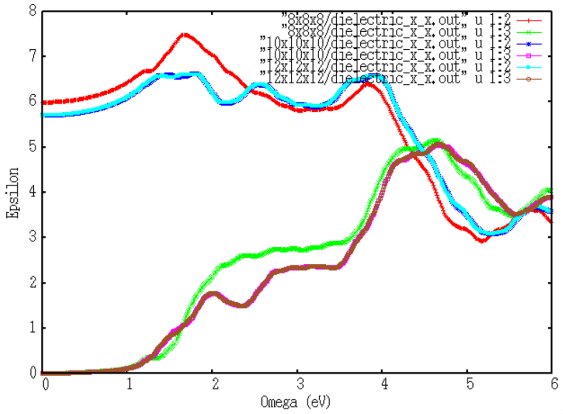

Figure 11: Convergence in the calculated optical dielectric function of enargite (Cu_3AsS_4), calculated with the HSE functional and SOC, with respect to the density of the k-point grid.

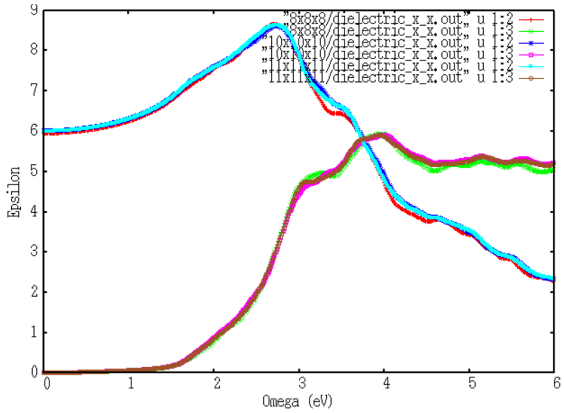

Figure 12: Convergence in the calculated optical dielectric function of stephanite (Ag_5SbS_4), calculated with the HSE functional and SOC, with respect to the density of the k-point grid.

6 Derivation of units of the absorption coefficient

The complex dielectric function is given by equation 1.

$$\underline{\epsilon} = \epsilon + i\tilde{\epsilon} \tag{1}$$

The extinction coefficient is given by equation 2, where $|\underline{\epsilon}|$ is given by equation 3.

$$\kappa = \sqrt{\frac{|\underline{\epsilon}| + \epsilon}{2}} \tag{2}$$

$$|\underline{\epsilon}| = \sqrt{\epsilon^2 + \tilde{\epsilon}^2} \tag{3}$$

The absorption coefficient is given by equation 4. $\frac{1}{\lambda}$ can be obtained from equation 5, where ω is the energy of the incident photon, to give the expression for α in equation 6

$$\alpha = \frac{4\pi\kappa}{\lambda} \tag{4}$$

$$\omega = \frac{hc}{\lambda} \tag{5}$$

$$\alpha(\omega) = \frac{4\pi}{hc}\omega\sqrt{\frac{-Re\epsilon(\omega) + \sqrt{Re^2\epsilon(\omega) + Im^2\epsilon(\omega)}}{2}} \tag{6}$$

From equation 6, we can obtain the units of the absorption coefficient. ϵ is dimensionless, the units of the α therefore are the units of $\frac{\omega}{hc}$. ω is in units of eV, Planck's constant, $h = 4.135667662 \times 10^{-15} eVs$ and the speed of light, c = $3{\times}10^8$ m s^{-1}. This gives $hc \approx 1.24 \times 10^{-6} eVm$ or $1.24 \times 10^{-4} eVcm$. Therefore α is in units of cm^{-1}.

7 Electron localisation function

The electron localisation function (ELF) [3] is calculated in VASP using the HSE06 functional and a $2 \times 2 \times 2$ k-mesh. The ELF gives the probability of finding an electron near a reference electron, and thus highlights the presence of bonds and lone pairs.

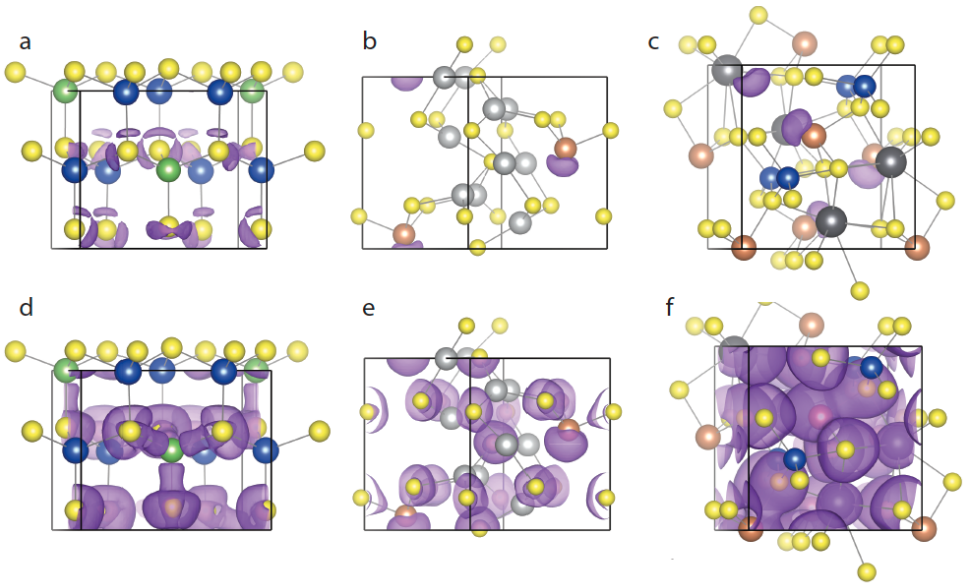

Figure 13: Electron localisation function of enargite (Cu_3AsS_4) (a and d), stephanite (Ag_5SbS_4) (b and e) and bournonite ($CuPbSbS_3$) (c and f). The values of the isosurfaces are a) 0.875, b-c) 0.925, d-e) 0.75 and f) 0.45.

The ELF is shown for enargite, bournonite and stephanite in Figure 13. At high values of the iso-surface (a-c) the lone pairs of Sb in stephanite and bournonite (b and c) are clearly seen. No lone pairs are seen for As in enargite(a), but at lower values of the ELF isosurface bonding is evident (d). The Pb atoms in bournonite do not show any lone pairs at high values of the isosurface either, but a localised spherical region around the Pb

atom is observed at lower values (f). The results for bournonite are in agreement with previous calculations [1].

8 Calculations of spontaneous lattice polarisation

Bournonite and enargite crystallise in the $Pmn2_1$ spacegroup (31), while stephanite crystallises in the $Cmc2_1$ spacegroup (36). Both of these groups have a mirror plane in the yz-plane, implying no polarisation in the x-direction and a screw axis along the z–direction, implying that polarisation is allowed along the z–direction only [2]. Indeed we can verify that the polarization is 0 along the x- and y-axes in our three structures.

To investigate the strength of polarity in the materials, calculations of the spontaneous electric polarisation, P_s, of each material were performed using the Berry-phase formalism [4] with the methodology outlined in reference [5]. Only differences in polarisation are physically meaningful, we therefore optimise the structure with polarisation $+P_s$ and invert this structure to get the opposite polarisation, $-P_s$. The polarisation difference between those two structures, $2P_s$, is calculated and we verify that the change in polarisation is continuous by also calculating the polarisation for a number of configurations connecting the two structures, with their coordinates $\mathbf{r}$ obtained from equation 7, where λ is a number between 0 and 1.

$$\mathbf{r} = \lambda \mathbf{r}_{P_s} + (1 - \lambda)\mathbf{r}_{-P_s} \tag{7}$$

Note that to make the path the atoms in the end structure are renumbered to make the path shorter. This can be done in several ways and our choice is arbitrary, made by inspection (the choice should not be important as the result should only depend on the end points). The calculations were performed in VASP using the HSE06 functional, PAW pseudopotentials and a 500

eV cutoff energy. Due to computational limitations we only use $2\times2\times2$ k-points for these calculations, however from comparison with Γ-point calculations the effect of k-points on the calculated polarization is found to be minimal (see Figure 14). We do however find that some of the intermediate structures close to λ=0.5 become metallic when more than one k-point is used, and the polarisation can thus not be calculated for these structures. Instead we perform the calculations for all structures along the path using the Γ-point only and use the results to construct the path connecting the non-metallic points calculated with $2\times2\times2$ k-points. The spontaneous polarisation is found to be 67.8 and 68.3 μ C cm^{-2} for the $2 \times 2 \times 2$ and $1 \times 1 \times 1$ k-point meshes respectively for enargite.

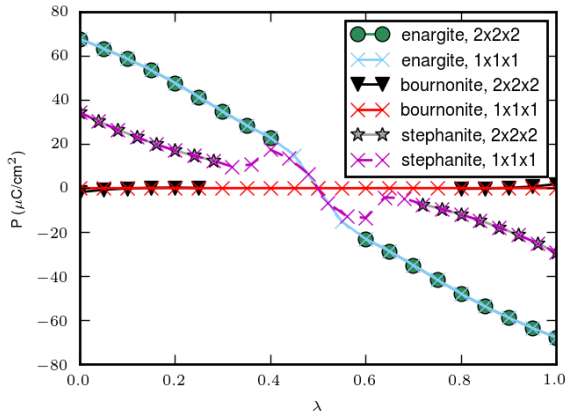

Figure 14: Calculated spontaneous polarisations of enargite (Cu_3AsS_4), stephanite (Ag_5SbS_4) and bournonite ($CuPbSbS_3$) using $1\times1\times1$ and $2\times2\times2$ k-points.

9 Energy barriers to switch direction of lattice polarisations

Figure 15 shows that the energy change along the paths used to calculate the spontaneous lattice polarisation. These provide an upper bound for the energy barrier for polarisation switching, however we note that since the path is not optimised (e.g. as in a nudged elastic band calculation) the real barrier is expected to be significantly lower.

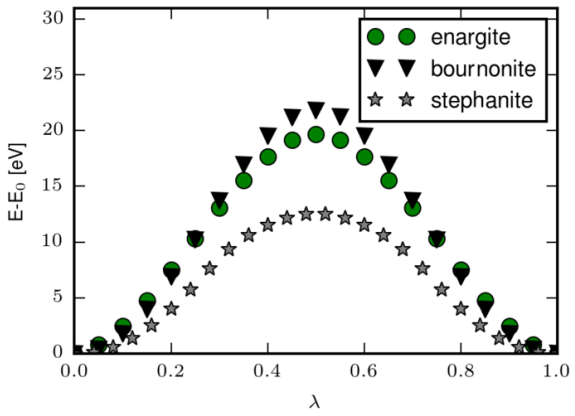

Figure 15: Energy barrier to switch the direction of lattice polarisation in enargite (Cu_3AsS_4), stephanite (Ag_5SbS_4) and bournonite ($CuPbSbS_3$).

A.3 Supplemental material for: 'Finding a junction partner for candidate solar cell absorbers enargite and bournonite from electronic band and lattice matching'

Supplemental material for: 'Finding a junction partner for candidate solar cell absorbers enargite and bournonite from electronic band and lattice matching'

Suzanne K. Wallace[a,b], Keith T. Butler[c], Yoyo Hinuma[d,e], and Aron Walsh[*b,f]

[a] *Department of Chemistry, Centre for Sustainable Chemical Technologies, University of Bath, Claverton Down, Bath, BA2 7AY, UK*

[b] *Department of Materials, Imperial College London, Exhibition Road, London SW7 2AZ, UK. Email: a.walsh@imperial.ac.uk*

[c] *ISIS Neutron and Muon Source, Rutherford Appleton Laboratories, Didcot, Oxfordshire, OX11 0QX*

[d] *Center for Frontier Science, Chiba University, Chiba 263-8522, Japan*

[e] *Center for Materials Research by Information Integration, Research and Services Division of Materials Data and Integrated System, National Institute for Materials Science, Tsukuba 305-0047, Japan*

[f] *Department of Materials Science and Engineering, Yonsei University, Seoul 03722, Korea*

1 Slab models

Symmetric and non-polar surface terminations for enargite (Cu_3AsS_4) and bournonite ($CuPbSbS_3$) cut using methodology in Ref. [2]. The VESTA[4] software package was used to create Fig. 1 and 2.

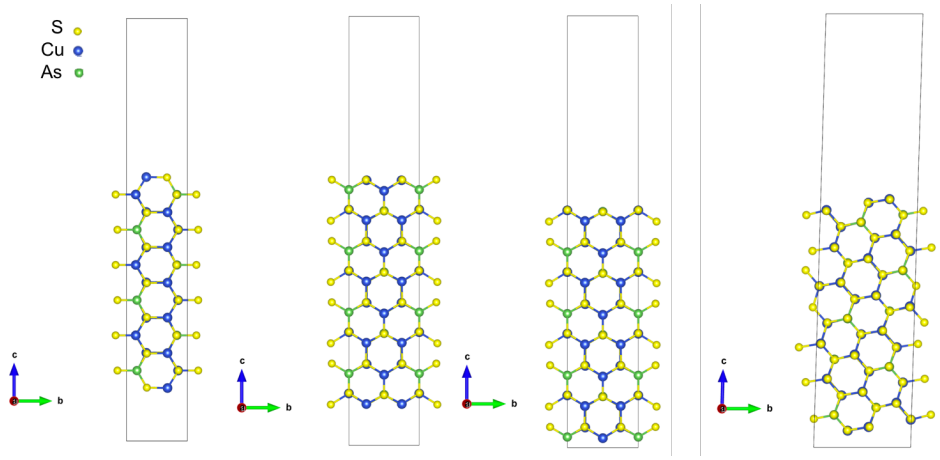

Figure 1: Enargite (Cu_3AsS_4) (100), (010)a, (010)b, (110) surface terminations.

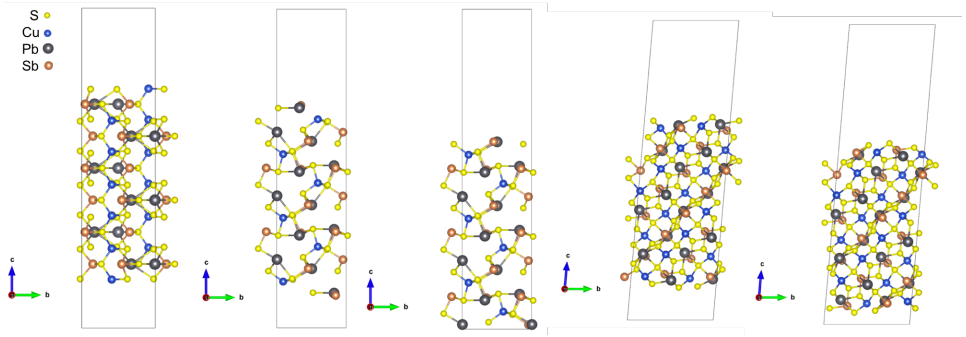

Figure 2: Bournonite ($CuPbSbS_3$) (100), (010)a, (010b), (110)a, (110)b surface terminations.

2 Slab potentials

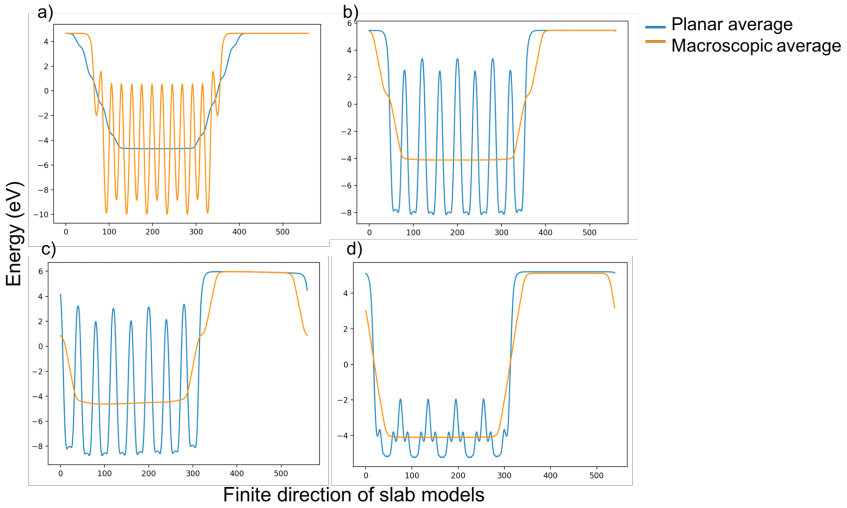

Figure 3: Electrostatic potentials across the finite direction of slab models for enargite (Cu_3AsS_4) a) (100), b) (010)a, c) (010)b, d) (110) surfaces.

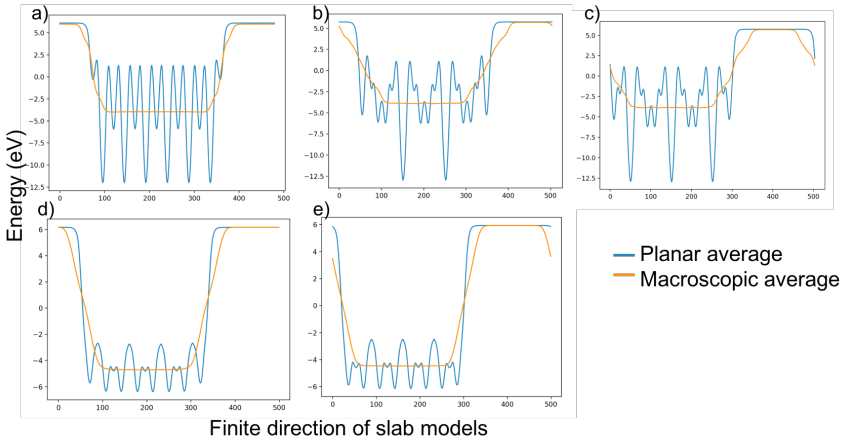

Figure 4: Electrostatic potentials across the finite direction of slab models for bournonite ($CuPbSbS_3$) a) (100), b) (010)a, c) (010)b, d) (110)a, e) (110)b surfaces.

3 Structure files for junction partners used for lattice matching

Table 1: Materials project IDs for structure files used for lattice matching step.

Candidate	Materials project ID
Dy_2S_3	mp-32826
La_2S_3	mp-7475
Nd_2S_3	mp-32586
Sm_2S_3	mp-32645
Tb_2S_3	mp-673644
WO_3	mp-19033
ZnTe	mp-2176
Ce_2S_3	mp-20973
$Zn_3In_2S_6$	mp-637614
SiC	mp-11714
GaP	mp-2490
ZnSe	mp-1190
Ce_2O_3	mp-542313
Bi_2O_3	mp-23262
$CoTiO_3$	mp-19424
$NiTiO_3$	mp-556251
SnS_2	mp-1170
Cu_2O	mp-361
Gd_2S_3	mp-608146
AlP	mp-1550
MoO_3	mp-18856
CuI	mp-570136
As_2S_3	mp-641
CdS	mp-672
PbO	mp-19921
CoO	mp-24864

4 Band alignment with final junction partners candidates for all absorber slabs

Below are band alignment plots of the final junction partner candidates for each absorber layer slab. Ionisation potentials, electronic band gaps and electron affinities for the absorber materials are calculated in this work, but those of the candidate junction partners are from the dataset used in Ref. [1] and contained in the ELS git repository. The minimum strain termination for each junction partner candidate were shown in the main manuscript in Tables 2 and 3.

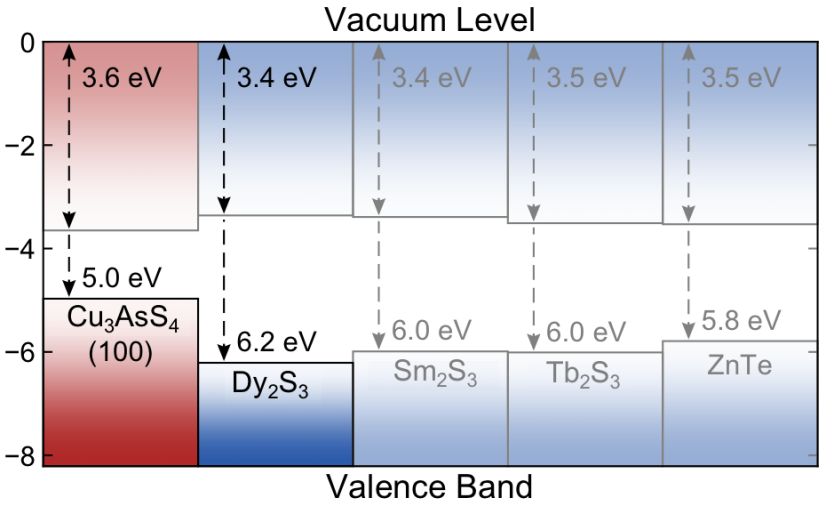

Figure 5: Spike conduction band offset (CBO) for enargite (Cu_3AsS_4) (100) termination.

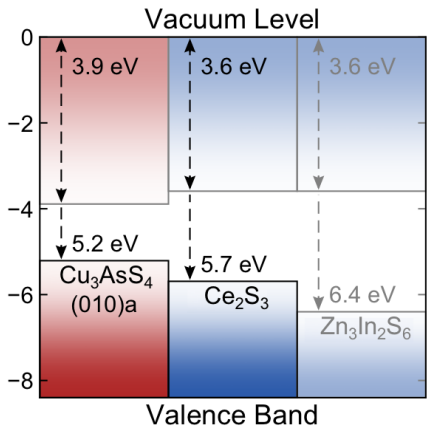

Figure 6: Spike conduction band offset (CBO) for enargite (Cu_3AsS_4) (010)a termination.

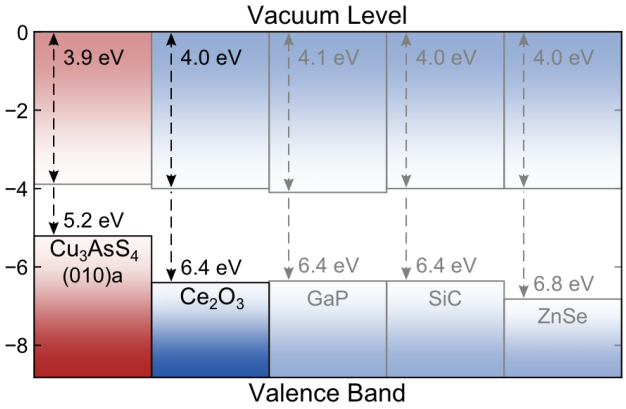

Figure 7: Cliff conduction band offset (CBO) for enargite (Cu_3AsS_4) (010)a termination.

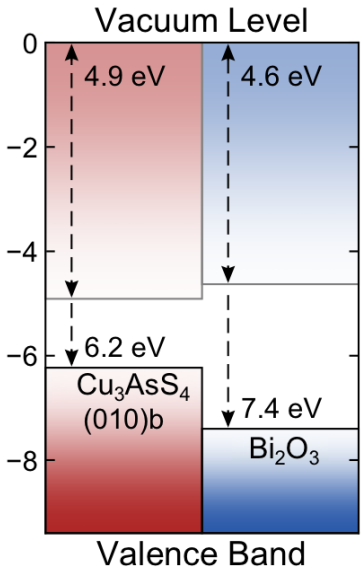

Figure 8: Spike conduction band offset (CBO) for enargite (Cu_3AsS_4) (010)b termination.

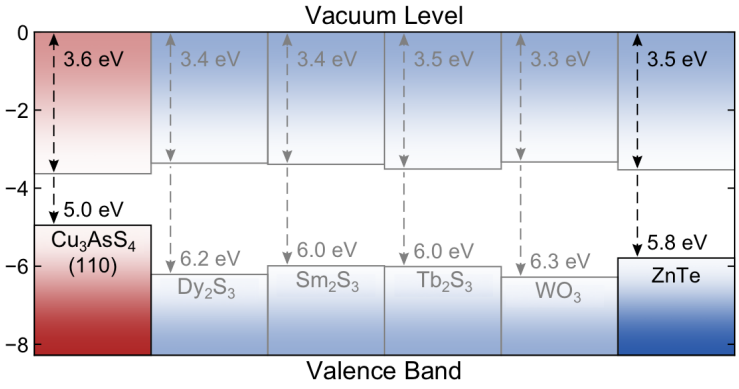

Figure 9: Spike conduction band offset (CBO) for enargite (Cu_3AsS_4) (110) termination.

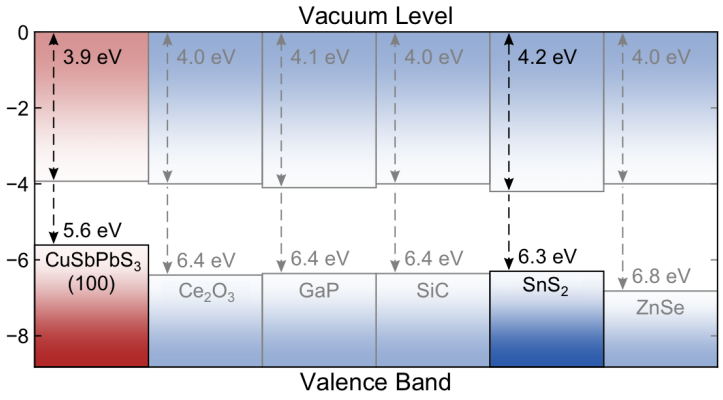

Figure 10: Cliff conduction band offset (CBO) for bournonite ($CuPbSbS_3$) (100) termination.

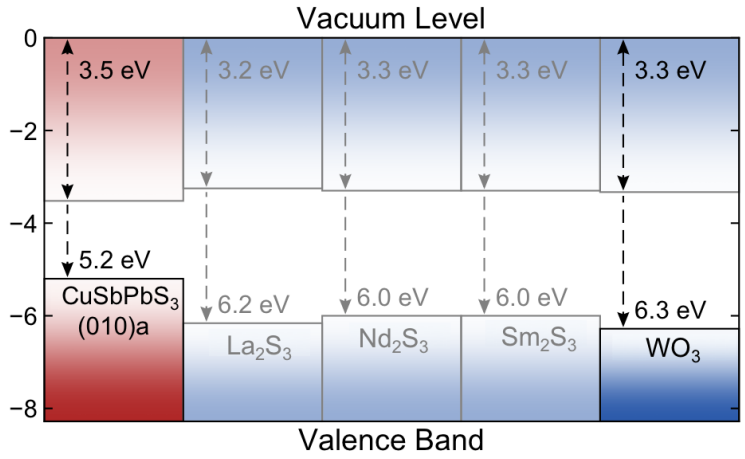

Figure 11: Spike conduction band offset (CBO) for bournonite ($CuPbSbS_3$) (010)a termination.

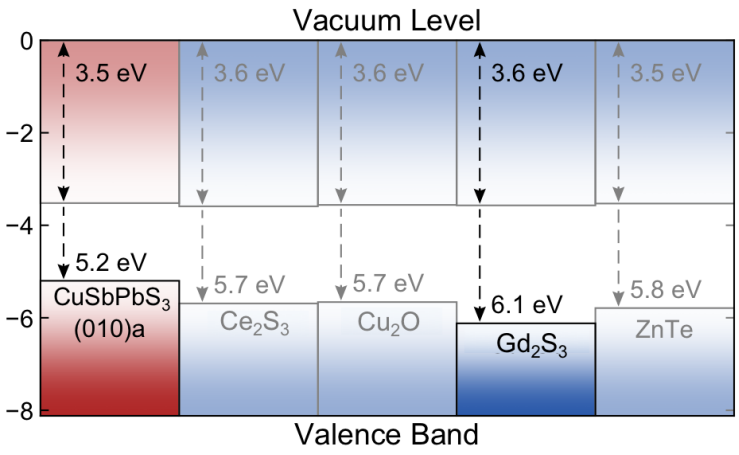

Figure 12: Cliff conduction band offset (CBO) for bournonite ($CuPbSbS_3$) (010)a termination.

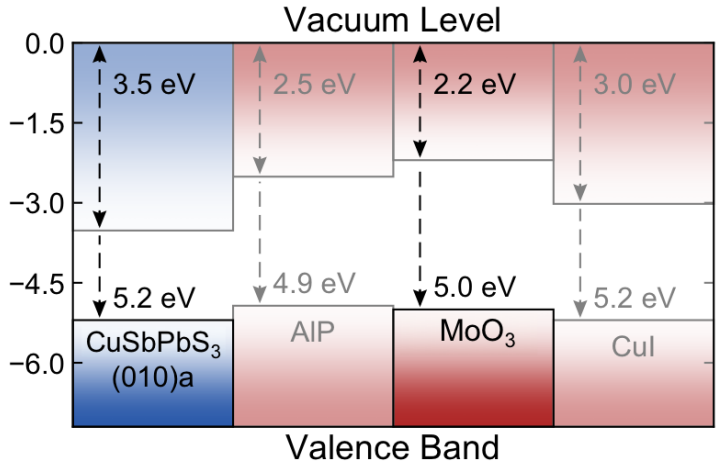

Figure 13: Cliff valence band offset (VBO) for bournonite ($CuPbSbS_3$) (010)a termination.

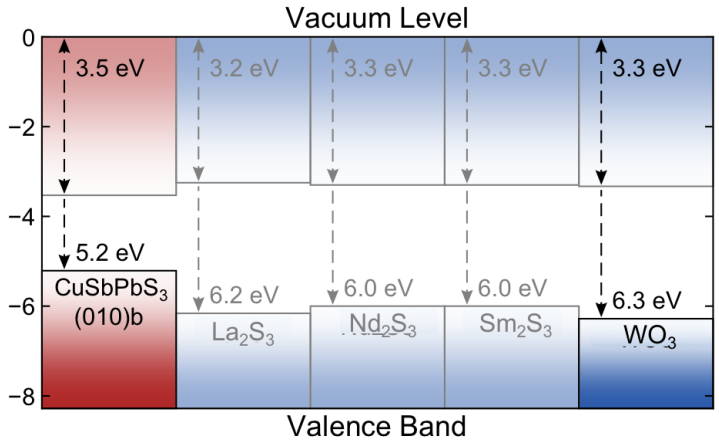

Figure 14: Spike conduction band offset (CBO) for bournonite ($CuPbSbS_3$) (010)b termination.

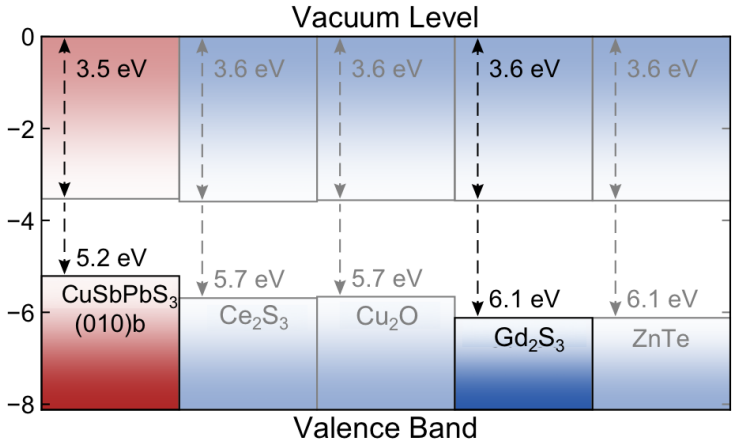

Figure 15: Cliff conduction band offset (CBO) for bournonite ($CuPbSbS_3$) (010)b termination.

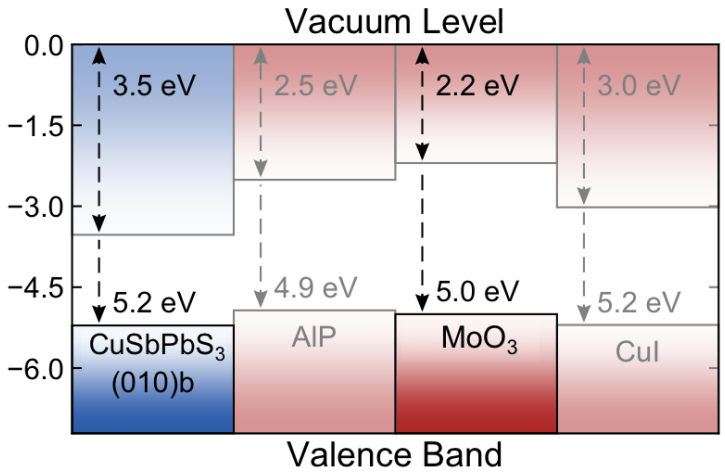

Figure 16: Cliff valence band offset (VBO) for bournonite ($CuPbSbS_3$) (010)b termination.

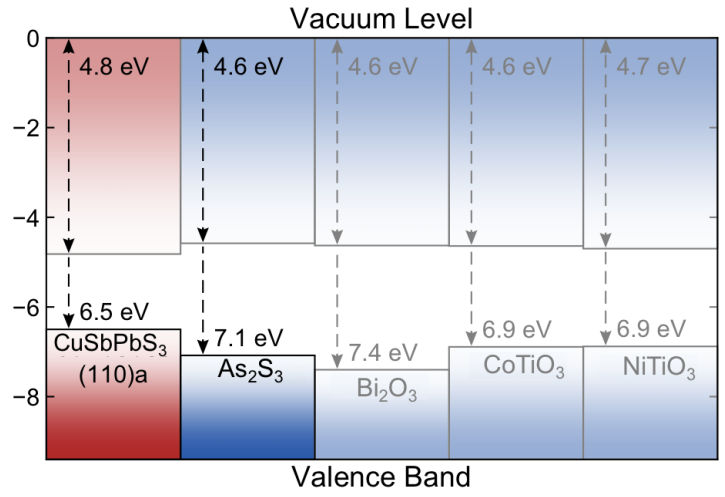

Figure 17: Spike conduction band offset (CBO) for bournonite ($CuPbSbS_3$) (110)a termination.

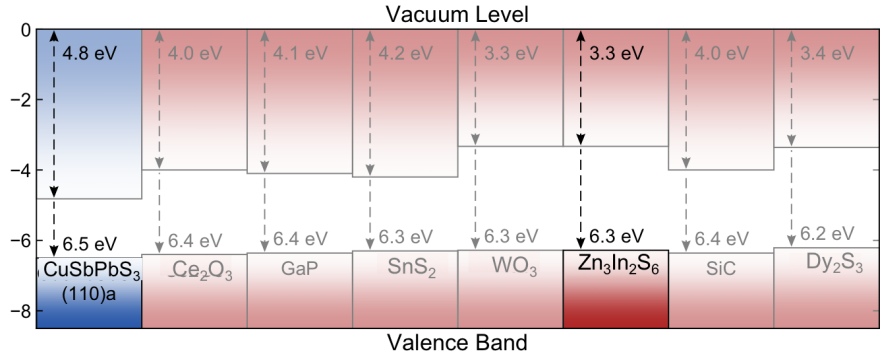

Figure 18: Cliff valence band offset (VBO) for bournonite ($CuPbSbS_3$) (110)a termination.

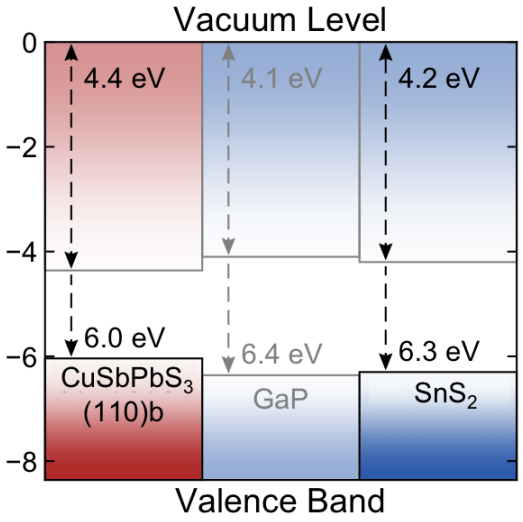

Figure 19: Spike conduction band offset (CBO) for bournonite ($CuPbSbS_3$) (110)b termination.

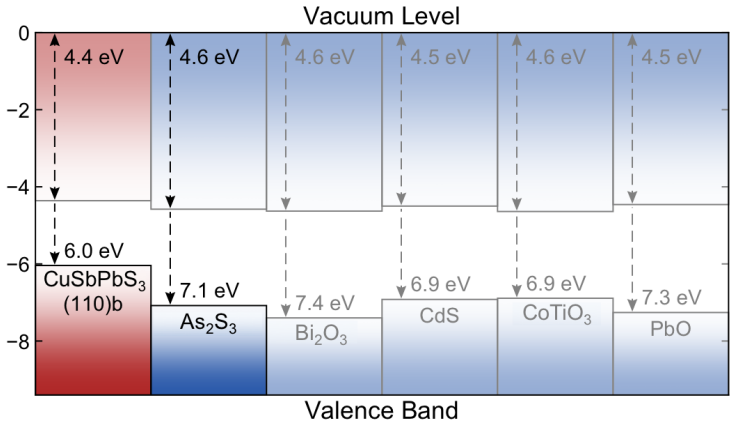

Figure 20: Cliff conduction band offset (CBO) for bournonite ($CuPbSbS_3$) (110)b termination.

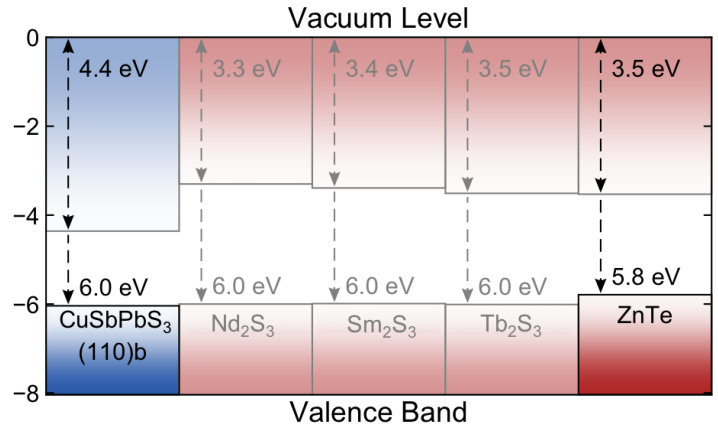

Figure 21: Cliff valence band offset (VBO) for bournonite ($CuPbSbS_3$) (110)b termination.

References

[1] K. T. Butler, Y. Kumagai, F. Oba, and A. Walsh. Screening procedure for structurally and electronically matched contact layers for high-performance solar cells: hybrid perovskites. *J. Mater. Chem. C*, 4(6):1149–1158, 2016.

[2] Y. Hinuma, Y. Kumagai, F. Oba, and I. Tanaka. Categorization of surface polarity from a crystallographic approach. *Computational Materials Science*, 113:221 – 230, 2016.

[3] Y. Kumagai, K. T. Butler, A. Walsh, and F. Oba. Theory of ionization potentials of nonmetallic solids. *Physical Review B*, 95(12), mar 2017.

[4] K. Momma and F. Izumi. VESTA for three-dimensional visualization of crystal, volumetric and morphology data. *Journal of Applied Crystallography*, 44(6):1272–1276, oct 2011.